Syracuse University
SURFACE at Syracuse University

Dissertations - ALL | SURFACE at Syracuse University

5-12-2024

Development and Application of Photoresponsive Small Molecule Probes to Modulate and Characterize Neuroreceptors

Spencer Kim
Syracuse University

Follow this and additional works at: https://surface.syr.edu/etd

Part of the Chemistry Commons

Recommended Citation

Kim, Spencer, "Development and Application of Photoresponsive Small Molecule Probes to Modulate and Characterize Neuroreceptors" (2024). *Dissertations - ALL*. 1941.
https://surface.syr.edu/etd/1941

This Dissertation is brought to you for free and open access by the SURFACE at Syracuse University at SURFACE at Syracuse University. It has been accepted for inclusion in Dissertations - ALL by an authorized administrator of SURFACE at Syracuse University. For more information, please contact surface@syr.edu.

Abstract

The field of neuroscience is rapidly evolving and so the development of novel tools that support innovative research is urgently needed. Two tools that have proven to be particularly impactful to the field of neuroscience are activity-based protein profiling (ABPP) and optogenetics, both of which have seen widespread application but with relatively limited advancement of the underlying technology. Limitations of ABPP and optogenetics have become increasingly apparent and research output is stalling due to lack of technological advancement. For example, few systems exist for targeting low-abundance and unstable proteins via ABPP and application of ABPP and optogenetic systems thus far has largely demonstrated the technology's utility across families of receptors rather than subtype specific targets. Direct modulation of subtype specific endogenous neuroreceptor activity is key to connecting molecular and systems neuroscience, so next generation molecular tools to address these limitations possess huge potential. Here, we have demonstrated (1) The development and application of photoactivatable forms of WAY-161503 and *N*-desmethylclozapine (NDMC), designed as a system that enables spectrally multiplexed, spatiotemporal controlled modulation of native human serotonin receptor 2C (5-HT_{2C}) calcium (Ca^{2+}) signaling and (2) The design and use of bioactive photoaffinity probes for human dopamine receptor D2 (DRD2), which demonstrate excellent activity in "workhorse" biochemical assays, receptor labeling, cell labeling, and chemoproteomics. The advancements of these technologies demonstrate an important step forward for optogenetics, where modulation of endogenous neuroreceptors has proven to be a challenge, and for ABPP, where underrepresentation of low-abundance and unstable proteins has limited the scope of

advancements in the field of proteomics. Future work will continue to develop neuroreceptor targeted photoactive probes, with lysergic acid (LSA) derivatives providing an initial family of targets that are both synthetically interesting and biologically important to the fields of neuroscience, chemical biology, and medicinal chemistry.

Development and Application of Photoresponsive Small Molecule Probes to Modulate and Characterize Neuroreceptors

by

Spencer Kim

BS, University of Maryland, 2016

MPhil, Syracuse University, 2020

Dissertation

Submitted in partial fulfillment of the requirements for the degree of

Doctor of Philosophy in Chemistry.

Syracuse University

June 2024

Copyright © Spencer Kim 2024

All Rights Reserved

Acknowledgments

I thank first and foremost my supervisor, Dr. Rachel C. Steinhardt, for her relentless encouragement, mentorship, flexibility, and support in all areas of scientific inquiry. Rachel, the time you have spent working with me the past five years has wholly made me the scientist I am today. Thank you.

I would like to express my appreciation for the members of my thesis defense committee: Dr. John D Chisholm and Dr. Micheal B. Sponsler for their insight and support of my work.

I would like to thank Dr. Jonathan French for his mentorship in chemistry education research, university teaching, and career planning.

I would like to acknowledge my friends in the lab, Ray, Keely, Emma, Jasmine, Pantea, and Sara, who made the work described herein fun and made living here tolerable.

Table of Contents

Abstract i

Acknowledgments v

Table of Contents vi

Listing of Figures xii

Listing of Tables xiv

Listing of Schemes xv

Abbreviations xvi

1 Review of photo-responsive probes in cellular and molecular neuroscience 1

1.1 Current state and future outlook of cellular and molecular neuroscience 1

1.1.1 Importance of cellular and molecular neuroscience 1

1.1.2 Advancements and future outlook 2

1.2 Survey of the current state of the art 4

1.2.1 Activity-based protein profiling 4

1.2.2 Optogenetics 8

1.3 References 14

2 Cloning and tissue culture 31

2.1 Chimeric G-protein (G_{qi5}) 31

2.1.1 Cloning of recombinant G_{qi5} 32

2.1.2 Validating G_{qi5} 33

2.1.3 Experimental 34

2.2 Stable DRD2 cell line generation 35

2.2.1 Cloning of DRD2 transfer plasmid 35

2.2.2 Lentivirus production and viral transduction 36

2.2.3 Cell line enrichment 37

2.2.4 Experimental 37

2.3 References 39

3 Photoaffinity probes for DRD2 41

3.1 Introduction 41

3.2 Design 43

3.3 Synthesis 46

3.4 Pharmacology 48

3.4.1 Intracellular Ca^{2+} mobilization bioactivty 48

3.4.2 TANGO bioactivty 51

3.5 Photoactivity 53

3.5.1 Click microscopy labelling propensity 53

3.6 Specificity 56

3.6.1 Flow cytometry quantification of probe labelling of cells. 56

3.6.2 Western blot analysis of DRD2-probe binding 59

3.7 Application 60

3.7.1 Proteomic identification of primary rat brain protein networks covalently modified by probes 60

3.8 Conclusion and future directions 68

3.9 Experimental 69

3.9.1 Chemistry 69

3.9.2 Intracellular Ca2+ mobilization assay 77

3.9.3 B-arrestin (TANGO) assay 78

3.9.4 Photo-cross-linking of DRD2-expressing 293T cells and primary neurons with probes. 79

3.9.5 Click chemistry conjugation and microscopy. 79

3.9.6 Western blot 80

3.9.7 Photoaffinity quantification using FACS. 82

3.9.8 LC/MS proteomics 83

3.10 References 87

4 Photocaged probes for $5HT_{2C}$ 100

4.1 Introduction 100

4.2 Synthesis 103

4.3 Pharmacology 106

4.3.1 TANGO bioactivity 106

4.4 Photoactivity 107

4.4.1 Uncaging efficiency via chromatography 107

4.4.2 Spontaneous hydrolysis via chromatography 109

4.5 Photoactivation of WinterGreen-WAY and WinterRed-NDMC in cells expressing the $5\text{-}HT_{2C}$ receptor 110

4.5.1 Aberrant uncaging. 110

4.5.2 Spectral orthogonality 111

4.5.3 Kinetics and spatial resolution of WinterGreen-WAY (5) activation. 112

4.5.4 Photoactivation of WinterRed-NDMC (12). 119

4.5.5 Orthogonal activation of WinterGreen-WAY (5) and WinterRed-NDMC (12). 121

4.6 Conclusion and future direction 123

4.7 Experimental 124

4.7.1 Synthetic chemistry general experimental procedures 124

4.7.2 HPLC photolysis characterization 127

4.7.3 TANGO assay biochemical characterization 127

4.7.4 Uncaging in cell culture 128

4.8 References 129

5 Progress toward the synthesis of dihydrolysergic acid 136

5.1 Introduction 136

5.2 Synthesis 137

5.2.1 Boger's preparation of dihydrolysergic acid 138

5.2.2 Studies toward a novel synthesis of dihydrolysergic acid 140

5.3 Conclusion 144

5.4 Experimental 145

5.5 References 149

6 Conclusion 153

7 Appendix A: NMR spectra 154

7.1 Chapter 3: Photoaffinity Probes for DRD2..... 154

7.2 Chapter 4: Photocaged Probes for 5HT2C 180

7.3 Chapter 5: Progress Toward the Synthesis of LSA 185

Appendix B: Curriculum Vitae..... 195

Listing of Figures

Figure 1. ABPP probe design and function. 7

Figure 2. Traditional and synthetic optogenetics. 10

Figure 3. Photoaffinity labeling for the simultaneous determination of protein targets and sites of probe labeling. 45

Figure 4. Intracellular calcium flux assay. 50

Figure 5. β-Arrestin recruitment analysis. 52

Figure 6. Photo-cross-linking of dye-clicked probe: confocal microscopy. 55

Figure 7. Flow cytometry quantification of probe labeling. 58

Figure 8. Photo-cross-linking of probes 5 and 7 to DRD2 visualized with Western blot. 60

Figure 9. Workflow for affinity purification and proteomic analysis. 61

Figure 10. Previously-known proteins modulated by ropinirole according to STICH 65

Figure 11. Previously-known proteins modulated by pramipexole according to STICH. 66

Figure 12. Protein networks identified by bioinformatic analysis. 68

Figure 13. Concept of tight receptor control via photocaged agonist/antagonist pairing. 103

Figure 14. TANGO assay confirmation of loss of bioactivity. 107

Figure 15. Photolysis kinetics. 109

Figure 16. Spectral orthogonality assay. 112

Figure 17. WinterGreen-WAY uncaging. 114

Figure 18. Live cell microscopy of 5-HT2C activation..... 115

Figure 19. Quantification of percent of cells activated surrounding a region of irradiation in response to a 200 ms pulse of 488 nm light. 116

Figure 20. Long time-scale WinterGreen-WAY uncaging. 117

Figure 21. Repeated irradiation of WinterGreen-WAY is able to envoke subsequent events of calcium mobilization. 118

Figure 22. Recapitulation of 200 ms irradiation WinterGreen-WAY calcium flux curve through the addition of 300 nM parent WAY-161503. 119

Figure 23. In vitro WinterRed-NDMC uncaging. 120

Figure 24. Recapitulation of parent WAY-161503/WinterRed-NDMC calcium flux curve through preincubation of 250 nM NDMC then 800 nM parent WAY-161503 addition. . 121

Figure 25. In vitro dual-wavelength uncaging. 122

Listing of Tables

Table 1. Constants from Ca Assay.[a] 51

Table 2. Constants from PRESTO-TANGO Assay[a] 53

Table 3. Screened Pd coupling conditions..... 142

Listing of Schemes

Scheme 1. Synthesis of Ropinirole-Based Targets with Multifunctional Cross-Linkers. 47

Scheme 2. Synthesis of Pramipexole-Based Targets with Multifunctional Cross-Linkers. 48

Scheme 3. Synthesis of WinterGreen-WAY-161503 (7). 104

Scheme 4. Synthesis of WinterRed-N-desmethylclozapine (12). 105

Scheme 5. Boger's preparation of tricyclic ketone 14.[10] 138

Scheme 6. Proposed derivatization of D ring. 139

Scheme 7. Proposed synthesis of tricyclic ketone **17**. 141

Scheme 8. Preparation of homopropargyl carboxylic acid 19. 141

Scheme 9. Failed ortho iodination. 143

Scheme 10. Failed synthesis of aryl iodide 24. 144

Abbreviations

5-HT_{2C}	serotonin receptor 2C
ABPP	activity-based protein profiling
ALS	amyotrophic lateral sclerosis
BODIPY	4,4-difluoro-4-bora-3a,4a-diaza-s-indacene
BRAIN	Brain Research Through Advancing Innovative Neurotechnologies
BSA	bovine serum albumin
ChR2	channelrhodopisin
CNS	central nervous system
CuAAC	copper catalyzed azide-alkyne cycloaddition
D_2L	dopamine receptor D2 long isoform
D_2S	dopamine receptor D2 short isoform
DIPEA	N,N-diisopropylethylamine
DMEM	Dulbecco's modified Eagle medium
DMF	dimethylformamide
DMSO	dimethyl sulfoxide
DNA	deoxyribonucleic acid
DRD2	dopamine receptor D2
DREADD	designer receptors exclusively activated by designer drugs
E2	bimolecular elimination
EC_{50}	half-maximal effective concentration
EDC	N-(3-dimethylaminopropyl)-N′-ethylcarbodiimide
EDTA	ethylenediaminetetraacetic acid
EtOAc	ethyl acetate
F-12	Ham’s F-12 nutrient mixture
FACS	fluorescence assisted cell sorting
FBS	fetal bovine serum
FDR	false discovery rate
GABA	gamma-aminobutyric acid
GECI	genetically encoded calcium indicator
GFP	green fluorescent protein
G_i	G_i protein alpha subunit

GPCR	G-protein coupled receptor
G_q	G_q protein alpha subunit
G_{qi5}	chimeric G_q protein containing the five carboxyl-terminal amino acids from G_i
HATU	hexafluorophosphate azabenzotriazole tetramethyl uronium
H-bond	hydrogen bond
HBSS	Hank's balance salt solution
HEK 293T	human embryonic kidney 293T cells
HOAt	1-Hydroxy-7-azabenzotriazole
HPLC	high-performance liquid chromatography
HTLA	HEK 293 line stably expressing a tetracycline transactivator-dependent luciferase reporter and βarrestin2 fused to a TEV protease
Hz	hertz
ICAT	isotope-coded affinity tag
IP3	inositol 1,4,5-trisphosphate
KEGG	Kyoto Encyclopedia of Genes and Genomes
LC-MS	liquid chromatography-mass spectroscopy
LN2	liquid nitrogen
LSA	lysergic acid
MAOI	monoamine oxidase inhibitor
MeOH	methanol
MHz	megahertz
Brain/MINDS	The Strategic International Brain Science Research Promotion Program
MDD	major depressive disorder
NDMC	N-desmethylclozapine
NEB	New England Biolabs
NIH	National Institutes of Health
NMR	nuclear magnetic resonance
nNOS	neuronal nitric oxide synthases
PBS	phosphate buffered saline
PEI	polyethyleneimine
ppm	parts per million

PRESTO-TANGO	parallel receptorome expression and screening via transcriptional output, with transcriptional activation following arrestin translocation
RAS	reticular activating system
RT	room temperature
rtPCR	real-time polymerase chain reaction
SDS-PAGE	Sodium dodecyl-sulfate polyacrylamide gel electrophoresis
SILAC	Stable Isotope Labeling by Amino acids in Cell culture
SIM-PAL	Small Molecule Interactome Mapping by Photo-Affinity Labeling
SM	starting material
SSRI	selective serotonin reuptake inhibitor
TBS	tris-buffered saline
TBST	tris buffered saline with tween 20
TFA	trifluoroacetic acid
THF	tetrahydrofuran
TLC	thin-layer chromatography
U	units
UV	ultraviolet

1 Review of photo-responsive probes in cellular and molecular neuroscience

1.1 Current state and future outlook of cellular and molecular neuroscience

1.1.1 Importance of cellular and molecular neuroscience

The field of neuroscience has seen immense advancement over the past three decades. New technologies have made it possible to visualize neural circuits in vivo[1], biorthogonally stimulate neuronal activity[2], and to elucidate elementary pathways from neural activity to behavior[3]. These discoveries were all powered by the development of molecular tools such as channelrhodopsins[4], genetically encoded Ca^{2+}-indicators (GECIs)[5], and designer receptors exclusively activated by designer drugs (DREADDs)[6]. Further, emerging genetic methods have enabled specific cell populations to be manipulated.[7-11] Leveraging this molecular toolbox available to neuroscientists has made it possible to observe the brain in ways we previously could not imagine. These developments have transformed neuroscience, leading to striking new insights. However, as a result, most of the prominent, current neuroscience papers deal with problems in systems neuroscience, most neuroscience students are trained in systems or computational neuroscience, and many new faculty hires are in systems and computational neuroscience.

This shift away from molecular and cellular neuroscience research may impede progress toward future neuroscience booms and ultimately hinder progress toward holistically understanding the brain. Basic research into biological processes at the cellular and molecular level, and the development of the next generation of chemical and biological tools are what support systems, cognitive, and behavioral neuroscience.

We need to continue creating new technologies that enable neuroscience in order to continue advancing neuroscience.

1.1.2 Advancements and future outlook

Molecular neuroscience saw an explosion of progress one to two decades prior to the systems neuroscience boom. The past 30 years have produced widespread advancements across cellular and molecular neuroscience. There were big early technical innovations, such as patch-clamp electrophysiology[12], rtPCR[13], and genomic sequencing[14], that allowed for an array of new experimental opportunities and as discussed, have shifted the focus of modern neuroscience research. But as we continue to advance tools in cellular and molecular neuroscience, it is imperative that the tools we develop support the research of a few key problems in neuroscience that currently hold the field back.

Two notable, longstanding, and current challenges include the completion of the neural connectome[15], and a comprehensive cellular atlas of the mammalian brain. The first macroscale atlas was recently published December 2023[16] and while this was a massive achievement that will remain impactful for years, a complete meso- to micro-scale atlas remains a challenge. As the resolution of mapping for both of these projects increases from the macroscale, through mesoscale, and into microscale, the challenge becomes obvious: The number of neurons comprising the brain ranges into the billions in more complex organisms[17], and current non-invasive imaging techniques cannot easily capture the brains activity on a single cell scale.[1,5-7,12] There is significant support available to overcome these challenges though the National Institutes of Health's

BRAIN Initiative[18], a 10 year program initiated in 2016 aiming to support the development and implementation of innovative neurotechnologies, as well as the Human Brain Project[19] funded by the European Union to support research at the interface of neuroscience and computation, and the Brain/MINDS project[20] in Japan focused on mapping higher brain function.

Among the new technologies born from cellular and molecular neuroscience support are high-throughput and innovative optical electrophysiological approaches.[21-23] With these, neuroscientists can begin to probe discrete cell populations, determining the roles of specific cell types. This, combined with recently developed approaches, such as targeted proteomics[24], and new methods for visualizing genetically encoded calcium indicators[25-26], will potentially revolutionize the way we probe the brain.

Recent advances in microscopy[27-30] are set to allow researchers to visualize and probe single cells and subcellular components with unprecedented resolution. Advances in chromatography[31-33] will allow researchers to interrogate discrete enzymes within increasingly complex samples. Along the same vein, we need to develop new molecular tools to keep pace with these advances. Tools to facilitate *in vivo* measurement and manipulation of the brain's molecular landscape, rather than today's cellular landscape, will revolutionize our ability to bridge the epigenome, genome, transcriptome, and proteome with behavior.[34] This level of innovation will enable next generation models of the developing brain to be selectively probed and proteomically analyzed, to understand the roles of specific cellular types and subcellular processes during the early stages of neurodevelopment. These tools will further our understanding

of synapse structure and regulation by non-neuronal elements by selective perturbation and selective analysis.

Although initial investment into advancing molecular neuroscience will likely reduce short term research output, this investment will serve to create the tools that circuit and systems neuroscientists will use to thoroughly understand the brain across developmental, environmental, and genetic factors in ways that are presently incomprehensible. Further, combining these advancements with clinically validated biomarkers of brain health will potentially open new avenues of therapeutic intervention, which is key to efficaciously treating Alzheimer's, Parkinson's, amyotrophic lateral sclerosis (ALS), and other incurable neurodegenerative diseases.

1.2 Survey of the current state of the art

As discussed above, functional proteomics and optogenetics are two recent technologies born from the development of modern cellular and molecular neurotechnology. Here, the theory, recent advancements, and current limitations of each technology will be discussed. Our rationale for pursuing the original research disclosed in the sections following this discussion is based on the demonstrated need for further advancement and utilization of these technologies.

1.2.1 Activity-based protein profiling

Chromosomal translocation, gene amplification, single cell sequencing, and inhibitory RNA -based gene silencing are all technologies that have provided insights into protein expression and pathological processes. These technologies have played a

major role in advancements across all human health research, but specific to neuroscience these technologies have been particularly critical in developing our understanding of the genetics of Parkinsons disease[35], neural differentiation[36], and Alzheimer's disease neuropathology.[37]

These methods, although powerful, rely on gene expression to characterize protein function rather than directly characterizing the protein itself. These upstream monitoring methods inherently lose the ability to capture posttranslational events, which are often key to understanding protein function and dynamics. The loss of this information is particularly detrimental to neuroscientists since several key neurodegenerative diseases are thought to be exacerbated and accelerated by posttranslational modification of overexpressed proteins.[38-44]

The field of proteomics addresses this unmet need by directly characterizing proteins. Technologies such as liquid chromatography-mass spectrometry (LC-MS) shotgun analytics[45], two-hybrid screening[46], and protein microarrays[47] have become powerful tools that are widely used across molecular biology. These tools have advanced our understanding of protein expression patterns[48-50], molecular interactions[51-53], and post translational modifications[54-55]. By directly profiling protein activity, the contrast between gene expression and functional protein content has become increasingly apparent. Further, since the post-transcriptional and -translational events vary gene to gene, it is impossible to predict and control all possible outcomes. Activity-based protein profiling (ABPP) fills this gap to directly modify proteins *in situ*, providing a direct method to probe and elucidate the function of proteins.

ABPP leverages a modular design, with an active-site-directed scaffold, a spacer to preserve bioactivity, a covalent modifier, and a reporter tag.[56] In principle, the active-site-directed scaffold enables the probe to target specific subsets of proteins within complex proteomes, while the covalent modifier and reporter tag facilitate target enrichment (see Figure 1). Commonly used reporter groups are fluorescent tags[57-58], biotin[59], and biorthogonal ("click" chemistry) tags[60]. The reporting group selected will largely depend on the experimental design since it will determine the post-capture processing and detection of your target proteins. For example, fluorescent tags are useful for identifying the localization and trafficking of proteins in cells but lack quantitative data, while biotin is useful for target enrichment and identification by LC-MS but lacks any spatial data.

ABPP probes often utilize a range of chemical scaffolds, including mechanism-based inhibitors[61], protein-reactive natural products[62], electrophilic warheads[63], as well as non-covalent pharmaceutical scaffolds[64]. Since the ABPP probes interrogate and report on the reactivity of receptor active sites, and receptor activity is often regulated a by post-transcriptional and -translational events,[38-44,54-55] ABPP can provide direct insight on the state, quantity, and activity your designed protein of interest. This direct interrogation provides a level of information that will forever be beyond the reach of upstream genomic profiling.

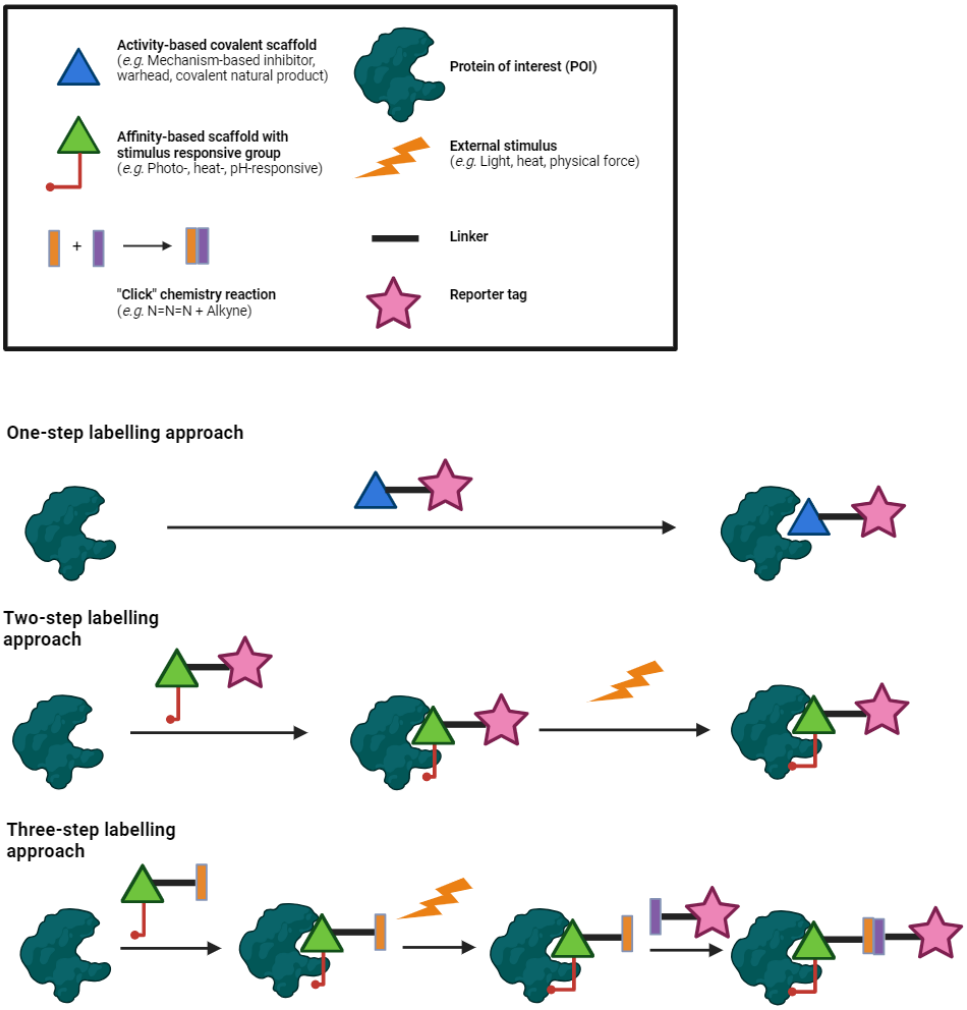

Figure 1. ABPP probe design and function.

Activity-based protein profiling probes are modular and can follow a one-step, two-step, or three-step protein capture workflow.

When surveying the field broadly, molecular biologists have used ABPP to reveal complex and dynamic enzyme–substrate interactions occurring in cells and tissue[65], discover new catalytic activity in enzymes[66], demonstrate new functions of enzymes[67-68], and monitor of the trafficking of enzymes in real time[69]. However, in neuroscience ABPP faces a unique challenge in that very low abundance proteins (neuroreceptors) are of the highest interest.[70] Most current ABPP techniques excel in high-throughput

identification of stable proteins of moderate-abundance, but face serious limitations when studying the function of hydrophobic, low-abundance targets.[71] Thus, a far more limited application of ABPP has taken form in numerous advanced quantitative proteomic approaches.[72] Mass spectrometry-based stable isotope labelling paired with ABPP probes is often necessary to enrich the signal of neuroreceptors[64,73-74]. Several such systems have emerged, including isotope-coded affinity tag (ICAT)[75-76], stable isotope labelling with amino acids in cell culture (SILAC)[77], and more recently small molecule interactome mapping by photo-affinity labeling (SIM-PAL)[78].

Although several systems for targeting low-abundance and unstable proteins have emerged, application of these systems thus far has largely demonstrated the technology's utility across families of receptors rather than subtype specific targets. Further, there is a very limited body of research that uses ABPP probes to target the specific receptors involved in synaptic function despite the broad reaching impact of such research. Here, we demonstrate a set of ABPP probes designed to target dopamine receptor D2 (DRD2) with high specificity and have adapted the MS-based systems described to show both broad target engagement of the probes and the specific peptides in the local environment of the probe when bound to the DRD2 receptor.

1.2.2 Optogenetics

Optogenetics is an important field for neuroscientists that has changed the way we approach non-invasive modulation of neuronal activity. Although the field is rapidly evolving, the basic premise of optogenetics leverages naturally occurring light-sensitive

proteins (microbial opsins, members of an ancient gene family adapted from archaebacteria) and repurposes them into genetically encoded light-gated actuators.[79] Thus, opsins allow us to modulate cellular activity by light (Figure 2). The type of modulation depends on the photoreceptor's biological function, but the optogenetic tool that is most relevant to neuroscientists is the family of engineered channelrhodopsin-2 (ChR2).[80] As a light-gated cation channel, ChR2 is used to depolarize the membranes of excitable cells with high intensity light.[81] With a rapid on-rate and moderate channel closing rate (greatly improved by protein engineering),[82-86] ChR2 has become a key tool for non-invasive modulation of neuronal activity.

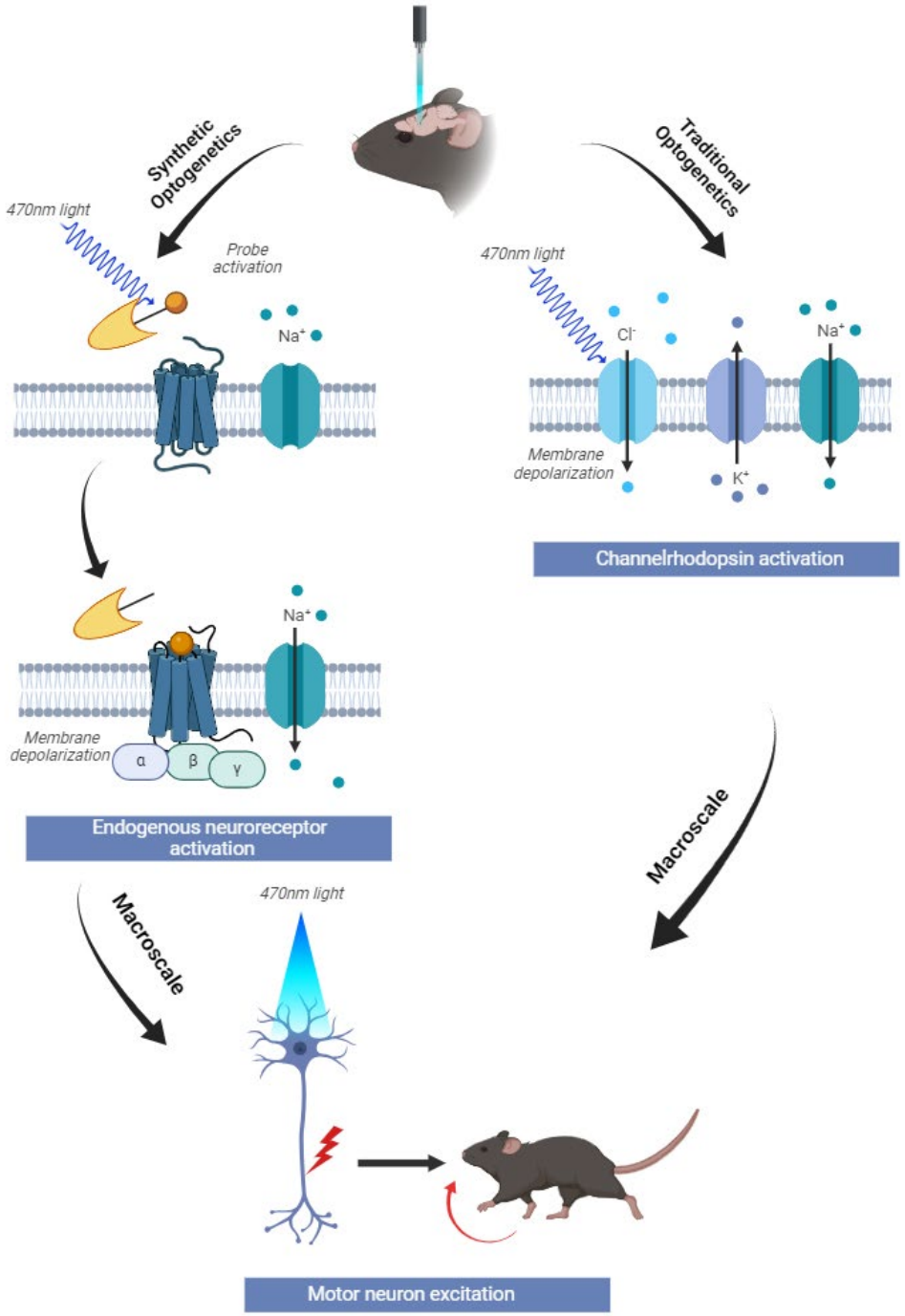

Figure 2. Traditional and synthetic optogenetics.

While the behavioral outcomes of traditional optogenetics are largely mirrored by synthetic optogenetics, the microscale mechanisms are importantly distinct. Traditional optogenetics uses engineered bacterial opsins to depolarize the membrane of neurons, while synthetic optogenetics uses stimulus responsive ligands of endogenous neuroreceptors to illicit membrane depolarization by a mechanism that closely recreates a real chemical synapse.

Since their introduction, opsins have faced several challenges in use as a model for neuronal function. Chiefly, the need for general methods for targeting strong and specific opsin expression to not only the membrane, but also specific subcellular components have been and remains an issue and area of active research.[87-90] Further, methods for delivering light that is sufficiently strong, and spatiotemporally confined to specific parts of cells remains a challenge.[91-95]

Optogenetic methods have broad implications in neuroscience, ranging from questions in behavior[96-98], physiology and pathology[99-102]. The use of optogenetic methods to modulate discrete cell types was pivotal to understanding the causal neuronal mechanisms of movement regulation[103], identifying the circuit mechanisms that control voluntary movements[104]. Patterns of activity arising from defined cell types have been identified through optogenetics, patterns that drive fundamental behavior (*i.e.* hunger, thirst, and energy).[105-107] It cannot be overstated that in the two decades that optogenetic tools have been available to neuroscientists, they have driven some of the most groundbreaking work in neuroscience and captivating research produced by modern science.

While great progress in circuit and behavioral neuroscience has been made by implementing optogenetic methods, there are significant limitations that need to be addressed through future research to continue to advance the field. First, the development of guided subcellular trafficking is becoming increasingly important as targeted optogenetics develops as a field.[108] Current optogenetic research has successfully targeted discreet cell populations within intermixed tissue[96-107], which is one of the chief advantages of optogenetics over traditional electrophysiological

methods. However, to understand and recreate a more comprehensive model of the brain, subcellular specificity is necessary. Membrane trafficking strategies have already improved the expression of opsins at the membrane[89], but further research in this area should focus on targeting strategies that allow selective optogenetic expression in subcellular compartments such as dendrites, somata, or axon terminals. Currently, efforts toward axon specific trafficking unfortunately still result in heterologously expressed optogenetic proteins[109-110], and while selective expression is advancing, true recreation of the chemical synapse is still quite far beyond the limitations of our current strategies.

Another limitation of optogenetics largely mirrors the inherent limitation of genomics when compared to proteomics. While optogenetics is a powerful, yet simple, model of neuronal activity, it is exactly that, a model. Regardless of how we optimize the trafficking patterns of opsins, and regardless of how they mimic endogenous neuroreceptor expression, they cannot recapitulate neuroreceptor activity. The mechanism of activation of opsins and the cellular biochemistry in response to activation will always be orthogonal to the biochemistry of a chemical synapse. With regard to neuronal synapses, optogenetic tools are limited in their ability to control endogenous signaling mechanisms and efforts to directly control endogenous signaling have largely fallen short in terms of kinetics, sensitivity, and available targets.[111-113]

Recent research, which we will call synthetic optogenetics (Figure 2), bridges this gap by employing light to regulate the function of proteins but, instead of the use of photoreceptors, relies on the use of synthetic chromophores to endogenous proteins (neuroreceptors).[26,114-116] This method enhances conventional pharmacology by

reversibly altering the ligands activity in a non-invasive manner, allowing for endogenous neuroreceptors to be targeted while leveraging the same optical advances designed for selective opsin modulation.[117] Here, we report on the development of selective serotonin receptor 2C photo-pharmacological probes and demonstrate their utility to modulate endogenous neuroreceptor activation and suppression on a timescale that is unachievable with traditional methods in pharmacology.

1.3 References

(1) Yang, W., Yuste, R. In vivo imaging of neural activity. Nat Methods 14, 349–359 (2017).

(2) Mitew S, Gobius I, Fenlon LR, McDougall SJ, Hawkes D, Xing YL, Bujalka H, Gundlach AL, Richards LJ, Kilpatrick TJ, Merson TD, Emery B. Pharmacogenetic stimulation of neuronal activity increases myelination in an axon-specific manner. Nat Commun. 2018 Jan 22;9(1):306.

(3) Musall S, Urai AE, Sussillo D, Churchland AK. Harnessing behavioral diversity to understand neural computations for cognition. Curr Opin Neurobiol. 2019 Oct;58:229-238.

(4) Deisseroth K, Hegemann P. The form and function of channelrhodopsin. Science. 2017 Sep 15;357(6356):eaan5544.

(5) Oh J, Lee C, Kaang BK. Imaging and analysis of genetically encoded calcium indicators linking neural circuits and behaviors. Korean J Physiol Pharmacol. 2019 Jul;23(4):237-249.

(6) Urban DJ, Roth BL. DREADDs (designer receptors exclusively activated by designer drugs): chemogenetic tools with therapeutic utility. Annu Rev Pharmacol Toxicol. 2015;55:399-417.

(7) Govorunova, E. G. et al. The expanding family of natural anion channelrhodopsins reveals large variations in kinetics, conductance, and spectral sensitivity. Sci. Rep. 7, 43358 (2017).

(8) Mahn, M. et al. High-efficiency optogenetic silencing with soma-targeted anion-conducting channelrhodopsins. Nat. Commun. 9, 4125 (2018).

(9) Sineshchekov, O. A., Govorunova, E. G., Li, H. & Spudich, J. L. Bacteriorhodopsin-like channelrhodopsins: alternative mechanism for control of cation conductance. Proc. Natl Acad. Sci. USA 114, E9512–E9519 (2017).

(10) Gradinaru, V. et al. Molecular and cellular approaches for diversifying and extending optogenetics. Cell 141, 154–165 (2010).

(11) Chang, K.-Y. et al. Light-inducible receptor tyrosine kinases that regulate neurotrophin signalling. Nat. Commun. 5, 4057 (2014).

(12) Hill CL, Stephens GJ. An Introduction to Patch Clamp Recording. Methods Mol Biol. 2021;2188:1-19.

(13) Kubista M, Andrade JM, Bengtsson M, Forootan A, Jonák J, Lind K, Sindelka R, Sjöback R, Sjögreen B, Strömbom L, Ståhlberg A, Zoric N. The real-time polymerase chain reaction. Mol Aspects Med. 2006 Apr-Jun;27(2-3):95-125.

(14) Logsdon, G.A., Vollger, M.R. & Eichler, E.E. Long-read human genome sequencing and its applications. Nat Rev Genet 21, 597–614 (2020).

(15) Toga AW, Clark KA, Thompson PM, Shattuck DW, Van Horn JD. Mapping the human connectome. Neurosurgery. 2012 Jul;71(1):1-5.

(16) Yao, Z., van Velthoven, C.T.J., Kunst, M. et al. A high-resolution transcriptomic and spatial atlas of cell types in the whole mouse brain. Nature 624, 317–332 (2023).

(17) Azevedo FA, Carvalho LR, Grinberg LT, Farfel JM, Ferretti RE, Leite RE, Jacob Filho W, Lent R, Herculano-Houzel S (April 2009). "Equal numbers of

neuronal and nonneuronal cells make the human brain an isometrically scaled-up primate brain". The Journal of Comparative Neurology. 513 (5): 532–41.

(18) U.S. Department of Health and Human Services. (n.d.). Home. National Institutes of Health. https://braininitiative.nih.gov/

(19) EBRAINS and the European Union. (n.d.). Human Brain Project. https://www.humanbrainproject.eu/en/

(20) Japan Agency for Medical Research and Development. (n.d.). Brain/MINDS Project. Brain/MINDS. Retrieved February 10, 2024, from https://brainminds.jp/en

(21) Priest BT, Cerne R, Krambis MJ, Schmalhofer WA, Wakulchik M, Wilenkin B, Burris KD (2004) Automated electrophysiology assays. In: Assay guidance manual (Sittampalam GS, Coussens NP, Brimacombe K, Grossman A, Arkin M, Auld D, Austin C, et al., eds). Bethesda, MD: Eli Lilly and the National Center for Advancing Translational Sciences.

(22) Zhang H, Reichert E, Cohen AE (2016) Optical electrophysiology for probing function and pharmacology of voltage-gated ion channels. Elife 5:e15202. 10.7554/eLife.15202

(23) Hochbaum, D., Zhao, Y., Farhi, S. et al. All-optical electrophysiology in mammalian neurons using engineered microbial rhodopsins. Nat Methods 11, 825–833 (2014).

(24) Lazear MR, Remsberg JR, Jaeger MG, Rothamel K, Her HL, DeMeester KE, Njomen E, Hogg SJ, Rahman J, Whitby LR, Won SJ, Schafroth MA, Ogasawara D, Yokoyama M, Lindsey GL, Li H, Germain J, Barbas S, Vaughan J,

Hanigan TW, Vartabedian VF, Reinhardt CJ, Dix MM, Koo SJ, Heo I, Teijaro JR, Simon GM, Ghosh B, Abdel-Wahab O, Ahn K, Saghatelian A, Melillo B, Schreiber SL, Yeo GW, Cravatt BF. Proteomic discovery of chemical probes that perturb protein complexes in human cells. Mol Cell. 2023 May 18;83(10):1725-1742.e12.

(25) Resendez SL, Stuber GD (2015) In vivo calcium imaging to illuminate neurocircuit activity dynamics underlying naturalistic behavior. Neuropsychopharmacology 40:238–239.

(26) Kim ST, Doukmak EJ, Shanguhyia M, Gray DJ, Steinhardt RC. ACS Chemical Neuroscience 2023 14 (19), 3665-3673.

(27) Gao R, Asano SM, Upadhyayula S, Pisarev I, Milkie DE, Liu TL, Singh V, Graves A, Huynh GH, Zhao Y, Bogovic J, Colonell J, Ott CM, Zugates C, Tappan S, Rodriguez A, Mosaliganti KR, Sheu SH, Pasolli HA, Pang S, et al. (2019) Cortical column and whole-brain imaging with molecular contrast and nanoscale resolution. Science 363:eaau8302.

(28) Pfeiffer, T.; Poll, S.; Bancelin, S.; Angibaud, J.; Inavalli, V. K.; Keppler, K.; Mittag, M.; Fuhrmann, M.; Nagerl, U. V. Chronic 2p-Sted Imaging Reveals High Turnover of Dendritic Spines in the Hippocampus in Vivo. Elife 2018, 7.

(29) Saka, S. K.; Wang, Y.; Kishi, J. Y.; Zhu, A.; Zeng, Y.; Xie, W.; Kirli, K.; Yapp, C.; Cicconet, M.; Beliveau, B. J. et al. Immuno-Saber Enables Highly Multiplexed and Amplified Protein Imaging in Tissues. Nat. Biotechnol. 2019, 37, 1080– 1090.

(30) Cnossen, J.; Hinsdale, T.; Thorsen, R. O.; Siemons, M.; Schueder, F.; Jungmann, R.; Smith, C. S.; Rieger, B.; Stallinga, S. Localization Microscopy at Doubled Precision with Patterned Illumination. Nat. Methods 2020, 17, 59– 63.

(31) Cui, M., Cheng, C. & Zhang, L. High-throughput proteomics: a methodological mini-review. Lab Invest 102, 1170–1181 (2022).

(32) Wuen Ma, J.Y.; Sze, Y.H.O.N.; Bian, J.F.; Lam, T.C. Critical role of mass spectrometry proteomics in tear biomarker discovery for multifactorial ocular diseases (Review). Int. J. Mol. Med. 2021, 47, 4916.

(33) Sataloff, R.T.; Johns, M.M.; Kost, K.M. Integration of Omics Approaches and Systems Biology for Clinical Applications; Vlahou, A., Mischak, H., Zoidakis, J., Magni, F., Eds.; John Wiley & Sons: Hoboken, NJ, USA, 2018.

(34) Hayashi-Takagi A, Yagishita S, Nakamura M, Shirai F, Wu YI, Loshbaugh AL, Kuhlman B, Hahn KM, Kasai H (2015) Labelling and optical erasure of synaptic memory traces in the motor cortex. Nature 525:333–338.

(35) Klein C, Westenberger A. Genetics of Parkinson's disease. Cold Spring Harb Perspect Med. 2012 Jan;2(1):a008888.

(36) Fischer U, Keller A, Voss M, Backes C, Welter C, Meese E (2012) Genome-Wide Gene Amplification during Differentiation of Neural Progenitor Cells In Vitro. PLoS ONE 7(5): e37422.

(37) Singer, O., Marr, R., Rockenstein, E. et al. Targeting BACE1 with siRNAs ameliorates Alzheimer disease neuropathology in a transgenic model. Nat Neurosci 8, 1343–1349 (2005).

(38) Gupta R, Sahu M, Srivastava D, Tiwari S, Ambasta RK, Kumar P. Post-translational modifications: Regulators of neurodegenerative proteinopathies. Ageing Res Rev. 2021 Jul;68:101336.

(39) Ross, C.A.; Poirier, M.A. Protein aggregation and neurodegenerative disease. Nat. Med. 2004, 10, S10–S17.

(40) Blokhuis, A.M.; Groen, E.J.N.; Koppers, M.; van den Berg, L.H.; Pasterkamp, R.J. Protein aggregation in amyotrophic lateral sclerosis. *Acta Neuropathol.* **2013**, *125*, 777–794.

(41) Guivernau, B.; Bonet, J.; Valls-Comamala, V.; Bosch-Morató, M.; Godoy, J.A.; Inestrosa, N.C.; Perálvarez-Marín, A.; Fernández-Busquets, X.; Andreu, D.; Oliva, B.; et al. Amyloid-β peptide nitrotyrosination stabilizes oligomers and enhances NMDAR-Mediated Toxicity. J. Neurosci. 2016, 36, 11693–11703.

(42) Prasad, A.; Sivalingam, V.; Bharathi, V.; Girdhar, A.; Patel, B.K. The amyloidogenicity of a C-terminal region of TDP-43 implicated in Amyotrophic Lateral Sclerosis can be affected by anions, acetylation and homodimerization. Biochimie 2018, 150, 76–87.

(43) Xiang, W.; Menges, S.; Schlachetzki, J.C.; Meixner, H.; Hoffmann, A.C.; Schlötzer-Schrehardt, U.; Becker, C.M.; Winkler, J.; Klucken, J. Posttranslational modification and mutation of histidine 50 trigger alpha synuclein aggregation and toxicity. Mol. Neurodegener. 2015, 10, 8.

(44) Shimizu, T.; Fukuda, H.; Murayama, S.; Izumiyama, N.; Shirasawa, T. Isoaspartate formation at position 23 of amyloid beta peptide enhanced fibril

formation and deposited onto senile plaques and vascular amyloids in Alzheimer's disease. J. Neurosci. Res. 2002, 70, 451–461.

(45) Meyer JG. Qualitative and Quantitative Shotgun Proteomics Data Analysis from Data-Dependent Acquisition Mass Spectrometry. Methods Mol Biol. 2021;2259:297-308.

(46) Brückner A, Polge C, Lentze N, Auerbach D, Schlattner U. Yeast two-hybrid, a powerful tool for systems biology. Int J Mol Sci. 2009 Jun 18;10(6):2763-2788.

(47) Sutandy FX, Qian J, Chen CS, Zhu H. Overview of protein microarrays. Curr Protoc Protein Sci. 2013 Apr;Chapter 27(1):Unit 27.1.

(48) Zhang B, VerBerkmoes NC, Langston MA, Uberbacher E, Hettich RL, Samatova NF. Detecting differential and correlated protein expression in label-free shotgun proteomics. J Proteome Res. 2006 Nov;5(11):2909-18.

(49) White CA, Oey N, Emili A. Global quantitative proteomic profiling through 18O-labeling in combination with MS/MS spectra analysis. J Proteome Res. 2009 Jul;8(7):3653-65.

(50) Pang M, Bai XY, Li Y, Bai JZ, Yuan LR, Ren SA, Hu XY, Zhang XR, Yu BF, Guo R, Wang HL. Label-free LC-MS/MS shotgun proteomics to investigate the anti-inflammatory effect of rCC16. Mol Med Rep. 2016 Nov;14(5):4496-4504.

(51) Gavin AC, Bosche M, Krause R, Grandi P, Marzioch M, Bauer A, Schultz J, Rick JM, Michon AM, Cruciat CM, Remor M, Hofert C, Schelder M, Brajenovic M, Ruffner H, Merino A, Klein K, Hudak M, Dickson D, Rudi T, Gnau V, Bauch A, Bastuck S, Huhse B, Leutwein C, Heurtier MA, Copley RR, Edelmann A,

Querfurth E, Rybin V, Drewes G, Raida M, Bouwmeester T, Bork P, Seraphin B, Kuster B, Neubauer G, Superti-Furga G. Functional organization of the yeast proteome by systematic analysis of protein complexes. Nature. 2002;415:141–147.

(52) Krogan NJ, Cagney G, Yu H, Zhong G, Guo X, Ignatchenko A, Li J, Pu S, Datta N, Tikuisis AP, Punna T, Peregrin-Alvarez JM, Shales M, Zhang X, Davey M, Robinson MD, Paccanaro A, Bray JE, Sheung A, Beattie B, Richards DP, Canadien V, Lalev A, Mena F, Wong P, Starostine A, Canete MM, Vlasblom J, Wu S, Orsi C, Collins SR, Chandran S, Haw R, Rilstone JJ, Gandi K, Thompson NJ, Musso G, St Onge P, Ghanny S, Lam MH, Butland G, Altaf-Ul AM, Kanaya S, Shilatifard A, O'Shea E, Weissman JS, Ingles CJ, Hughes TR, Parkinson J, Gerstein M, Wodak SJ, Emili A, Greenblatt JF. Global landscape of protein complexes in the yeast Saccharomyces cerevisiae. Nature. 2006;440:637–643.

(53) Zanzoni A, Montecchi-Palazzi L, Quondam M, Ausiello G, Helmer-Citterich M, Cesareni G. MINT: a Molecular INTeraction database. FEBS Lett. 2002;513:135–140.

(54) Johnson H, Eyers CE. Analysis of post-translational modifications by LC-MS/MS. Methods Mol Biol. 2010;658:93-108.

(55) Zolg DP, Wilhelm M, Schmidt T, Médard G, Zerweck J, Knaute T, Wenschuh H, Reimer U, Schnatbaum K, Kuster B. ProteomeTools: Systematic Characterization of 21 Post-translational Protein Modifications by Liquid Chromatography Tandem Mass Spectrometry (LC-MS/MS) Using Synthetic Peptides. Mol Cell Proteomics. 2018 Sep;17(9):1850-1863.

(56) Niphakis, M. J., and Cravatt, B. F. (2014). Enzyme inhibitor discovery by activity-based protein profiling. Annu. Rev. Biochem. 83, 341–377.

(57) Husaini AM, Morimoto K, Chandrasekar B, Kelly S, Kaschani F, Palmero D, Jiang J, Kaiser M, Ahrazem O, Overkleeft HS, van der Hoorn RAL. Multiplex Fluorescent, Activity-Based Protein Profiling Identifies Active α-Glycosidases and Other Hydrolases in Plants. Plant Physiol. 2018 May;177(1):24-37.

(58) Lu H, Chandrasekar B, Oeljeklaus J, Misas-Villamil JC, Wang Z, Shindo T, Bogyo M, Kaiser M, van der Hoorn RAL (2015) Subfamily-specific fluorescent probes for cysteine proteases display dynamic protease activities during seed germination. Plant Physiol 168: 1462–1475

(59) Schiapparelli LM, McClatchy DB, Liu HH, Sharma P, Yates JR 3rd, Cline HT. Direct detection of biotinylated proteins by mass spectrometry. J Proteome Res. 2014 Sep 5;13(9):3966-78.

(60) Verhelst SHL, Bonger KM, Willems LI. Bioorthogonal Reactions in Activity-Based Protein Profiling. Molecules. 2020 Dec 18;25(24):5994.

(61) McGregor NGS, Artola M, Nin-Hill A, Linzel D, Haon M, Reijngoud J, Ram A, Rosso MN, van der Marel GA, Codée JDC, van Wezel GP, Berrin JG, Rovira C, Overkleeft HS, Davies GJ. Rational Design of Mechanism-Based Inhibitors and Activity-Based Probes for the Identification of Retaining α-l-Arabinofuranosidases. J Am Chem Soc. 2020 Mar 11;142(10):4648-4662.

(62) Drahl C, Cravatt BF, Sorensen EJ. Protein-reactive natural products. Angew Chem Int Ed Engl. 2005 Sep 12;44(36):5788-809.

(63) Liu Y, Lv S, Peng L, Xie C, Gao L, Sun H, Lin L, Ding K, Li Z. Development and application of novel electrophilic warheads in target identification and drug discovery. Biochem Pharmacol. 2021 Aug;190:114636.

(64) Kim ST, Doukmak EJ, Flax RG, Gray DJ, Zirimu VN, de Jong E, Steinhardt RC. Developing Photoaffinity Probes for Dopamine Receptor D2 to Determine Targets of Parkinson's Disease Drugs. ACS Chem Neurosci. 2022 Oct 19;13(20):3008-3022.

(65) Flierman D, van der Heden van Noort GJ, Ekkebus R, Geurink PP, Mevissen TE, Hospenthal MK, Komander D, Ovaa H. Non-hydrolyzable Diubiquitin Probes Reveal Linkage-Specific Reactivity of Deubiquitylating Enzymes Mediated by S2 Pockets. Cell Chem Biol. 2016 Apr 21;23(4):472-82.

(66) Alcaide A, Trapero A, Pérez Y. Galacto configured N-aminoaziridines: a new type of irreversible inhibitor of β-galactosidases. Org. Biomol. Chem., 2015,13, 5690-5697.

(67) Sanman LE, Bogyo M. Activity-based profiling of proteases. Annu Rev Biochem. 2014;83:249-73.

(68) Niphakis MJ, Cravatt BF. Enzyme inhibitor discovery by activity-based protein profiling. Annu Rev Biochem. 2014;83:341-77.

(69) Buntz A, Wallrodt S, Gwosch E, Schmalz M, Beneke S, Ferrando-May E, Marx A, Zumbusch A. Real-Time Cellular Imaging of Protein Poly(ADP-ribos)ylation. Angew Chem Int Ed Engl. 2016 Sep 5;55(37):11256-60.

(70) Teleanu RI, Niculescu AG, Roza E, Vladâcenco O, Grumezescu AM, Teleanu DM. Neurotransmitters-Key Factors in Neurological and

Neurodegenerative Disorders of the Central Nervous System. Int J Mol Sci. 2022 May 25;23(11):5954.

(71) Galmozzi A, Dominguez E, Cravatt BF, Saez E. Application of activity-based protein profiling to study enzyme function in adipocytes. Methods Enzymol. 2014;538:151-69.

(72) Sethi, S., Chourasia, D. & Parhar, I.S. Approaches for targeted proteomics and its potential applications in neuroscience. J Biosci 40, 607–627 (2015).

(73) West AV, Amako Y, Woo CM. Design and Evaluation of a Cyclobutane Diazirine Alkyne Tag for Photoaffinity Labeling in Cells. J Am Chem Soc. 2022 Nov 23;144(46):21174-21183.

(74) Wang, X., He, Y., Ye, Y. et al. SILAC–based quantitative MS approach for real-time recording protein-mediated cell-cell interactions. Sci Rep 8, 8441 (2018).

(75) Gygi, S., Rist, B., Gerber, S. et al. Quantitative analysis of complex protein mixtures using isotope-coded affinity tags. Nat Biotechnol 17, 994–999 (1999).

(76) Chan JCY, Zhou L, Chan ECY. The Isotope-Coded Affinity Tag Method for Quantitative Protein Profile Comparison and Relative Quantitation of Cysteine Redox Modifications. Curr Protoc Protein Sci. 2015 Nov 2;82:23.2.1-23.2.19.

(77) Ong SE, Blagoev B, Kratchmarova I, Kristensen DB, Steen H, Pandey A, Mann M. Stable isotope labeling by amino acids in cell culture, SILAC, as a

simple and accurate approach to expression proteomics. Mol Cell Proteomics. 2002 May;1(5):376-86.

(78) Flaxman HA, Miyamoto DK, Woo CM. Small Molecule Interactome Mapping by Photo-Affinity Labeling (SIM-PAL) to Identify Binding Sites of Small Molecules on a Proteome-Wide Scale. Curr Protoc Chem Biol. 2019 Dec;11(4):e75.

(79) Shichida Y, Matsuyama T. Evolution of opsins and phototransduction. Philos Trans R Soc Lond B Biol Sci. 2009 Oct 12;364(1531):2881-95.

(80) Nagel G, Szellas T, Huhn W, Kateriya S, Adeishvili N, Berthold P, Ollig D, Hegemann P, Bamberg E (2003) Channelrhodopsin-2, a directly light-gated cation-selective membrane channel. Proc Natl Acad Sci USA 100: 13940–13945

(81) Boyden ES, Zhang F, Bamberg E, Nagel G, Deisseroth K. Millisecond-timescale, genetically targeted optical control of neural activity. Nat Neurosci. 2005;8:1263–1268.

(82) Lin JY, Lin MZ, Steinbach P, Tsien RY. Characterization of engineered channelrhodopsin variants with improved properties and kinetics. Biophys J. 2009b

(83) Feldbauer K, Zimmermann D, Pintschovius V, Spitz J, Bamann C, Bamberg E. Channelrhodopsin-2 is a leaky proton pump. Proc Natl Acad Sci U S A. 2009;106:12317–12322.

(84) Berndt A, Yizhar O, Gunaydin LA, Hegemann P, Deisseroth K. Bi-stable neural state switches. Nat Neurosci. 2009;12:229–234.

(85) Gunaydin LA, Yizhar O, Berndt A, Sohal VS, Deisseroth K, Hegemann P. Ultrafast optogenetic control. Nat Neurosci. 2010;13:387–392.

(86) Zhang F, Wang LP, Boyden ES, Deisseroth K. Channelrhodopsin-2 and optical control of excitable cells. Nat Methods. 2006;3:785–792.

(87) Gobbo F, Marchetti L, Jacob A, Pinto B, Binini N, Pecoraro Bisogni F, Alia C, Luin S, Caleo M, Fellin T, Cancedda L, Cattaneo A. Activity-dependent expression of Channelrhodopsin at neuronal synapses. Nat Commun. 2017 Nov 20;8(1):1629.

(88) Chen TW, et al. Ultrasensitive fluorescent proteins for imaging neuronal activity. Nature. 2013;499:295–300.

(89) Schoenenberger P, Grunditz Aring, Rose T, Oertner TG. Optimizing the spatial resolution of Channelrhodopsin-2 activation. Brain Cell Biol. 2008;6:119–127.

(90) Guzowski JF, Setlow B, Wagner EK, McGaugh JL. Experience-dependent gene expression in the rat hippocampus after spatial learning: a comparison of the immediate-early genesArc, c-fos, and zif268. J. Neurosci. 2001;21:5089–zif5098.

(91) Kramer MM, Lataster L, Weber W, Radziwill G. Optogenetic Approaches for the Spatiotemporal Control of Signal Transduction Pathways. Int J Mol Sci. 2021 May 18;22(10):5300.

(92) Strickland D., Lin Y., Wagner E., Hope C.M., Zayner J., Antoniou C., Sosnick T.R., Weiss E.L., Glotzer M. TULIPs: Tunable, light-controlled interacting protein tags for cell biology. Nat. Methods. 2012;9:379–384.

(93) Grusch M., Schelch K., Riedler R., Reichhart E., Differ C., Berger W., Inglés-Prieto Á., Janovjak H. Spatio-temporally precise activation of engineered receptor tyrosine kinases by light. EMBO J. 2014;33:1713–1726.

(94) Ma G., He L., Liu S., Xie J., Huang Z., Jing J., Lee Y.-T., Wang R., Luo H., Han W., et al. Optogenetic engineering to probe the molecular choreography of STIM1-mediated cell signaling. Nat. Commun. 2020;11:1039.

(95) Legnini, I., Emmenegger, L., Zappulo, A. et al. Spatiotemporal, optogenetic control of gene expression in organoids. Nat Methods 20, 1544–1552 (2023).

(96) Fenno LE, Mattis J, Ramakrishnan C, Hyun M, Lee SY, He M, Tucciarone J, Selimbeyoglu A, Berndt A, Grosenick L, et al. 2014. Targeting cells with single vectors using multiple-feature Boolean logic. Nat Methods 11: 763–772.

(97) Godsil BP, Fanselow MS 2004. Light stimulus change evokes an activity response in the rat. Learn Behav 32: 299–310.

(98) Zhang W, Ge W, Wang Z 2007b. A toolbox for light control of Drosophila behaviors through Channelrhodopsin 2-mediated photoactivation of targeted neurons. Eur J Neurosci 26: 2405–2416.

(99) Girardeau G, Benchenane K, Wiener SI, Buzsaki G, Zugaro MB. Selective suppression of hippocampal ripples impairs spatial memory. Nat Neurosci. 2009;12:1222–1223.

(100) Jacobsen JS, Wu C-C, Redwine JM, Comery TA, Arias R, Bowlby M, Martone R, Morrison JH, Pangalos MN, Reinhart PH, Bloom FE. Early-onset

behavioral and synaptic deficits in a mouse model of Alzheimer's disease. Proc Natl Acad Sci U S A. 2006;103:5161–5166.

(101) Wykes RC, Heeroma JH, Mantoan L, Zheng K, MacDonald DC, Deisseroth K, Hashemi KS, Walker MC, Schorge S, Kullmann DM. Optogenetic and potassium channel gene therapy in a rodent model of focal neocortical epilepsy. Sci Transl Med. 2012;4:161ra152.

(102) Wykes RC, Heeroma JH, Mantoan L, Zheng K, MacDonald DC, Deisseroth K, Hashemi KS, Walker MC, Schorge S, Kullmann DM. Optogenetic and potassium channel gene therapy in a rodent model of focal neocortical epilepsy. Sci Transl Med. 2012;4:161ra152.

(103) Hägglund M, Borgius L, Dougherty KJ, Kiehn O. Activation of groups of excitatory neurons in the mammalian spinal cord or hindbrain evokes locomotion. Nat Neurosci. 2010 Feb;13(2):246-52.

(104) Proville RD, Spolidoro M, Guyon N, Dugué GP, Selimi F, Isope P, Popa D, Léna C. Cerebellum involvement in cortical sensorimotor circuits for the control of voluntary movements. Nat Neurosci. 2014 Sep;17(9):1233-9.

(105) Domingos AI, Vaynshteyn J, Voss HU, Ren X, Gradinaru V, Zang F, Deisseroth K, de Araujo IE, Friedman J. Leptin regulates the reward value of nutrient. Nat Neurosci. 2011 Nov 13;14(12):1562-8.

(106) Yang Y, Atasoy D, Su HH, Sternson SM. Hunger states switch a flip-flop memory circuit via a synaptic AMPK-dependent positive feedback loop. Cell. 2011 Sep 16;146(6):992-1003.

(107) Kong D, Tong Q, Ye C, Koda S, Fuller PM, Krashes MJ, Vong L, Ray RS, Olson DP, Lowell BB. GABAergic RIP-Cre neurons in the arcuate nucleus selectively regulate energy expenditure. Cell. 2012 Oct 26;151(3):645-57.

(108) Rost BR, Schneider-Warme F, Schmitz D, Hegemann P. Optogenetic Tools for Subcellular Applications in Neuroscience. Neuron. 2017 Nov 1;96(3):572-603.

(109) Yizhar O, Fenno LE, Davidson TJ, Mogri M, Deisseroth K (2011) Optogenetics in neural systems. Neuron 71:9–34.

(110) Hamada, S., Nagase, M., Yoshizawa, T. et al. An engineered channelrhodopsin optimized for axon terminal activation and circuit mapping. Commun Biol 4, 461 (2021).

(111) Redchuk TA, Karasev MM, Verkhusha PV, Donnelly SK, Hülsemann M, Virtanen J, Moore HM, Vartiainen MK, Hodgson L, Verkhusha VV. Optogenetic regulation of endogenous proteins. Nat Commun. 2020 Jan 30;11(1):605.

(112) Li, LL., Klein, F.M., Li Greci, L. et al. Resonance energy transfer sensitises and monitors in situ switching of LOV2-based optogenetic actuators. Nat Commun 11, 5107 (2020).

(113) Kim N, Kim JM, Lee M, Kim CY, Chang KY, Heo WD. Spatiotemporal control of fibroblast growth factor receptor signals by blue light. Chem Biol. 2014 Jul 17;21(7):903-12.

(114) Laprell, L., Repak, E., Franckevicius, V. et al. Optical control of NMDA receptors with a diffusible photoswitch. Nat Commun 6, 8076 (2015).

(115) Bidoret, C., Ayon, A., Barbour, B. & Casado, M. Presynaptic NR2A-containing NMDA receptors implement a high-pass filter synaptic plasticity rule. Proc. Natl Acad. Sci. USA 106, 14126–14131 (2009) .

(116) Izquierdo-Serra, M. et al. Two-photon neuronal and astrocytic stimulation with azobenzene-based photoswitches. J. Am. Chem. Soc. 136, 8693–8701 (2014) .

(117) Kienzler MA, Isacoff EY. Precise modulation of neuronal activity with synthetic photoswitchable ligands. Curr Opin Neurobiol. 2017 Aug;45:202-209.

2 Cloning and tissue culture

The aim of this section is to develop the cellular and biochemical tools needed to validate the pharmacology and function of photoactive probes. Described first is the development of an assay which quantitatively measures G_i coupled G-protein coupled receptor (GPCR) activation and inhibition relative to intracellular calcium concentration. Next, we describe the design and application of a lentiviral transduction system for the stable expression of a DRD2-Step Tag II fusion protein in HEK 293T cells. Selection for high expressing cells is described, and large-scale production of DRD2 in HEK293 cell lines is used for ABPP proteomics.

2.1 Chimeric G-protein (G_{qi5})

Neuromodulation by endogenous ligands and synthetic probes is a key focus of the research presented in this report. One such endogenous ligand, dopamine, plays a key regulatory role in reward and movement responses in the brain and is implicated in many neurological diseases and disorders.[1] These functions of dopamine act through a family of receptors identified as dopamine receptors D_{1-5} (DRD_{1-5}). Pharmacologically, dopamine receptors are grouped as D_1-like (D_1 and D_5) or D_2-like (D_2S, D_2L, D_3, and D_4). The D_2-like family of receptors couple the G_i type of G protein, which exhibits the function of inhibitory effects on the adenylate cyclase.[2] Further, D_2-like receptors are the main targets of antipsychotics.[3] Therefore, to investigate the roles of the two receptor subtypes, selective drugs for dopamine receptor subtypes are urgently needed.

The aim of this section is to develop an assay which quantitatively measures G_i coupled G-protein coupled receptor (GPCR) activation and inhibition relative to

intracellular calcium concentration. Quantifying receptor activation at various concentrations is a validated method of quantifying ligand-receptor binding characteristics, which is key for characterizing probes and drugs. Calcium mobilization assays mediated by G_q recruitment are currently the most widely used functional assays to evaluate the potency of GPCR agonists and antagonists.[4-5] The assay detects intracellular calcium levels in response to receptor signaling with a calcium-sensitive fluorescent dye. However, G_i coupled receptors, including dopamine D_2-like receptors, generate no intracellular calcium mobilization due to lack of G_q recruitment and subsequent inositol 1,4,5-trisphosphate (IP3) signaling pathway transduction.[6] The recently reported G_{qi5} construct, a chimeric G_q protein containing five carboxyl-terminal amino acids from G_i, interacts with G_i-coupled receptors and while conserving G_q pathway activation, generating intracellular calcium mobilization.[7] To measure D_2-like receptor modulation via changes in the calcium concentration, we have constructed and validated a human-codon optimized expression vector for chimeric G_{qi5}. When co-expressed with human DRD_2 in human embryonic kidney 293T cells (HEK 293T), robust, repeatable, and quantifiable levels of intracellular calcium can be detected as a signal of receptor activation.

2.1.1 Cloning of recombinant G_{qi5}

A human codon-optimized DNA fragment of the G_{qi5} chimera was designed (SnapGene, Dotmatics), synthesized (IDT Technologies), and amplified from the following primers: FORWARD 5′-AGCTGTACCCGGTCGCAATGACCCTGGAGAGCAT-CATGG-3′, REVERSE 5′-TGTGCGGGCAGGCAGAGTCAGAA-CAGGCCGCAGTCC-3′. A pcDNA3.1 vector was derived from GFP-DRD2 (Addgene #24099) was linearized with

the following primers: FORWARD 5′-AGGACTGCGGCCTGTTCTGACTCTGCTGC-CTGCCCG-3′. REVERSE: 5’-CCAGGGT-CATGGTGGCGACCGGG-3’. Linearized fragments were assembled via Gibson assembly. The assembled plasmid was expressed (DH5-alpha E. coli, New England Biolabs), purified (QIAGEN anion exchange plasmid purification) and sequenced to confirm fragment insertion.

2.1.2 Validating G_{qi5}

The assembled fragment was then validated via intracellular calcium mobilization measurement mediated by DRD2 activation. To reiterate, the goal of the assay is to quantitatively measure intracellular calcium levels in response to receptor signaling with a calcium-sensitive fluorescent dye. The chimeric G_{qi5} construct interacts with G_i-coupled receptors while conserving G_q pathway activation, which is key to IP_3 signaling pathway transduction.

Co-transfection of G_{qi5} and GFP-DRD2 was optimized using lipid mediated delivery (Optifect, Invitrogen). Expression of DRD2 was validated using fluorescence microscopy, while expression of G_{qi5} was validated via functional live cell calcium mobilization assay.

The calcium mobilization assay was performed by first loading the co-expressing cells with a calcium-sensing dye (Cal-590 AM, AAT Bioquest) and recording basal fluorescence of the dye. DRD2 receptor agonist solutions of various concentrations were prepared and to the cell culture media. Binding of the ligand to the receptor results in an influx of calcium to the cytoplasm, which was characterized in real time by monitoring the increase in dye fluorescence with confocal microscopy.

Our calcium flux bioactivity data suggests that the G_{qi5} construct is adequately expressed and functionally active after 24 hours post transfection at a concentration of 2 μg/mL plasmid DNA and a 3:1 ratio of DNA to lipid transfection reagent. The observed half-maximal effective concentrations of pramipexol and ropinirole are comparable to those observed in other GPCR functional assays.

2.1.3 Experimental

2.1.3.1 Calcium mobilization microscopy assay

HEK293T- cells were maintained in DMEM supplemented with 10% FBS, 100 U/mL penicillin, and 100 μg/mL streptomycin in a humidified atmosphere at 37 °C in 5% CO_2. On day 1, cells were plated at a density of 4×10^4 cells/cm^2 in a poly-D-lysine-coated 18-well chambered coverslip (Ibidi). The following day (day 2), cells were transfected with a 10× solution of 3:1 mixture of G_{qi5}/GFP-DRD2/Optifect Transfection Reagent (Thermo) in unsupplemented DMEM (Final concentration: 2 μg/mL G_{qi5}, 2 μg/mL GFP-DRD2). On day 3, the transfection media was removed, and calcium-sensitive dye loading was performed following the protocol of the Cal-590 AM Calcium Assay Kit (AAT Bioquest). 5× drug stimulation solutions were prepared in filter-sterilized HBSS. Once Cal-590 loading was complete, a time series acquisition at a rate of 1 fps was recorded using a Zeiss LSM 980 with Airyscan 2. Basal fluorescence was recorded for 20 s, followed by the addition of drug solution to a 1× final concentration and acquisition for an additional 40 s. Results in the form of fold fluorescence increase over basal were averaged over 50 cells in ImageJ (NIH), and GraphPad Prism was used for the analysis of data.

2.2 Stable DRD2 cell line generation

The ABPP biochemical studies, described in Chapter 3, required production of milligram quantities human cell line expressed DRD2. Although transient expression of GPCRs in mammalian cells is a well-established strategy, large-scale production following this method is associated with high consumable costs and limited transfection efficiency. Lentiviral transduction provides an efficient method of transgene delivery and results in a stably expressing cell line that can be cultured, stored, and used in functional assays without the expense of transient expression consumables or time.[8] In this section, we describe the design and application of a lentiviral transduction system for the stable expression of a DRD2-Step Tag II fusion protein in HEK 293T cells. Selection for high expressing cells is described, and large-scale production of DRD2 in HEK293 cell lines is used for ABPP proteomics.

2.2.1 Cloning of DRD2 transfer plasmid

The transfer plasmid vector was derived from pHR-CMV-TetO2-IRES-mRuby2 (addgene #113885) linearized with the following primers: FORWARD 5′-TCCTGAAGATCCACTGCCTTGAGGTGCTGTTTCAGGG-3′, REVERSE 5′-CAGGA-CAGATTCAGTGGATCTTTCAGCTACGCAACCCATCAG-3′. The gene insert was amplified from GFP-DRD2 (addgene #24099) linearized with the following primers: FORWARD 5′-GATGGGTTGCGTAGCTGAAAGATCCACTGAATCTGTCCTGGTATGA-3′, REVERSE 5′-CCCTGAAACAGCACCTCAAGGCAGTGGAGGATCTTCAGGA-AGG-3′. Linearized fragments were assembled via Gibson assembly. The assembled plasmid was expressed (DH5-alpha E. coli, New England Biolabs), purified (QIAGEN

anion exchange plasmid purification) and sequenced to confirm fragment insertion. The design of the DRD2 transfer plasmid retained the C-terminal Strep Tag II purification tag from the pHR-CMV-TetO2-IRES-mRuby2 template. Bicistronic expression of mRuby was removed and the tetracycline induction motif was removed.

The transfer plasmid was used in conjunction with the second-generation envelope plasmid, pMD2.G (Addgene #12259) and the second-generation packaging plasmid, psPAX2 (Addgene #12260).

2.2.2 Lentivirus production and viral transduction

The DRD2 transfer plasmid, envelope plasmid and packaging plasmid were co-transfected into a lentivirus production cell line (LentiX 293T, Takara Bio) with polyethyleneimine (PEI) transfection reagent following the procedure of Elegheert *et al.*[8]. Cells were incubated for three days to produce soluble lentivirus before the lentivirus containing media was collected and sterile filtered. Polybrene was added to the lentivirus containing media to reduce charge repulsion between the lentivirus and cell membrane.

A confluent flask of HEK 293T cells was washed with PBS and the lentivirus containing media was added. Three days after the addition of the lentivirus containing media, the cells were imaged on a fluorescent microscope to assess infection efficiency and DRD2 expression levels. Polyclonal integration of the viral DNA was deemed successful upon strong GFP signal among a fraction of the population.

2.2.3 Cell line enrichment

The polyclonally transduced cells were expanded to >30 x 10^6 cells. Following initial expansion, the polyclonally transduced cells were enriched for the top 10% of expressing cells via fluorescence-assisted cell sorting (BD FACS Aria III) with GFP fluorescence guiding relative expression. The enriched cells were expanded, and flash frozen for long-term storage. DRD2 expression levels remained high for >90% of the population after 15 passages, as measured by flow cytometry.

2.2.4 Experimental

2.2.4.1 Lentivirus production

General procedures followed the protocol of Elegheert *et al.*[8].

On day 1, HEK 293T Lenti-X cells were seeded in a T75 tissue culture flask at a density of 9 x 10^6 HEK293T Lenti-X cells in 12 mL DMEM/F-12/10% FBS. The flask was incubated for 24 h at 37°C with 5% CO_2 (until 90% confluence). On day 2, the plasmid DNA-transfection reagent mix (30 µg total DNA; 1:1:1 (wt:wt:wt) transfer:packaging:envelope plasmid ratio) was prepared (10 µg DRD2 transfer plasmid, 10 µg psPAX2 packaging plasmid, 10 µg pMD2.G envelope plasmid). DMEM/F-12 was added to the DNA mixture to a total volume of 0.25 mL. A solution of 75 µL PEI (1:2.5 (wt:wt) DNA:PEI ratio) in DMEM/F-12 to a total volume of 0.25 mL was prepared and added to the DNA mixture and allowed to incubate at room temperature for 30 minutes. The confluent T75 flask with HEK293T Lenti-X cells was removed from the incubator and the DNA-transfection reagent mixture was added. The flask was returned to the

incubator for three days at 37 °C with 5% CO_2. On day 5, the conditioned media was removed from the flask of transfected LentiX cells and sterile-filtered through a 0.45 µm syringe filter. Polybrene was added to the conditioned media to a final concentration of 10 µg/mL. A confluent T75 flask of HEK293T cells was washed with PBS before adding the conditioned media. The flask was returned to the incubator three days at 37 °C with 5% CO_2. On day 8 (three days post-infection), the media was exchanged for DMEM supplemented with 10% FBS, 100 U/mL penicillin, and 100 µg/mL streptomycin. The cells were visualized for GFP expression using a fluorescence microscope (Zeiss AxioVert.A1). The flask was expanded to a T300 tissue culture flask until 70% confluence. Enrichment via FACS followed.

2.2.4.2 Enrichment of polyclonally transduced cells via FACS

At confluency, media was removed and cells were washed once with HBSS, followed by incubation for 5 min in Trypsin-EDTA solution (0.25%, Gibco). Following incubation, the cell suspension was transferred to a 50 mL conical tube and then pelleted at 300 xg for 5 min. The supernatant was removed, and the cell pellet was resuspended in HBSS followed by centrifugation at 300 xg for 5 min. The supernatant was removed, and the cell pellet was resuspended in HBSS containing 10% FBS and was analyzed with a BD FACS Aria III fluorescence assisted cell sorter. Samples were gated on forward scatter and side scatter to exclude cell debris and aggregates, blue channel fluorescence was analyzed the top 10% fluorescence to be collected. The enriched population was plated in a T75 flask, expanded, and flash frozen in LN2 for long term storage.

2.3 References

(1) Juárez Olguín H, Calderón Guzmán D, Hernández García E, Barragán Mejía G. The Role of Dopamine and Its Dysfunction as a Consequence of Oxidative Stress. Oxid Med Cell Longev. 2016;2016:9730467.

(2) Yin J, Chen KM, Clark MJ, Hijazi M, Kumari P, Bai XC, Sunahara RK, Barth P, Rosenbaum DM. Structure of a D2 dopamine receptor-G-protein complex in a lipid membrane. Nature. 2020 Aug;584(7819):125-129.

(3) Zhang, C., Li, Q., Meng, L., Ren, Y. (2020). Design of novel dopamine D2 and serotonin 5-HT2A receptors dual antagonists toward schizophrenia: An integrated study with QSAR, molecular docking, virtual screening and molecular dynamics simulations. J. Biomol. Struct. Dyn. 38 (3), 860–885.

(4) Vetter I. Development and optimization of FLIPR high throughput calcium assays for ion channels and GPCRs. Adv Exp Med Biol. 2012;740:45-82.

(5) Ma Q, Ye L, Liu H, Shi Y, Zhou N. An overview of Ca2+ mobilization assays in GPCR drug discovery. Expert Opin Drug Discov. 2017 May;12(5):511-523.

(6) Billups D, Billups B, Challiss RA, Nahorski SR. Modulation of Gq-protein-coupled inositol trisphosphate and Ca2+ signaling by the membrane potential. J Neurosci. 2006 Sep 27;26(39):9983-95.

(7) Yokoyama T, Kato N, Yamada N. Development of a high-throughput bioassay to screen melatonin receptor agonists using human melatonin receptor expressing CHO cells. Neurosci Lett. 2003 Jun 19;344(1):45-8.

(8) Elegheert, J., Behiels, E., Bishop, B. et al. Lentiviral transduction of mammalian cells for fast, scalable and high-level production of soluble and membrane proteins. Nat Protoc 13, 2991–3017 (2018).

3 Photoaffinity probes for DRD2

3.1 Introduction

Physiological states ranging from euphoria to psychosis are governed by the neuroanatomical pathways of the dopaminergic nervous system.[1] The dopaminergic neurons comprising this system function via binding of the neurotransmitter dopamine to its receptors. There are a handful of subtypes of dopamine receptors expressed by these neurons that control diverse aspects of behavior, and it is hypothesized that individual subtypes combine and contribute to different biochemical pathways.[2,3] Unfortunately, though, it is extremely difficult to selectively target individual dopamine receptor subtypes, let alone pathways, with drugs or other non- endogenous stimuli.[1] From the standpoint of directing neurochemistry via small molecules, the wide variety of physiological responses controlled by the dopaminergic system, coupled with the lack of selective drugs, makes drug/probe development highly challenging.

There are canonically five subtypes of dopamine receptors, D_{1-5}, which are separated into two families: D_1-like (D_1 and D_5) and D_2-like (D_{2-4}), with receptors D_1 and D_2 exhibiting the highest expression density of all dopamine receptors in the human central nervous system.[4] Further, there are several isoforms of the individual receptor subtypes.[5] Perhaps, the best-studied and most medically important dopamine receptor is D_2 (DRD2), which is the focus of therapeutic intervention for diseases such as psychosis and Parkinson's.[6] In fact, dopamine receptors 1, 3, and 4 are also bound/blocked to some degree by drugs targeting DRD2, but it is unclear how much the pharmacodynamics of these subtypes contribute to the drug's clinical effectiveness.[1]

This poor selectivity of available drugs is likely due in large part to the lack of structural data regarding DRD2, coupled with the high structural homology between receptor subtypes.[7–9] Only a handful of structures exist, and those that do rely on extensive mutation to enable easier isolation and temperature stability, even to the point of altering the receptor's ligand binding.[10,11] It is hypothesized that DRD2 does not have a "rigid" orthosteric site, further complicating analysis.[11]

Combined photoaffinity labeling and proteomic analysis are powerful tools for showing the breadth of proteins bound by a drug, as well as the specific peptide sequence in the vicinity of the drug binding site.[12] These works are enabled by the strategies used in ABPP, photoaffinity labeling, and advances in mass spectrometry.[13] This strategy has recently been used to great effect to study the activity profiles of NSAIDs, cannabinoid drugs, and meth- amphetamine, for example.[14–16] Detailed receptor binding site studies have been enabled by photo-cross-linking the CNS drugs granisetron, propofol, glutamate receptor modulators, and others.[17–19] DRD2 itself has a long history of use with photoaffinity technology to aid the biochemical characterization of this hard-to-handle membrane-bound protein.[20,21]

Here, we have adapted these technologies to show both broad target engagement of probes based on DRD2-binding pharmacophores and the specific peptides in the local environment of the probe when bound to the DRD2 receptor. Together, these data may show potential targets of drugs based on similar scaffolds, as well as provide more insight into the functional structure of DRD2.

3.2 Design

The framework for our probe design was to employ a DRD2-binding pharmacophore attached to a photoreactive group and an alkyne for copper catalyzed azide-alkyne cycloaddition (CuAAC) chemistry. To fabricate novel ligands for DRD2, we required a pharmacophore to retain high affinity while tolerating the addition of (1) a photoaffinity group for covalent attachment to the receptor and (2) an alkyne as a handle for attachment of a fluorophore. For the photoaffinity moiety, two of the most common photo-cross-linking groups are benzophenones and diazirines, which upon irradiation with UV light generate ketyl radicals and carbenes, respectively.[22] There are benefits and drawbacks to both groups; for example, benzophenone generates a longer-lived reactive intermediate and is relatively easy to synthesize but is hampered by its large size. In contrast, the carbene is highly reactive and shorter-lived, which can be advantageous, but is relatively harder to synthesize in high yield and may degrade quickly. Additionally, off-target/nonspecific binding proteomic profiles vary for probes incorporating the two different cross-linkers.[23–25] We thus chose to assay the performance of both groups as cross-linking moieties in our probes and synthesized a panel of derivatives to assay, which focused on replacing the *N*-alkyl groups of ropinirole with photo-cross-linking groups. This allowed us to leave the ropinirole pharmacophore mostly intact while adding new functionality for photo-cross-linking and CuAAC chemistry.

We chose to build our probes based on the core structures of two highly prescribed DRD2 agonists: ropinirole and pramipexole (Figure 3) (in 2018, they were ranked as the 147th and 187th most-prescribed drugs in the United States, although

ropinirole's manufacture has since been discontinued).[26,27] The drugs treat the symptoms of Parkinson's disease and other neurological maladies. However, both come with many serious adverse drug reactions, such as confusion, hallucinations, psychosis, excessive somnolence, which may persist even after discontinuing use, and tardive dyskinesia.[11,28] Troublingly, as much as 74% of patients experience such adverse drug reactions in the case of pramipexole.[29] The high demand for such treatments and the high adverse reaction rate to currently available drugs highlight the need for (1) a better understanding of how DRD2 ligands bind the receptor; (2) elucidation of the biophysics of how small molecules can direct DRD2 to various signaling pathways; and (3) the other off-target proteins such drugs engage. These three factors are critical for both effective DRD2 drugs and preventing off-target effects.

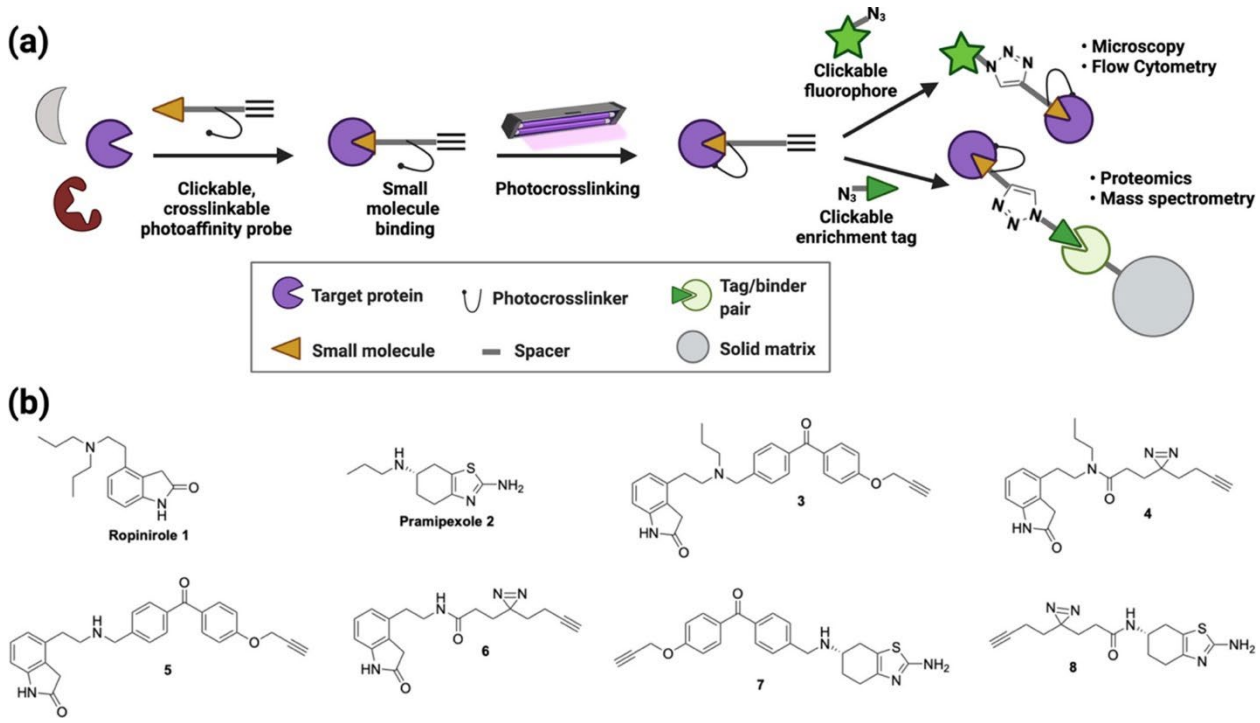

Figure 3. Photoaffinity labeling for the simultaneous determination of protein targets and sites of probe labeling.

(a) Probes bear two handles: one for visualization and one for enrichment. This allows monitoring of probe–target interactions by imaging as well as enrichment for proteomics. (b) Ropinirole, pramipexole, and clickable, photo-cross-linkable target probes based on their pharmacophores.

From a chemical perspective, these scaffolds represent two very distinct structures. Ropinirole is a substituted oxindole, while pramipexole is a cyclohexyl-thiazoline with a chiral center. The two molecules have different three-dimensional structures and surface areas, and H-bond donating and accepting potential. Their most critical similarity is that they are both substituted with an alkylamine. Through structure−activity studies and comparison with the native ligand, dopamine, it can be surmised that this basic nitrogen is critical to receptor binding.[30−36] Conversely, the analysis of DRD2 ligands, as well as work on structurally related receptors, indicated that this basic

nitrogen was a likely region to permit more steric bulk to be attached to a pharmacophore.[33,37,38]

3.3 Synthesis

The synthesis of ropinirole derivatives started with the commercially available 4-substituted hydroxyindole **9** (Scheme 1). With the goal of substituting the alcohol for an amino group as in published ropinirole syntheses, we began by mesylating the alcohol to provide **10**. This is because, in our hands, tosylation of **9** gave a mixture of products, which were challenging to separate via chromatography, whereas mesylate **10** synthesis proceeded cleanly. The yield suffers some from the likely competing elimination reaction; this may be due to the easier formation of an antiperiplanar conformation for a more facile E2 elimination reaction versus syn elimination.[39] The mesyl was displaced with sodium azide to provide **11**, which was then reduced to amine **12** using polymer-bound triphenylphosphine. To alkylate or acylate amines **12** and **13**, we synthesized known linkers **14** and **15**.

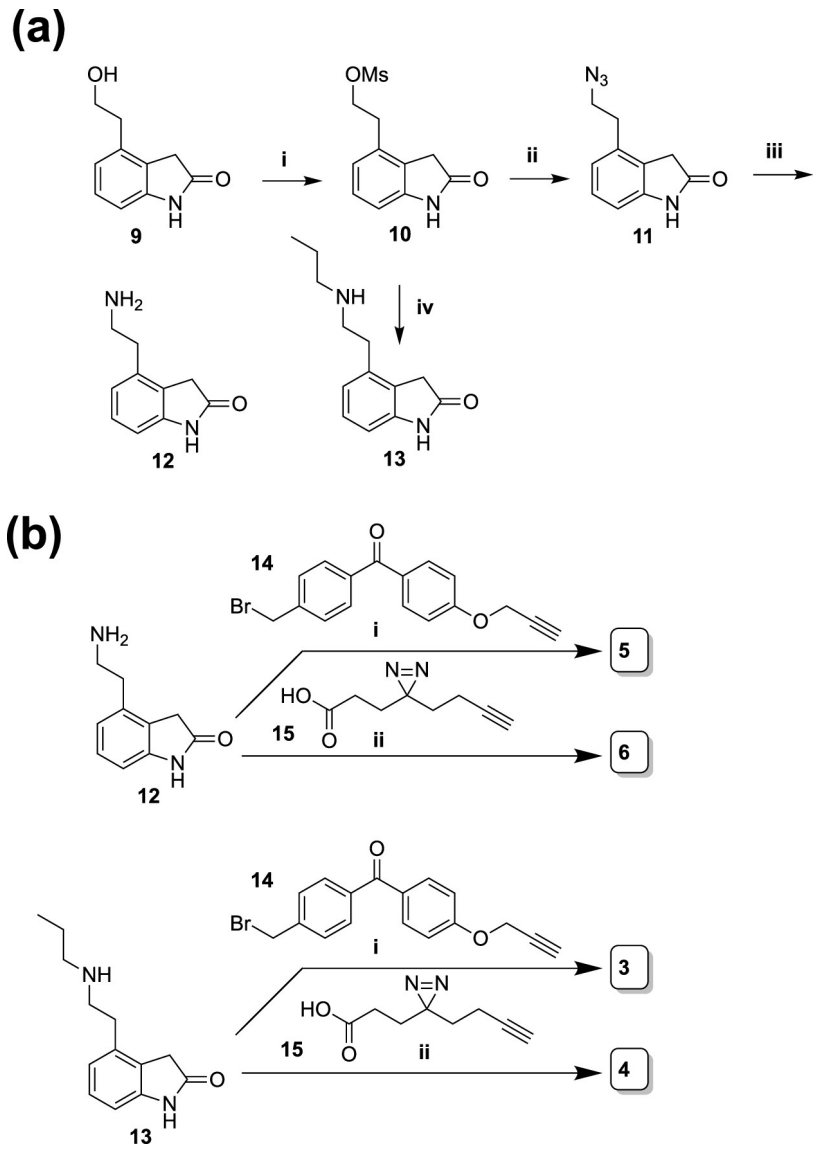

Scheme 1. Synthesis of Ropinirole-Based Targets with Multifunctional Cross-Linkers.

(a) (i) MsCl, TEA, CH_2Cl_2, 74%; (ii) NaN_3, H_2O, 72%; (iii) polymer-bound PPh_3, 22%; (iv) N-propylamine, reflux 29%.
*(b) (i) $CsCO_3$, KI, **14**, 33% for **5**, 10% for **3**; (ii) EDC-HCl, HATU, DIPEA, **15**, 27% for **6**; 32% for **4***

For pramipexole, derivatives were synthesized by alkylation or acylation of commercially available aminothiazole **2** to furnish a set of pramipexole derivatives (Scheme 2). With the probes in hand, we then turned our attention to biochemical analysis.

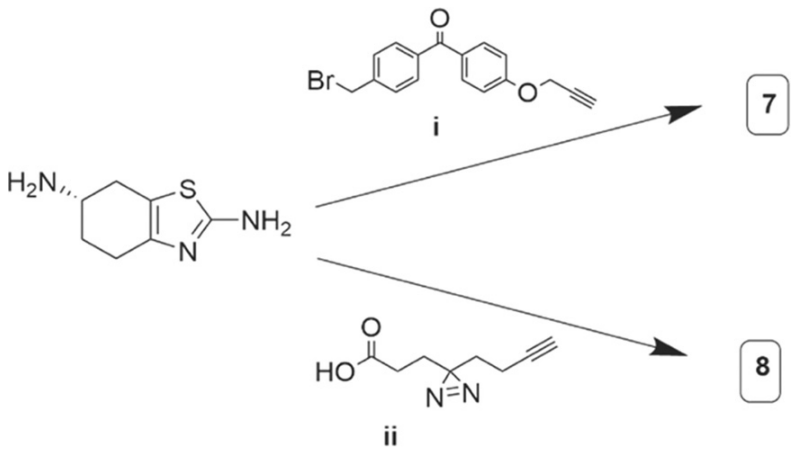

Scheme 2. Synthesis of Pramipexole-Based Targets with Multifunctional Cross-Linkers.

*(i) $CsCO_3$, KI, **14**, 79%; (ii) EDC-HCl, HATU, DIPEA, **15**, 45%*

3.4 Pharmacology

DRD2 can transduce extracellular ligand binding into intracellular signals via a variety of effector molecules, notably the Gi protein and β-arrestin.[40,41] We reasoned that if our probes could recapitulate the biological activity of the core pharmacophore, it was likely that they were binding the receptor in a similar fashion to the original receptor. We thus focused on these two pharmacologically important signal transduction pathways, G_i protein and β-arrestin, to determine how well our derivatized pramipexole and ropinirole recreated the activity of the original drug.

3.4.1 Intracellular Ca^{2+} mobilization bioactivty

Intracellular calcium measurement was used to determine G-protein- mediated signaling by DRD2. Because DRD2 is linked to the G-protein subtype G_i, agonist binding inhibits adenyl cyclase activity.[42] To mitigate this effect, we created an HEK293T

cell line stably expressing human DRD2, long form, and a chimeric G-protein, G_{qi}, which alters the DRD2 receptor's G-protein coupling so that signaling can occur through G_q, resulting in an intracellular calcium flux.[43] The assay is performed by first loading the cell line with a calcium-sensing dye. Binding of the ligand to the receptor results in an influx of calcium to the cytoplasm, which can be characterized in real time by monitoring the increase in dye fluorescence with confocal microscopy.

Our calcium flux bioactivity data, shown in Figure 4, suggest regions on the pramipexole and ropinirole pharmacophores that are highly tolerant toward extensive elaboration into a multifunctional probe, as well as those necessary for receptor binding. We found that ropinirole derivative 5 and pramipexole derivative 7 are active with low micromolar potency. Both probes have extensive bulk and molecular weight added to the basic nitrogen. The key requirement appears to be the retention of basicity of the nitrogen within the context of the pharmacophore, as evidenced by the greatly diminished activity of probes 4 and 8. These probes contain chemically similar substitutions, except for the employment of an amide bond to derivatize the key nitrogen. The activity constants are tabulated in Table 1.

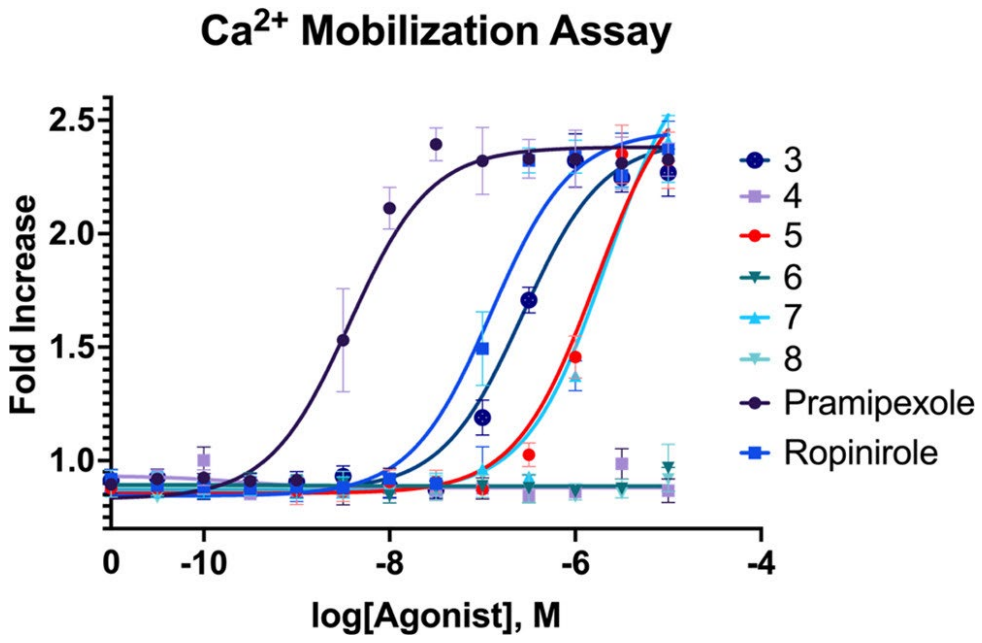

Figure 4. Intracellular calcium flux assay.

HEK293T cell line stably expressing constructs for human DRD2 and a chimeric G-protein is loaded with calcium-sensing dye, Fura-4. After dosing the probe, confocal microscopy is used to determine the calcium flux in the cell by change in dye fluorescence. EC_{50} curves determined with GraphPad software using a Hill slope of 1.0.

compound	EC_{50}	R^2
5	1.67 μM	0.95
7	2.19 μM	0.95
ropinirole	124 nM	0.95
pramipexole	3.72 nM	0.96

Table 1. Constants from Ca Assay.[a]

[a] R^2 value is calculated using nonlinear regression.

3.4.2 TANGO bioactivty

To characterize the response of the β-arrestin effector pathway to our ligands, we used the Parallel-Receptor-ome Expression and Screening via Transcriptional Output TANGO (PRESTO-TANGO) assay developed in the Roth lab.[44,45] This assay uses luciferase activity to monitor β-arrestin recruitment by DRD2 (Figure 5).

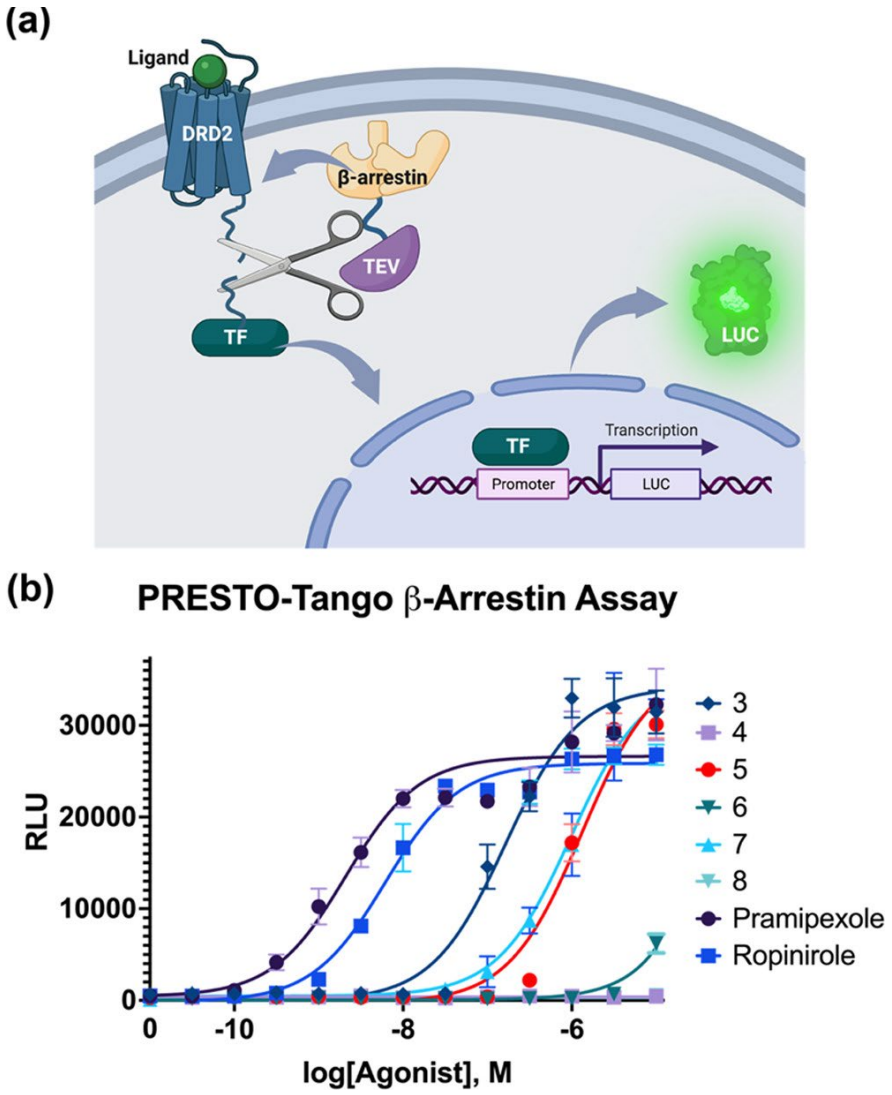

Figure 5. β-Arrestin recruitment analysis.

(a) PRESTO-TANGO assay schematic: a ligand binds a chimeric DRD2 receptor, which then recruits β-arrestin fused with a TEV protease. The protease cuts a site between the receptor and a fused transcription factor, which then transits to the nuclease to initiate transcription of a luciferase gene. The luciferase activity is subsequently quantified. (b) Agonism of β-arrestin recruitment is quantified in EC_{50} curves via the detection of luciferase activity, using a Hill slope of 1.0.

The β-arrestin recruitment data (Figure 5) indicate that probes 5 and 7 are again the most active derivatives, like what was found with the calcium assay. However, in contrast to the calcium assay, both pramipexole and ropinirole demonstrate low nanomolar activity, and probes 5 and 7 exhibit low micromolar activity, a difference of approximately ~1000× for both probes vs their parent compounds. This is different than the calcium assay, where ropinirole and 5 instead showed only an approximate 10× difference. This may indicate that the substitutions on 5 are more disruptive of receptor binding interactions involving G-protein signaling vs β-arrestin. The activity constants are tabulated in Table 2.

compound	**EC_{50}**	***R^2***
5	1.32 μM	0.96
7	990 nm	0.97
ropinirole	6.14 nm	0.99
pramipexole	2.09 nm	0.94

Table 2. Constants from PRESTO-TANGO Assay[a]

[a]R^2 value is calculated using nonlinear regression.

3.5 Photoactivity

3.5.1 Click microscopy labelling propensity

After the biochemical characterization of the dynamic interaction between the probe and target, we set out to characterize the static interaction: colocalization of probe and receptor in cells, with an emphasis on both on- and off-target labeling. Specifically,

due to the known propensity for photo- cross-linking groups to nonspecifically label, we wanted a holistic view of how the probes interacted with whole cells. Thus, we treated our DRD2-expressing cell line with a 5 μM solution of the probe, photo-cross-linked, “clicked” on an azido fluorophore, and labeled the DRD2 receptor via an antibody conjugated to a complementary fluorophore (Figure 6a). Our results (Figure 6b) indicate that there is indeed background labeling with the probes. However, it was also possible to see some qualitative differences, probes **5** and **7** appeared to label DRD2-expressing cells with a higher avidity relative to the other probes. We therefore proceeded to quantify the specific vs nonspecific binding of the probe.

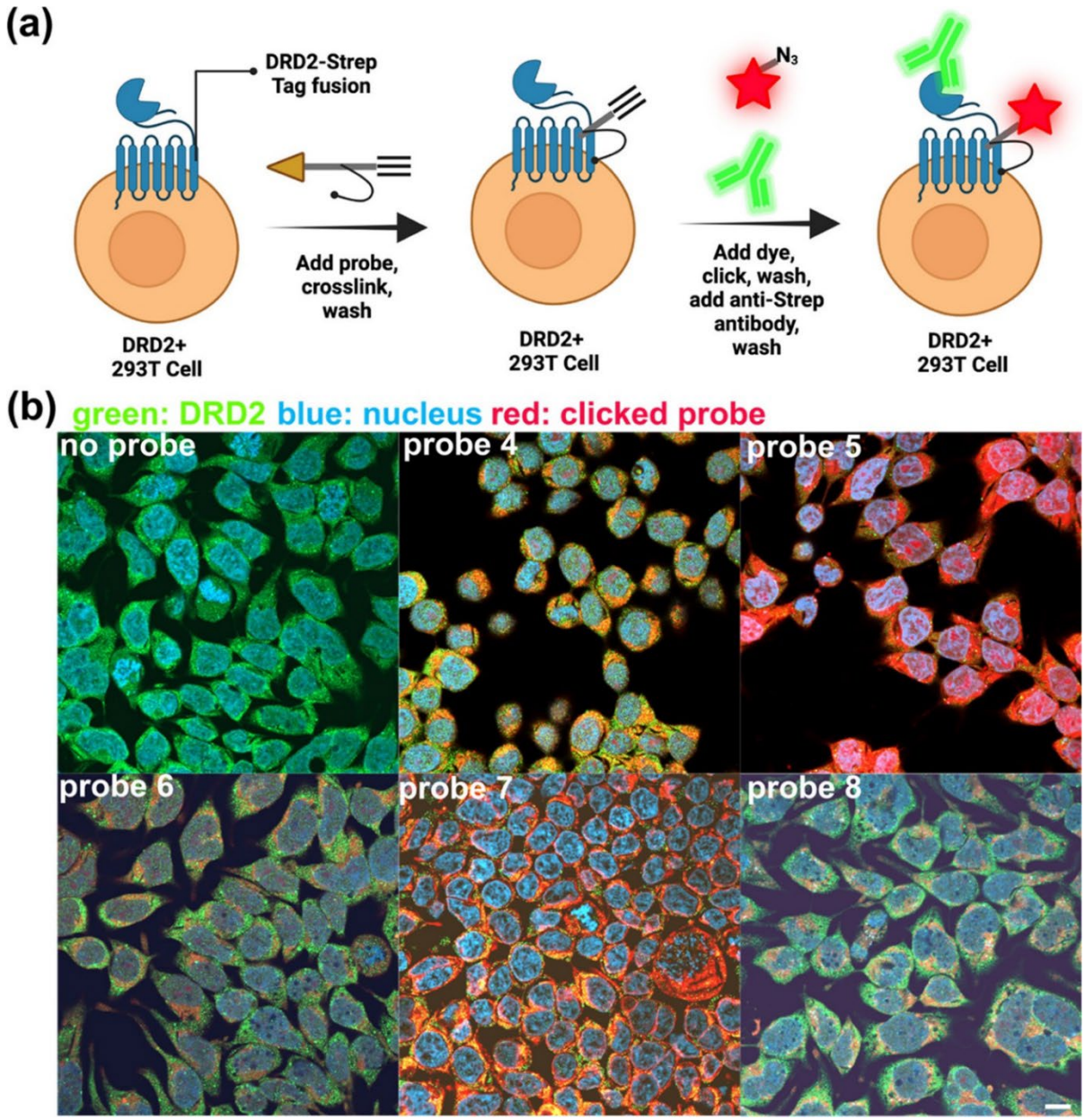

Figure 6. Photo-cross-linking of dye-clicked probe: confocal microscopy.

*(a) Schematic of the methodology used in the labeling process. Cells stably expressing DRD2 fused to an N-terminal Strep Tag II are treated with DRD2-targeting probes **5** or **7** at 5 μM, photo-cross-linked, and excess probe is washed out. An Alexa Fluor 555 azide is then clicked to the probe, washed out, and cells are treated with an anti-Strep-Tag II antibody and fluorescent secondary to visualize DRD2. Nuclei were stained with DAPI. (b) Confocal microscopy results of labeled cells. All probes show some degree of labeling. However, probes **5** and **7** show a notable increase in the labeling density. Images taken with 40× magnification, scale bar: 10 μm.*

3.6 Specificity

With positive bioactivity and photoactivity data in hand, we were encouraged to evaluate the specificity of labelling for probes **5** and **7** in complimentary assays to demonstrate specificity across biochemical settings. A flow cytometry assay was developed to quantify the labelling efficiency of DRD2 overexpressing cells versus background surface protein labelling, and western blot assay was developed to visualize the protein specificity of the system.

3.6.1 Flow cytometry quantification of probe labelling of cells.

Flow cytometry was used to quantify the number of cells that were successfully labeled by probes **5** and **7** as these were the most promising biochemically and seemed to display the highest propensity for labeling DRD2-expressing cells. To perform the quantification, our 293T cell line- expressing DRD2 or unmodified 293T cells as a negative control were treated with probes at a 100 nM concentration, the lower concentration than the EC_{50} determination, likely due in large part to the covalent nature of the binding event versus the noncovalent EC_{50} assays. The probes were covalently cross-linked to the cells with UV, and the unbound probe was washed out. The azide-containing fluorescent dye was then clicked onto the probe, the unbound dye was washed out, and the cells were analyzed by flow cytometry (Figure 7a). The results show that there is a highly statistically significant increase in the labeling of cells expressing DRD2 over those that do not (Figure 7b), with a P-value of less than 0.0001. High background labeling is well known for photo-cross- linking methodologies and has been extensively discussed in the literature.[23–25] In these experiments, we were

encouraged to see that the inclusion of the DRD2-binding pharmacophore enhanced the probes' selectivity for DRD2-expressing cells.

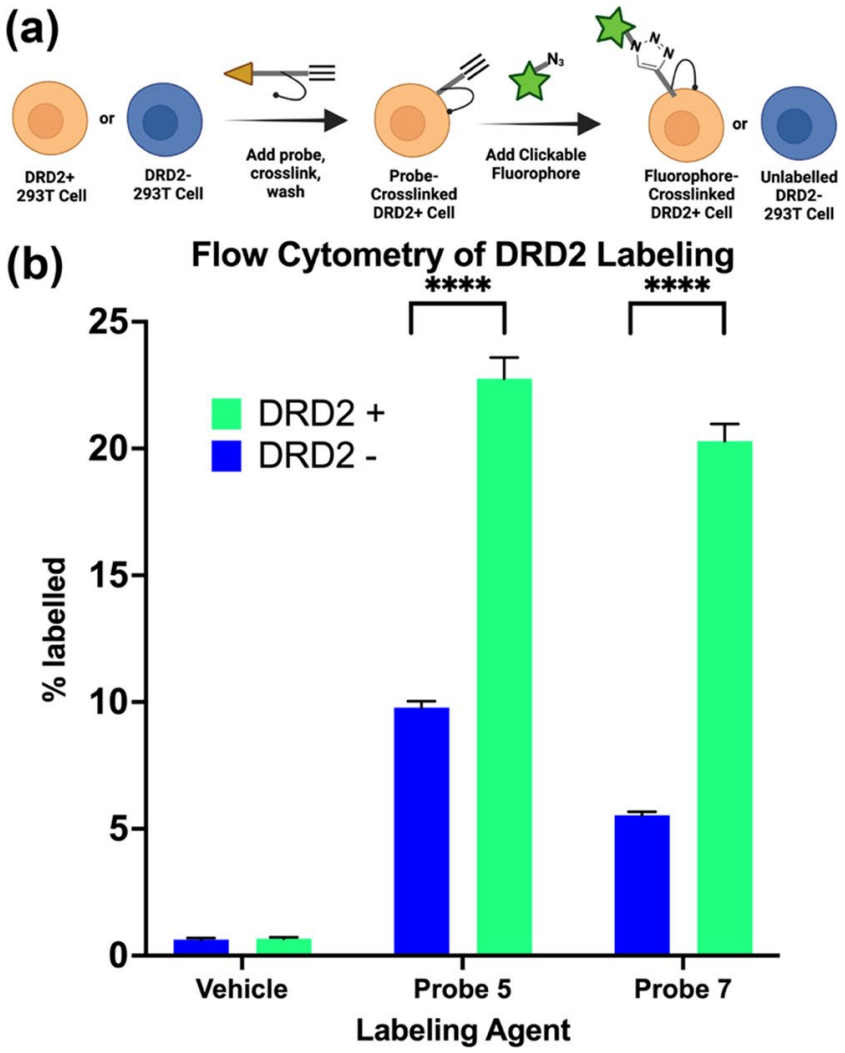

Figure 7. Flow cytometry quantification of probe labeling.

*(a) Schematic of flow cytometry workflow. (b) DRD2-expressing 293T cells or untransduced 293T cells (negative control) are treated with a 100 nm probe, which is photo-cross-linked, and an Alexa Fluor 555 azide is then "clicked" onto the probe. The cells were then analyzed by flow cytometry. P values determined using two-way ANOVA in GraphPad; **** corresponds to P < 0.0001.*

3.6.2 Western blot analysis of DRD2-probe binding

To observe the photo-cross-linking of DRD2 at the protein level, we analyzed the colocalization of DRD2 by clicking a fluorophore on the probe and performing Western blots. We further observed the competition with the parent pharmacophore of each probe and the ability of a negative control benzophenone (**16**) to cross-link to DRD2. Our DRD2- expressing cells or unmodified 293T cells (control group) were suspended in media, treated with the probe at a 100 nM concentration, and photo-cross-linked. The cells were then lysed, and the membrane fraction was separated and enriched for DRD2 by pulldown of the Strep Tag II fusion using magnetic beads. After “clicking” a fluorescent tag to the probe, the membrane fraction was run on an SDS-PAGE gel, transferred to a nitrocellulose membrane, and treated with antibodies against DRD2 and Strep Tag II. The Western blot (Figure 8) showed that the probe fluorescence colocalized with the signal for the anti- DRD2 antibody, suggesting that the probe was binding DRD2. We also observed many nonspecific binding bands for the probe, which is consistent with our other studies, as well as the observations of the field when it relates to photo-cross-linking groups. The competition assay showed that a 50 μM concentration of competitor was sufficient to greatly diminish the binding of **5** and **7**, indicating that the probes bind at the same site as the parent pharmacophore. The negative control probe 16 did not show colocalization with the DRD2 band. Overall, these results supported the conclusion that probes **5** and **7** were binding to the DRD2 receptor. With this confirmation, we proceeded to proteomic analysis of probe interactions.

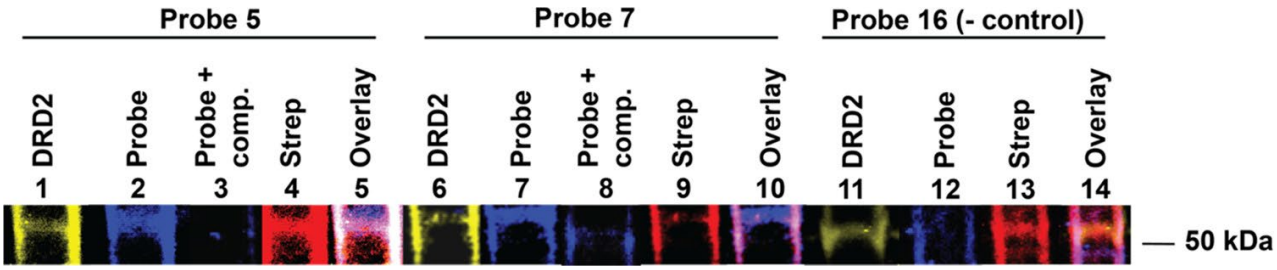

Figure 8. Photo-cross-linking of probes 5 and 7 to DRD2 visualized with Western blot.

*Lanes 1–5 correspond to samples with probe **5** at 100 nm, lanes 6–10 correspond to samples treated with probe **7** at 100 nm, and lanes 11–14 correspond to samples treated with negative control probe **16**. Lanes: 1, 6, and 11 are the anti-DRD2 antibody channel, lanes 2, 3, 7, 8, and 12 are fluorescence of the Alexa Fluor 555 clicked to the probes **5**, **7**, or **16**, lanes 4, 9, and 13 are the anti-Strep Tag antibody channel, and lanes 5, 10, and 14 are the overlaid channels for the respective probes.*

3.7 Application

3.7.1 Proteomic identification of primary rat brain protein networks covalently modified by probes

We used a combination of affinity purification and proteomic analysis to identify the pathways that associate with proteins bound by probes 5 and 7, following the workflow shown in Figure 9. DRD2 is a membrane bound GPCR, and, as mentioned previously, it is known to be exceedingly difficult to study in isolation from its host cell. Further, DRD2 expression levels differ widely according to brain region, layer, and other biochemical variables.[46–48] Thus, to validate our approach, we first determined whether we could detect the DRD2 expression using our mutant cell line, which exogenously expresses DRD2. We found that DRD2 protein could indeed be detected via mass spectrometry following photo-cross-linking of probe and biotin−streptavidin pulldown. We were encouraged that we were able to detect the DRD2 protein, although we were

unable to determine the specific peptide modified by our probes (see Supporting Information Excel File 1). With these data, we proceeded to our experiments in primary cells.

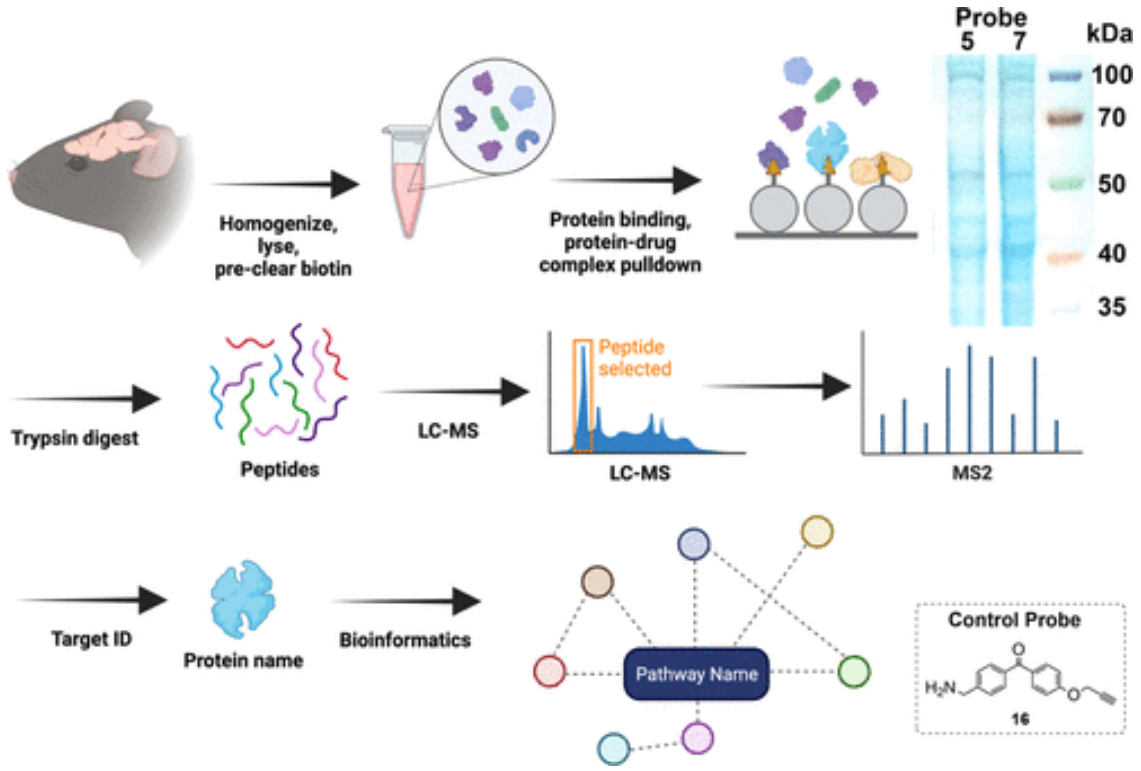

Figure 9. Workflow for affinity purification and proteomic analysis.

Whole brain tissue is homogenized and lysed, and endogenous biotin is removed. The lysate is treated with probe, photo-cross-linked, and biotin is clicked onto the probe. Streptavidin beads pull down proteins and their interactors via the linked biotin. An example Coomassie-stained gel of resulting proteins is shown in the inset. The proteins are trypsin-digested while on-bead, eluted, desalted, and peptides are run on LC-MS. Proteomic analysis (SEQUEST) is performed to ID the proteins, followed by bioinformatic analysis of functional protein association networks (KEGG, STRING).

Whole brain assays were designed to assay the binding partners of **5** and **7,** as well as a control for the inherent binding of the benzophenone cross-linker using molecule **16** (Figure 9). Here, we use a protein extraction methodology that does not bias the assay toward the membrane fraction. We chose this methodology to maximize

the amount of unique hits we were likely to record. A drawback to this assay, however, is that GPCRs need highly specific extraction/purification conditions to be detected by LC-MS (or other protein detection methodologies) at the end point. Thus, by biasing our assay toward a “wide lens” to record a picture of diverse interactions, we missed the specific focus necessary to observe DRD2 and structurally related GPCRs, and we were unable to directly observe DRD2 in the proteomic analysis.

To perform the assay, the whole brain minus the olfactory bulb from an adult female Sprague Dawley rat was homogenized and treated with probes or linker control 16 at a 50 μM concentration and photo-cross-linked. A streptavidin resin was used to deplete endogenous biotin and then clicked with azido biotin, followed by streptavidin pulldown. Coomassie gels of the pulldowns are shown in Figure 9. The streptavidin beads were processed by tryptic digest, followed by LC/MS proteomic analysis. Proteins identified in both control **16** and the **5** and **7** treated samples were removed as background. We found that probes **5** and **7** had 58 proteins in common, probe **5** showed 81 unique proteins, and probe **7** had 57 hits. All targets (peptides and proteins) were identified with a maximum false discovery rate of 5% or a q-value of >0.05. Most peptides and proteins were identified with a false discovery rate of 1%, q-value of >0.01. γ-Aminobutyric acid receptor subunit α1 and neuronal nitric oxide synthase (nNOS) were two of the most interesting hits in common between the two probes. γ-Aminobutyric acid is the major inhibitory neurotransmitter, and the γ-aminobutyric acid receptor subunit α1 is the target of sedative/hypnotic drugs.[49–51] nNOS catalyzes the production of the neuro-transmitter nitric oxide in the brain. Nitric oxide regulation contributes to a variety of physiological states, such as long- term potentiation, and

diseases, such as schizophrenia.[52,53] The inclusion of these neurotransmission-associated proteins as hits in our pulldown assay for both the ropinirole- and pramipexole-derived probes suggests that these neurotransmitter pathways may be contributing to the pharmacology of these drugs. In the hits unique to each of the probes, for **5** two of the standout hits were the muscarinic acetylcholine receptor M1 and CB1 cannabinoid receptor-interacting protein 1. The muscarinic acetylcholine receptors are GPCRs for the neurotransmitter acetylcholine. These receptors are critical to the fundamental neurological function, in addition to being effective drug targets.[54] Endogenous cannabinoids typically act presynaptically to suppress neurotransmitter release, and endocannabinoid receptors are GPCRs and are abundantly expressed in the brain.[55] CB1 cannabinoid receptor-interacting protein 1 competes with β-arrestin for binding to the cannabinoid receptor and may inhibit β-arrestin-mediated internalization of the cannabinoid receptor.[56] These proteins may play a role in eliciting distinctive physiological responses for ropinirole.

As many of the most medically relevant brain proteins (including DRD2) have highly variable and exquisitely controlled expression levels, their presence at any one point in time may be extremely low in abundance. Therefore, we used bioinformatic analysis on the LC/MS hits to understand the broader pathways that may be targeted by these probes. In an initial search, we determined pathways that ropinirole and pramipexole are already known to interact with, via the STICH platform, which catalogs drug−pathway interactions, and KEGG database, which here we used to determine disease- associated pathways.[57−64] For ropinirole, KEGG analysis indicated that in addition to the anticipated dopaminergic synapse and neuroactive ligand−receptor

interaction pathways, ropinirole also interacts with the tryptophan metabolism, cocaine addiction, alcoholism, gap junction, and chemical carcinogenesis pathways. For pramipexole, the dopaminergic synapse, neuroactive ligand−receptor interaction, cocaine addiction, alcoholism, and gap junction pathways are again represented, with the addition of the serotonergic synapse pathways via the serotonin receptors 5-HT_{2a} and 5-HT_{2c} (Figure 10 and Figure 11). With this information in mind, we then turned to analyzing the pathways represented by the hits from our LC-MS experiments.

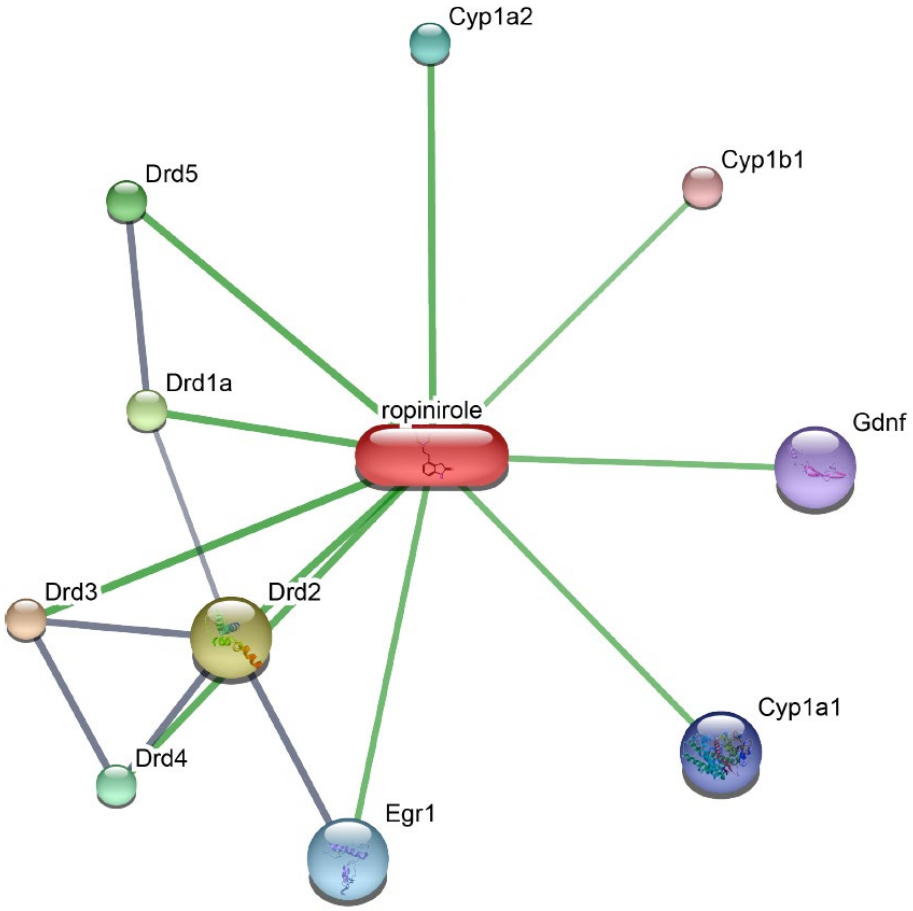

Figure 10. Previously-known proteins modulated by ropinirole according to STICH

Stronger associations are represented by thicker lines. Protein-protein interactions are shown in grey, chemical-protein interactions in green. Image generated using STICH database and user interface, stich.embl.de.

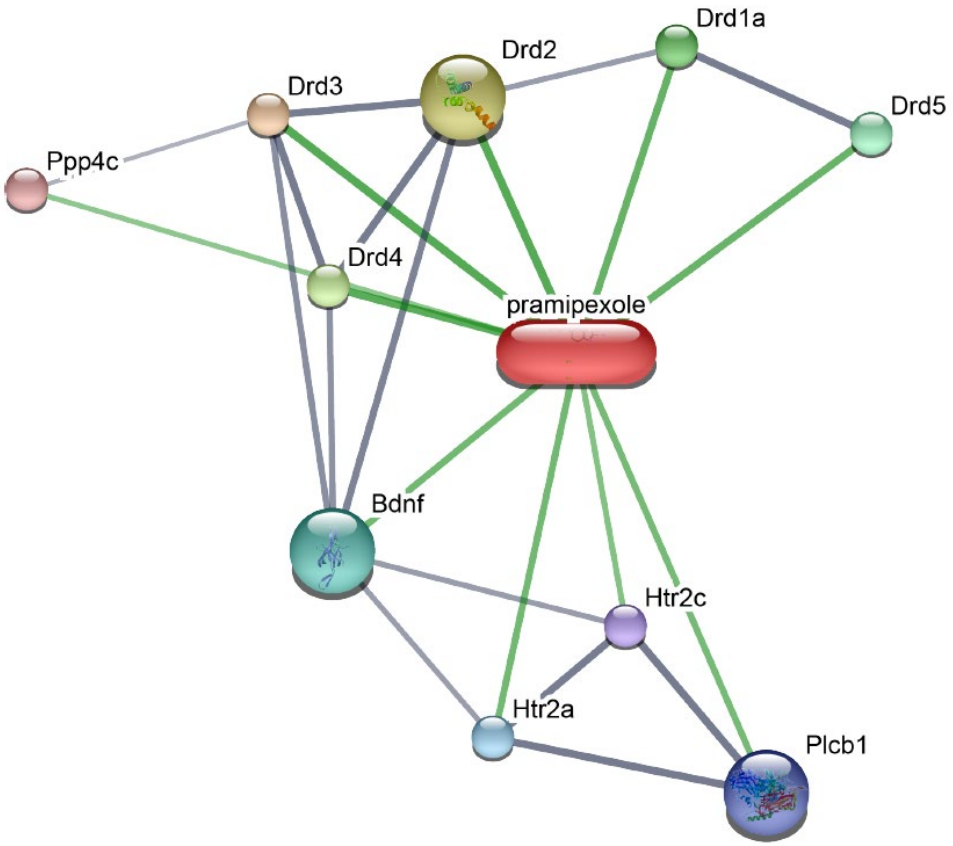

Figure 11. Previously-known proteins modulated by pramipexole according to STICH.

Stronger associations are represented by thicker lines. Protein-protein interactions are shown in grey, chemical-protein interactions in green. Image generated using STICH database and user interface, stich.embl.de.

For the hits in common between probes **5** and **7**, KEGG analysis indicated that there was significant enrichment in proteins from pathways directly involved in Parkinson's disease, Alzheimer's disease, and amyotrophic lateral sclerosis, among others. These data serve as a positive confirmation that probes **5** and **7** are recapitulating the mechanism of action of their parent pharmacophores, which are Parkinson's disease treatments. We next analyzed and visualized the biochemical connections between hits using the STRING database. The hits had significantly more

interactions than expected for a random collection of proteins (p-value < 1×10^{-16}). There was significant enrichment in Parkinson's disease, Alzheimer's disease, regulation of ornithine decarboxylase and RAS signaling pathways, par- kin−ubiquitin pathway (early-onset Parkinson's disease), and this pathway is particularly intriguing as this mechanism suppresses neurotransmitter release, as well as regulating motor control.[66] We then analyzed hits unique to **7**. A combination of molecular function (gene ontology) analysis and STRING analysis indicated that the dopamine receptor D_1 receptor binding pathway as a hit. Dopamine receptor D_1 is bound poorly by pramipexole. However, dopamine receptors dimerize, multimerize, and oligomerize, and our assay may be detecting some of the more biochemically robust members of this pathway: the cytosolic intracellular signal transduction proteins.[67,68] These combined data suggest that there may be multiple disease- related and neurological targets for these drugs, which may contribute to their overall pharmacology.

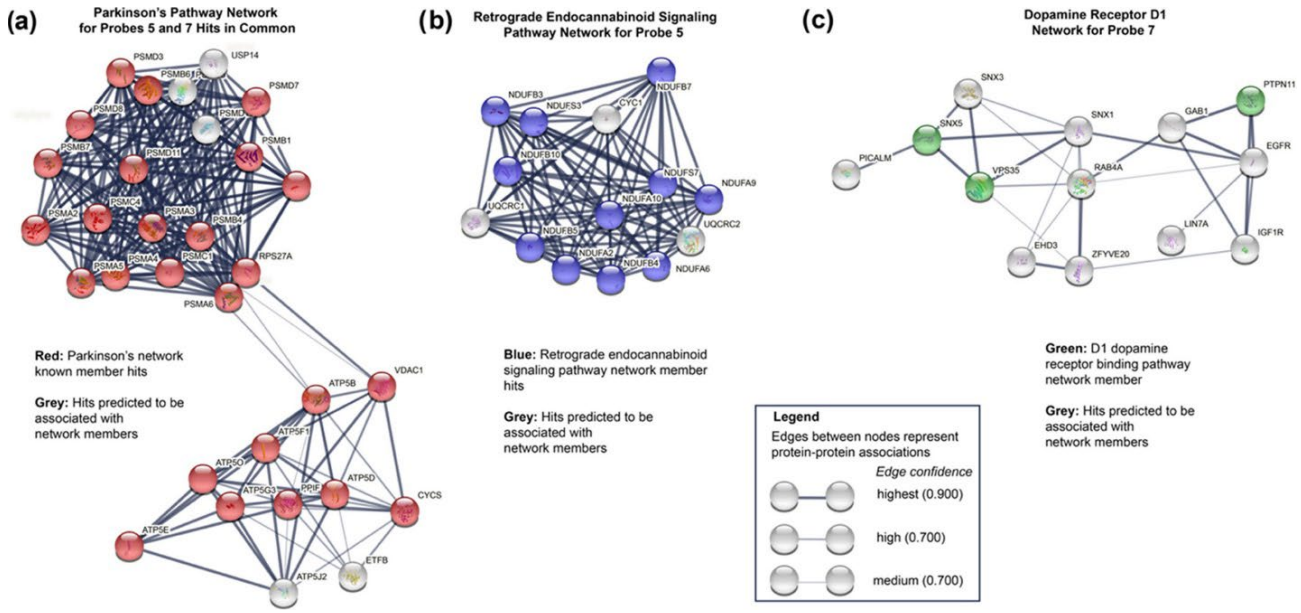

Figure 12. Protein networks identified by bioinformatic analysis.

*(a) Both probes **5** and **7** hit multiple genes in Parkinson's disease network according to STRING and KEGG analyses. (b) Probe **5** (ropinirole-based) hit many genes in the retrograde endocannabinoid signaling pathway according to STRING and KEGG analyses. (c) Probe **7** (pramipexole-based) hit genes in the dopamine receptor D_1 (DRD1) signaling network according to STRING and gene ontology analyses.*

3.8 Conclusion and future directions

In conclusion, the design and use of bioactive photoaffinity probes for DRD2 were demonstrated. These probes demonstrated excellent activity in "workhorse" biochemical assays used for traditional dopamine receptor-targeted drugs, as well as chemical−biological techniques of receptor and cell labeling, and chemi-proteomics. Most drugs have a variety of targets that may be missed by focusing on a small set of biochemical assays or looking at drug activity through the lens of a particular disease symptom. Here, our work reinforces the notion that omics-based approaches, which provide a broad picture of a molecule's "interactome", may also give insight into the pleiotropy of effects observed for a drug or perhaps indicate new applications.[22,69−71]

Specifically, probes **5** and **7** bound other protein networks including the retrograde endocannabinoid signaling pathway, neuronal nitric oxide synthase, GABA receptor components, and muscarinic acetylcholine receptor M1. Follow-up analysis may yield insights into how this pathway relates specifically to Parkinson's disease symptoms or provide new targets for treatments.

3.9 Experimental

3.9.1 Chemistry

All reactions were performed in flame- or oven-dried glassware under positive pressure of nitrogen or argon unless otherwise noted. Dichloromethane, dimethylacetamide, *N,N*-dimethylformamide, triethylamine, and toluene were dried by columns packed with activated alumina on a solvent purification system. Anhydrous pyridine and DMSO were purchased from Acros Organics in AcroSeal bottles. All reagents were used as purchased without further purification. Thin layer chromatography (TLC) was performed on Merck 60 F_{254} pre-coated silica gel plates, and plates were visualized with UV light and ninhydrin stain when appropriate. Flash-column chromatography was performed using silica gel (60 Å, 230-240 mesh, Merck KGA). HPLC runs were conducted on a Waters 2545 binary gradient pump equipped with UV-Vis Detector. Analytical runs were performed using a Phenomenex C18 column (4.6 x 50 mm). Separations were monitored at 254 nm. NMR spectra were recorded with Bruker Avance spectrometers using deuterated solvents. ^{1}H NMR spectra were recorded at 500 MHz as indicated. ^{13}C spectra were recorded at 125 MHz. ^{1}H NMR data are reported in the following order: chemical shift (δ ppm), multiplicity, coupling

constant (Hz), and integration. ^{13}C NMR data are reported in terms of chemical shift. Infrared spectra were recorded using a Thermo Scientific iD5 ATR infrared spectrophotometer. High-resolution mass spectra were obtained from the University of Delaware Mass Spectrometry Facility. The abbreviations used can be found in the document JOC Standard Abbreviations and Acronyms. Compounds **14** and **15** were synthesized as described previously; compound 16 was obtained commercially from Sigma-Aldrich.[72,73]

3.9.1.1 2-(2-Oxoindolin-4-yl)ethyl Methanesulfonate (10).

To a solution of 4-(2-hydroxyethyl)oxyindole (10 g, 56.4 mmol) in pyridine (22 mL, 282 mmol) was added methanesulfonyl chloride (5.24 mL, 67.7 mmol) in CH_2Cl_2 (50 mL) dropwise at 5−10 °C. The reaction was stirred at this temperature for 3 h, then aqueous $NaHSO_4$ (50 mL) was added, and the organics were extracted with CH_2Cl_2 (3 × 50 mL). The combined organic layers were washed with saturated aqueous Na2CO3, water, saturated aqueous NH_4Cl, and brine. The layers were then dried over $MgSO_4$, filtered, and concentrated in vacuo to yield 10 as a pale yellow solid (12.7 g, 49.9 mmol, 88%). ^1H NMR ($CDCl_3$) δ 8.63 (s, 1H), 7.22 (t, J = 7.8 Hz, 1H), 6.91 (d, J = 7.6 Hz, 1H), 6.83 (d, J = 7.6 Hz, 1H), 4.46 (t, J = 6.8 Hz, 2H), 3.54 (s, 2H), 3.03 (t, J = 6.7 Hz, 2H), 2.93 (s, 3H); 13C NMR (100 MHz, acetone-d6) δ 177.3, 142.7, 132.8, 128.5, 124.7, 122.8, 108.7, 68.9, 37.5, 35.1, 32.9; HRMS (ESI+) m/z calcd for fragment $C_{11}H_{13}NO_4S$ [M + H]+ 256.06, found 256.0644.

3.9.1.2 4-(2-Azidoethyl)indolin-2-one (11).

To a solution of mesylate **10** (1.53 g, 5.99 mmol) in DMF (234 mL) was added NaN_3 (1.17 g, 18.0 mmol) and the reaction mixture was refluxed at 60°C. After 5 h, water (1000 mL) and diethyl ether (500 mL) were added, and the phases were separated. The aqueous layer was extracted with diethyl ether (2 × 100 mL), and the combined organics were washed with water, dried over $MgSO_4$, and concentrated in vacuo. Purification by column chromatography (silica, 40% EtOAc in hexanes) afforded **11** as a yellow solid (573 mg, 2.83 mmol, 72%). ^{1}H NMR (400 MHz, CDCl3) δ 9.02 (bs, 1H), 7.19 (t, J = 8.0 Hz, 1H), 6.88 (d, J = 7.6 Hz, 1H), 6.81 (d, J = 7.6 Hz, 1H), 3.55 (t, J = 6.8 Hz, 2H), 3.52 (s, 2H), 2.82 (t, J = 6.8 Hz, 2H); 13C NMR (100 MHz, CDCl3) δ 177.2, 142.6, 134.6, 128.4, 124.4, 122.6, 108.3, 51.4, 35.0, 32.5; HRMS (ESI+) m/z calcd for fragment $C_{10}H_{11}ON_4$ [M + H]+ 203.09, found 203.0934.

3.9.1.3 4-(2-Aminoethyl)indolin-2-one (12).

To a solution of **11** (1.25 g, 6.18 mmol) in THF (100 mL) were added water (0.67 mL, 37.11 mmol) and resin-linked triphenylphosphine (mesh, 3 mmol/g, 4.12 g), and the resulting slurry was stirred gently at 85° C overnight. The reaction mixture was then filtered by gravity, rinsed 3× with THF, and concentrated in vacuo. The resulting residue was then dissolved in 1 M $NaHSO_4$ (80 mL) and poured into a separatory funnel containing 80 mL of diethyl ether. The aqueous layer was basified to pH 9 with 2 M NaOH, extracted with ethyl acetate (3 × 80 mL), dried over $MgSO_4$, filtered, and concentrated in vacuo. The resulting oil was purified by column chromatography (Biotage Sfar KP-Amino, 0−10% MeOH in CH_2Cl_2) yielding **12** as a light brown solid

(240 mg, 1.36 mmol, 22%). ^{1}H NMR (400 MHz, acetone-d6) δ 9.30 (bs, 1H), 7.10 (t, 1H, J = 8 Hz), 6.84 (d, 1H, J = 8.4 Hz), 6.72 (d, 1H, J = 8 Hz), 3.48 (s, 2H), 3.44 (t, 2H, J = 7.6 Hz), 2.81 (t, 2H, J = 6.8 Hz), 2.82 (bs, 2H); ^{13}C NMR (100 MHz, D2O) δ 180.1, 142.5, 133.2, 128.4,124.9, 122.9, 109.0, 39.2, 30.8, 23.2; HRMS (ESI+) m/z calcd for fragment $C_{10}H_{12}N_2O$ [M + H]+ 177.09, found 177.1019.

3.9.1.4 2-(2-Oxoindolin-4-yl)ethyl Methanesulfonate (13).

Compound **13** was synthesized from **10** according to the general method of Capuano et al.[33] The spectra matched those reported.

3.9.1.5 4-(2-((4-(4-(Prop-2-yn-1-yloxy)benzoyl)benzyl)(propyl)-amino)ethyl)indolin-2-one (3).

Compound **3** was made according to the general method of Chen et al., with some modifications.[74] A 10 mL round-bottomed flask was charged with **13** (100 mg, 0.46 mmol), benzophenone cross-linker **14** (158 mg, 0.46 mmol), cesium carbonate (150 mg, 0.46 mmol), and potassium iodide (115 mg, 0.69 mmol). Acetonitrile (3 mL) was added to the mixture, and the reaction was stirred under reflux at 85 °C for 2 h. The solvent was evaporated in vacuo, washed with water (5 mL), and extracted with ethyl acetate (3 × 5 mL). The combined organic layers were washed with water and brine, dried over $MgSO_4$, filtered, and concentrated. The resulting crude product was purified by column (silica, 2.5% MeOH in CH_2Cl_2) to yield **3** as an amorphous orange solid (71 mg, 0.015 mmol, 33%) (400 MHz, acetone-d6) δ 9.29 (bs, 1H), 7.82 (d, J = 8.8 Hz, 2H), 7.67 (d, J = 8.2 Hz, 2H), 7.46 (d, J = 8.1 Hz, 2H), 7.17 (d, J = 8.8 Hz, 2H), 7.09 (t, J = 7.8 Hz, 1H), 6.79 (d, J = 7.8 Hz, 1H), 6.71 (d, J = 7.7 Hz, 1H), 4.93 (d, J = 2.4 Hz, 2H), 3.75 (s, 2H),

3.31 (s, 2H), 3.16 (t, J = 2.4 Hz, 1H), 2.74 (m, 4H), 2.57 (t, J = 7.2 Hz, 2H), 1.56 (m, 2H), 0.91 (t, J = 7.4 Hz, 3H).; ^{13}C (100 MHz, CDCl3) δ 195.3, 177.1, 160.9, 144.7, 142.3, 137.1, 136.7, 132.5, 132.4, 131.2, 129.9, 128.3, 128.0, 123.9, 123.1, 114.4, 107.5, 77.9, 76.1, 58.5, 55.9, 53.9, 34.9, 31.0, 20.4, 11.9. HRMS (ESI+) m/z calcd for fragment $C_{30}H_{30}N_2O_3$ [M + H]+ 467.23, found 467.2315.

3.9.1.6 3-(3-(But-3-yn-1-yl)-3H-diazirin-3-yl)-N-(2-(2-oxoindolin-4- yl)ethyl)-N-propylpropanamide (4).

Compound **4** was made according to the general method of Saghatelian et al., with modifications.75 To a 5 mL vial containing 3-(3-(but-3-yn-1-yl)-3H- diazirin-3-yl)propanoic acid **15** (25 mg, 0.15 mmol) in CH_2Cl_2 (2 mL), amine **13** (42 mg, 0.16 mmol), DIPEA (79 µL, 0.45 mmol), EDC-HCl (43 mg, 0.22 mmol), and HATU (86 mg, 0.23 mmol) were added. The reaction mixture was stirred at room temperature overnight in the dark for 24 h and concentrated in vacuo. The crude residue was diluted with CH_2Cl_2 (5 mL), washed with water (5 × 10 mL) and brine, then dried over anhydrous Na_2SO_4, and volatiles were removed in vacuo. The resulting oil was purified by flash column chromatography (silica, 70% EtOAc in hexanes) to provide **4** as a colorless solid (14.81 mg, 0.04 mmol, 27% yield). ^1H NMR (600 MHz, CDCl3) isomer 1 (66%): δ 8.42 (bs, 1H), 7.14 (t, J = 7.7 Hz, 1H), 6.85 (d, J = 7.8 Hz, 1H), 6.74 (d, J = 7.7 Hz, 1H), 3.51 (s, 2H), 3.47 (t, J = 7.8 Hz, 2H), 3.10 (t, J = 7.6 Hz, 2H), 2.77 (m, 2H), 2.03 (t, J = 7.3 Hz, 2H), 1.98 (m, 2H), 1.87 (t, J = 7.1 Hz, 2H), 1.81 (m, 1H), 1.66 (t, J = 7.4 Hz, 2H), 1.58 (t, J = 7.3 Hz, 2H), 0.90 (t, J = 7.4 Hz, 3H); isomer 2 (33%): δ 8.531 (bs, 1H), 7.19 (t, J = 7.7 Hz, 1H), 6.80 (d, J = 1.9 Hz, 1H), 6.79 (d, J = 1.9 Hz, 1H), 3.46 (s, 2H), 3.42 (t, J = 7.4 Hz, 2H), 3.29 (t, J = 7.7 Hz, 2H), 2.70 (m, 2H), 2.031 (t, J = 7.5

Hz, 2H), 2.03 (m, 2H), 1.73 (m, 3H), 1.58 (m, 2H), 1.54 (m, 2H), 0.88 (t, J = 7.6 Hz, 3H); 13C NMR (150 MHz, CDCl3); isomer 1 (66%): δ 177.4, 170.9, 142.6, 135.6, 128.2, 124.4, 122.9, 108.0, 82.9, 69.3, 50.2, 46.8, 38.8, 35.1, 32.7, 31.3, 28.0, 27.0, 22.3, 13.4, 11.4; isomer 2 (33%): δ 176.9, 170.7, 142.9, 134.6, 128.7, 124.1, 122.9, 108.5, 77.3, 69.3, 47.8, 47.7, 34.9, 32.7, 32.5, 28.1, 28.0, 26.7, 21.0, 13.4, 11.5. HRMS (ESI+) m/z calcd for fragment $C_{21}H_{26}N_4O_2$ [M + H]+ 367.21, found 367.2138.

3.9.1.7 4-(2-((4-(4-(Prop-2-yn-1-yloxy)benzoyl)benzyl)amino)- ethyl)indolin-2-one (5).

Compound **5** was made according to the general method of Chen *et al.*, with modifications.[59] The reaction vessel was charged with **12** (40 mg, 0.22 mmol), benzophenone **14** (78 mg, 0.22 mmol), cesium carbonate (108 mg, 0.33 mmol), and potassium iodide (55 mg, 0.33 mmol). Acetonitrile (5 mL) was added, and the reaction was stirred under reflux at 100 °C for 24 h, concentrated in vacuo, washed with water, and extracted with ethyl acetate. The combined organic layers were washed with brine and dried over $MgSO_4$, filtered, and concentrated. The resulting crude residue was purified by flash column (silica, 0−10% MeOH in CH2Cl2) to afford product 5 as an orange oil (10 mg, 0.024 mmol, 10%). ^{1}H NMR (400 MHz, acetonitrile-d3) δ 8.32 (bs, 1H), 7.78 (m, 2H), 7.67 (t, J = 7.2 Hz, 2H), 7.52 (m, 2H), 7.08 (m, 3H), 6.69 (t, J = 8.2 Hz, 1H), 4.84 (d, J = 2.4 Hz, 2H), 4.61 (m, 1H), 4.28 (m, 1H), 3.93 (s, 1H), 2.86 (t, J = 2.4 Hz, 1H), 2.27 (bs, 1H), 1.56 (s, 2H), 1.03 (s, 2H); ^{13}C δ (100 MHz, acetonitrile-d3) δ 195.6, 177.9, 161.8, 147.6, 145.3, 142.8, 138.2, 137.4, 133.1, 133.0, 132.0, 131.6, 131.0, 130.5, 129.6, 128.9, 128.7, 123.0, 115.4, 115.2, 107.4, 79.1, 77.3, 56.7, 54.1,

45.6, 23.0 HRMS (ESI+) m/z calcd for fragment $C_{27}H_{24}N_2O_3$ [M + H]+ 425.18, found 425.1852.

3.9.1.8 3-(3-(But-3-yn-1-yl)-3H-diazirin-3-yl)-N-(2-(2-oxoindolin-4-yl)ethyl)propanamide (6).

Compound **6** was made according to the general method of Saghatelian et al., with modifications.[75] To a 5 mL vial containing 3-(3-(but-3-yn-1-yl)-3H-diazirin-3-yl)propanoic acid **15** (25 mg, 0.15 mmol) in CH_2Cl_2 (2 mL), amine **12** (29 mg, 0.16 mmol), DIPEA (79 µL, 0.45 mmol), EDC-HCl (43 mg, 0.22 mmol), and HATU (86 mg, 0.23 mmol) were added. The reaction mixture was stirred at room temperature overnight in the dark for 20 h and concentrated in vacuo. The crude residue was diluted with CH_2Cl_2 (5 mL), washed with water (5 × 10 mL) and brine, then dried over anhydrous Na_2SO_4, and volatiles were removed in vacuo. The crude residue was dissolved in acetonitrile and washed with hexanes, and the acetonitrile layer was evaporated to provide **6** as a colorless solid (17 mg, 0.052 mmol, 32%). ^{1}H NMR (400 MHz, CDCl3) δ 7.83 (bs, 1 h), 7.18 (t, J = 8.0 Hz, 1H), 6.83 (d, J = 8.0 Hz, 1H), 6.69 (d, J = 7.6 Hz, 1H), 3.93 (s, 2H), 3.63 (d, J = 16.4 Hz, 1H), 3.10 (d, J = 5.2 Hz, 2H), 2.17 (m, 1H), 2.02 (td, J = 7.2 Hz, 1.6 Hz, 3H), 1.95 (t, J = 2.6 Hz, 1H), 1.86 (m, 4H), 1.65 (td, J = 7.6 Hz, 2.8 Hz, 2H); ^{13}C (100 MHz, acetone-d6) δ 176.7, 172.0, 143.7, 136.3, 129.2, 126.0, 123.1, 107.2, 83.7, 70.4, 54.2, 42.6, 41.9, 38.7, 35.7, 33.3, 32.9, 13.6; HRMS (ESI−) m/z calcd for fragment $C_{18}H_{20}N_4O_2$ [M]- 324.16, found 324.1545.

3.9.1.9 (S)-(4-(((2-Amino-4,5,6,7-tetrahydrobenzo[d]thiazol-6-yl)-amino)methyl)phenyl)(4-(prop-2-yn-1-yloxy)phenyl)methanone (7).

A 10 mL round-bottom flask was charged with **2** (42 mg, 0.25 mmol), benzophenone cross-linker **14** (83 mg, 0.25 mmol), cesium carbonate (123 mg, 0.38 mmol), and potassium iodide (56 mg, 0.38 mmol). Acetonitrile (5 mL) was added to the mixture, and the reaction was stirred at room temperature for 48 h. The solvent was evaporated in vacuo, washed with water, and extracted with ethyl acetate (3 × 5 mL). The combined organic layers were washed with water and brine, dried over MgSO4, filtered, and concentrated. The resulting crude product was purified by column (silica, MeOH/ EtOAc, 10:90) to provide **7** as a yellow solid (66 mg, 0.052 mmol, 79%). ^{1}H NMR (400 MHz, DMSO-d6) δ 7.74 (d, 2H, J = 6.2 Hz), 7.65 (d, 2H, J = 8.0 Hz), 7.52 (d, 2H, J = 8.0 Hz), 7.13 (d, 2H, J = 8.8 Hz), 6.59 (s, 2H), 4.92 (d, 2H, J = 2.4 Hz), 3.87 (s, 2H), 3.64 (d, 1H, J = 2.4 Hz), 2.76 (m, 2H), 2.46 (s, 1H), 2.32 (m, 2H), 1.96 (m, 1H), 1.56 (m, 1H), 1.22 (m, 1H); ^{13}C NMR (100 MHz, DMSO-d6) δ 194.6, 166.3, 161.1, 146.6, 145.0, 136.3, 132.4, 130.8, 129.9, 128.3, 115.1, 113.5, 79.2, 79.1, 56.2, 53.5, 50.4, 31.1, 29.9, 29.5, 25.3; HRMS (ESI+) m/z calcd for fragment $C_{24}H_{23}N_3O_2S$ [M + H]+ 418.15, found 418.1588.

3.9.1.10 (S)-N-(2-Amino-4,5,6,7-tetrahydrobenzo[d]thiazol-6-yl)-3-(3-(but-3-yn-1-yl)-3H-diazirin-3-yl)propanamide (8).

To a 10 mL round-bottom flask containing 3-(3-(but-3-yn-l-yl)-3H-diazirin- 3-yl)propanoic acid 15 (50 mg, 0.30 mmol) in CH_2Cl_2 (5 mL), **2** (56 mg, 0.33 mmol), DIPEA (157 µL, 0.9 mmol), EDC-HCl (87 mg, 0.45 mmol), and HOAt (172 mg, 0.45

mmol) were added. The reaction mixture was stirred at room temperature, protected from light, for 48 h. The reaction was diluted with CH_2Cl_2 (10 mL) and washed successively with saturated aqueous NH_4Cl (10 mL) and saturated aqueous $NaHCO_3$ (10 mL), then dried over $MgSO_4$, filtered, and concentrated. The resulting crude product was purified by column (silica, MeOH/EtOAc, 15:85) to yield **8** as a yellow solid (43 mg, 0.14 mmol, 45%). ^{1}H NMR (400 MHz, DMSO-d6) δ 7.93 (d, 1H, J = 4.8 Hz), 6.64 (s, 2H), 3.96 (m, 1H), 2.73 (m, 2H), 2.36 (m, 2H), 1.95 (m, 5H), 1.62 (m, 5H), 1.24 (s, 1H); ^{13}C NMR (100 MHz, DMSO-d6) δ 170.6, 166.5, 144.7, 112.8, 83.6, 72.2, 45.4, 31.9. 30.0, 29.2, 28.7, 28.6, 24.9, 13.1; HRMS (ESI+) m/z calcd for fragment $C_{15}H_{19}N_5OS$ [M + H]+ 318.13, found 318.1379.

3.9.2 Intracellular Ca2+ mobilization assay

A stable HEK293T- derived cell line-expressing DRD2-Strep Tag II fusion was maintained in DMEM supplemented with 10% FBS, 100 U/mL penicillin, and 100 µg/mL streptomycin in a humidified atmosphere at 37 °C in 5% CO2. On day 1, cells were plated at a density of 4 × 10^4 cells/cm^2 in a poly-D-lysine-coated 18-well chambered coverslip (Ibidi). The following day (day 2), cells were transfected with a 10× solution of 3:1 mixture of Gqi5/Optifect Transfection Reagent (Thermo) in unsupplemented DMEM. On day 3, the transfection media was removed, and calcium-sensitive dye loading was performed following the protocol of the Fluo-4 Direct Calcium Assay Kit (Invitrogen). 5× drug stimulation solutions were prepared in filter-sterilized HBSS. Once Fluo-4 loading was complete, a time series acquisition at a rate of 1 frame per second was recorded using a Zeiss LSM 980 with Airyscan 2. Basal fluorescence was recorded for 20 s, followed by the addition of drug solution to a 1× final concentration and acquisition for

an additional 40 s. Results in the form of fold fluorescence increase over basal were averaged over 50 cells in ImageJ (NIH), and GraphPad Prism was used for the analysis of data.

3.9.3 B-arrestin (TANGO) assay

HTLA cells were a gift from the laboratory of G. Barnea and were maintained in DMEM supplemented with 10% FBS, 100 U/mL penicillin, 100 μg/mL streptomycin, 2 μg/mL puromycin, 100 μg/mL hygromycin B, and 100 μg/mL G418 in a humidified atmosphere at 37 °C in 5% CO2. On day 1, cells were plated at a density of 1×10^5 cells/cm2 in a black wall, clear-bottom 96-well plate (Nunc). The following day (day 2), cells were transfected with a 10× solution of 3:1 mixture of DRD2-TANGO/Optifect Transfection Reagent (Thermo) in unsupplemented DMEM. On day 3, 1× drug stimulation solutions were prepared in filter- sterilized unsupplemented DMEM. The transfection media was shaken or aspirated from the wells, and drug stimulation solutions were gently added. On day 4, drug solutions were removed from one well every 10 s (to maintain consistency of incubation time) and 50 μL per well of Bright-Glo solution (Promega) diluted 20-fold in HBSS was added. After incubation for 2 min at room temperature, luminescence was counted with an integration time of 10 s in a Spectramax i3x plate reader (Molecular Devices).

3.9.4 Photo-cross-linking of DRD2-expressing 293T cells and primary neurons with probes.

For all irradiation experiments, a Chemglass Biogrow CLS-1625 UV Lamp (New Jersey) was used and set to an irradiation wavelength of 365 nm, with a lamp power of 6 W. All samples were irradiated for 30 min at approximately 2 cm from the lamp.

3.9.5 Click chemistry conjugation and microscopy.

HEK293T cells and a stable HEK293T-derived cell line-expressing DRD2-Strep Tag II fusion were maintained in DMEM supplemented with 10% FBS, 100 U/mL penicillin, and 100 μg/mL streptomycin in a humidified atmosphere at 37 °C in 5% CO2. Cells were plated at a density of 4×10^4 cells/cm^2 in a poly-D-lysine-coated 18-well chambered coverslip (Ibidi) and allowed to grow to a 70% confluency. Probe solutions at a concentration of 5 μM were prepared in sterile-filtered HBSS. Media was removed from the wells, and probe solutions were added and allowed to incubate for 2 min. The probe solutions were removed, and the cells were washed twice with HBSS and irradiated with a 365 nm UV lamp (8 W, 2 cm distance) for 30 min at room temperature. The HBSS was removed, and the cells were fixed in 4% paraformaldehyde solution in PBS (15 min at room temperature), washed twice with PBS, and permeabilized in 0.2% Tween-20 in PBS for 20 min at room temperature. Permeabilized cells were then blocked for 1 h at room temperature, then treated with freshly premixed Click-iT Kit (Invitrogen) reaction buffer (1× reaction buffer, 5 μM AF555 picolyl azide (AAT Bioquest), 100:0 CuSO4/copper protectant, 1× reaction buffer additive), and incubated in the dark with constant shaking for 30 min at room temperature. The cells were then washed 3

times with TBS with 3% BSA and incubated with 1 μg/mL Anti-Strep Tag II rabbit polyclonal antibody (Abcam, ab76949) in TBS with 3% BSA overnight at 4 °C. The primary antibody solution was then removed, and the cells were washed 3 times with a 5 min TBS incubation. The cells were then incubated with a 0.1 μg/mL Alexa Fluor 488 conjugated goat antirabbit IgG (Abcam, ab150077) in TBS with 3% BSA for 1 h at room temperature with constant shaking. The cells were then washed 3 times with TBS and imaged for Alexa Fluor 488 fluorescence and AF555 fluorescence using a Zeiss LSM 980 with Airyscan 2. Images were processed using Fiji (NIH).

3.9.6 Western blot

A stable HEK293T-derived cell line-expressing DRD2-Strep Tag II fusion was maintained in DMEM supplemented with 10% FBS, 100 U/mL penicillin, and 100 μg/mL streptomycin in a humidified atmosphere at 37 °C in 5% CO_2. Cells were plated at a density of 4×10^4 cells/cm^2 in T300 tissue culture flasks (CellTreat) and allowed to grow to an 80% confluency. At confluency, media was removed and cells were washed once with cold HBSS, followed by incubation for 15 min in cold HBSS with 0.53 mM EDTA. Following incubation, cells were scraped off the bottom of the flask and the cell suspension was transferred to a 15 mL conical tube and then pelleted at 500 xg for 5 min. The supernatant was removed, and the cell pellet was resuspended in HBSS followed by centrifugation at 500 xg for 5 min. Probe solutions (5, 7, and 16) at a concentration of 100 nM and competitor (ropinirole or pramipexole) at a concentration of 50 μM were prepared in both sterile-filtered HBSS. The supernatant of the cell pellet was removed, and the cells were resuspended in probe solution and incubated at room temperature for 2 min followed by centrifugation at 500 xg for 5 min. The cell pellet was

resuspended in either HBSS or 50 μM competitor solution in HBSS and irradiated with a 365 nm UV lamp (8 W, 2 cm distance) for 30 min at room temperature. The cells were then pelleted at 500 xg for 5 min, and the supernatant was removed. Membrane fractionation was performed following the MEM-PER Membrane Protein Extraction Kit (Thermo). The solubilized membrane fraction was incubated with hydrophilic streptavidin magnetic beads (NEB) for 1 h at room temperature. The flow-through was removed, and the beads were washed twice with PBS. The beads were then treated with freshly premixed Click-iT Kit (Invitrogen) reaction buffer (1× reaction buffer, 5 μM AF555 picolyl azide (AAT Bioquest), 100:0 CuSO4:Copper Protectant, 1× reaction buffer additive) and incubated in the dark with constant shaking for 30 min at room temperature. The captured proteins were eluted by incubation in 6 M urea SDS- PAGE loading buffer (6 M urea, 200 mM tris, 4% SDS, 20% glycerol, 2% β-mercaptoethanol, 20 mM EDTA, 0.04% bromophenol blue, pH 7.4) at 65 °C for 10 min. Samples were then separated via SDS-PAGE using a NuPAGE 4−12% bis−tris precast gel (Invitrogen). The gel was then transferred to a PVDF membrane via an iBlot 2 gel transfer device, and the membrane was blocked for 1 h at room temperature in TBST with 5% BSA. Following blocking, the membrane was incubated with either 1 μg/mL Anti-Strep Tag II rabbit polyclonal antibody (Abcam, ab76949) or 2 μg/mL Anti-DRD2 rabbit polyclonal antibody (AbClonal, A12930) in TBST with 5% BSA overnight at 4 °C. The primary antibody solution was removed, and the membrane was washed 3 times with a 5 min TBST incubation. The membrane was then incubated with 0.1 μg/mL IRdye680RD conjugated goat antirabbit IgG (Abcam, ab216777) in TBST with 5% BSA for 1 h at room temperature with constant shaking. The membrane was washed 3 times

with TBST and imaged using an Azure Sapphire Biomolecular Imager. Images were processed using Fiji (NIH).

3.9.7 Photoaffinity quantification using FACS.

HEK293T cells and a stable HEK293T-derived cell line-expressing DRD2-Strep Tag II fusion were maintained in DMEM supplemented with 10% FBS, 100 U/mL penicillin, and 100 µg/mL streptomycin in a humidified atmosphere at 37 °C in 5% CO2. Cells were plated at a density of 4×10^4 cells/cm^2 in T75 tissue culture flasks (CellTreat) and allowed to grow to an 80% confluency. At confluency, media was removed, and cells were washed once with cold HBSS, followed by incubation for 15 min in cold HBSS with 0.53 mM EDTA. Following incubation, cells were scraped off the bottom of the flask and the cell suspension was transferred to a 15 mL conical tube and then pelleted at 500 xg for 5 min. The supernatant was removed, and the cell pellet was resuspended in HBSS followed by centrifugation at 500 xg for 5 min. Probe solutions at a concentration of 100 nM were prepared in sterile-filtered HBSS. The supernatant of the cell pellet was removed, and the cells were resuspended in probe solution and incubated at room temperature for 2 min followed by centrifugation at 500 xg for 5 min. The cell pellet was then washed twice with HBSS and irradiated with a 365 nm UV lamp (8 W, 2 cm distance) for 30 min at room temperature. The cells were then pelleted at 500g for 5 min, the supernatant was removed, and the cell pellet was fixed in 4% paraformaldehyde solution in PBS (15 min at room temperature), washed twice with PBS, and permeabilized in 0.2% Tween-20 in PBS for 20 min at room temperature. Permeabilized cells were then incubated in PBS with 5% BSA for 1 h at room temperature and then treated with freshly premixed Click-iT Kit (Invitrogen) reaction

buffer (1× reaction buffer, 5 μM AF555 picolyl azide (AAT Bioquest), 100:0 CuSO4:Copper Protectant, 1× reaction buffer additive) and incubated in the dark with constant shaking for 30 min at room temperature. The cells were then washed 3 times with PBS with 5% BSA and analyzed with a BD Accuri C6 flow cytometer. Samples were gated on forward scatter and side scatter to exclude cell debris and aggregates, and red channel fluorescence was analyzed for the percent of events with increased fluorescence over basal.

3.9.8 LC/MS proteomics

3.9.8.1 LC/MS Sample Prep of DRD2 Stable Cell Line with Probe 5 or 7.

HEK293T cells and a stable HEK293T-derived cell line-expressing DRD2-Strep Tag II fusion were maintained in DMEM supplemented with 10% FBS, 100 U/mL penicillin, and 100 μg/mL streptomycin in a humidified atmosphere at 37 °C in 5% CO2. Cells were plated at a density of 4×10^4 cells/cm^2 in T300 tissue culture flasks (CellTreat) and allowed to grow to an 80% confluency. At confluency, media was removed, and cells were washed once with cold HBSS, followed by incubation for 15 min in cold HBSS. Following incubation, cells were scraped off the bottom of the flask and the cell suspension was transferred to a 50 mL conical tube and then pelleted at 500 xg for 5 min. Solutions containing a 30 μM probe were prepared in sterile-filtered HBSS. The supernatant of the cell pellet was removed, and the cells were resuspended in probe solution and incubated at room temperature for 2 min followed by centrifugation at 500 xg for 5 min. The cell pellet was then resuspended in HBSS and irradiated with a 365 nm UV lamp (8 W, 2 cm distance) for 30 min at room temperature. The cells were

then pelleted at 500 xg for 5 min, and the supernatant was removed. Membrane fractionation was performed following the MEM-PER Membrane Protein Extraction Kit (Thermo). The solubilized membrane fraction was incubated with hydrophilic streptavidin magnetic beads (NEB) for 1 h at room temperature. The flow-through was removed, and the beads were washed twice with PBS.

3.9.8.2 Rat Whole Brain Photo-Cross-Linking.

To prepare the homogenate, adult rat brain tissue was micro-dissected, and the olfactory bulb was discarded and sliced into 1 mm pieces. The pieces were suspended in a phosphate-based NP-40 lysis buffer (150 mM NaCl, 50 mM phosphate, 1% NP-40, pH 8.0), homogenized with a handheld homogenizer (IKA T-18 digital homogenizer), and incubated on ice for 30 min. The homogenate was then cleared via centrifugation (16,000 xg, 20 min), and the supernatant was reserved. The total protein concentration was determined via BCA assay (Pierce) and adjusted to 6 mg/mL. Probe solutions at a concentration of 5 mM were prepared in sterile-filtered HBSS and were added to protein solutions to a final concentration of 50 μM. Samples were inverted 3× to mix and irradiated with a 365 nm UV lamp (8 W, 2 cm distance) for 30 min at room temperature. Samples were then buffer- swapped (10k MWCO, Pierce) into fresh phosphate-based NP-40 lysis buffer and freshly premixed Click-iT Kit (Invitrogen) reaction buffer (1× reaction buffer, 50 μM PC biotin azide (Click Chemistry Tools), 70:30 CuSO4/copper protectant, 1× reaction buffer additive) and incubated in the dark with constant shaking for 30 min at room temperature. Samples were then buffer-swapped (10k MWCO, Pierce) into fresh phosphate-based NP-40 lysis buffer and incubated with hydrophilic streptavidin magnetic beads (NEB) for 1 h at room temperature. The flow-through was

removed, and the beads were washed twice with PBS. The protein was then eluted into PBS (150 mM NaCl, 20 mM phosphate, pH 8.0) by 365 nm irradiation (8 W, 2 cm distance) and submitted for LC-MS processing.

3.9.8.3 Sample Processing for Mass Spectrometry.

Samples were reduced and alkylated by sequentially adding TCEP and iodoacetamide to final concentrations of 5 and 10 mM, respectively. The reaction was allowed to proceed in the dark for 25 min. Samples were digested with 125 ng of trypsin gold (Promega), overnight at 37°C. The following day, samples were acidified using trifluoroacetic acid (TFA, Sigma-Aldrich) to pH ≤ 3 and desalted using 2-core MCX stage tips (3M, 2241).[77] The stage tips were activated with acetonitrile followed by 3% acetonitrile with 0.1% TFA. Next, samples were applied, followed by two washes with 3% acetonitrile with 0.1% TFA and one wash with 65% acetontrile with 0.1% TFA. Peptides were eluted with 75 µL of 65% acetonitrile with 5% NH_4OH (Sigma-Aldrich) and dried.

3.9.8.4 LC/MS Methods.

Samples were dissolved in 20 µL of water containing 2% acetonitrile and 0.5% formic acid, and 5 µL was diluted with 25 µL in a sample vial. Of this solution, 2 µL was injected onto a pulled tip nano-LC column with 75 µm inner diameter packed to 25 cm with 3 µm, 120 Å, C18AQ particles (Dr. Maisch). The peptides were separated using a 60 min gradient from 3 to 28% acetonitrile, followed by a 7 min ramp to 85% acetonitrile and a 3 min hold at 85% acetonitrile. The column was connected inline with an Orbitrap Lumos via a nanoelectrospray source operating at 2.2 kV. The mass spectrometer was

operated in data-dependent top speed mode with a cycle time of 2.5 s. MS1 scans were collected at a 120,000 resolution with a maximum injection time of 50 ms. Dynamic exclusion was applied for 15 s. HCD fragmentation was used followed by MS2 scans in the ion trap with a 35 ms maximum injection time.

3.9.8.5 Database Searching and Label-Free Quantification.

The MS data was searched using SequestHT in Proteome Discoverer (version 2.4, Thermo Scientific) against a human protein database (Uniprot, containing 20392 reviewed entries, retrieved 5/27/2021) and a list of common laboratory contaminant proteins (Thermo Scientific, 298 entries, 2015). Enzyme specificity for trypsin was set to semitryptic with up to two missed cleavages. Precursor and product ion mass tolerances were 10 ppm and 0.6 Da, respectively. Cysteine carbamidomethylation was set as a fixed modification. Methionine oxidation, protein N-terminal acetylation, and the mass of the appropriate photoaffinity tag, allowed on all 20 proteogenic amino acids, were set as variable modification. The output was filtered using the Percolator algorithm with a strict FDR set to 0.01.

3.10 References

(1) Stahl, S. M. Stahl's Essential Psychopharmacology: Neuroscientific Basis and Practical Application, 4th ed.; Cambridge University Press: Cambridge; New York, 2013.

(2) Xin, J.; Fan, T.; Guo, P.; Wang, J. Identification of Functional Divergence Sites in Dopamine Receptors of Vertebrates. Comput. Biol. Chem. 2019, 83, No. 107140.

(3) Martel, J. C.; Gatti McArthur, S. Dopamine Receptor Subtypes, Physiology and Pharmacology: New Ligands and Concepts in Schizophrenia. Front. Pharmacol. 2020, 11, No. 1003.

(4) Kebabian, J. W.; Calne, D. B. Multiple Receptors for Dopamine. Nature 1979, 277, 93−96.

(5) Ariano, M. A.; Monsma, F. J.; Barton, A. C.; Kang, H. C.; Haugland, R. P.; Sibley, D. R. Direct Visualization and Cellular Localization of D1 and D2 Dopamine Receptors in Rat Forebrain by Use of Fluorescent Ligands. Proc. Natl. Acad. Sci. U.S.A. 1989, 86, 8570−8574.

(6) Boyd, K. N.; Mailman, R. B. Dopamine Receptor Signaling and Current and Future Antipsychotic Drugs. In Current Antipsychotics; Gross, G.; Geyer, M. A., Eds.; Handbook of Experimental Pharmacology; Springer Berlin Heidelberg: Berlin, Heidelberg, 2012; Vol. 212, pp 53−86.

(7) Wang, Q.; Mach, R. H.; Luedtke, R. R.; Reichert, D. E. Subtype Selectivity of Dopamine Receptor Ligands: Insights from Structure and Ligand-Based Methods. J. Chem. Inf. Model. 2010, 50, 1970− 1985.

(8) Michino, M.; Beuming, T.; Donthamsetti, P.; Newman, A. H.; Javitch, J. A.; Shi, L. What Can Crystal Structures of Aminergic Receptors Tell Us about Designing Subtype-Selective Ligands? Pharmacol. Rev. 2015, 67, 198−213.

(9) Moritz, A. E.; Free, R. B.; Sibley, D. R. Advances and Challenges in the Search for D2 and D3 Dopamine Receptor-Selective Compounds. Cell. Signalling 2018, 41, 75−81.

(10) Yin, J.; Chen, K.-Y. M.; Clark, M. J.; Hijazi, M.; Kumari, P.; Bai, X.; Sunahara, R. K.; Barth, P.; Rosenbaum, D. M. Structure of a D2 Dopamine Receptor−G-Protein Complex in a Lipid Membrane. Nature 2020, 584, 125−129.

(11) Fan, L.; Tan, L.; Chen, Z.; Qi, J.; Nie, F.; Luo, Z.; Cheng, J.; Wang, S. Haloperidol Bound D2 Dopamine Receptor Structure Inspired the Discovery of Subtype Selective Ligands. Nat. Commun. 2020, 11, No. 1074.

(12) Smith, E.; Collins, I. Photoaffinity Labeling in Target- and Binding-Site Identification. Future Med. Chem. 2015, 7, 159−183.

(13) Cravatt, B. F.; Wright, A. T.; Kozarich, J. W. Activity-Based Protein Profiling: From Enzyme Chemistry to Proteomic Chemistry. Annu. Rev. Biochem. 2008, 77, 383−414.

(14) Gao, J.; Mfuh, A.; Amako, Y.; Woo, C. M. Small Molecule Interactome Mapping by Photoaffinity Labeling Reveals Binding Site Hotspots for the NSAIDs. J. Am. Chem. Soc. 2018, 140, 4259−4268.

(15) Soethoudt, M.; Alachouzos, G.; van Rooden, E. J.; Moya-Garzón, M. D.; van den Berg, R. J. B. H. N.; Heitman, L. H.; van der Stelt, M. Development of a Cannabinoid-Based Photoaffinity Probe to Determine the Δ8/9 -Tetrahydrocannabinol Protein Interaction Landscape in Neuroblastoma Cells. Cannabis Cannabinoid Res. 2018, 3, 136−151.

(16) Tackie-Yarboi, E.; Wisner, A.; Horton, A.; Chau, T. Q. T.; Reigle, J.; Funk, A. J.; McCullumsmith, R. E.; Hall, F. S.; Williams, F. E.; Schiefer, I. T. Combining Neurobehavioral Analysis and In Vivo Photoaffinity Labeling to Understand Protein Targets of Metham- phetamine in Casper Zebrafish. ACS Chem. Neurosci. 2020, 11, 2761− 2773.

(17) Jack, T.; Leuenberger, M.; Ruepp, M.-D.; Vernekar, S. K. V.; Thompson, A. J.; Braga-Lagache, S.; Heller, M.; Lochner, M. Mapping the Orthosteric Binding Site of the Human 5-HT 3 Receptor Using Photo-Cross-Linking Antagonists. ACS Chem. Neurosci. 2019, 10, 438−450.

(18) Yang, E.; Bu, W.; Suma, A.; Carnevale, V.; Grasty, K. C.; Loll, P. J.; Woll, K.; Bhanu, N.; Garcia, B. A.; Eckenhoff, R. G.; Covarrubias, M. Binding Sites and the Mechanism of Action of Propofol and a Photoreactive Analogue in Prokaryotic Voltage-Gated Sodium Channels. ACS Chem. Neurosci. 2021, 12, 3898−3914.

(19) Gregory, K. J.; Velagaleti, R.; Thal, D. M.; Brady, R. M.; Christopoulos, A.; Conn, P. J.; Lapinsky, D. J. Clickable Photoaffinity Ligands for Metabotropic Glutamate Receptor 5 Based on Select Acetylenic Negative Allosteric Modulators. ACS Chem. Biol. 2016, 11, 1870−1879.

(20) Niznik, H. B.; Guan, J. H.; Neumeyer, J. L.; Seeman, P. A Photoaffinity Ligand for Dopamine D2 Receptors: Azidoclebopride. Mol. Pharmacol. 1985, 27, 193−199.

(21) Niznik, H. B.; Dumbrille-Ross, A.; Guan, J. H.; Neumeyer, J. L.; Seeman, P. Dopamine D2 Receptors Photolabeled by Iodo-Azido- Clebopride. Neurosci. Lett. 1985, 55, 267−272.

(22) Burton, N. R.; Kim, P.; Backus, K. M. Photoaffinity Labelling Strategies for Mapping the Small Molecule−Protein Interactome. Org. Biomol. Chem. 2021, 19, 7792−7809.

(23) O'Brien, J. G. K.; Jemas, A.; Asare-Okai, P. N.; am Ende, C. W.; Fox, J. M. Probing the Mechanism of Photoaffinity Labeling by Dialkyldiazirines through Bioorthogonal Capture of Diazoalkanes. Org. Lett. 2020, 22, 9415−9420.

(24) Hill, J. R.; Robertson, A. A. B. Fishing for Drug Targets: A Focus on Diazirine Photoaffinity Probe Synthesis. J. Med. Chem. 2018, 61, 6945−6963.

(25) West, A. V.; Muncipinto, G.; Wu, H.-Y.; Huang, A. C.; Labenski, M. T.; Jones, L. H.; Woo, C. M. Labeling Preferences of Diazirines with Protein Biomolecules. J. Am. Chem. Soc. 2021, 143, 6691−6700.

(26) Fuentes, A.; Pineda, M.; Venkata, K. Comprehension of Top 200 Prescribed Drugs in the US as a Resource for Pharmacy Teaching, Training and Practice. Pharmacy 2018, 6, 43.

(27) https://www.mayoclinic.org/drugs-supplements/ropinirole- oral-route/side-effects/drg-20066810.

(28) https://www.mayoclinic.org/drugs-supplements/pramipexole- oral-route/side-effects/drg-20065603.

(29) Lipford, M. C.; Silber, M. H. Long-Term Use of Pramipexole in the Management of Restless Legs Syndrome. Sleep Med. 2012, 13, 1280−1285.

(30) Gallagher, G.; Lavanchy, P. G.; Wilson, J. W.; Hieble, J. P.; DeMarinis, R. M. 4-[2-(Di-n-Propylamino)Ethyl]-2(3H)-Indolone: A Prejunctional Dopamine Receptor Agonist. J. Med. Chem. 1985, 28, 1533−1536.

(31) DeMarinis, R. M.; Hall, R. F.; Franz, R. G.; Webster, C.; Huffman, W. F.; Schwartz, M. S.; Kaiser, C.; Ross, S. T.; Gallagher, G. Syntheses and in Vitro Evaluation of 4-(2-Aminoethyl)-2(3H)- Indolones and Related Compounds as Peripheral Prejunctional Dopamine Receptor Agonists. J. Med. Chem. 1986, 29, 939−947.

(32) Schneider, C. S.; Mierau, J. Dopamine Autoreceptor Agonists: Resolution and Pharmacological Activity of 2,6-Diaminotetrahydro- benzothiazole and an Aminothiazole Analog of Apomorphine. J. Med. Chem. 1987, 30, 494−498.

(33) Jörg, M.; May, L. T.; Mak, F. S.; Lee, K. C. K.; Miller, N. D.; Scammells, P. J.; Capuano, B. Synthesis and Pharmacological Evaluation of Dual Acting Ligands Targeting the Adenosine A 2A and Dopamine D 2 Receptors for the Potential Treatment of Parkinson's Disease. J. Med. Chem. 2015, 58, 718−738.

(34) Das, B.; Vedachalam, S.; Luo, D.; Antonio, T.; Reith, M. E. A.; Dutta, A. K. Development of a Highly Potent D 2 /D 3 Agonist and a Partial Agonist from Structure−Activity Relationship Study of N 6 -(2- (4-(1 H -Indol-5-Yl)Piperazin-1-Yl)Ethyl)- N 6 -Propyl-4,5,6,7- Tetrahydrobenzo[d]Thiazole-2,6-Diamine Analogues: Implication in the Treatment of Parkinson's Disease. J. Med. Chem. 2015, 58, 9179−9195.

(35) Jaen, J. C.; Caprathe, B. W.; Wise, L. D.; Smith, S. J.; Pugsley, T. A.; Heffner, T. G.; Meltzer, L. T. Novel 4,5,6,7-Tetrahydrobenzo- thiazole Dopamine Agonists Display Very Low Stereoselectivity in Their Interaction with Dopamine Receptors. Bioorg. Med. Chem. Lett. 1991, 1, 189−192.

(36) Sipos, A.; Mueller, F. K. U.; Lehmann, J.; Berényi, S.; Antus, S. Synthesis and Pharmacological Evaluation of Thiazole and Isothiazole Derived Apomorphines. Arch. Pharm. Chem. Life Sci. 2009, 342, 557− 568.

(37) McRobb, F. M.; Crosby, I. T.; Yuriev, E.; Lane, J. R.; Capuano, B. Homobivalent Ligands of the Atypical Antipsychotic Clozapine: Design, Synthesis, and Pharmacological Evaluation. J. Med. Chem. 2012, 55, 1622−1634.

(38) Jörg, M.; Kaczor, A. A.; Mak, F. S.; Lee, K. C. K.; Poso, A.; Miller, N. D.; Scammells, P. J.; Capuano, B. Investigation of Novel Ropinirole Analogues: Synthesis, Pharmacological Evaluation and Computational Analysis of Dopamine D 2 Receptor Functionalized Congeners and Homobivalent Ligands. Med. Chem. Commun. 2014, 5, 891−898.

(39) Hjerrild, P.; Tørring, T.; Poulsen, T. B. Dehydration Reactions in Polyfunctional Natural Products. Nat. Prod. Rep. 2020, 37, 1043− 1064.

(40) Allen, J. A.; Roth, B. L. Strategies to Discover Unexpected Targets for Drugs Active at G Protein−Coupled Receptors. Annu. Rev. Pharmacol. Toxicol. 2011, 51, 117−144.

(41) Lefkowitz, R. J.; Shenoy, S. K. Transduction of Receptor Signals by SS-Arrestins. Science 2005, 308, 512−517.

(42) Usiello, A.; Baik, J.-H.; Rougé-Pont, F.; Picetti, R.; Dierich, A.; LeMeur, M.; Piazza, P. V.; Borrelli, E. Distinct Functions of the Two Isoforms of Dopamine D2 Receptors. Nature 2000, 408, 199−203.

(43) Coward, P.; Chan, S. D. H.; Wada, H. G.; Humphries, G. M.; Conklin, B. R. Chimeric G Proteins Allow a High-Throughput Signaling Assay of Gi-Coupled Receptors. Anal. Biochem. 1999, 270, 242−248.

(44) Kroeze, W. K.; Sassano, M. F.; Huang, X.-P.; Lansu, K.; McCorvy, J. D.; Giguère, P. M.; Sciaky, N.; Roth, B. L. PRESTO-Tango as an Open-Source Resource

for Interrogation of the Druggable Human GPCRome. Nat. Struct. Mol. Biol. 2015, 22, 362−369.

(45) Barnea, G.; Strapps, W.; Herrada, G.; Berman, Y.; Ong, J.; Kloss, B.; Axel, R.; Lee, K. J. The Genetic Design of Signaling Cascades to Record Receptor Activation. Proc. Natl. Acad. Sci. U.S.A. 2008, 105, 64−69.

(46) Yu, Q.; Liu, Y.-Z.; Zhu, Y.-B.; Wang, Y.-Y.; Li, Q.; Yin, D.-M. Genetic Labeling Reveals Temporal and Spatial Expression Pattern of D2 Dopamine Receptor in Rat Forebrain. Brain Struct. Funct. 2019, 224, 1035−1049.

(47) Zhou, H.-Q.; Zhuang, L.-J.; Bao, H.-Q.; Li, S.-J.; Dai, F.-Y.; Wang, P.; Li, Q.; Yin, D.-M. Olfactory Regulation by Dopamine and DRD2 Receptor in the Nose. Proc. Natl. Acad. Sci. U.S.A. 2022, 119, No. e2118570119.

(48) Islam, K. U. S.; Meli, N.; Blaess, S. The Development of the Mesoprefrontal Dopaminergic System in Health and Disease. Front. Neural Circuits 2021, 15, No. 746582.

(49) Kash, T. L.; Jenkins, A.; Kelley, J. C.; Trudell, J. R.; Harrison, N. L. Coupling of Agonist Binding to Channel Gating in the GABAA Receptor. Nature 2003, 421, 272−275.

(50) Jenkins, A.; Andreasen, A.; Trudell, J. R.; Harrison, N. L. Tryptophan Scanning Mutagenesis in TM4 of the GABAA Receptor A1 Subunit: Implications for Modulation by Inhaled Anesthetics and Ion Channel Structure. Neuropharmacology 2002, 43, 669−678.

(51) Sigel, E.; Ernst, M. The Benzodiazepine Binding Sites of GABAA Receptors. Trends Pharmacol. Sci. 2018, 39, 659−671.

(52) Freudenberg, F.; Alttoa, A.; Reif, A. Neuronal Nitric Oxide Synthase (NOS1) and Its Adaptor, NOS1AP, as a Genetic Risk Factors for Psychiatric Disorders: NOS1 as a Risk Gene for Psychiatric Disorders. Genes, Brain Behav. 2015, 14, 46−63.

(53) Hardingham, N.; Dachtler, J.; Fox, K. The Role of Nitric Oxide in Pre-Synaptic Plasticity and Homeostasis. Front. Cell. Neurosci. 2013, 7, No. 190.

(54) Frohlich, F. Network Neuroscience; Elsevier, 2016.

(55) Turu, G.; Hunyady, L. Signal Transduction of the CB1 Cannabinoid Receptor. J. Mol. Endocrinol. 2010, 44, 75−85.

(56) Blume, L. C.; Patten, T.; Eldeeb, K.; Leone-Kabler, S.; Ilyasov, A. A.; Keegan, B. M.; O'Neal, J. E.; Bass, C. E.; Hantgan, R. R.; Lowther, W. T.; Selley, D. E.; Howlett, A. C. Cannabinoid Receptor Interacting Protein 1a Competition with β -Arrestin for CB 1 Receptor Binding Sites. Mol. Pharmacol. 2017, 91, 75−86.

(57) Szklarczyk, D.; Gable, A. L.; Nastou, K. C.; Lyon, D.; Kirsch, R.; Pyysalo, S.; Doncheva, N. T.; Legeay, M.; Fang, T.; Bork, P.; Jensen, L. J.; von Mering, C. The STRING Database in 2021: Customizable Protein−Protein Networks, and Functional Character- ization of User-Uploaded Gene/Measurement Sets. Nucleic Acids Res. 2021, 49, D605−D612.

(58) Szklarczyk, D.; Gable, A. L.; Lyon, D.; Junge, A.; Wyder, S.; Huerta-Cepas, J.; Simonovic, M.; Doncheva, N. T.; Morris, J. H.; Bork, P.; Jensen, L. J.; von Mering, C. STRING V11: Protein−Protein Association Networks with Increased Coverage, Supporting Func- tional Discovery in Genome-Wide Experimental Datasets. Nucleic Acids Res. 2019, 47, D607−D613.

(59) Szklarczyk, D.; Morris, J. H.; Cook, H.; Kuhn, M.; Wyder, S.; Simonovic, M.; Santos, A.; Doncheva, N. T.; Roth, A.; Bork, P.; Jensen, L. J.; von Mering, C. The STRING Database in 2017: Quality- Controlled Protein−Protein Association Networks, Made Broadly Accessible. Nucleic Acids Res. 2017, 45, D362−D368.

(60) Franceschini, A.; Lin, J.; von Mering, C.; Jensen, L. J. SVD-Phy: Improved Prediction of Protein Functional Associations through Singular Value Decomposition of Phylogenetic Profiles. Bioinformatics 2016, 32, 1085−1087.

(61) Szklarczyk, D.; Franceschini, A.; Wyder, S.; Forslund, K.; Heller, D.; Huerta-Cepas, J.; Simonovic, M.; Roth, A.; Santos, A.; Tsafou, K. P.; Kuhn, M.; Bork, P.; Jensen, L. J.; von Mering, C. STRING V10: Protein−Protein Interaction Networks, Integrated over the Tree of Life. Nucleic Acids Res. 2015, 43, D447−D452.

(62) Snel, B. STRING: A Web-Server to Retrieve and Display the Repeatedly Occurring Neighbourhood of a Gene. Nucleic Acids Res. 2000, 28, 3442−3444.

(63) Mering, C. v. STRING: A Database of Predicted Functional Associations between Proteins. Nucleic Acids Res. 2003, 31, 258−261.

(64) von Mering, C. STRING: Known and Predicted Protein- Protein Associations, Integrated and Transferred across Organisms. Nucleic Acids Res. 2004, 33, D433−D437.

(65) Arkinson, C.; Walden, H. Parkin Function in Parkinson's Disease. Science 2018, 360, 267−268.

(66) Castillo, P. E.; Younts, T. J.; Chávez, A. E.; Hashimotodani, Y. Endocannabinoid Signaling and Synaptic Function. Neuron 2012, 76, 70−81.

(67) Asher, W. B.; Geggier, P.; Holsey, M. D.; Gilmore, G. T.; Pati, A. K.; Meszaros, J.; Terry, D. S.; Mathiasen, S.; Kaliszewski, M. J.; McCauley, M. D.; Govindaraju, A.; Zhou, Z.; Harikumar, K. G.; Jaqaman, K.; Miller, L. J.; Smith, A. W.; Blanchard, S. C.; Javitch, J. A. Single-Molecule FRET Imaging of GPCR Dimers in Living Cells. Nat. Methods 2021, 18, 397−405.

(68) Zhu, Y.; Mészáros, J.; Walle, R.; Fan, R.; Sun, Z.; Dwork, A. J.; Trifilieff, P.; Javitch, J. A. Detecting G Protein-Coupled Receptor Complexes in Postmortem Human Brain with Proximity Ligation Assay and a Bayesian Classifier. BioTechniques 2020, 68, 122−129.

(69) Kambe, T.; Correia, B. E.; Niphakis, M. J.; Cravatt, B. F. Mapping the Protein Interaction Landscape for Fully Functionalized Small-Molecule Probes in Human Cells. J. Am. Chem. Soc. 2014, 136, 10777−10782.

(70) Spradlin, J. N.; Zhang, E.; Nomura, D. K. Reimagining Druggability Using Chemoproteomic Platforms. Acc. Chem. Res. 2021, 54, 1801−1813.

(71) Backus, K. M.; Correia, B. E.; Lum, K. M.; Forli, S.; Horning, B. D.; González-Páez, G. E.; Chatterjee, S.; Lanning, B. R.; Teijaro, J. R.; Olson, A. J.; Wolan, D. W.; Cravatt, B. F. Proteome-Wide Covalent Ligand Discovery in Native Biological Systems. Nature 2016, 534, 570−574.

(72) Walko, M.; Hewitt, E.; Radford, S. E.; Wilson, A. J. Design and Synthesis of Cysteine-Specific Labels for Photo-Crosslinking Studies. RSC Adv. 2019, 9, 7610−7614.

(73) Yarravarapu, N.; Geffert, L.; Surratt, C. K.; Cascio, M.; Lapinsky, D. J. Clickable Photoaffinity Ligands for the Human Serotonin Transporter Based on the Selective Serotonin Reuptake Inhibitor (S)-Citalopram. Bioorg. Med. Chem. Lett. 2018, 28, 3431−3435.

(74) Chen, J.; Collins, G. T.; Zhang, J.; Yang, C.-Y.; Levant, B.; Woods, J.; Wang, S. Design, Synthesis, and Evaluation of Potent and Selective Ligands for the Dopamine 3 (D 3) Receptor with a Novel in Vivo Behavioral Profile. J. Med. Chem. 2008, 51, 5905−5908.

(75) Saghatelian, A.; Jessani, N.; Joseph, A.; Humphrey, M.; Cravatt, B. F. Activity-Based Probes for the Proteomic Profiling of Metal- loproteases. Proc. Natl. Acad. Sci. U.S.A. 2004, 101, 10000−10005.

(76) Behiels, E.; Elegheert, J. High-Level Production of Recombinant Eukaryotic Proteins from Mammalian Cells Using Lentivirus. In Structural Proteomics; Owens, R.

J., Ed.; Methods in Molecular Biology; Springer US: New York, NY, 2021; Vol. 2305, pp 83−104.

(77) Rappsilber, J.; Ishihama, Y.; Mann, M. Stop and Go Extraction Tips for Matrix-Assisted Laser Desorption/Ionization, Nanoelectrospray, and LC/MS Sample Pretreatment in Proteomics. Anal. Chem. 2003, 75, 663−670.

4 Photocaged probes for $5HT_{2C}$

4.1 Introduction

Serotonergic signaling is essential for processes ranging from homeostasis to executive function and emotional regulation. In mammals, serotonin is thought to play a modulatory role in almost every physiological function.[1] Dysfunction in the serotonergic signaling system is associated with anxiety, depression, schizophrenia, migraines, autism, Parkinson's disease and Alzheimer's disease.[2–8] Due to its importance, the serotonergic system is the target of many pharmaceuticals, such as the antidepressant drug families of monoamine oxidase inhibitors (MAOIs), selective serotonin reuptake inhibitors (SSRIs), and tricyclic antidepressants (TCAs).[9,10] There are 7 types of serotonin receptors, and a number of subtypes. In dysfunction, these diverse receptors contribute to many diseases and therefore provide important therapeutic potential for drugs targeted to individual serotonin receptor subtypes.[11] Each subtype also contributes to varied physiological states, for example, subtype-selective drugs can treat symptoms of migraine, anxiety, psychosis, or in contrast, can cause hallucinations.[11] In fundamental research, studies are underway to determine the effect of stimulating a serotonin receptor subtype on brain dynamics, to determine the origin of the brain's flexibility to produce different states.[12]

The role of serotonergic signaling in health and disease is an area of intense research. However, there is a lack of tools to enable researchers to tease apart the signaling processes in the exquisitely interconnected networks controlled by the serotonin receptor family. One such challenge is that of re-creating the unique kinetics

of the chemical synapse, where a bolus of neurotransmitter is rapidly released then quickly cleared by active reuptake machinery. Mimicking this system requires a tool that can provide an incredibly rapid rise in signal, followed by an equally rapid fall. To understand how signals at distinct members of the serotonin receptor family affect physiological response, such a tool should ideally be selective for a single subtype.

One strategy to produce a rapid rise in an orthogonally controlled signal is via photocaged compounds.[13] Photocages are photoremovable protecting groups that greatly reduce a compound's affinity for its receptor. Removal of this protecting group with the appropriate wavelength and intensity of light can result in the delivery of the active compound in less than a microsecond.[14] A number of compounds important for neuroscience have been caged, including: serotonin (NPEC-5HT, BHQ-O-5HT, $[Ru(bpy)_2(PMe_3)(5HT)]2+$), dopamine (BBHCM-DA, CNB-DA, CNV-DA, NPEC-DA, RuBi-DA), and subtype selective dopamine receptor D2/D3 antagonists dechloroeticlopride and sulpiride.[15–22] Thus, although dopamine and serotonin have been caged multiple times (including commercial products), there is almost no work disclosing caged subtype-selective modulators.

Here, we report on a matched pair of caged subtype selective serotonin receptor agonist and antagonist for serotonin receptor $5HT_{2C}$. The agonist, WAY161503, is caged with a green light responsive BODIPY photocage, and the antagonist, *N*-desmethylclozapine, is caged with a red light responsive BODIPY photocage. illumination with a green laser provides the agonist and red laser unveils the antagonist, this activity is demonstrated in HEK293T cells expressing human $5HT_{2C}$ (Fig. 1a). This spectral multiplexing also permits us to use both probes in the same experiment, using

a green light to deliver an activating bolus of agonist and a red light to deliver a deactivating bolus of antagonist (Fig. 1b and c). We show that this may be used to target single $5HT_{2C}$ transfected HEK293T cells such that we can observe a rise in a stimulation-induced intracellular calcium flux which may then be rapidly quenched with the uncaging of the antagonist.

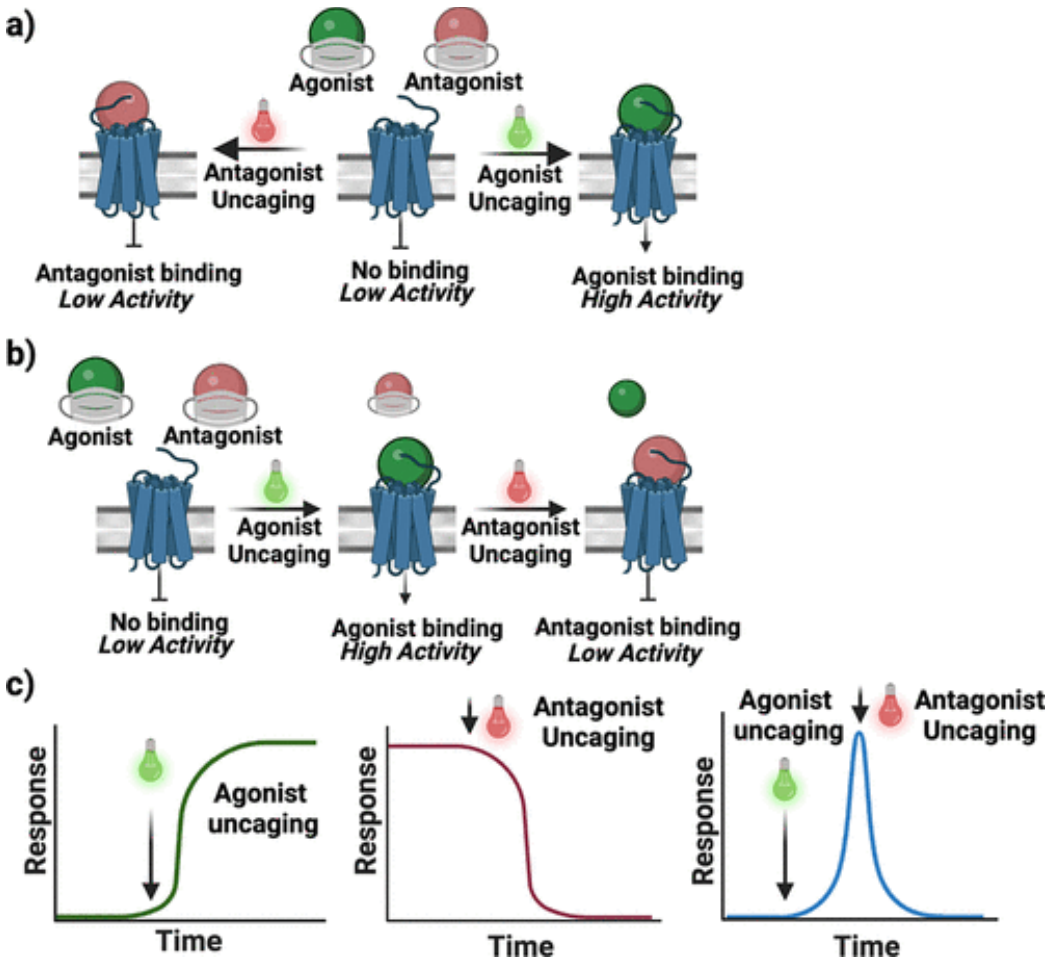

Figure 13. Concept of tight receptor control via photocaged agonist/antagonist pairing.

(a) Uncaging of a photocaged agonist or antagonist unveils the hidden biological activity of the drug, rendering its activity controllable by the uncaging wavelengths of light. In one mode, the agonist may be uncaged to initiate receptor signaling. In a second mode, in the presence of free agonist, uncaging the antagonist results in a decrease in receptor activity. (b) Sequential uncaging of agonist and antagonists with suitable potencies results in agonism/antagonism. (c) Using light as a trigger, extremely rapid signal induction and reduction are possible, also with high spatial resolution.

4.2 Synthesis

We prepared photocaged WAY161563 by first synthesizing the drug and then conjugating it to the photocage. The synthesis of WAY161563 followed the general procedure of Welmaker *et al.* with modifications (Scheme 3).[23] Accordingly, a

nucleophilic aromatic substitution reaction with 1,2-dichloro-4-fluoro-5-nitrobenzene 1 and commercially available 4-benzyloxycarbonylpiperazine-2-carboxylic acid **2** formed **3** in a 60% yield. Tandem Bechamp reduction and cyclization of **3** formed 4 in 50% yield. The Cbz-amine of 4 was reduced with palladium on carbon under hydrogen atmosphere to yield racemic **5** (WAY-161503) in 66% yield. As $5HT_{2C}$ receptors have been shown not to discriminate between the two enantiomers, they are typically not separated when preparing this drug.[23] To install the cage, WAY161503 was condensed with commercially available WinterGreen photocage carbonyldiimidazole adduct **6** following the method of Peterson et al. to provide the caged compound **7** in 58% yield.[24–26]

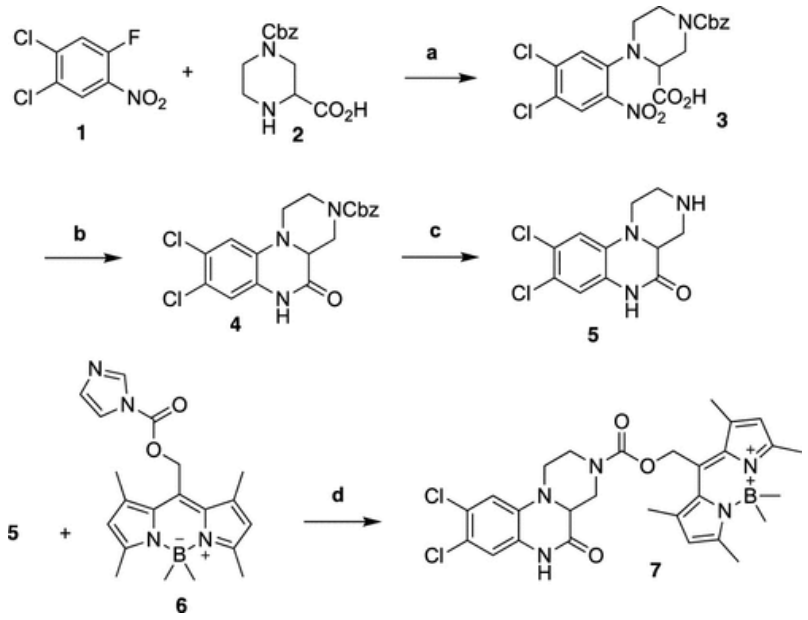

Scheme 3. Synthesis of WinterGreen-WAY-161503 (7).

(a) NEt_3, DMSO, 50 °C 5 h, 25 °C 16 h, 60%; (b) Fe, AcOH, 60 °C 3 h, 50%; (c) H_2, Pd/C 1:1 THF:H_2O, 25 °C 3 h, 66%; (d) NEt_3, THF 25 °C 24 h, 58%.

Caged antagonist *N*-desmethylclozapine was synthesized by first demethylating clozapine following the method of McRobb *et al.*[27] Briefly, 1-chloroethyl chloroformate was added to a solution of clozapine **8** and heated to reflux for 24 hours. The crude residue was dissolved in methanol and heated at 50 °C for 2 hours to yield *N*-desmethylclozapine 9 in 53% yield. Commercially available WinterRed photocage **10** was condensed with carbonyldiimidazole to form the carbamoyl imidazole adduct **11.**[24] The adduct is then incubated with desmethylclozapine 9 to provide WinterRed photocaged desmethylclozapine **12** in 52% yield (Scheme 4).

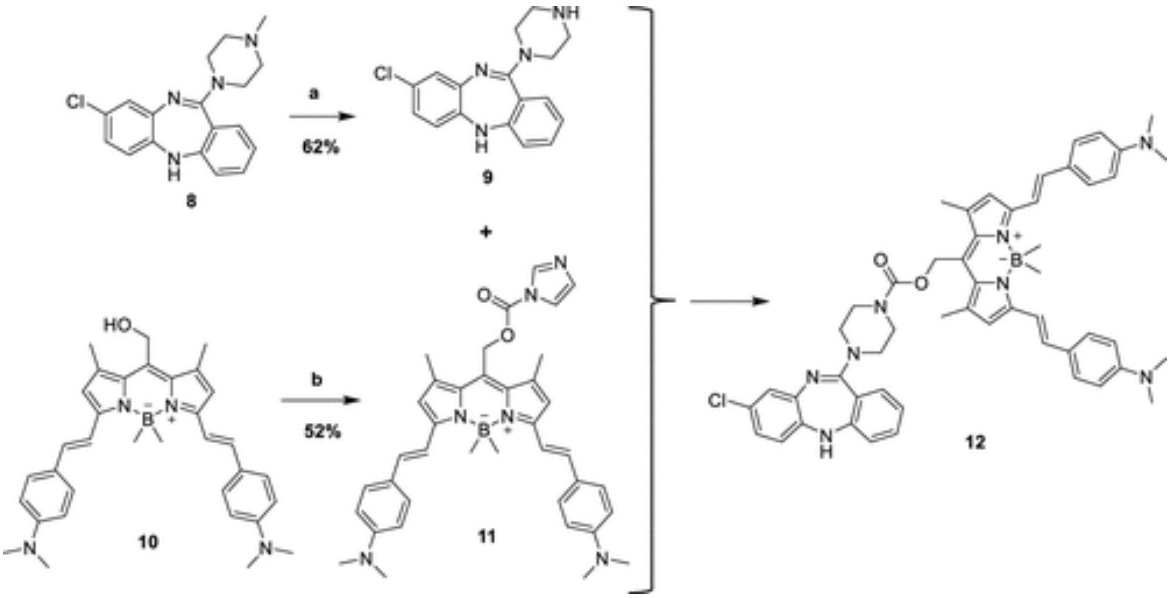

Scheme 4. Synthesis of WinterRed-N-desmethylclozapine (12).

*(a) 1-Chloroethyl chloroformate, 1,2-dichloroethane reflux 24 h, then MeOH 50 °C 2 h, 62%; (b) CDI, NEt_3, DIPEA, THF, 25 °C 2 h then **9**, 48 h, 52%.*

4.3 Pharmacology

As with all GPCRs, the $5HT_{2C}$ receptor detects extracellular effector molecules to activate intracellular responses. An intracellular signaling pathway that is commonly exploited to measure $5HT_{2C}$ activation is β-arrestin signaling. Here, we monitored the β-arrestin pathway to determine whether the installed photocages effectively diminished the binding capacity of both pharmacophores beyond any physiologically relevant concentration. We reasoned that if we could confirm activity by the parent pharmacophores and inactivity of the caged drugs through β-arrestin signaling pathways, the caged drugs did not act as ligands for the $5\text{-}HT_{2C}$ receptor.

4.3.1 TANGO bioactivity

β-arrestin binding is a pathway linked to G-protein signal transduction.[31] We measured $5HT_{2C}$ activity in response to ligand binding via the PRESTO-TANGO assay, which is based upon an engineered $5HT_{2C}$ fusion protein with a cleavable C-terminal transcription factor in HEK293T cells.[32] Upon ligand binding and recruitment of a protease-tagged β-arrestin, the intracellular C-terminal transcription factor is released, resulting in the transcriptional output of the reporter gene, luciferase, which is quantified.

The transcriptional output data indicated that at all physiologically relevant concentrations WinterGreen-WAY is inactive for β-arrestin recruitment (Figure 14a). The assay was then performed in antagonist mode by adding a fixed concentration of test compound and observing changes to the curve of the control agonist. Upon incubation with 200 nm WinterRed-NDMC as the test compound, the response curve to WAY-161503 was not shifted, indicating WinterRed-NDMC is inactive as an antagonist

for $5HT_{2C}$ (Figure 14b, red curve). In contrast, the curve shows a dramatic shift with the addition of uncaged *N*-desmethylclozapine (Figure 14b, teal curve).

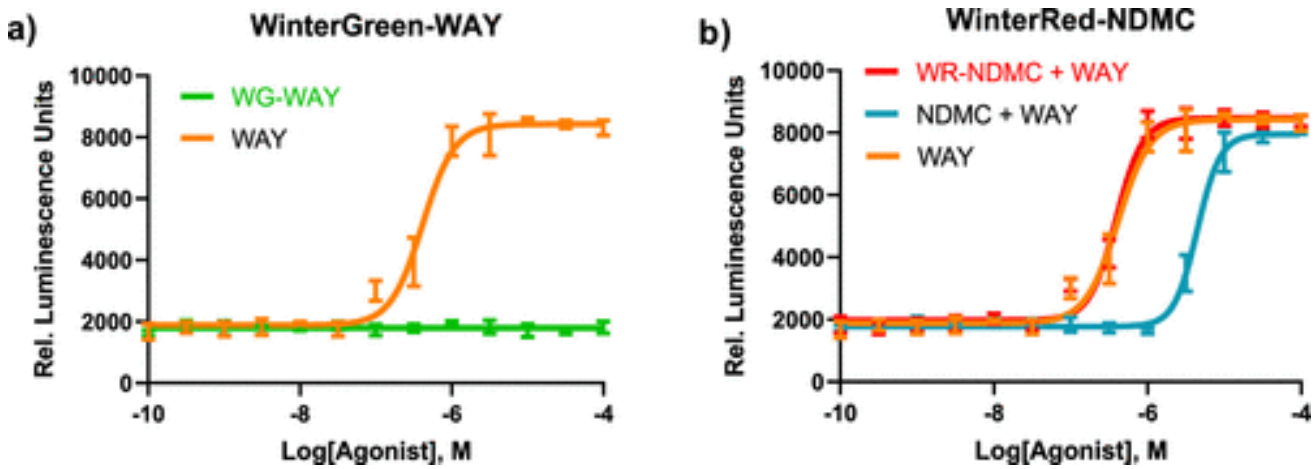

Figure 14. TANGO assay confirmation of loss of bioactivity.

*Arrestin transcriptional output data from HEK293T cells exogenously expressing human 5-HT_{2C}. Luminescence from luciferase expression corresponds to β-arrestin recruitment activity/5-HT_{2C} binding. (a) Wintergreen-WAY-161563 (**5**) vs positive control (uncaged WAY-161563), assayed for 5-HT_{2C} agonism. Green: WinterGreen caged WAY-161563 (**5**); orange: unprotected (free) WAY-161563. (b) WinterRed-NDMC assayed for 5-HT_{2C} antagonism. Red: WinterRed-NDMC (**12**) with WAY-161563 (200 nM constant concentration of WinterRed-NDMC). Teal: uncaged NDMC with WAY-161563 (200 nM constant concentration of NDMC). Orange: unprotected (free) WAY-161563.*

4.4 Photoactivity

4.4.1 Uncaging efficiency via chromatography

While there are many known photocages, of particular importance to our synthetic design were amine compatible photocages, due to the necessity of the amine in the active forms of WAY-161563 and N-desmethylclozapine. The amine photocages we selected covalently shield the amine with a BODIPY cage, through a cleavable carbamate linker. Upon irradiation, this generates an ion paired intermediate between the carbocation of the cage and the carbamate anion pendant on the caged drug. Once

a solvated ion pair is generated, the carbocation rapidly reacts with water to generate the BODIPY alcohol[28] and the carbamate anion on the drug undergoes elimination to the amine and carbon dioxide.[29] The quantum yield of the release of leaving groups by WinterRed and WinterGreen have been previously determined by ferrioxalate actinometry to be 0.11% and 5.5%, respectively.[30]

To determine the uncaging rates, we employed reaction monitoring by HPLC, where we detected the disappearance of photocage-pharmacophore conjugate with increasing irradiation time. Fluorescence spectra of each compound in acetonitrile revealed a WinterGreen-WAY excitation maxima of 491 nm and emission maxima at 529 nm. WinterRed-NDMC was far-red shifted with an excitation of 683 nm and emission maxima at 730 nm. Using a mercury-arc lamp as a photolysis light source, WinterGreen-WAY (Figure 15a) photolyzed with a half-life of 4.565 seconds (first-order exponential decay R2=0.9652) in DMSO. The predominant products of the reaction were BODIPY alcohol and free WAY-161503 with no significant amounts of other photoproducts detected. The yield of uncaging was quantitative at irradiation times greater than 25 seconds. WinterRed-NDMC (Figure 15b) photolyzed with a half-life of 16.26 seconds (first-order exponential decay R2=0.9883) in ethyl acetate. No significant photoproducts were detectable upon uncaging. The yield of uncaging was quantitative at irradiation times greater than 75 seconds. The nearly one order of magnitude increase in half life is likely explained by the significantly lower quantum yield of WinterRed photocage. The half-life of both compounds was deemed to be relevant on a biological timescale and indicated that, upon irradiation, payloads of WAY-161503

and NDMC could be released at a concentration relevant for $5HT_{2C}$ receptor modulation.

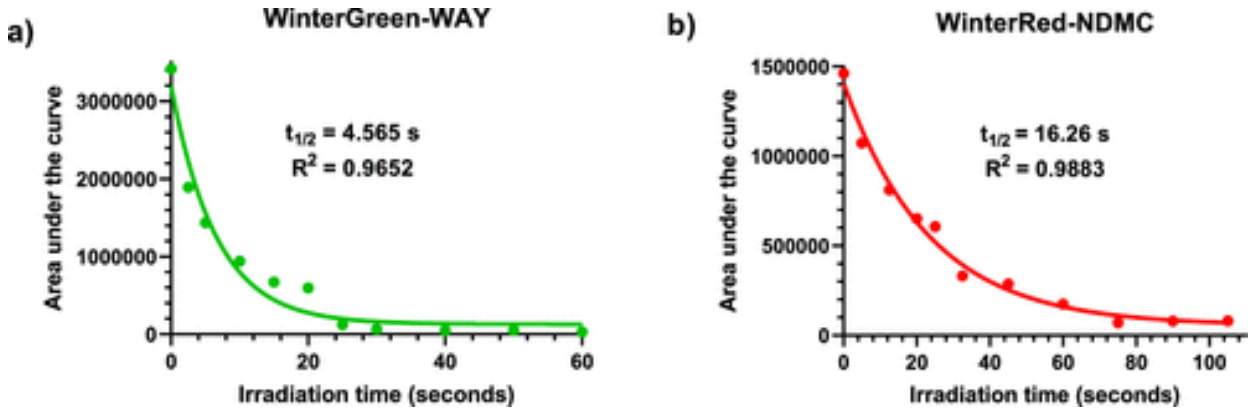

Figure 15. Photolysis kinetics.

*Uncaging photolysis and subsequent release of payload monitored by HPLC. (a) WinterGreen-WAY-161503 (**5**). (b) WinterRed-NDMC (**12**).*

4.4.2 Spontaneous hydrolysis via chromatography

To test the susceptibility of each compound toward spontaneous hydrolysis, WinterGreen-WAY and WinterRed-NDMC were stored protected from light as a 1 mg/mL solution in 60% DMSO in phosphate buffer saline (pH 7.4). The concentration and purity of both solutions remained unchanged after 24 and 48 hours in the dark at room temperature, indicated by HPLC. This result, combined with the biologically relevant half-life of each compound encouraged us to further assay our photocaged compounds for bioactivity at the $5HT_{2C}$ receptor.

4.5 Photoactivation of WinterGreen-WAY and WinterRed-NDMC in cells expressing the 5-HT_{2C} receptor

4.5.1 Aberrant uncaging.

With positive biochemical and photolysis data in hand we were encouraged to assay the uncaging efficacy in living cells. Thus, we set up experiments where the culture media was loaded with one or both caged compounds. The single compound experiments track the uncaging of the compounds, while these experiments are designed to control for whether the wavelength and intensity used to uncage one compound also uncages the second (wavelength overlap). First, we needed to confirm that we could monitor levels of intracellular calcium without initiating aberrant photolysis and release of WAY-161503 and NDMC. To do so, HEK293T cells were plated on glass-bottom chambered coverslips and transiently transfected to express both $5HT_{2C}$-GFP fusion protein and jRCaMP-1a, a genetically encoded calcium indicator.[33] Imaging and uncaging photolysis was performed with a laser scanning confocal microscope.

Activation of WinterGreen-WAY or WinterRed-NDMC by laser irradiation occurred at 488 nm or 639 nm, respectively. The 561 nm laser channel was used to observe RCaMP-1a fluorescence before and after irradiation. Media loaded with 3.7 μM WinterGreen-WAY was irradiated at 561 nm for 800 seconds to check for aberrant release of WAY-161503. No response was observed, so we concluded that WinterGreen-WAY is not activated by extended irradiation of low intensity 561 nm light. To test for aberrant release of NDMC, media loaded with 2.1 μM WinterRed-NDMC was irradiated at 561 nm for 800 seconds, then the media was spiked with 3.7 μM WAY-

161503. The fluorescence intensity was compared to that of a positive control sample containing no WinterRed-NDMC in the media. No change in fluorescence intensity relative to the control was observed, so we concluded that WinterRed-NDMC is also unaffected by extended irradiation of low intensity 561 nm light.

4.5.2 Spectral orthogonality

To test for spectral orthogonality, media containing saturated WinterGreen-WAY was irradiated under the same conditions necessary to uncage WinterRed-NDMC (60% laser power, 639 nm) and observed for aberrant activation. No response was observed, so it was concluded that WinterGreen-WAY was sufficiently spectrally orthogonal to WinterRed-NDMC uncaging conditions. Similarly, media containing saturated WinterRed-NDMC was irradiated under the conditions necessary to uncage WinterGreen-WAY (60% laser power, 488 nm) prior to the addition of 800 nM WAY-161503. The calcium flux curve was compared to a sample containing no WinterRed-NDMC and no significant change in overall peak fluorescence intensity of shape of calcium flux curve was observed, so it was concluded that WinterRed-NDMC is sufficiently spectrally orthogonal to WinterGreen-WAY uncaging conditions.

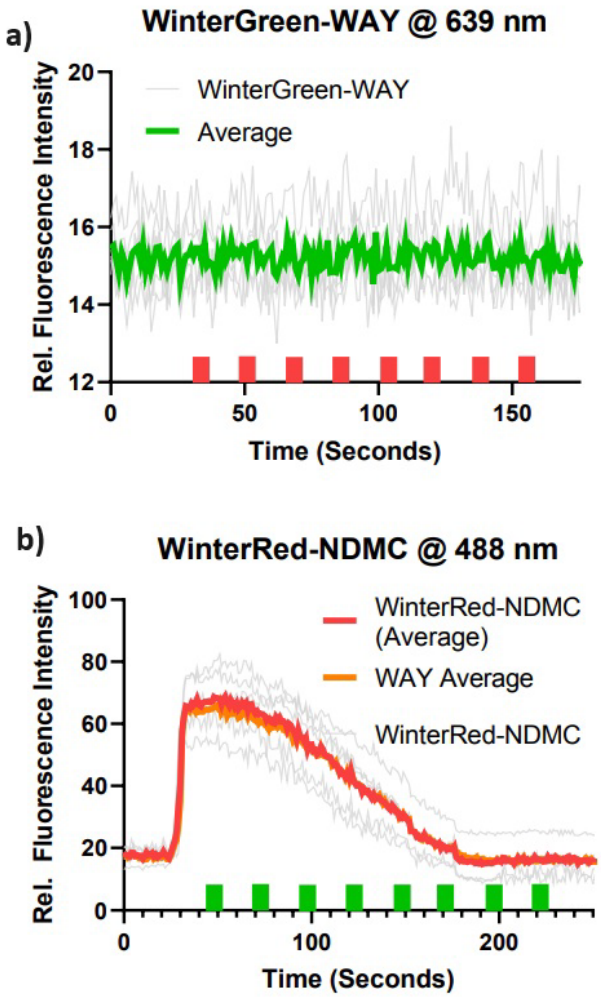

Figure 16. Spectral orthogonality assay.

The alternate laser wavelength at the relevant laser power and scan speed does not uncage the corresponding compound.

4.5.3 Kinetics and spatial resolution of WinterGreen-WAY (5) activation.

To study the kinetics of WinterGreen-WAY photolysis under cell culture conditions, calcium response with respect to irradiation time was measured (Fig. 4). A region adjacent to a cell of interest was illuminated with a 488 nm laser (the uncaging wavelength), and the subsequent calcium flux due to the binding of uncaged drug to its

receptor was monitored via the increase in fluorescence of the calcium indicator protein RCaMP-1a. A 200 ms pulse of high intensity irradiation was found to be sufficient to elicit calcium signaling (Figure 17b-c). In the presence of 488 nm irradiation but absence of WinterGreen-WAY, no calcium response was observed.

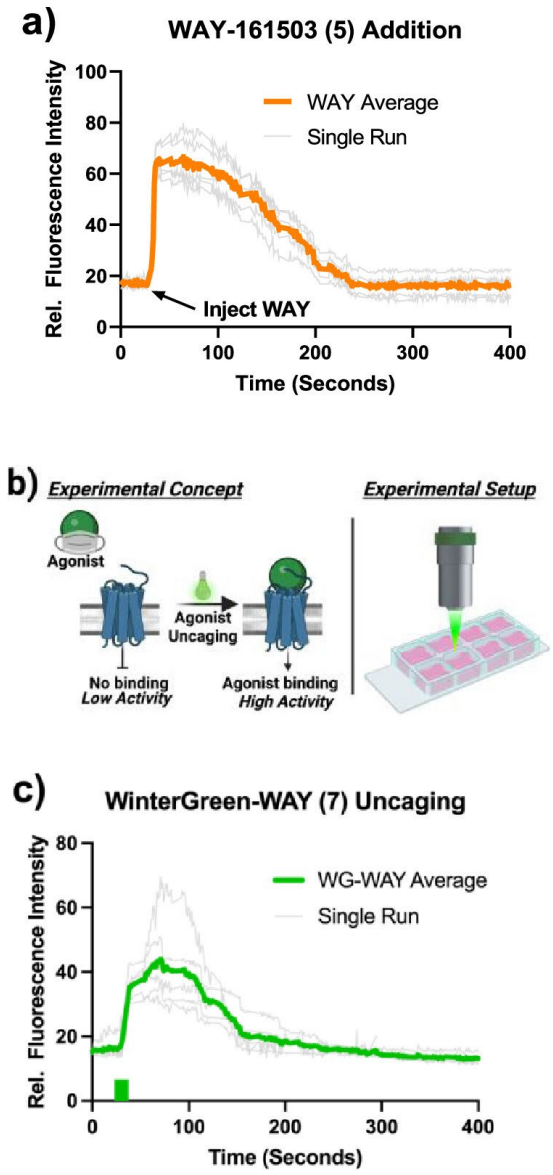

Figure 17. WinterGreen-WAY uncaging.

*(a) 800 nM WAY-161503 was injected into cell culture media as a control to establish typical calcium flux duration and characteristics under traditional drug dosing conditions. (b) Schematic of experimental design: active agonist is unveiled via a 488 nm laser, which is focused via a confocal microscope into cells plated on a microscope slide. (c) WinterGreen-WAY (**5**) (3.7 μM) uncaging induces a similar calcium mobilization curve and calcium flux duration but with lower maximum fluorescence intensity, indicative of lower local drug concentrations. Green block on the line graph indicates the event of 488 nm irradiation. WG-WAY average curves were generated as the average relative fluorescence intensity of 10 cells where basal fluorescence was normalized.*

We next determined the spatial resolution for cell activation with an uncaging event. Importantly, $5HT_{2C}$ activation was only observed within an approximate 100 μm radius beyond the focus of irradiation (Figure 18, quantitation in Figure 19). This provides a high level of spatial control of activation and could serve as a powerful tool for studying cell-cell communication.

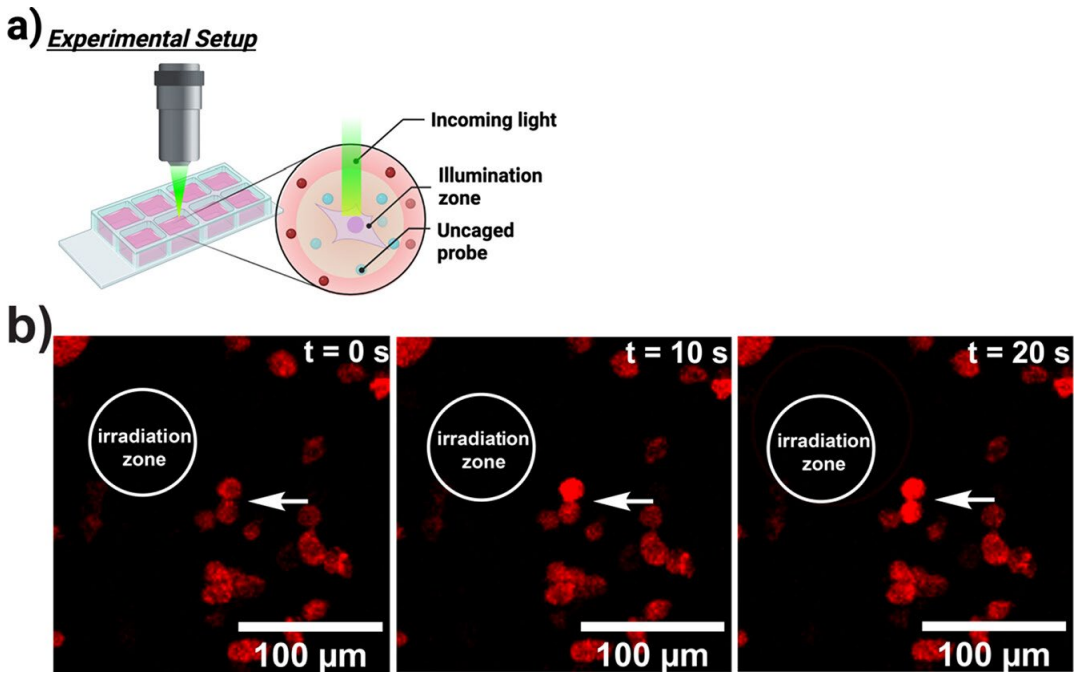

Figure 18. Live cell microscopy of 5-HT2C activation.

(a) Laser-scanning confocal microscopy enables discrete areas of uncaging. (b) Photoinduced release of WAY-161503 produces highly localized areas with WAY-161503 concentrations high enough to induce $5HT_{2C}$ activation and subsequent intracellular calcium mobilization. White circles indicate areas of irradiation event, and white arrows point to cells demonstrating increased calcium flux.

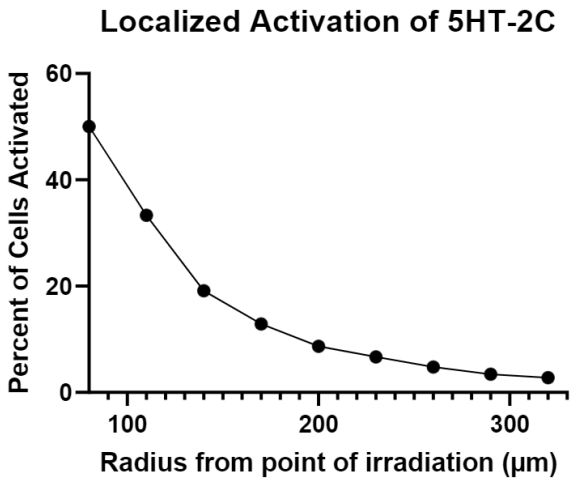

Figure 19. Quantification of percent of cells activated surrounding a region of irradiation in response to a 200 ms pulse of 488 nm light.

To quantitate, we look at the number of cells activated in radii of different lengths from the focal point of the laser. To maximize cell viability and minimize the chance for experimental artefacts, the laser is never pointed directly at a cell. All cells within the radius are counted.

Repeated 200 ms irradiation in the presence of WinterGreen-WAY elicited extended calcium signaling, with a statistically significantly longer calcium flux duration than 800 nM WAY-161503 (Figure 20). This indicated light-dose dependent signaling for $5HT_{2C}$ that could be achieved without deterioration of the response or high global drug concentration.

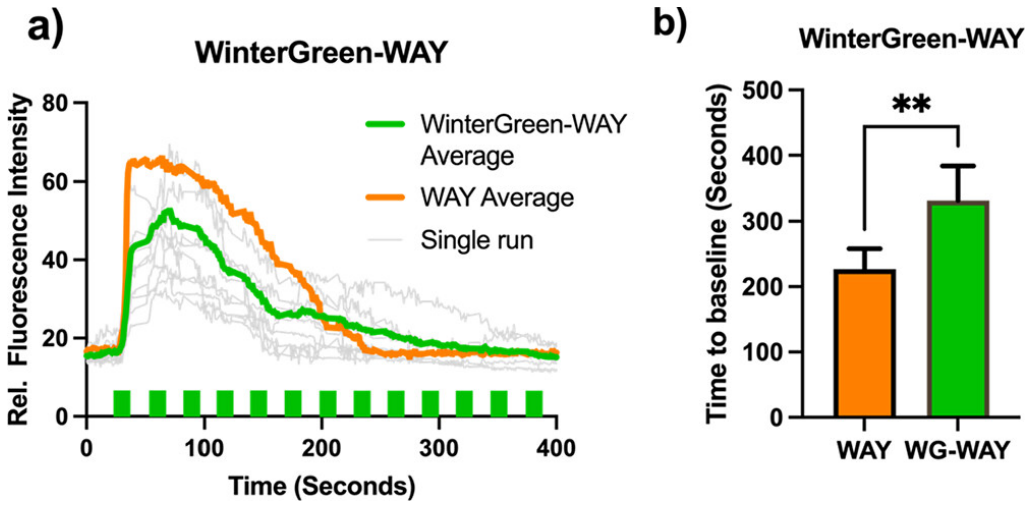

Figure 20. Long time-scale WinterGreen-WAY uncaging.

*(a) WinterGreen-WAY (**5**) uncaging induces lower maximum concentrations of intracellular calcium, but repeated irradiation can produce significantly longer calcium flux durations. Green blocks on the line graph indicate events of 488 nm irradiation. 800 nM WAY-161503 injected into cell culture media as a control to determine calcium flux duration using traditional drug dosing techniques. (b) Bar chart of calcium flux durations comparing 800 nM WAY-161503 and WinterGreen-WAY (**5**). Average curves were generated as the average relative fluorescence intensity of 10 cells where basal fluorescence was normalized.*

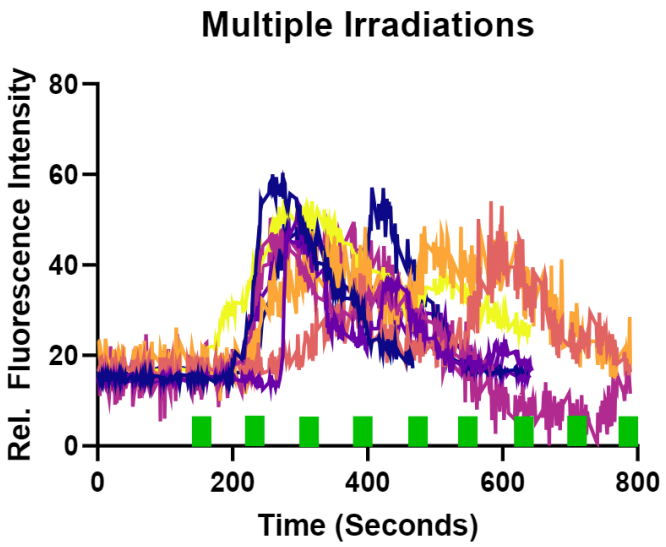

Figure 21. Repeated irradiation of WinterGreen-WAY is able to envoke subsequent events of calcium mobilization.

Each colored line corresponds to an individual cell, in an ensemble of 10 cells.

Quantitation indicated the amount of drug released corresponds to approximately 300 nM of free drug (Figure 22). Overall, this demonstrates the utility of this tool as a method of performing experiments of long duration and repeatable dosing without the need to exchange cell culture media, an experimentally simple setup and mode of stimulus.

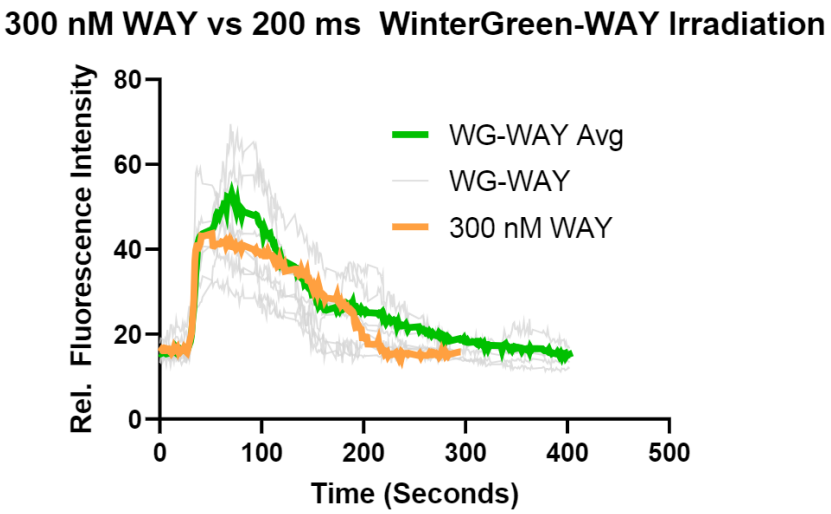

Figure 22. Recapitulation of 200 ms irradiation WinterGreen-WAY calcium flux curve through the addition of 300 nM parent WAY-161503.

4.5.4 Photoactivation of WinterRed-NDMC (12).

With the kinetics of WinterGreen-WAY uncaging defined, we sought to test WinterRed-NDMC uncaging under cell culture conditions. As an initial test of WinterRed-NDMC antagonistic efficacy, we designed a competition assay to test for spatially controlled NDMC binding of $5HT_{2C}$ against WAY-161503. Media was loaded with 2.10 μM WinterRed-NDMC, 800 nM WAY-161503 was injected into the media, then the entire field of view was irradiated with 639 nm light to uncage NDMC. The concentration of WinterRed-NDMC corresponds to the concentration in solution post-filtration based on a standardization curve. The calcium flux duration was compared to that of a sample containing no WinterRed-NDMC. A statistically significant decrease in both calcium flux duration and amplitude of calcium signaling was observed (Figure 23). From this we concluded that the photolysis reaction of WinterRed-NDMC is active in cell

culture media and demonstrated spatial modulation of calcium signaling within a large population of $5HT_{2C}$ expressing cells.

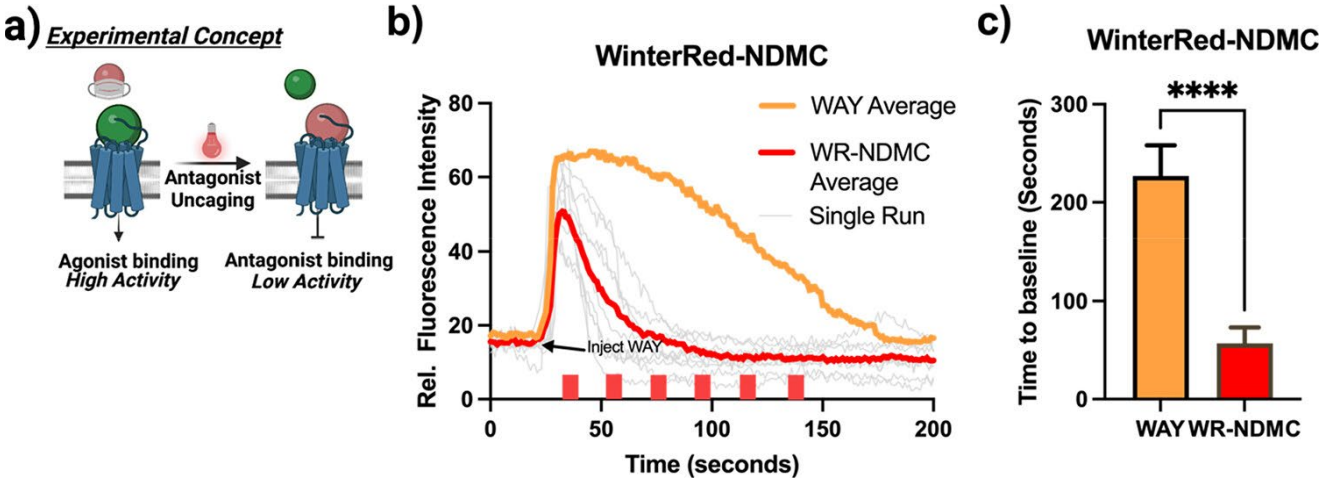

Figure 23. In vitro WinterRed-NDMC uncaging.

(a) Schematic of experimental design: active antagonist is unveiled in the media, which will compete for active site binding. (b) Line graph comparing 800 nM WAY-161503 injection with (red line) and without (orange line) WinterRed-NDMC uncaging. Red blocks indicate events of 639 nm irradiation. (c) Bar chart comparing calcium flux durations of 800 nM WAY-161503 injection with and without WinterRed-NDMC uncaging. Average curves were generated as the average relative fluorescence intensity of 10 cells where basal fluorescence was normalized.

To determine the local concentration of uncaged NDMC, recapitulation of the experimental calcium flux curve was approximated through preincubation of free-NDMC then the addition of 800 nM free-WAY-161503. Quantitation indicated the amount of drug released within a 100 µm radius corresponds to approximately 250 nM of free-NDMC (Figure 24).

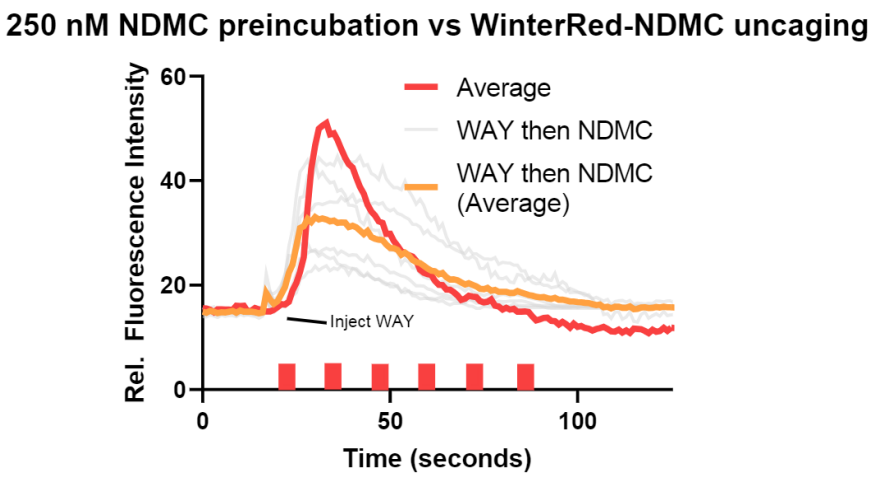

Figure 24. Recapitulation of parent WAY-161503/WinterRed-NDMC calcium flux curve through preincubation of 250 nM NDMC then 800 nM parent WAY-161503 addition.

4.5.5 Orthogonal activation of WinterGreen-WAY (5) and WinterRed-NDMC (12).

With both compounds confirmed to be photoactive under cell culture conditions, we proceeded to investigate how they could be used in tandem to demonstrate a high degree of both spatial and temporal control of calcium signaling. To accomplish this, we loaded both WinterGreen-WAY and WinterRed-NDMC at a concentration of 3.71 and 2.10 μM respectively into cell culture media, chose a region of cells to activate by 488 nm uncaging, then immediately upon activation irradiated the same region with 639 nm light. The result of which is markedly tighter control of calcium flux durations and amplitude (Figure 25). Here the on/off or activated/inactivated state of the receptor is controlled by pulses of light. This represents not only a novel avenue to reproducibly control the activation and signaling pattern of the $5HT_{2C}$ receptor but allows precise spatial control of the population induced.

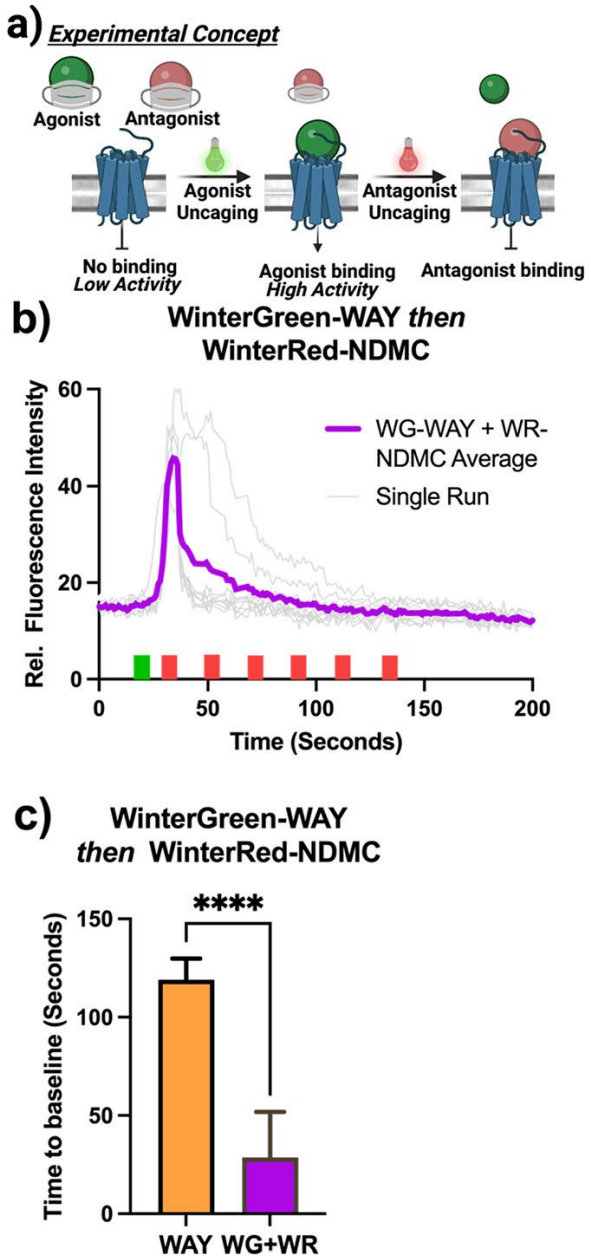

Figure 25. In vitro dual-wavelength uncaging.

(a) Schematic of experimental design: active agonist is unveiled in the media to bind 5-HT$_{2C}$, immediately followed by unveiled antagonist, which will compete for active site binding. (b) Line graph depicting dual-wavelength WinterGreen-WAY uncaging preceding WinterRed-NDMC uncaging. Green and red blocks indicate events of 488 nm and 639 nm irradiation, respectively. (c) Bar chart comparing calcium flux durations of 800 nM WAY-161503 injection with dual-wavelength WinterGreen-WAY and WinterRed-NDMC uncaging. "Average" curves were generated as the average relative fluorescence intensity of 10 cells where basal fluorescence was normalized.

4.6 Conclusion and future direction

Photoactivatable forms of WAY-161503 and NDMC were designed as a system that allows for spectral multiplexing enabling tight spatiotemporal control of $5HT_{2C}$ calcium signaling. WinterGreen-WAY and WinterRed-NDMC were synthesized, characterized, and tested for loss of bioactivity at physiologically relevant concentrations. The kinetics of photolysis were characterized using HPLC and confirmation of functional drug release was performed in live cell culture. Both compounds had acceptable photolysis half-lives of 4.565 seconds for WinterGreen-WAY and 16.26 seconds for WinterRed-NDMC, and quantitatively photolyzed in under 25 and 75 seconds, respectively. Importantly, both compounds remained stable in solution for 48 hours in the dark, and WinterGreen-WAY could release physiologically relevant payloads with a 200 ms pulse of 488 nm light in cell culture media. WinterGreen-WAY mediated the activation of $5HT_{2C}$ signaling similar to that of commercially available WAY-161503, and with repeated 200 ms pulses of 488 nm light demonstrated longer calcium flux durations than that of 800 nM WAY-161053. This indicated light-dose dependent signaling for $5HT_{2C}$ that could be achieved without deterioration of the response or high global drug concentration. Upon 639 nm irradiation, WinterRed-NDMC was demonstrated to diminish the effect of up to 800 nM WAY-161503 injected into cell culture media. Importantly, tandem uncaging of WinterGreen-WAY then WinterRed-NDMC produced markedly shorter calcium flux duration and amplitude, with precise spatial control. These tools enable a greater degree of spatiotemporal control of 5-HT2C modulation and will allow for more detailed studies of receptors signaling, interactions with other proteins, and native physiology. Future studies will focus on

applying this system to spatiotemporally control synaptic transmission of primary neurons on a receptor subtype specific level.

4.7 Experimental

4.7.1 Synthetic chemistry general experimental procedures

All reactions were performed in flame- or oven-dried glassware under positive pressure of nitrogen or argon unless otherwise noted. Dichloromethane, 1,2-dichloroethane, dimethylacetamide, *N,N*-dimethylformamide, triethylamine, and toluene were dried by columns packed with activated alumina on a solvent purification system. Anhydrous DMSO was purchased from Acros Organics in AcroSeal bottles. All reagents were used as purchased without further purification. Thin layer chromatography (TLC) was performed on Merck 60 F_{254} pre-coated silica gel plates, and plates were visualized with UV light and ninhydrin stain when appropriate. Flash-column chromatography was performed using silica gel (60 Å, 230-240 mesh, Merck KGA). HPLC runs were conducted on a Waters 2545 binary gradient pump equipped with UVVis Detector. Analytical runs were performed using a Phenomenex C18 column (4.6 x 50 mm) and a Phenomenex Luna 5 µm silica column (4.6 x 50 mm). Separations were monitored at 325 nm and 254 nm. NMR spectra were recorded with Bruker Avance spectrometers using deuterated solvents. ^{1}H NMR spectra were recorded at 400 MHz as indicated. ^{13}C spectra were recorded at 100 MHz. ^{1}H NMR data are reported in the following order: chemical shift (δ ppm), multiplicity, coupling constant (Hz), and integration. ^{13}C NMR data are reported in terms of chemical shift. UV-Visible spectroscopy was preformed using an Agilent Technologies Cary 60 UV-Visible

Spectrophotometer. Fluorescence spectroscopy was performed using a Horiba Scientific FluoroMax+ Spectrofluorimeter.

*4.7.1.1 8,9-dichloro-2,3,4,4a-tetrahydro-1H,6H-pyrazino[1,2-a]quinoxalin-5-one (**7**).*

Compound **7** was prepared from **1** following the procedure of Welmaker *et al.*[23] The spectra matched those reported previously.

*4.7.1.2 N-desmethylclozapine (**9**)*

Compound 9 was prepared from **8** following the procedure of McRobb et al.[27] The spectra matched those reported previously.

*4.7.1.3 WinterGreen-WAY (**7**)*

To a solution of **5** (14.9 mg, 0.055mmol, 1.0 eq) stirring in dry THF was added 4-dimethylaminopyridine (4.6 mg, 0.055 mmol, 1.0 eq) and 6 (20 mg, 0.055 mmol, 1.0 eq) were added. The reaction was stirred at room temperature overnight. The reaction mixture was washed with water and extracted with ethyl acetate. The organic layer was dried over magnesium sulfate and the solvent was removed under vacuum. The crude mixture was purified using silica gel column chromatography with 0-50% ethyl acetate in hexanes as the eluent to yield **7** as a bright red solid (0.0319 mmol, 58% yield). ^{1}H NMR (400 MHz, $CDCl_3$) 6.85 (s, 1H), 6.80 (m, 1H), 6.08 (s, 2H), 5.39 (s, 2H), 3.49 (m, 2H), 3.07 (t, 2H, J=12.8 Hz), 2.63 (S, 1H), 2.47 (s, 6H), 2.38 (s, 6H), 2.18 (t, 2H, J=2.2Hz), 1.25 (s, 6H), 0.20 (s, 6H). ^{13}C NMR (100 MHz, CDCl3) 153.3, 137.1, 134.8, 131.4, 127.3, 125.7, 123.6, 123.2, 122.7, 116.6, 113.9, 69.5, 56.4, 53.8, 44.4, 31.8,

29.7, 29.3, 25.4, 16.6, 15.9, 15.8, 14.1, 9.5. UV-Visible λ_{max} = 515 nm. Fluorescence excitation/emission = 491 nm/529 nm.

4.7.1.4 WinterRed-NDMC (12).

To a solution of **9** (10 mg, 0.032 mmol, 1.0 eq) stirring in dry THF was added carbonyldiimidazole (7.7 mg, 0.048 mmol, 1.5 eq). The reaction was stirred under argon for 2 h. Then, 4-dimethylaminopyridine (3.8 mg, 0.032 mmol, 1.0 eq) and 11 (16.8 mg, 0.032 mmol, 1.0 eq) were added. The reaction was stirred at room temperature overnight. The reaction mixture was washed with water and extracted with ethyl acetate. The organic layer was dried over magnesium sulfate and the solvent was removed under vacuum. The crude mixture was purified using silica gel column chromatography with 0-50% ethyl acetate in hexanes as the eluent to yield **12** as a dark green solid (0.017 mmol, 52% yield). ^{1}H NMR (400 MHz, CDCl3) 7.48 (d, 4H, J=8.6Hz), 7.44 (s, 1H), 7.30 (d, 1H, J=7.4), 7.24 (d, (1H, J=8.0Hz), 7.07 (m, 3H), 6.99 (s, 4H), 6.84 (dd, 1H, J=10.6Hz), 6.80 (d, 1H, J=7.8Hz), 6.73 (m, 7H), 6.60 (d, 1H, J=8.4Hz), 5.41 (s, 2H), 5.02 (s, 1H), 4.91 (m, 1H), 3.51 (m, 7H), 3.03 (s, 12H), 2.59 (s, 2H), 2.45 (s, 5H), 2.28 (s, 5H), 1.26 (s, 6H), 0.86 (m, 3H), 0.47 (s, 6H). ^{13}C NMR (100 MHz, CDCl3) 155.1, 152.9, 151.5, 151.4, 150.8, 150.6, 150.6, 141.4, 140.4, 136.1, 135.8, 135.7, 133.4, 132.2, 130.0, 129.1, 128.4, 128.3, 128.2, 126.9, 125.6, 125.5, 123.5, 123.2, 120.1, 118.5, 117.1, 112.4, 67.9, 59.8, 40.4, 34.5, 30.2, 29.7, 25.6, 21.2, 16.1. UV-Visible λ_{max} = 672 nm. Fluorescence excitation/emission = 683 nm/730 nm.

4.7.2 HPLC photolysis characterization

For WinterGreen-WAY characterization, compound was taken up in DMSO as a 1.5 mg/mL solution and sterile filtered to remove any aggregates. 100 µL aliquots were irradiated with a 4500 mW/cm^2 spot Hg-arc light source (Hamamatsu LC8) for various time points. Aliquots were then purified on a Waters HPLC, with a Waters 2545 binary gradient pump equipped with Waters 2489 UV-Vis Detector. The column was a Phenomenex C18 column (4.6 x 50 mm) run with a gradient of 5%-95% acetonitrile in water for 20 minutes. Percent WinterGreen-WAY remaining was calculated from the integrated peak area.

For WinterRed-NDMC characterization, compound was taken up in ethyl acetate as a 1.5 mg/mL solution and sterile filtered to remove any aggregates. Irradiation procedure and HPLC instrument were the same as above. The column was a Phenomenex Luna 5 µm silica column (4.6 x 50 mm) run with a gradient of 5%-95% ethyl acetate in hexanes for 20 minutes. Percent WinterRed-NDMC remaining was calculated from the integrated peak area.

4.7.3 TANGO assay biochemical characterization

HTLA cells were a gift from the laboratory of G. Barnea and were maintained in DMEM supplemented with 10% FBS, 100 U/ml penicillin and 100 µg/ml streptomycin, 2 µg/ml puromycin, 100 µg/ml hygromycin B, and 100 µg/ml G418, in a humidified atmosphere at 37 °C in 5% CO2. On day 1, cells were plated at a density of 1x105 cells/cm2 in a black wall, clear bottom 96 well plate (Nunc). The following day (day 2), cells were transfected with a 10x solution of 3:1 mixture of HTR2C-TANGO (Addgene

#66411):Optifect Transfection Reagent (Thermo) in un-supplemented DMEM. On day 3, 1× drug stimulation solutions were prepared in filter-sterilized unupplemented DMEM. The transfection media was shaken or aspirated from the wells, and drug stimulation solutions were gently added. On day 4, drug solutions were removed from one well every ten seconds (to maintain consistency of incubation time) and 50 µl per well of Bright-Glo solution (Promega) diluted 20-fold in HBSS was added. After incubation for 2 min at room temperature, luminescence was counted with an integration time of 10 sec in a Spectramax i3x plate reader (Molecular Devices). Drug concentrations were experimentally measured in triplicate. Statistical analysis was performed using GraphPad Prism 9.

4.7.4 Uncaging in cell culture

HEK293T cells were maintained in DMEM supplemented with 10% FBS, 100 U/ml penicillin and 100 µg/ml streptomycin, in a humidified atmosphere at 37 °C in 5% CO2. On day 1, cells were plated at a density of 4x104 cells/cm2 in a poly-D-lysine coated 18-well chambered coverslip (Ibidi). The following day (day 2), cells were transfected with a 10x solution of 3:1 mixture of FRT-5HT-GFP (Addgene #79677):Optifect Transfection Reagent (Thermo) and a 3:1 mixture of jRCaMP-1a (Addgene # 61562):Optifect Transfection Reagent (Thermo) in unsupplemented DMEM. On day 3 the transfection media was removed and freshly prepared unsupplemented media loaded with either 10 µM WinterGreen-WAY, 10 µM WinterRed-NDMC, or 10 µM of both compounds was added to the wells. Live cell uncaging and imaging was performed on a Zeiss LSM 980 with Airyscan 2. Basal fluorescence was recorded for 20 seconds, followed by spot bleaching of the region of interest at 60% laser intensity

using the appropriate wavelength. Nominal power for the 488 nm and 639 nm lasers used were 10.0 mW and 7.5 mW, respectively. Calcium response was recorded for 800 seconds after initial irradiation. Data extraction was completed with ImageJ. "Average" curves were generated from the average relative fluorescence intensity of ten cells, where basal fluorescence was normalized.

4.8 References

(1) Charnay, Y.; Leger, L. Brain Serotonergic Circuitries. Dialogues in Clinical Neuroscience 2010, 12 (4), 471–487. https://doi.org/10.31887/DCNS.2010.12.4/ycharnay.

(2) Akimova, E.; Lanzenberger, R.; Kasper, S. The Serotonin-1A Receptor in Anxiety Disorders. Biological Psychiatry 2009, 66 (7), 627–635. https://doi.org/10.1016/j.biopsych.2009.03.012.

(3) Nemeroff, C. B.; Owens, M. J. The Role of Serotonin in the Pathophysiology of Depression: As Important As Ever. Clinical Chemistry 2009, 55 (8), 1578–1579. https://doi.org/10.1373/clinchem.2009.123752.

(4) Rasmussen, H.; Erritzoe, D.; Andersen, R.; Ebdrup, B. H.; Aggernaes, B.; Oranje, B.; Kalbitzer, J.; Madsen, J.; Pinborg, L. H.; Baaré, W.; Svarer, C.; Lublin, H.; Knudsen, G. M.; Glenthoj, B. Decreased Frontal Serotonin2A Receptor Binding in Antipsychotic-Naive Patients With First-Episode Schizophrenia. Arch Gen Psychiatry 2010, 67 (1), 9. https://doi.org/10.1001/archgenpsychiatry.2009.176.

(5) Goadsby, P. J. Serotonin Receptor Ligands: Treatments of Acute Migraine and Cluster Headache. In Analgesia; Stein, C., Ed.; Handbook of Experimental Pharmacology; Springer Berlin Heidelberg: Berlin, Heidelberg, 2006; Vol. 177, pp 129–143. https://doi.org/10.1007/978-3-540-33823-9_5.

(6) Azmitia, E. C.; Nixon, R. Dystrophic Serotonergic Axons in Neurodegenerative Diseases. Brain Research 2008, 1217, 185–194. https://doi.org/10.1016/j.brainres.2008.03.060.

(7) Newhouse, P.; Tatro, A.; Naylor, M.; Quealey, K.; Delgado, P. Alzheimer Disease, Serotonin Systems, and Tryptophan Depletion. Am J Geriatr Psychiatry 2002, 10 (4), 483–484.

(8) Ouchi, Y.; Yoshikawa, E.; Futatsubashi, M.; Yagi, S.; Ueki, T.; Nakamura, K. Altered Brain Serotonin Transporter and Associated Glucose Metabolism in Alzheimer Disease. J Nucl Med 2009, 50 (8), 1260–1266. https://doi.org/10.2967/jnumed.109.063008.

(9) Köhler, S.; Cierpinsky, K.; Kronenberg, G.; Adli, M. The Serotonergic System in the Neurobiology of Depression: Relevance for Novel Antidepressants. J Psychopharmacol 2016, 30 (1), 13–22. https://doi.org/10.1177/0269881115609072.

(10) Taylor, C.; Fricker, A. D.; Devi, L. A.; Gomes, I. Mechanisms of Action of Antidepressants: From Neurotransmitter Systems to Signaling Pathways. Cellular Signalling 2005, 17 (5), 549–557. https://doi.org/10.1016/j.cellsig.2004.12.007.

(11) Pithadia, A. 5-Hydroxytryptamine Receptor Subtypes and Their Modulators with Therapeutic Potentials. J Clin Med Res 2009. https://doi.org/10.4021/jocmr2009.05.1237.

(12) Jancke, D.; Herlitze, S.; Kringelbach, M. L.; Deco, G. Bridging the Gap between Single Receptor Type Activity and Whole-brain Dynamics. The FEBS Journal 2022, 289 (8), 2067–2084. https://doi.org/10.1111/febs.15855.

(13) Josa-Culleré, L.; Llebaria, A. In the Search for Photocages Cleavable with Visible Light: An Overview of Recent Advances and Chemical Strategies. ChemPhotoChem 2021, 5 (4), 296–314. https://doi.org/10.1002/cptc.202000253.

(14) Klán, P.; Šolomek, T.; Bochet, C. G.; Blanc, A.; Givens, R.; Rubina, M.; Popik, V.; Kostikov, A.; Wirz, J. Photoremovable Protecting Groups in Chemistry and Biology: Reaction Mechanisms and Efficacy. Chem. Rev. 2013, 113 (1), 119–191. https://doi.org/10.1021/cr300177k.

(15) Rea, A. C.; Vandenberg, L. N.; Ball, R. E.; Snouffer, A. A.; Hudson, A. G.; Zhu, Y.; McLain, D. E.; Johnston, L. L.; Lauderdale, J. D.; Levin, M.; Dore, T. M. Light-Activated Serotonin for Exploring Its Action in Biological Systems. Chemistry & Biology 2013, 20 (12), 1536–1546. https://doi.org/10.1016/j.chembiol.2013.11.005.

(16) Cabrera, R.; Filevich, O.; García-Acosta, B.; Athilingam, J.; Bender, K. J.; Poskanzer, K. E.; Etchenique, R. A Visible-Light-Sensitive Caged Serotonin. ACS Chem. Neurosci. 2017, 8 (5), 1036–1042. https://doi.org/10.1021/acschemneuro.7b00083.

(17) Hagen, V.; Kilic, F.; Schaal, J.; Dekowski, B.; Schmidt, R.; Kotzur, N. [8-[Bis(Carboxymethyl)Aminomethyl]-6-Bromo-7-Hydroxycoumarin-4-Yl]Methyl Moieties as Photoremovable Protecting Groups for Compounds with COOH, NH 2 , OH, and C=O Functions. J. Org. Chem. 2010, 75 (9), 2790–2797. https://doi.org/10.1021/jo100368w.

(18) Lee, T. H.; Gee, K. R.; Ellinwood, E. H.; Seidler, F. J. Combining 'Caged-Dopamine' Photolysis with Fast-Scan Cyclic Voltammetry to Assess Dopamine Clearance and Release Autoinhibition in Vitro. Journal of Neuroscience Methods 1996, 67 (2), 221–231. https://doi.org/10.1016/0165-0270(96)00068-4.

(19) Robinson, B. G.; Bunzow, J. R.; Grimm, J. B.; Lavis, L. D.; Dudman, J. T.; Brown, J.; Neve, K. A.; Williams, J. T. Desensitized D2 Autoreceptors Are Resistant to Trafficking. Sci Rep 2017, 7 (1), 4379. https://doi.org/10.1038/s41598-017-04728-z.

(20) Araya, R.; Andino-Pavlovsky, V.; Yuste, R.; Etchenique, R. Two-Photon Optical Interrogation of Individual Dendritic Spines with Caged Dopamine. ACS Chem. Neurosci. 2013, 4 (8), 1163–1167. https://doi.org/10.1021/cn4000692.

(21) Asad, N.; McLain, D. E.; Condon, A. F.; Gore, S.; Hampton, S. E.; Vijay, S.; Williams, J. T.; Dore, T. M. Photoactivatable Dopamine and Sulpiride to Explore the Function of Dopaminergic Neurons and Circuits. ACS Chem. Neurosci. 2020, 11 (6), 939–951. https://doi.org/10.1021/acschemneuro.9b00675.

(22) Gienger, M.; Hübner, H.; Löber, S.; König, B.; Gmeiner, P. Structure-Based Development of Caged Dopamine D2/D3 Receptor Antagonists. Sci Rep 2020, 10 (1), 829. https://doi.org/10.1038/s41598-020-57770-9.

(23) Welmaker, G. S.; Nelson, J. A.; Sabalski, J. E.; Sabb, A. L.; Potoski, J. R.; Graziano, D.; Kagan, M.; Coupet, J.; Dunlop, J.; Mazandarani, H.; Rosenzweig-Lipson, S.; Sukoff, S.; Zhang, Y. Synthesis and 5-Hydroxytryptamine (5-HT) Activity of 2,3,4,4a-Tetrahydro-1H-Pyrazino[1,2-a]Quinoxalin-5-(6H)Ones and 2,3,4,4a,5,6-Hexahydro-1H-Pyrazino[1,2-a]Quinoxalines. Bioorganic & Medicinal Chemistry Letters 2000, 10 (17), 1991–1994. https://doi.org/10.1016/S0960-894X(00)00400-5.

(24) Peterson, J. A.; Wijesooriya, C.; Gehrmann, E. J.; Mahoney, K. M.; Goswami, P. P.; Albright, T. R.; Syed, A.; Dutton, A. S.; Smith, E. A.; Winter, A. H. Family of BODIPY Photocages Cleaved by Single Photons of Visible/Near-Infrared Light. J. Am. Chem. Soc. 2018, 140 (23), 7343–7346. https://doi.org/10.1021/jacs.8b04040.

(25) Goswami, P. P.; Syed, A.; Beck, C. L.; Albright, T. R.; Mahoney, K. M.; Unash, R.; Smith, E. A.; Winter, A. H. BODIPY-Derived Photoremovable Protecting Groups Unmasked with Green Light. J. Am. Chem. Soc. 2015, 137 (11), 3783–3786. https://doi.org/10.1021/jacs.5b01297.

(26) Slanina, T.; Shrestha, P.; Palao, E.; Kand, D.; Peterson, J. A.; Dutton, A. S.; Rubinstein, N.; Weinstain, R.; Winter, A. H.; Klán, P. In Search of the Perfect Photocage: Structure–Reactivity Relationships in Meso -Methyl BODIPY Photoremovable Protecting Groups. J. Am. Chem. Soc. 2017, 139 (42), 15168–15175. https://doi.org/10.1021/jacs.7b08532.

(27) McRobb, F. M.; Crosby, I. T.; Yuriev, E.; Lane, J. R.; Capuano, B. Homobivalent Ligands of the Atypical Antipsychotic Clozapine: Design, Synthesis, and Pharmacological Evaluation. J. Med. Chem. 2012, 55 (4), 1622–1634. https://doi.org/10.1021/jm201420s.

(28) Shrestha, P.; Dissanayake, K. C.; Gehrmann, E. J.; Wijesooriya, C. S.; Mukhopadhyay, A.; Smith, E. A.; Winter, A. H. Efficient Far-Red/Near-IR Absorbing BODIPY Photocages by Blocking Unproductive Conical Intersections. Journal of the American Chemical Society 2020, 142 (36), 15505–15512. https://doi.org/10.1021/JACS.0C07139/ASSET/IMAGES/LARGE/JA0C07139_0007.JPEG.

(29) Caplow, M. Kinetics of Carbamate Formation and Breakdown. Journal of the American Chemical Society 1968, 90 (24), 6795–6803. https://doi.org/10.1021/JA01026A041/ASSET/JA01026A041.FP.PNG_V03.

(30) Peterson, J. A.; Wijesooriya, C.; Gehrmann, E. J.; Mahoney, K. M.; Goswami, P. P.; Albright, T. R.; Syed, A.; Dutton, A. S.; Smith, E. A.; Winter, A. H. Family of BODIPY Photocages Cleaved by Single Photons of Visible/Near-Infrared Light. Journal of the American Chemical Society 2018, 140 (23), 7343–7346. https://doi.org/10.1021/jacs.8b04040.

(31) Freedman, N.; research, R. L.-R. progress in hormone; 1996, undefined. Desensitization of G Protein-Coupled Receptors. europepmc.org.

(32) Kroeze, W. K.; Sassano, M. F.; Huang, X.-P.; Lansu, K.; McCorvy, J. D.; Giguère, P. M.; Sciaky, N.; Roth, B. L. PRESTO-Tango as an Open-Source Resource for Interrogation of the Druggable Human GPCRome. Nat Struct Mol Biol 2015, 22 (5), 362–369. https://doi.org/10.1038/nsmb.3014.

(33) Dana, H.; Mohar, B.; Sun, Y.; Narayan, S.; Gordus, A.; Hasseman, J. P.; Tsegaye, G.; Holt, G. T.; Hu, A.; Walpita, D.; Patel, R.; Macklin, J. J.; Bargmann, C. I.; Ahrens, M. B.; Schreiter, E. R.; Jayaraman, V.; Looger, L. L.; Svoboda, K.; Kim, D. S. Sensitive Red Protein Calcium Indicators for Imaging Neural Activity. eLife 2016, 5, e12727. https://doi.org/10.7554/eLife.12727.

5 Progress toward the synthesis of dihydrolysergic acid

5.1 Introduction

Animal behavior is largely mediated by a complex cascade of effects ultimately initiated by neurotransmitter regulation.[1] Elucidating the activity of neural proteins in response to neurotransmitter binding and transport is commonly thought to be key in our ability to define the circuits that mediate downstream behavioral effects. However, the path connecting neurotransmitter regulation, cell specific protein activity, and downstream behavioral effects is largely unknown due to a lack of cell specific pharmacological studies.[1] Elucidation of this connection has potential to profoundly impact the development of treatments for a number of neuropsychiatric disorders[2], one such example being major depressive disorder (MDD). Despite the prevalence (16%)[3] of MDD, the molecular mechanisms that cause the disorder have remained unclear for quite some time. Large scale proteomic studies have been conducted to identify proteins related to MDD.[4–7] However, due to broad expression of these biomarkers, it is difficult to causally link protein dysregulation to behavioral changes.[2]

This work aims to combat this issue by spatially affixing modular probes to the membrane of targeted cells as a method of observing cell specific protein activity of receptors that are broadly expressed in several cell lines. The system will consist of a probe covalently coupled to a flexible polymer linker, which can then be attached to the surface of the cell either enzymatically or chemically.

The first step in the development of this system is to synthesize several serotonin receptor agonists to act as probes. The targets currently being pursued are derivatives

of the ergot alkaloid family.[8,9] The ergoline core contains the same structural features as several native neurotransmitters, and as such, numerous derivatives are used for the treatment of neurological disorders. As a result, studies to efficiently synthesize derivatives of the ergoline core have occurred extensively for decades.[10] Given the history of neurological disorder treatment with ergoline scaffold derivatives and the existence of multiple synthetic routes to access these derivatives, probes derived from an ergoline core would likely be both synthetically attainable and biologically active. Here, progress toward the synthesis of the first ergoline scaffold dihydrolysergic acid is disclosed.

5.2 Synthesis

Two avenues are currently being pursued to synthesize dihydrolysergic acid derivatives. Initial efforts focused on replicating a synthesis by Boger *et al.*,[10] which involves a total of 13 linear steps to synthesize tricyclic ketone **14**, and 18 linear steps to synthesize dihydrolysergic acid. Development of a novel route to synthesize a close derivative of tricyclic ketone **14** (tricyclic ketone **17**) in six linear steps, utilizing the same starting material, is also being explored.

Both routes allow for late-stage derivatization of the **D** ring via an inverse electron demand Diels-Alder reaction. This work has been briefly explored by Boger and coworkers, and we plan to further explore the promiscuity of this substrate as a means of creating a library of LSA derivatives.

5.2.1 Boger's preparation of dihydrolysergic acid

Thus far work has progressed toward a stable intermediate, tricyclic ketone **14**. Beginning with benzoic acid **1**, the starting material (SM) is reduced with borane-tetrahydrofuran complex to produce benzyl alcohol **2**. The nitro group of **2** is then reduced via treatment with iron powder in acetic acid/ethanol (1:1 v/v), to afford amine **3**. Bis-acetylation of the amine and alcohol followed by *o*-methanolysis affords the *N*-acetyl benzyl alcohol, **4**.

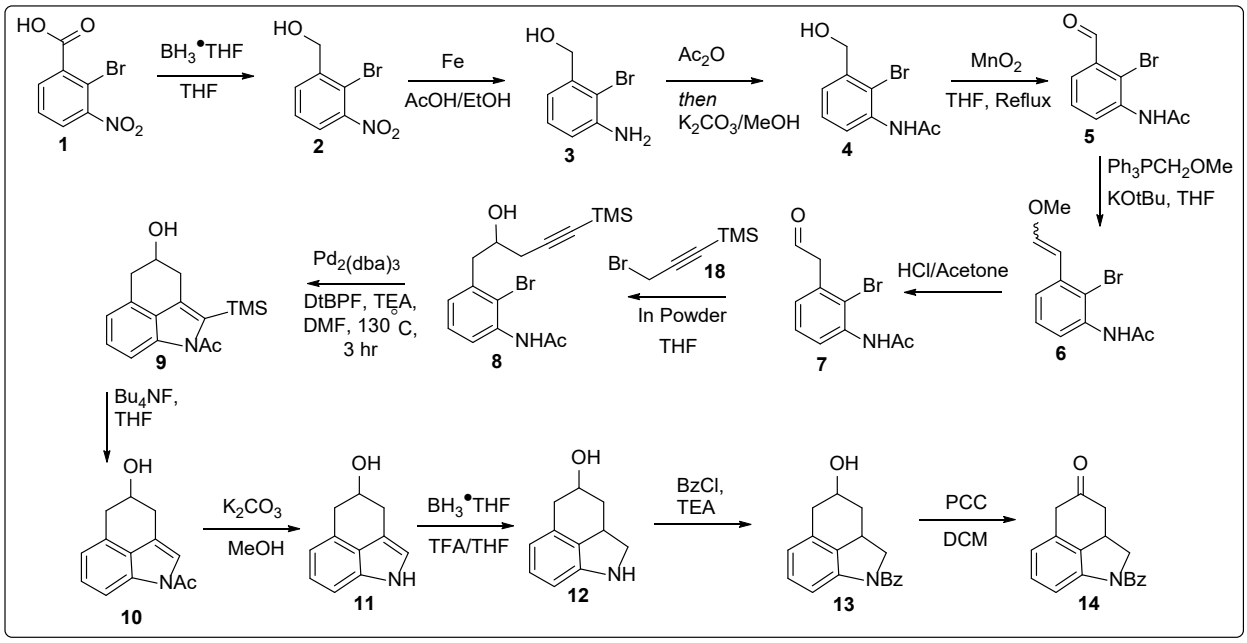

Scheme 5. Boger's preparation of tricyclic ketone 14.[10]

Oxidation of benzyl alcohol, **4**, with manganese dioxide required a divergence from Boger's protocol. At room temperature (RT), conversion was significantly slower than reported in Boger's experimental (>3 days RT, SM not fully consumed). At reflux in THF, **4** was fully consumed in 2 hours with quantitative yield, to afford benzaldehyde **5.**

Treatment of methoxymethyl-triphenylphosphine with potassium tert-butoxide then benzaldehyde **5** resulted in the Wittig olefination products (E/Z), **6**. Subsequent methanolysis of the methyl ether with 6N hydrochloric acid in acetone cleanly affords aldehyde **7**. Propargyl bromide, **18**, is treated with indium powder in THF to generate the indium Grignard reagent in situ. A solution of aldehyde **7** is then added to afford homopropargylic alcohol, **8**. A palladium catalyzed cascade reaction is then carried out using tris(dibenzylideneacetone)dipalladium(0) ($Pd_2(dba)_3$) with 1,1′-bis(di-tert-butylphosphino)ferrocene (DtBPF) as an added ligand to afford tricyclic alcohol, **9**.

Work is currently being done to carry forward this synthesis and generate tricyclic ketone **14**, which will then be used to create dihydrolysergic acid and supply starting material for studies toward **D** ring analogs.

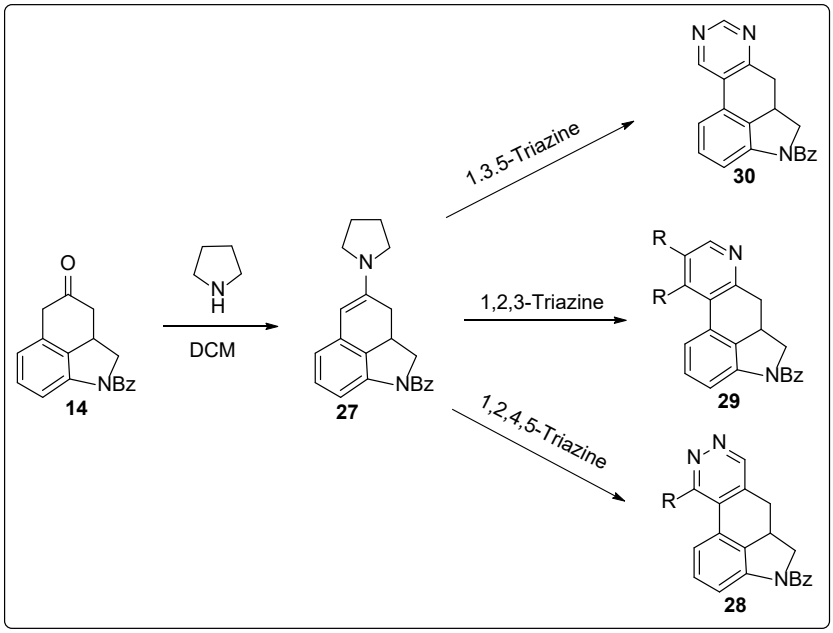

Scheme 6. Proposed derivatization of D ring.

5.2.2 Studies toward a novel synthesis of dihydrolysergic acid

Current studies aimed at creating a shorter synthesis of tricyclic ketone **14** have led to an adoption of the Boger starting material to generate a close analog of **14** in 6 linear steps. The key step in generation of tricyclic ketone **17** is a three part one-pot Pd catalyzed cascade reaction between benzyl stannane, **16**, and homopropargylic acyl chloride, **19**. The theory behind controlling the regiochemistry of Pd coupling is a combination of reagent design and reaction mixture additives. In terms of reagent design, the high reactivity of the acyl chloride paired with the benzyl stannane should favor a Stille coupling between the two reagents rather than a coupling of two aryl species via the ortho-bromine. As for reaction mixture additives, it is proposed that the cascade Heck reaction can be staved off by allowing the reaction mixture to be heated for some time prior to the addition of base. At which point the aryl bromide and alkyne can couple, leading to a cascade formation of tricyclic ketone, **17**.

From the established Boger preparation,[10] we have produced *N*-acetyl benzyl alcohol, **4**, from benzoic acid **1**. It is proposed that the benzyl alcohol can then be brominated with phosphorous tribromide in DCM[11] to afford benzyl bromide **15**. The benzyl bromide **15** can then undergo stannation to afford benzyl stannane, **16**. This transformation has been demonstrated on a number of similar substrates by Tagliavini et al.[12]

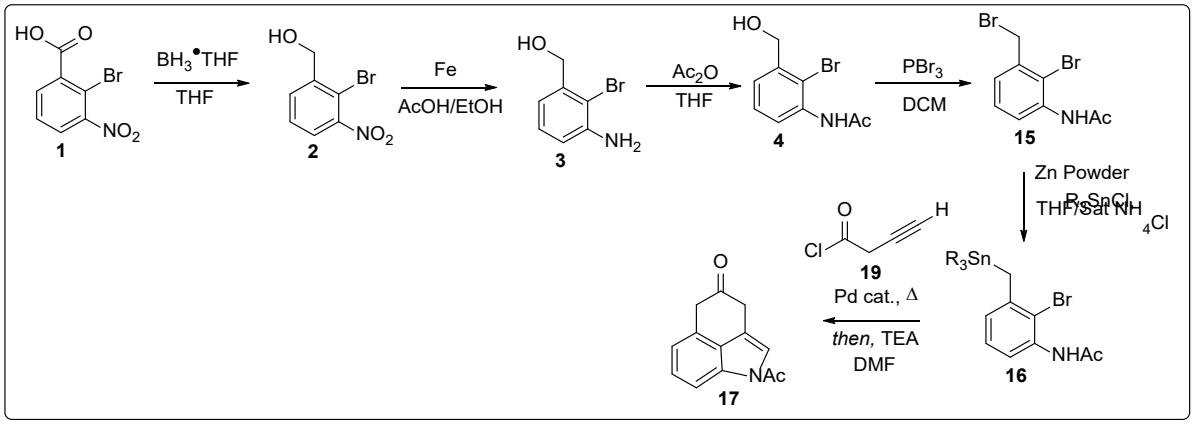

*Scheme 7. Proposed synthesis of tricyclic ketone **17**.*

Preparation of homopropargylic acyl chloride, **19**, from propargyl bromide is a straightforward two step synthesis. Propargyl bromide is able to form majority alkyne (85:15 alkyne:allene) Grignard reagent under Hg-Mg amalgam conditions.[13] Upon treatment with excess CO_2, the corresponding homopropargyl carboxylic acid, **26,** is formed in 34% yield. Once benzyl stannane **16** is prepared, **26** can be converted to the corresponding acyl chloride via treatment with oxalyl chloride,[14] to afford **19**.

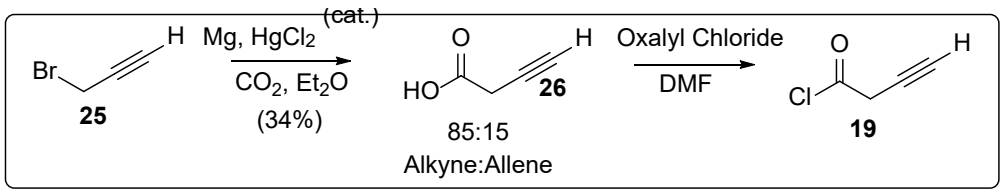

Scheme 8. Preparation of homopropargyl carboxylic acid 19.

Recent studies have focused on screening reaction conditions for the key palladium catalyzed cyclization of **16**. Initially a number of Pd(0), Pd(II) and

palladacycle catalysts were screened without additives. The major product formed was a biaryl system likely due to homocoupling of the stannane. Studies to observe the effect of additives, and catalyst reapplication have recently begun. A brief summary of screened conditions is shown below.

Catalyst	***Ligand***	***Base***	***Result***
$Pd_2(dba)_3$ $CHCl_3$	XPhos (30 mol%)	K_2CO_3 (2.0 eq)	No product formed
$Pd(dba)_2$	XPhos (30 mol%)	K_2CO_3 (2.0 eq)	No product formed
$PdACN_2Cl_2$	XPhos (30 mol%)	K_2CO_3 (2.0 eq)	No product formed
$Pd(PPh_3)_2Cl_2$	XPhos (30 mol%)	K_2CO_3 (2.0 eq)	No product formed
$PdCl_2$	XPhos (30 mol%)	K_2CO_3 (2.0 eq)	No product formed
XPhos Pd (G1)	NONE	K_2CO_3 (2.0 eq)	No product formed
XPhos Pd (G2)	NONE	K_2CO_3 (2.0 eq)	No product formed
JackiePhos Pd (G3)	NONE	K_2CO_3 (2.0 eq)	No product formed
tBuBrettPhos (G3)	NONE	K_2CO_3 (2.0 eq)	No product formed
tBuXPhos	NONE	K_2CO_3 (2.0 eq)	No product formed

Table 3. Screened Pd coupling conditions.

Previously, other avenues were explored as attempts to generate **16** as an aryl iodide rather than an aryl bromide. Initial studies attempted to convert the inexpensive starting material of *m*-toluidine to 2-iodo-3-methylaniline via directed ortho iodination using IPy_2BF_4 (Barluenga's reagent). Barluenga's reagent has been shown to iodinate ortho to electron rich groups in a number of cases[15–17]. However, the desired ortho-

iodination was not observed for either m-toluidine or the N-acetyl derivative under neutral or acidic conditions. The possibility of directed ortho metalation/iodination was considered, but the steps added due to introducing temporary directing groups pushed my thinking toward a new starting material.

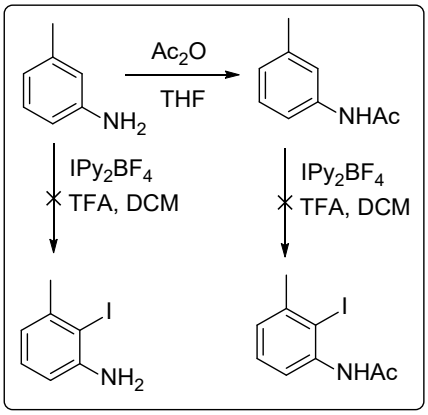

Scheme 9. Failed ortho iodination.

A Sandmeyer iodination of 2-methyl-6-nitroaniline has been shown to afford the ortho iodination product[18]. So, a new synthetic route to aryl iodide **24** was developed, as shown in Scheme 10, below. The Sandmeyer iodination of **20** proceeded smoothly to afford aryl iodide **21** in a 93% yield. Reduction of the nitro group and N-acylation also proceeded without issue. However, the benzyl bromide would not form after a three-day reflux with NBS (3.5 eq) and AIBN (15 mol%) in carbon tetrachloride. It is proposed that the steric bulk of the iodine ortho to the benzylic position is preventing bromination, and as a result aryl bromides are being pursued as potential starting material for the Pd catalyzed cascade reaction.

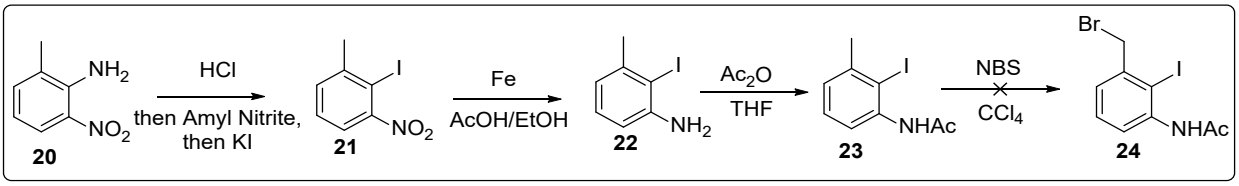

Scheme 10. Failed synthesis of aryl iodide 24.

5.3 Conclusion

Two avenues are currently being pursued to synthesize dihydrolysergic acid derivatives. An established synthesis by Boger et al.,[10] which involves a total of 13 linear steps to synthesize a stable tricyclic ketone intermediate, and 18 linear steps to synthesize dihydrolysergic acid is progressing toward a family of derivatized D-ring analogs. Development of a novel route to synthesize a close derivative of the stable tricyclic ketone intermediate in six linear steps, utilizing the same starting material as Boger, is also being explored. Current efforts toward the novel synthesis are focusing on the optimization of a key palladium catalyzed cascade coupling reaction, where conditions must initially favor an intermolecular Stille coupling then shift to efficiently catalyze an intramolecular Heck/Larock coupling. Future work will proceed to develop a small library of D-ring analogs via IEDDA reaction and test the library for bioactivity and photoactivity against neuroreceptors.

5.4 Experimental

General Information: Chemicals were purchased from Acros Organics and used without further purification. All reactions were performed under anhydrous conditions unless otherwise stated. All reactions were monitored by TLC on Kieselgel 60 F_{254} (EMD). Detection was performed by examination under UV light (254 nm). Flash chromatography was performed using a Biotage Isolera One equipped with SNAP Ultra columns. Proton nuclear magnetic resonance spectra (^{1}H-NMR) were recorded at 400 MHz at 20 ºC using a Bruker Avance III HD 400 MHz NMR.

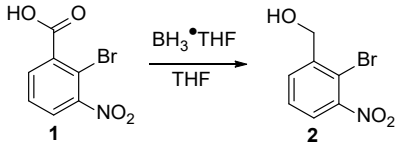

(2-bromo-3-nitrophenyl)methanol (2)

Following an adapted procedure developed by Boger et al.[1] A solution of benzoic acid **1** (9.0531 g, 36.8 mmol, 1.0 eq) in THF (92 mL) is to be chilled to 0 °C and slowly treated with BH_3THF (73.60 mL, 1M in THF, 2.0 eq). Remove the ice bath and stir at room temperature for 24 hours. Quench with 1N NaOH/Sat $NaHCO_3$, dilute and extract with EtOAc, dry with $MgSO_4$, concentrate in vacuo. Product is isolated as a yellow powder, 97% yield. ^{1}H NMR (400 MHz, $CDCl_3$): 7.77 (d, J=8.0 Hz, 1H), 7.67 (d, J=6.8, 1H), 7.49 (t, J=8.0 Hz, 1H), 4.85 (s, 2H), 2.17 (brs, 1H).

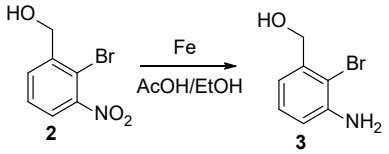

2-bromo-3-methoxyaniline (3)

Following an adapted procedure developed by Boger et al.[1] Benzyl alcohol **2** (8.319 g, 35.9 mmol, 1.0 eq) is to be dissolved in EtOH:AcOH mixture (92 mL, 1:1, v:v) and concentrated HCl (4.5 mL) is to be added. Iron powder (8.019 g, 143.6 mmol, 4.0 eq) is the be added and the reaction mixture is to be heated to reflux for 3 hours. Once cool, quench with 1N NaOH/Sat $NaHCO_3$, extract with Et_2O, dry with $MgSO_4$, concentrate in vacuo. Product is isolated as a yellow powder, 99% yield. 1H NMR (400 MHz, Acetone-d6): 7.07 (t, J=8.0 Hz, 1H), 8.86 (d, J=7.6 Hz, 1H), 6.77 (d, J=8 Hz, 1H), 4.90 (brs, 2H), 4.61 (d, J=6.0 Hz, 2H), 4.27 (t, J=6.0 Hz, 1H).

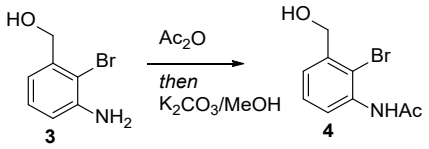

(3-Acetylamino-2-bromophenyl)methanol (4)

Following a procedure developed by Boger et al.[1] Product is isolated as a white powder, 79% yield. 1H NMR (400 MHz, Acetone-d6): 8.49 (s, 1H), 7.94 (d, J=7.2 Hz, 1H), 7.38 (t, J=6.0 Hz, 1H), 7.34 (d, J=7.6 Hz, 1 H), 4.67 (d, J=6.0 Hz, 2H), 4.48 (t, J=6.0 Hz, 1 H)

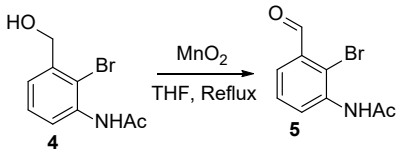

N-(2-Bromo-3-formylphenyl)acetamide (5)

Following an adapted procedure developed by Boger et al.[1]. Benzyl alcohol **4** is to be dissolved in THF and MnO2 is to be added. The resulting heterogenous mixture is to be heated to reflux for 2 hours. The reaction mixture is to be filtered through a pad of celite, eluting with Et2O, and concentrated in vacuo. Product is isolated as a white powder, 94% yield. 1H NMR (400 MHz, Acetone-d6): 10.34 (s, 1H), 8.79 (brs, 1H), 8.39 (d, J=6.0 Hz, 1H), 7.67 (dd, J=8.0 Hz, 1H), 7.51 (t, J=6.0 Hz, 1H), 2.23 (s, 3H).

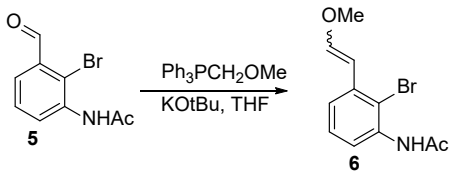

(E,Z)-N-(2-Bromo-3-(2-methoxyvinyl)phenyl)acetamide (6)

Following a procedure developed by Boger et al.[1]. Product is isolated as a white powder, 64% yield. 1H NMR (400 MHz, $CDCl_3$): 7.96 (t, J=8 Hz, 1H), 7.79 (s, 1H), 7.11 (t, J=6.0 Hz, 1H), 7.02 (d, J=7.6 Hz, 1H), 6.89 (d, J=12.8 Hz, 1H), 6.00 (d, J=12.8 Hz, 1H), 3.66 (s, 3H), 2.15 (s, 3H).

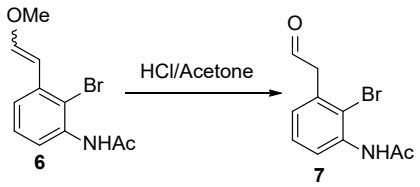

N-(2-Bromo-3-(2-acyl)phenyl)acetamide (7)

Following a procedure developed by Boger et al.[10]. Product is isolated as a white powder, 99% yield. 1H NMR (400 MHz, $CDCl_3$): 9.74 (t, J=1.6 Hz, 1H), 8.30 (d, J=8.0 Hz, 1H), 7.68 (s, 1H), 7.33 (t, J=8.0 Hz, 1H), 7.01 (d, J=6.8 Hz, 1H), 3.89 (d, J=1.6 Hz, 2H), 2.25 (s, 3H).

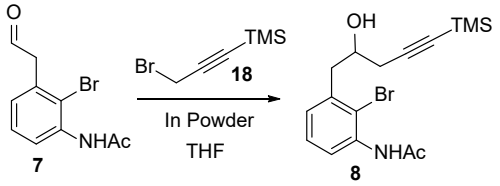

N-(2-Bromo-3-(2-hydroxy-5-(trimethylsilyl)pent-4-yn-1-yl) phenyl)acetamide (8)

Following a procedure developed by Boger et al.[10]. Product is isolated as a white powder, 64% yield. 1H NMR (400 MHz, $CDCl_3$): 8.21 (d, J=8.0 Hz, 1H), 7.70 (s, 1H), 7.19-7.34 (m, 1H), 7.06 (d, J=7.2 Hz, 1H), 4.06 (t, J=6.4 Hz, 1H), 3.12 (dd, J=13.4, 4.8 Hz, 1H), 2.96 (dd, J=13.8, 7.8 Hz, 1H), 2.52 (dd, J=16.8, 5.4 Hz, 1H), 2.45 (dd, J=16.8, 6.0 Hz, 1H), 2.24 (s, 3H), 0.18 (s, 9H).

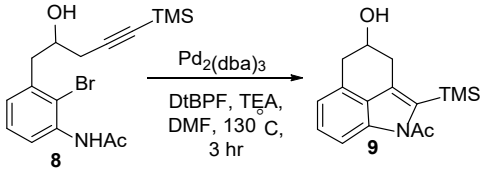

1-(4-Hydroxy-2-(trimethylsilyl)-4,5-dihydrobenzo[cd]indol- 1(3H)-yl)ethan-1-one (9).

Following a procedure developed by Boger et al.[10]. Product is isolated as a tan brown oil, 53% yield. 1H NMR (400 MHz, $CDCl_3$) 7.41 (d, J=8.0 Hz, 1H), 7.27 (t, J=7.6 Hz, 1H), 7.02 (d, J=7.2 Hz, 1H), 4.39 (d, J=7.6 Hz, 1H), 3.22 (dd, J=16.0, 4.0 Hz, 1H), 3.14 (d, J=14.8 Hz, 1H), 3.00 (d, J=7.2 Hz 1H), 2.97 (d, J=8.0 Hz, 1H), 2.77 (s, 3H), 2.07 (d, J=4.8 Hz, 1H), 0.36 (s, 9H).

Experimental Procedure – 5-Azidotryptamine Preparation

2-(5-nitro-1H-indol-3-yl)-2-oxoacetamide

Following a procedure developed by O'Connor et al.[2]. Product is isolated as a yellow powder, 64% yield. 1H NMR (400 MHz, $CDCl_3$) 12.75 (brs, 2H), 9.07 (d, J=2.4 Hz, 1H), 8.93 (s, 1H), 8.17 (d, J=2.4 Hz, 1H), 8.14 (d, J=2.4 Hz, 1H), 7.84 (s, 1H), 7.74 (d, J=8.4, 1H).

5.5 References

(1) Monteggia, L. M. Put Therapies First. **2014**, 4–5.

(2) Shields, B. C.; Kahuno, E.; Kim, C.; Apostolides, P. F.; Brown, J.; Lindo, S.; Mensh, B. D.; Dudman, J. T.; Lavis, L. D.; Tadross, M. R. Deconstructing Behavioral Neuropharmacology with Cellular Specificity. *Science (80-.).* **2017**.

(3) Kessler, R. C.; Berglund, P.; Demler, O.; Jin, R.; Koretz, D.; Merikangas, K. R.; Rush, A. J.; Walters, E. E.; Wang, P. S. The Epidemiology of Major Depressive Disorder. *J. Am. Med. Assoc.* **2003**, *289* (23), 3095–3105.

(4) Huang, T. L.; Lin, C. C. Advances in Biomarkers of Major Depressive Disorder. In *Advances in Clinical Chemistry*; **2015.**

(5) Zheng, P.; Wang, Y.; Chen, L.; Yang, D.; Meng, H.; Zhou, D.; Zhong, J.; Lei, Y.; Melgiri, N. D.; Xie, P. Identification and Validation of Urinary Metabolite Biomarkers for Major Depressive Disorder. *Mol. Cell. Proteomics* **2013**.

(6) Bot, M.; Chan, M. K.; Jansen, R.; Lamers, F.; Vogelzangs, N.; Steiner, J.; Leweke, F. M.; Rothermundt, M.; Cooper, J.; Bahn, S.; et al. Serum Proteomic Profiling of Major Depressive Disorder. *Transl. Psychiatry* **2015**, *5* (7), e599-9.

(7) Martins-de-Souza, D. Proteomics, Metabolomics, and Protein Interactomics in the Characterization of the Molecular Features of Major Depressive Disorder. *Dialogues Clin. Neurosci.* **2014**.

(8) De Costa, C. St Anthony's Fire and Living Ligatures: A Short History of Ergometrine. *Lancet* **2002**, *359* (9319), 1768–1770.

(9) Schneider, H. R.; Stadler, P. A.; Stütz, P.; Troxler, F.; Seres, J. Synthesis and Properties of Bromocriptine. *Experientia* **1977**, *33* (11), 1412–1413.

(10) Lee, K.; Poudel, Y. B.; Glinkerman, C. M.; Boger, D. L. Total Synthesis of Dihydrolysergic Acid and Dihydrolysergol: Development of a Divergent Synthetic Strategy Applicable to Rapid Assembly of D-Ring Analogs. *Tetrahedron* **2015**, *71* (35), 5897–5905.

(11) Božinović, N.; Opsenica, I.; Šolaja, B. A. Double Palladium-Catalyzed Synthesis

of Azepines. *Synlett* **2013**, *24* (1), 49–52.

(12) Marton, D.; Russo, U.; Stivanello, D.; Tagliavini, G.; Ganis, P.; Valle, G. C. Preparation of Benzylstannanes by Zinc-Mediated Coupling of Benzyl Bromides with Organotin Derivatives. Physicochemical Characterization and Crystal Structures. *Organometallics* **1996**, *15* (6), 1645–1650.

(13) Romanov-michailidis, F.; Guønøe, L.; Alexakis, A. Enantioselective Organocatalytic Fluorination-Induced Wagner – Meerwein Rearrangement. *Angewandte* **2013**, *0905* (200020), 9266–9270.

(14) Keane, H. A.; Hess, W.; Burton, J. W. Manganese(III)-Mediated Radical Cyclisations for the (Z)-Selective Synthesis of Exo-Alkylidene Pyrrolidinones and Pyrrolidines. *Chem. Commun.* **2012**, *48* (52), 6496–6498.

(15) Sarkar, S.; Jana, M.; Narender, T. Metal-Free Directed Ortho C-H Iodination: Synthesis of 2'-Iodobiaryl-2- Carbonitriles. *European J. Org. Chem.* **2013**, No. 29, 6491–6495.

(16) Ezquerra, J.; Pedregal, C.; Lamas, C.; Barluenga, J.; Pérez, M.; García-Martín, M. A.; González, J. M. Efficient Reagents for the Synthesis of 5-, 7-, and 5,7-Substituted Indoles Starting from Aromatic Amines: Scope and Limitations. *J. Org. Chem.* **1996**, *61* (17), 5804–5812.

(17) Praveen, C.; Perumal, P. T. Revisiting the Gold-Catalyzed Dimerization of 2-Ethynylanilines: A Room-Temperature and Silver-Free Protocol for the Synthesis of Multifunctional Quinolines. *Synth.* **2016**, *48* (6), 855–864.

(18) Gillespie, K. M.; Sanders, C. J.; O'Shaughnessy, P.; Westmoreland, I.; Thickitt, C. P.; Scott, P. Enantioselective Aziridination Using Copper Complexes of Biaryl Schiff Bases. *J. Org. Chem.* **2002**, *67* (10), 3450–3458.

(19) Friedrich, A.; Bräse, S.; O'Connor, S. E. Synthesis of 4-, 5-, 6-, and 7-Azidotryptamines. *Tetrahedron Lett.* **2009**, *50* (1), 75–76.

6 Conclusion

The field of neuroscience is rapidly evolving and so, the development of novel tools that support innovative research is urgently needed. Here, we have demonstrated (1) The development and application of photoactivatable forms of WAY-161503 and NDMC, designed as a system to allow spectrally multiplexed, spatiotemporal control of 5-HT_{2C} calcium signaling and (2) The design and use of bioactive photoaffinity probes for DRD2, which demonstrated excellent activity in “workhorse” biochemical assays, receptor labeling, and cell labeling, and chemoproteomics. The advancements of these technologies demonstrate an important step forward for optical electrophysiology, where modulation of endogenous neuroreceptors has proven to be a challenge, and for ABPP, where underrepresentation of low-abundance and unstable proteins has limited the scope of advancements in the field of proteomics. Future work will continue to develop neuroreceptor targeted photoactive probes, with LSA derivatives providing an initial family of targets that are both synthetically interesting and biologically important to the fields of neuroscience, chemical biology, and medicinal chemistry.

7 Appendix A: NMR spectra

7.1 Chapter 3: Photoaffinity Probes for DRD2

NMR Spectra begin on the following page.

STK_Probe 3_C1F22-E

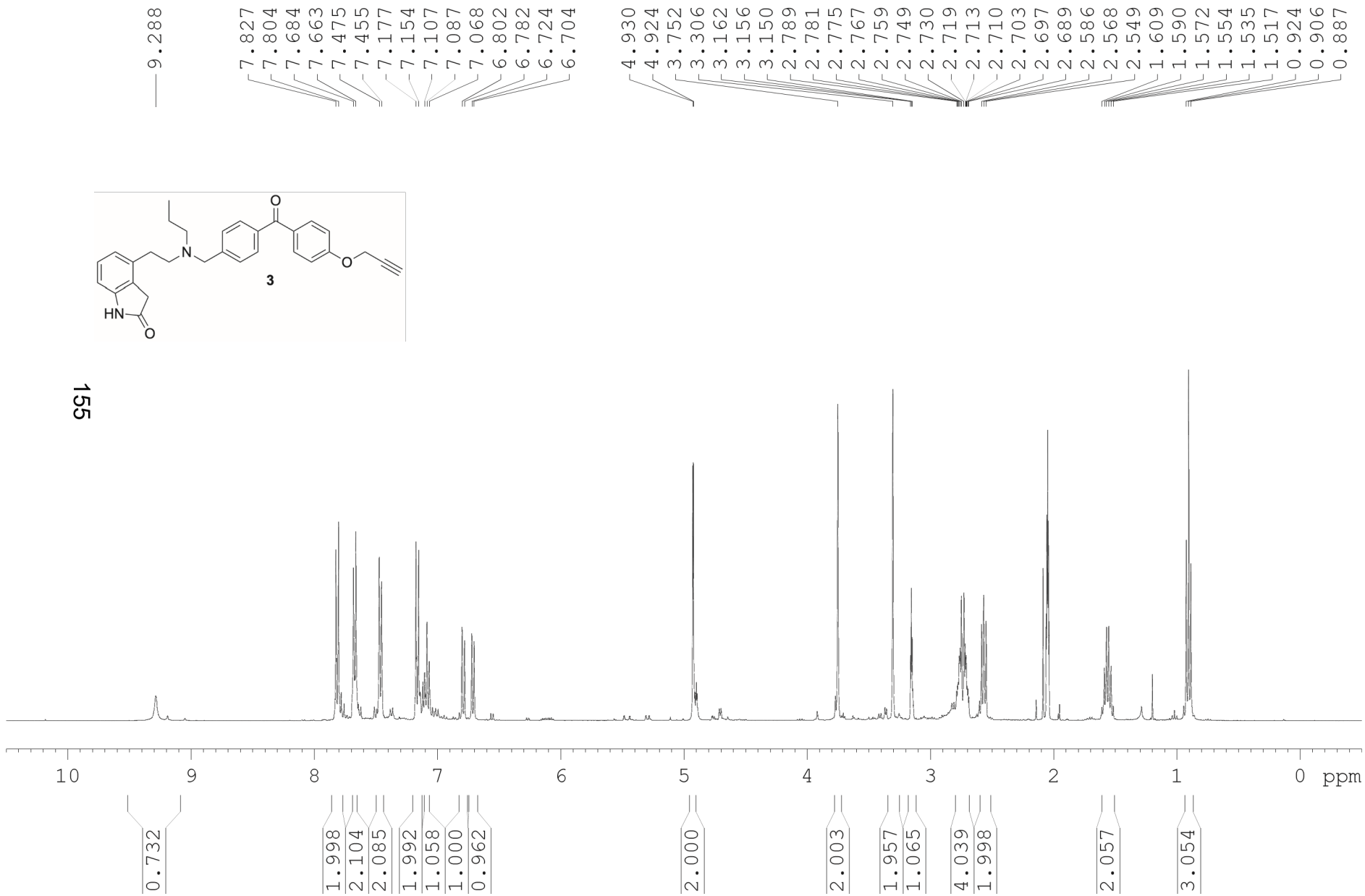

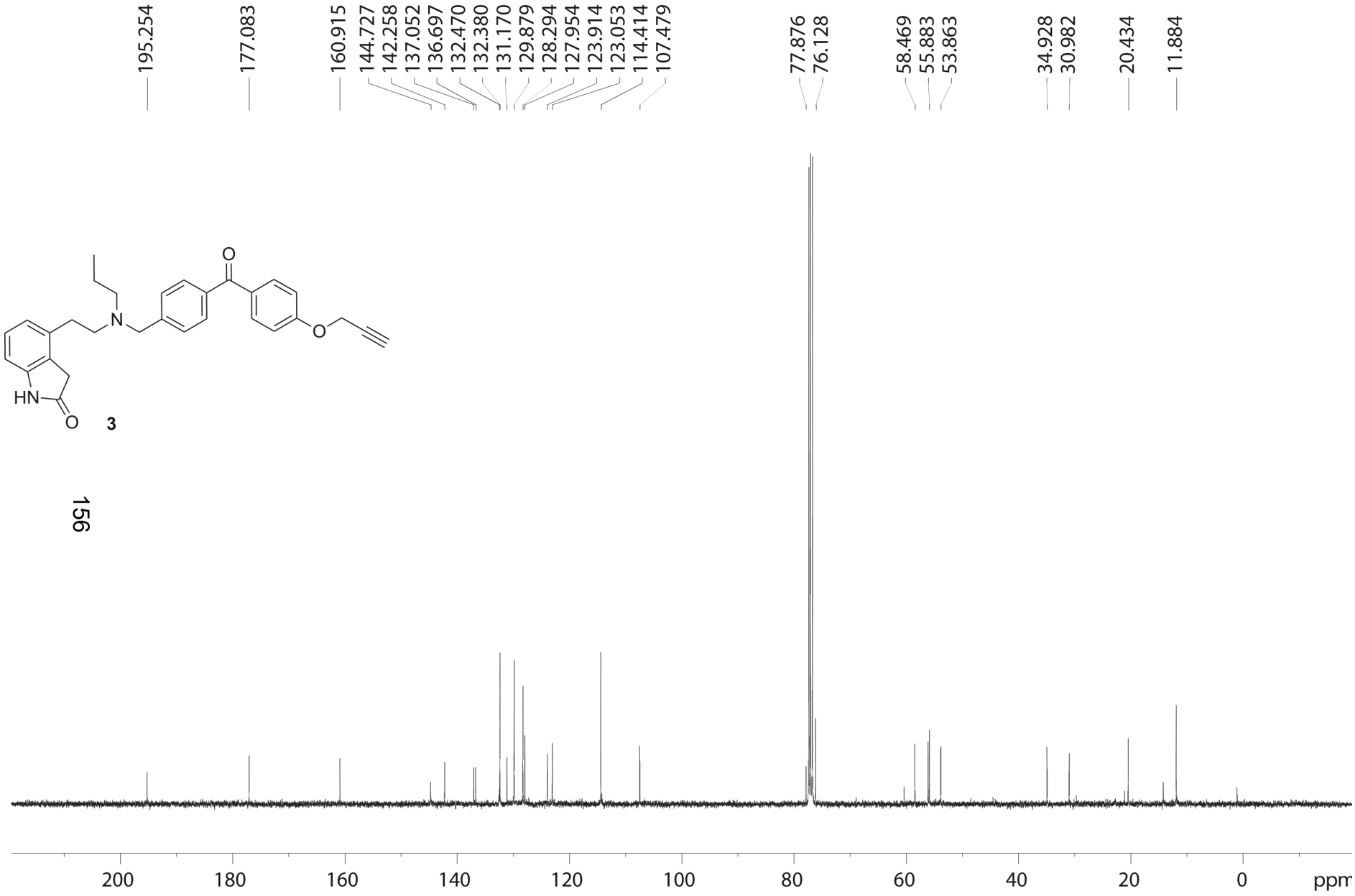
195.254
177.083
160.915
144.727
142.258
137.052
136.697
132.470
132.380
131.170
129.879
128.294
127.954
123.914
123.053
114.414
107.479
77.876
76.128
58.469
55.883
53.863
34.928
30.982
20.434
11.884
HN
O
N
O
O
3
200
180
160
140
120
100
80
60
40
20
0
ppm

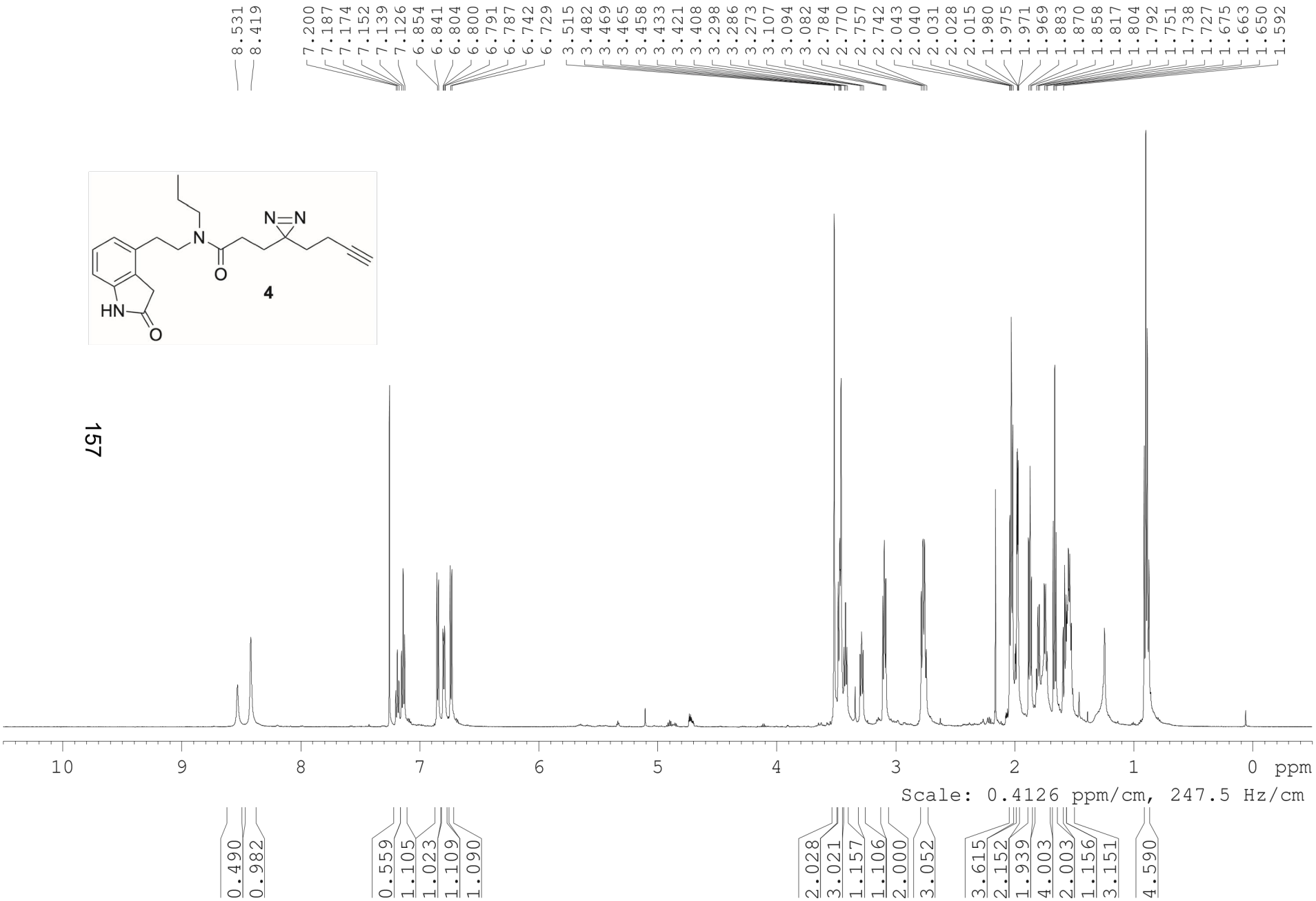
8.531
8.419
7.200
7.187
7.174
7.152
7.139
7.126
6.854
6.841
6.804
6.800
6.791
6.787
6.742
6.729
3.515
3.482
3.469
3.465
3.458
3.433
3.421
3.408
3.298
3.286
3.273
3.107
3.094
3.082
2.784
2.770
2.757
2.742
2.043
2.040
2.031
2.028
2.015
1.980
1.975
1.971
1.969
1.883
1.870
1.858
1.817
1.804
1.792
1.751
1.738
1.727
1.675
1.663
1.650
1.592
N
N
O
HN
O
4
10
9
8
7
6
5
4
3
2
1
0 ppm
Scale: 0.4126 ppm/cm, 247.5 Hz/cm
0.490
0.982
0.559
1.105
1.023
1.109
1.090
2.028
3.021
1.157
1.106
2.000
3.052
3.615
2.152
1.939
4.003
2.003
1.156
3.151
4.590

ppm
10
20
30
40
50
60
70
80
90
100
110
120
130
140
150
160
170
180
190
200
11.351
11.488
13.417
20.971
22.340
26.659
26.945
27.954
28.036
28.107
31.345
32.504
32.646
32.693
34.930
35.065
38.788
46.788
47.705
47.794
50.200
69.252
77.338
82.910
108.002
108.541
122.858
122.903
124.141
124.369
128.239
128.695
134.631
135.635
142.595
142.939
170.725
170.898
176.941
177.396
4
HN
O
N
O
N
N

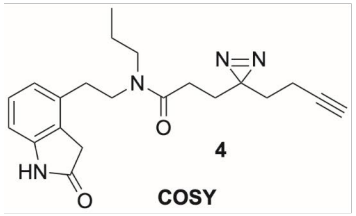

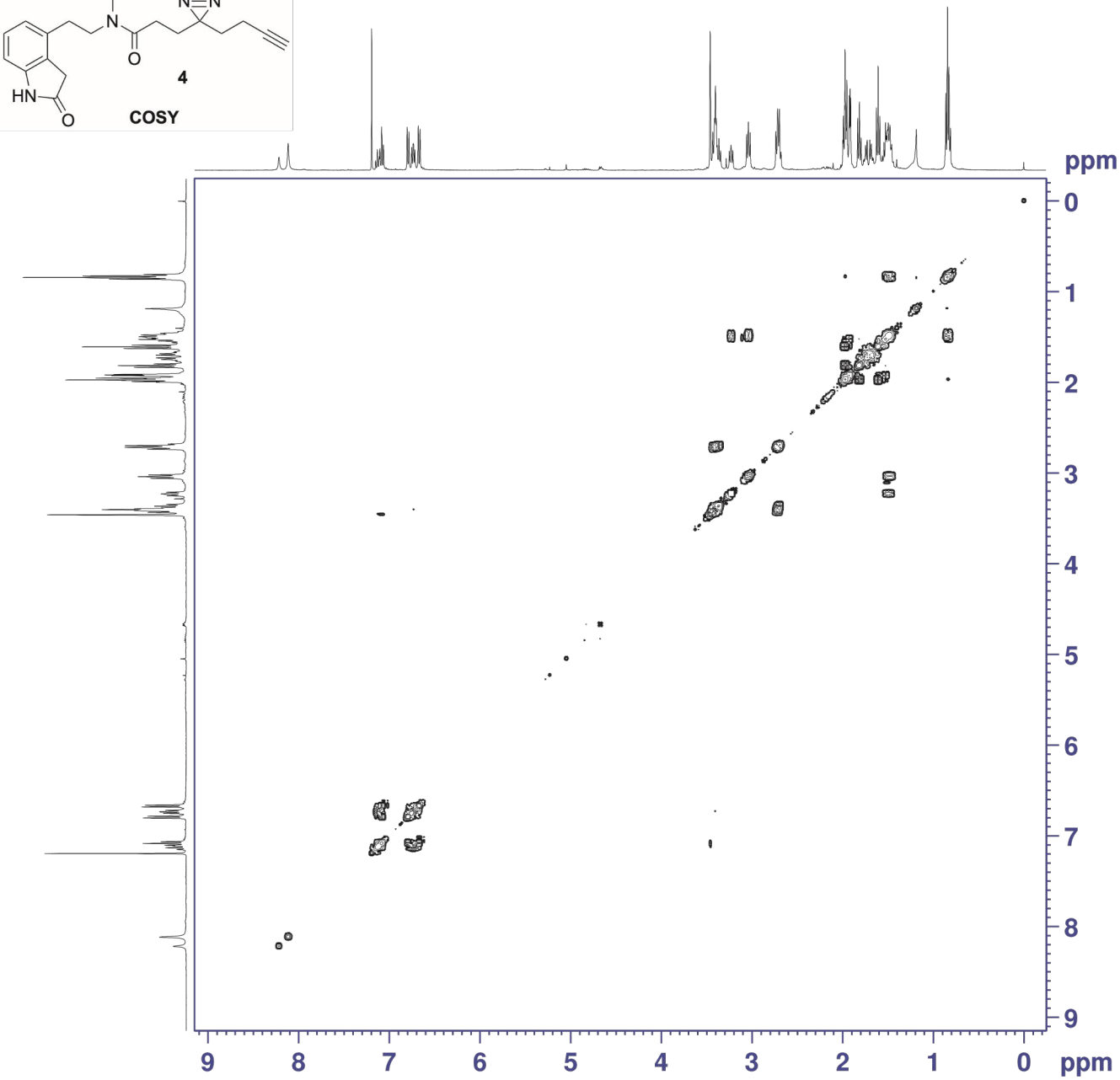


```
Current Data Parameters
NAME          cmpd 4 cosy
EXPNO                   4
PROCNO                  1

F2 - Acquisition Parameters
Date_            20220825
Time                18.10 h
INSTRUM             spect
PROBHD   Z116098_0203 (
PULPROG       cosygpppqf
TD                   2048
SOLVENT             CDCl3
NS                      1
DS                     16
SWH              3759.398 Hz
FIDRES           3.671288 Hz
AQ              0.2723840 sec
RG                  66.01
DW                133.000 usec
DE                   6.50 usec
TE                  298.0 K
D0            0.00000300 sec
D1            1.92463398 sec
D11           0.03000000 sec
D12           0.00002000 sec
D13           0.00000400 sec
D16           0.00020000 sec
IN0           0.00026600 sec
TDav                    1
SFO1         400.1318173 MHz
NUC1                   1H
P0                  10.00 usec
P1                  10.00 usec
P17               2500.00 usec
PLW1         16.20000076 W
PLW10         1.79999995 W
GPNAM[1]      SMSQ10.100
GPZ1                10.00 %
P16               1000.00 usec

F1 - Acquisition parameters
TD                     128
SFO1             400.1318 MHz
FIDRES          58.740601 Hz
SW                   9.395 ppm
FnMODE                  QF

F2 - Processing parameters
SI                    1024
SF           400.1300361 MHz
WDW                 QSINE
SSB                     0
LB                      0 Hz
GB                      0
PC                   1.40

F1 - Processing parameters
SI                    1024
MC2                     QF
SF           400.1300361 MHz
WDW                 QSINE
SSB                     0
LB                      0 Hz
GB                      0
```

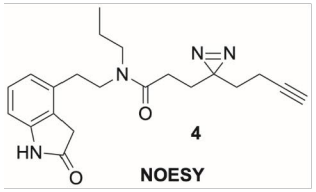

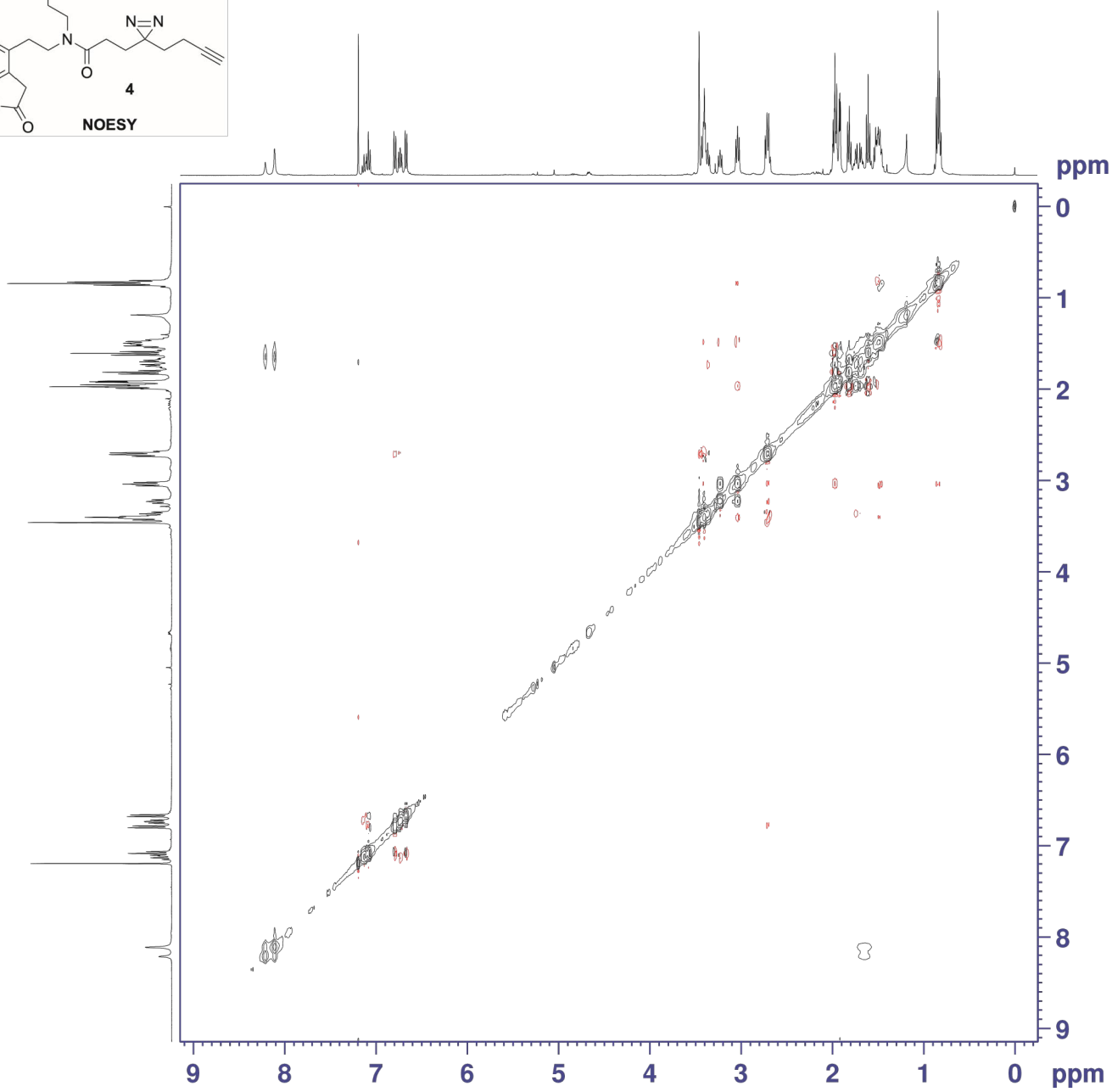


```
Current Data Parameters
NAME      cmpd 4 noesy try 2
EXPNO                     2
PROCNO                    1

F2 - Acquisition Parameters
Date_            20220825
Time                 2.30 h
INSTRUM             spect
PROBHD   Z116098_0203 (
PULPROG     noesygpphpp
TD                   2048
SOLVENT             CDCl3
NS                      4
DS                     32
SWH              3759.398 Hz
FIDRES           3.671288 Hz
AQ             0.2723840 sec
RG                 66.01
DW               133.000 usec
DE                 18.79 usec
TE                 298.0 K
D0            0.00012027 sec
D1            1.98361599 sec
D8            0.30000001 sec
D11           0.03000000 sec
D12           0.00002000 sec
D16           0.00020000 sec
IN0           0.00026600 sec
TDav                    1
SFO1         400.1318162 MHz
NUC1                   1H
P1                 10.00 usec
P2                 20.00 usec
P17              2500.00 usec
PLW1         16.20000076 W
PLW10         1.79999995 W
GPNAM[1]      SMSQ10.100
GPZ1               40.00 %
P16              1000.00 usec

F1 - Acquisition parameters
TD                    256
SFO1            400.1318 MHz
FIDRES         29.370300 Hz
SW                 9.395 ppm
FnMODE       States-TPPI

F2 - Processing parameters
SI                   1024
SF           400.1300361 MHz
WDW                 QSINE
SSB                     2
LB                      0 Hz
GB                      0
PC                   1.00

F1 - Processing parameters
SI                   1024
MC2          States-TPPI
SF           400.1300361 MHz
WDW                 QSINE
SSB                     2
LB                      0 Hz
GB                      0
```

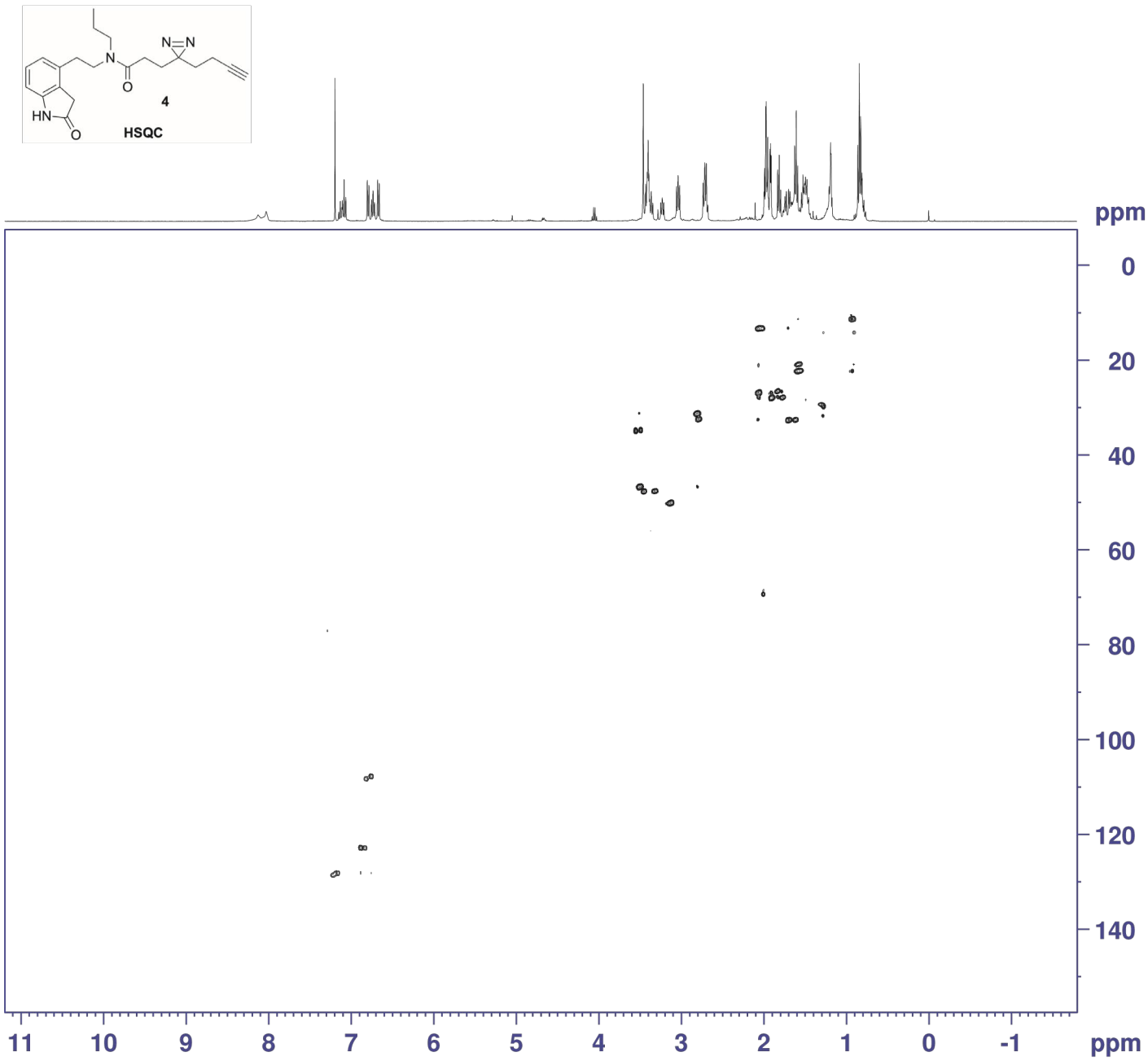


```
Current Data Parameters
NAME          cmpd 4 hsqc
EXPNO                   2
PROCNO                  1

F2 - Acquisition Parameters
Date_            20220831
Time                 1.12 h
INSTRUM             spect
PROBHD   Z116098_0203 (
PULPROG  hsqcedetgpsisp2.3
TD                   2048
SOLVENT             CDCl3
NS                      4
DS                     32
SWH             5197.505 Hz
FIDRES          5.075689 Hz
AQ             0.1970176 sec
RG                 208.09
DW                 96.200 usec
DE                  12.92 usec
TE                  298.0 K
CNST2        145.0000000
CNST17        -0.5000000
D0            0.00000300 sec
D1            1.50000000 sec
D4            0.00172414 sec
D11           0.03000000 sec
D16           0.00020000 sec
D21           0.00344800 sec
D24           0.00086200 sec
IN0           0.00003010 sec
TDav                    1
ZGOPTNS
SFO1         400.1318806 MHz
NUC1                   1H
P1                  10.00 usec
P2                  20.00 usec
PLW1         16.20000076 W
SFO2         100.6203145 MHz
NUC2                  13C
CPDPRG[2            garp4
P3                  10.00 usec
P14                500.00 usec
P24               2000.00 usec
P31               2119.00 usec
PCPD2               80.00 usec
PLW0                    0 W
PLW2         70.00000000 W
PLW12         1.09379995 W
SPNAM[3] Crp60,0.5,20.1
SPOAL3              0.500
SPOFFS3                 0 Hz
SPW3         10.69499969 W
SPNAM[7]     Crp60comp.4
SPOAL7              0.500
SPOFFS7                 0 Hz
SPW7         10.69499969 W
SPNAM[18  Crp60_xfilt.2
SPOAL18             0.500
SPOFFS18                0 Hz
SPW18         2.06040001 W
GPNAM[1]      SMSQ10.100
GPZ1                80.00 %
GPNAM[2]      SMSQ10.100
GPZ2                20.10 %
GPNAM[3]      SMSQ10.100
GPZ3                11.00 %
GPNAM[4]      SMSQ10.100
GPZ4                -5.00 %
P16               1000.00 usec
P19                600.00 usec

F1 - Acquisition parameters
TD                    256
SFO1            100.6203 MHz
FIDRES        129.775742 Hz
SW               165.089 ppm
FnMODE    Echo-Antiecho

F2 - Processing parameters
SI                   1024
SF           400.1300000 MHz
WDW                 QSINE
SSB                     2
LB                      0 Hz
GB                      0
PC                   1.40

F1 - Processing parameters
SI                   1024
MC2        echo-antiecho
SF           100.6127690 MHz
WDW                 QSINE
SSB                     2
LB                      0 Hz
GB                      0
```

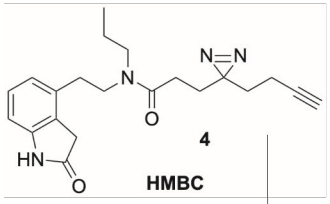

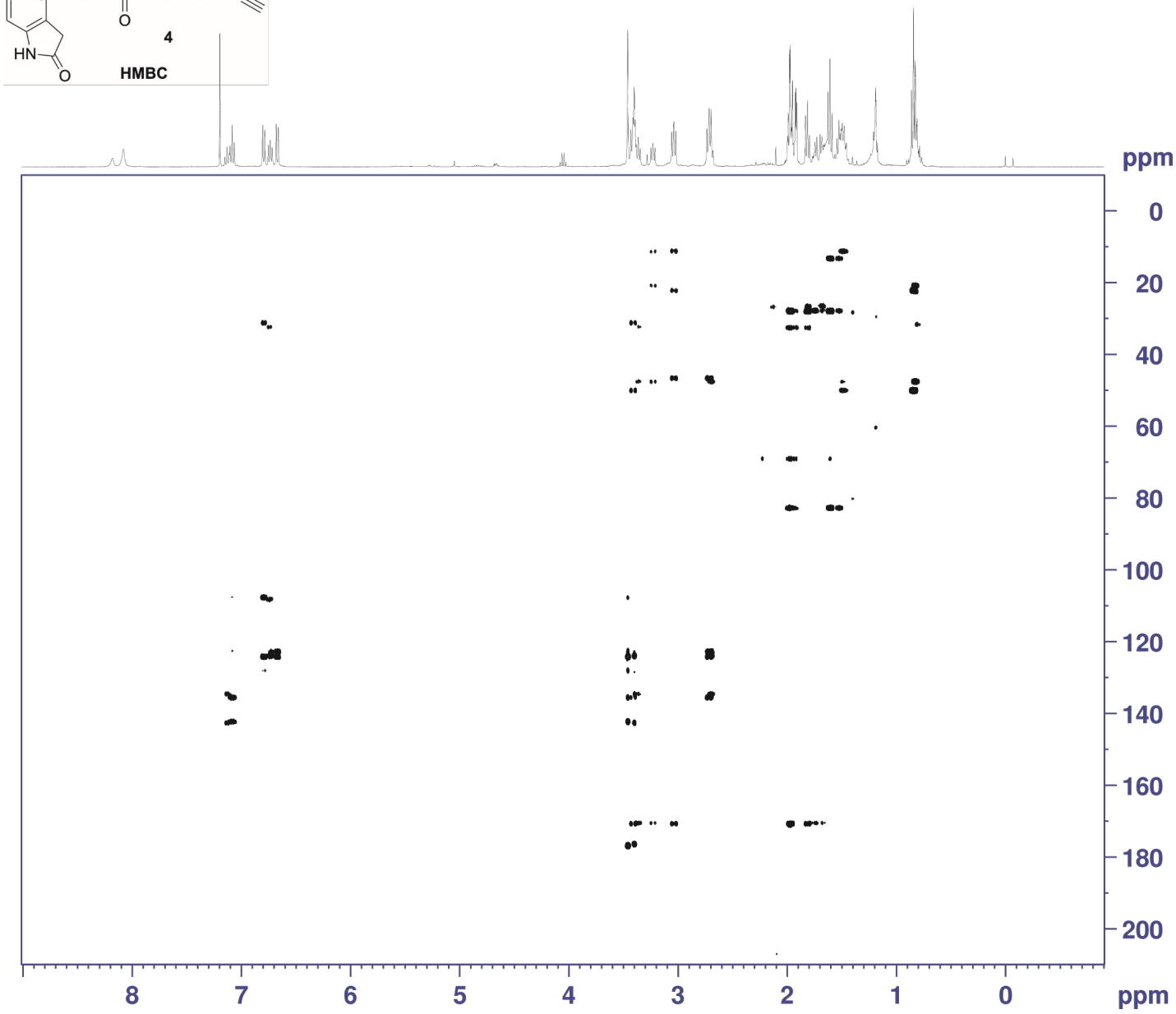


```
Current Data Parameters
NAME          cmpd 4 hmbc
EXPNO                   2
PROCNO                  1

F2 - Acquisition Parameters
Date_            20220831
Time                18.54 h
INSTRUM             spect
PROBHD    Z116098_0203 (
PULPROG     hmbcetgpl3nd
TD                   4096
SOLVENT             CDCl3
NS                      4
DS                     16
SWH               3968.254 Hz
FIDRES            1.937624 Hz
AQ               0.5160960 sec
RG                  208.09
DW                 126.000 usec
DE                    6.50 usec
TE                   298.0 K
CNST6          120.0000000
CNST7          170.0000000
CNST13           8.0000000
D0              0.00000300 sec
D1              2.00000000 sec
D6              0.06250000 sec
D16             0.00020000 sec
IN0             0.00002260 sec
TDav                     1
SFO1           400.1316582 MHz
NUC1                    1H
P1                   10.00 usec
P2                   20.00 usec
PLW1           16.20000076 W
SFO2           100.6228298 MHz
NUC2                   13C
P3                   10.00 usec
P24                2000.00 usec
PLW2           70.00000000 W
SPNAM[7]       Crp60comp.4
SPOAL7                0.500
SPOFFS7                   0 Hz
SPW7           10.69499969 W
GPNAM[1]        SMSQ10.100
GPZ1                  80.00 %
GPNAM[3]        SMSQ10.100
GPZ3                  14.00 %
GPNAM[4]        SMSQ10.100
GPZ4                  -8.00 %
GPNAM[5]        SMSQ10.100
GPZ5                  -4.00 %
GPNAM[6]        SMSQ10.100
GPZ6                  -2.00 %
P16                 1000.00 usec

F1 - Acquisition parameters
TD                     256
SFO1             100.6228 MHz
FIDRES          172.842926 Hz
SW                 219.870 ppm
FnMODE       Echo-Antiecho

F2 - Processing parameters
SI                    4096
SF             400.1300359 MHz
WDW                   QSINE
SSB                       4
LB                        0 Hz
GB                        0
PC                     1.40

F1 - Processing parameters
SI                    1024
MC2           echo-antiecho
SF             100.6127690 MHz
WDW                   QSINE
SSB                       2
LB                        0 Hz
GB                        0
```

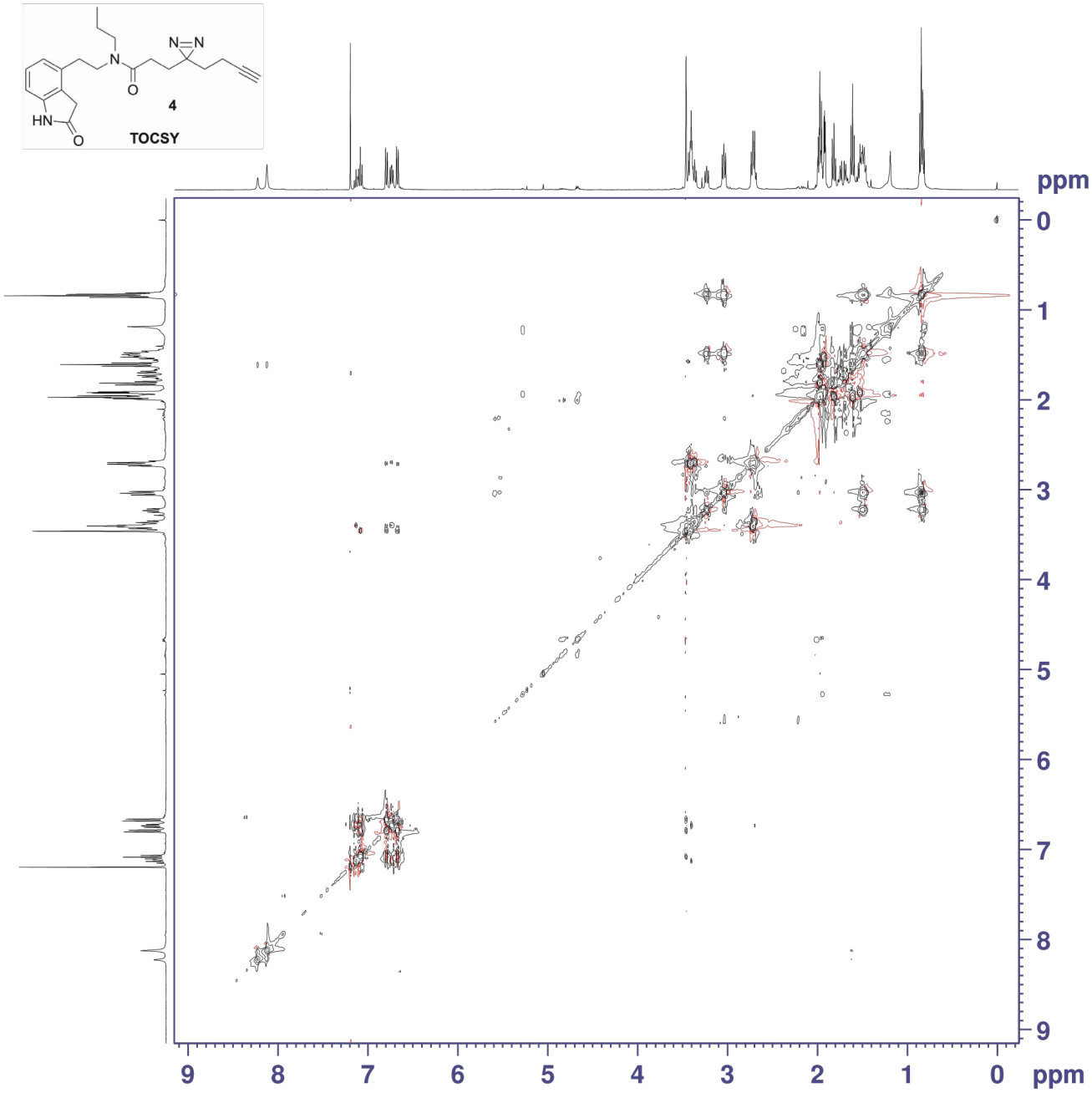


```
Current Data Parameters
NAME        cmpd 4 tocsy
EXPNO                  2
PROCNO                 1

F2 - Acquisition Parameters
Date_           20220827
Time               11.38 h
INSTRUM            spect
PROBHD   Z116098_0203 (
PULPROG         mlevphpp
TD                 2048
SOLVENT            CDCl3
NS                     8
DS                    16
SWH             3759.398 Hz
FIDRES          3.671288 Hz
AQ             0.2723840 sec
RG                 66.01
DW               133.000 usec
DE                  6.50 usec
TE                 298.0 K
D0            0.00012263 sec
D1            1.98361599 sec
D9            0.08000000 sec
D11           0.03000000 sec
D12           0.00002000 sec
IN0           0.00026600 sec
L1                    36
TDav                   1
SFO1         400.1318190 MHz
NUC1                  1H
P1                 10.00 usec
P5                 20.01 usec
P6                 30.00 usec
P7                 60.00 usec
P17              2500.00 usec
PLW1         16.20000076 W
PLW10         1.79999995 W

F1 - Acquisition parameters
TD                   256
SFO1            400.1318 MHz
FIDRES         29.370300 Hz
SW                 9.395 ppm
FnMODE       States-TPPI

F2 - Processing parameters
SI                  1024
SF          400.1300361 MHz
WDW                QSINE
SSB                    2
LB                     0 Hz
GB                     0
PC                  1.40

F1 - Processing parameters
SI                  1024
MC2          States-TPPI
SF          400.1300361 MHz
WDW                QSINE
SSB                    2
LB                     0 Hz
GB                     0
```

Probe 4 2D NMR Assignments

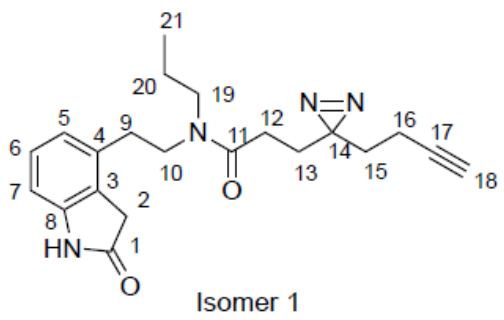

Isomer 1

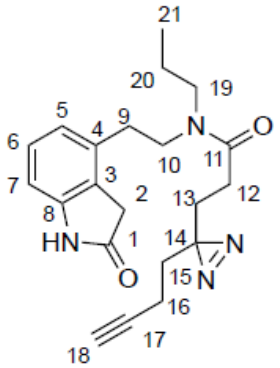

Isomer 2

Isomer 1

	Cδ	HSQC	Hδ	multiplicity	J-value	COSY	HMBC
C1	177.405						H1
C2	35.07	H1	3.51	s		H5, H6	H2, H3, H4, H13
C3	124.37						H1, H2, H4
C4	135.63						H1, H3
C5	122.9	H2	6.847	d	7.8 Hz	H3	H1, H2
C6	128.24	H3	7.1388	t	7.7 Hz	H2, H4	H1
C7	108	H4	6.736	d	7.7 Hz	H3	H1, H2
C8	142.59						H1, H3
C9	31.34	H5	2.77	m		H1,H7	H3
C10	46.79	H6	3.095	t	7.6 Hz	H14	H13
C11	170.9						H6
C12	28.04	H10	2.028	t	7.3 Hz	H11	H2
C13	32.69	H11	1.663	t	7.4 Hz	H10	H3
C14	13.42						H11
C15	38.79	H12	1.87	t	7.1 Hz	H11, H13	H3
C16	11.35	H13	1.975	m		H12, H14	H1
C17	82.91						H8
C18	69.25	H14	1.805	m		H13	H6, H14
C19	50.2	H7	3.469	t	7.8 Hz	H1, H5	
C20	22.34	H8	1.58	t	7.3 Hz	H9	H6
C21	26.95	H9	0.898	t	7.4 Hz	H8	H2

Isomer 2

	Cδ	HSQC	Hδ	multiplicity	J-value	COSY	HMBC
C1	176.94						H1
C2	34.835	H1	3.46	s		H5	H2, H3, H4
C3	124.4						H1
C4	134.63						H1
C5	122.86	H2	6.8	d	1.9 Hz	H3	H1, H4
C6	128.7	H3	7.187	t	7.7 Hz	H2, H4	H1
C7	108.54	H4	6.79	d	1.9 Hz	H3	H1, H2
C8	142.94						
C9	32.67	H5	2.695	m		H1, H6	H2, H4
C10	34.93	H6	3.286	t	7.7 Hz	H5, H11	H8, H14
C11	170.72						H14
C12	28.11	H10	2.031	t	7.5 Hz	H11	H8, H12
C13	32.5	H11	1.73	m		H6, H10	
C14	13.42						H12
C15	47.79	H12	1.58	m		H13	H5, H6, H9,
C16	11.49	H13	2.03	m		H12, H14	H11
C17	77.34						H13
C18	69.25	H14	1.73	m		H13	
C19	47.71	H7	3.421	t	7.4 Hz	H8	H11
C20	20.97	H8	1.54	m		H7, H9	H9, H13
C21	27.95	H9	0.883	t	7.6 Hz	H8	H7, H11

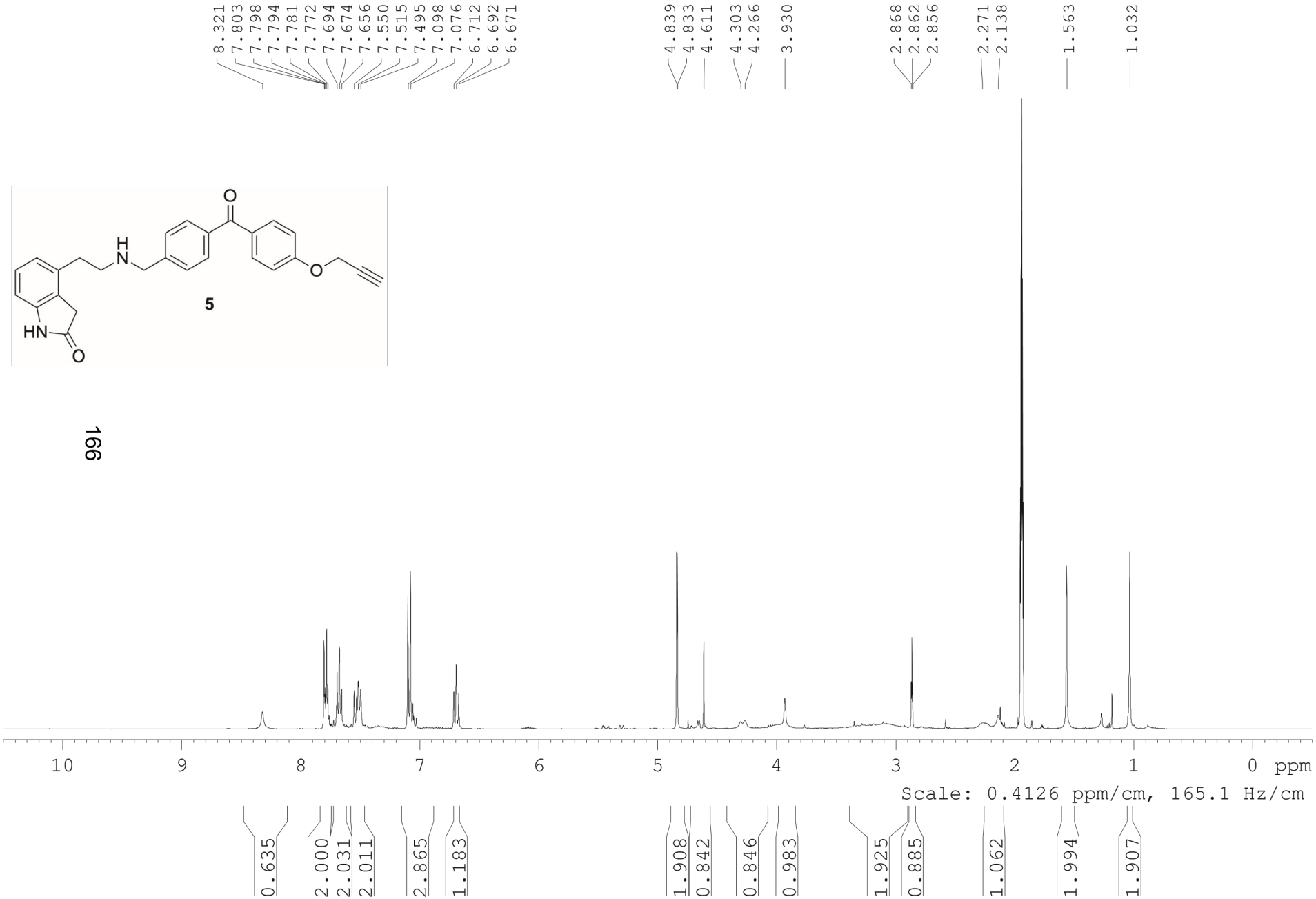
8.321
7.803
7.798
7.794
7.781
7.772
7.694
7.674
7.656
7.550
7.515
7.495
7.098
7.076
6.712
6.692
6.671
4.839
4.833
4.611
4.303
4.266
3.930
2.868
2.862
2.856
2.271
2.138
1.563
1.032
H
N
O
O
O
HN
O
5
10
9
8
7
6
5
4
3
2
1
0 ppm
Scale: 0.4126 ppm/cm, 165.1 Hz/cm
0.635
2.000
2.031
2.011
2.865
1.183
1.908
0.842
0.846
0.983
1.925
0.885
1.062
1.994
1.907

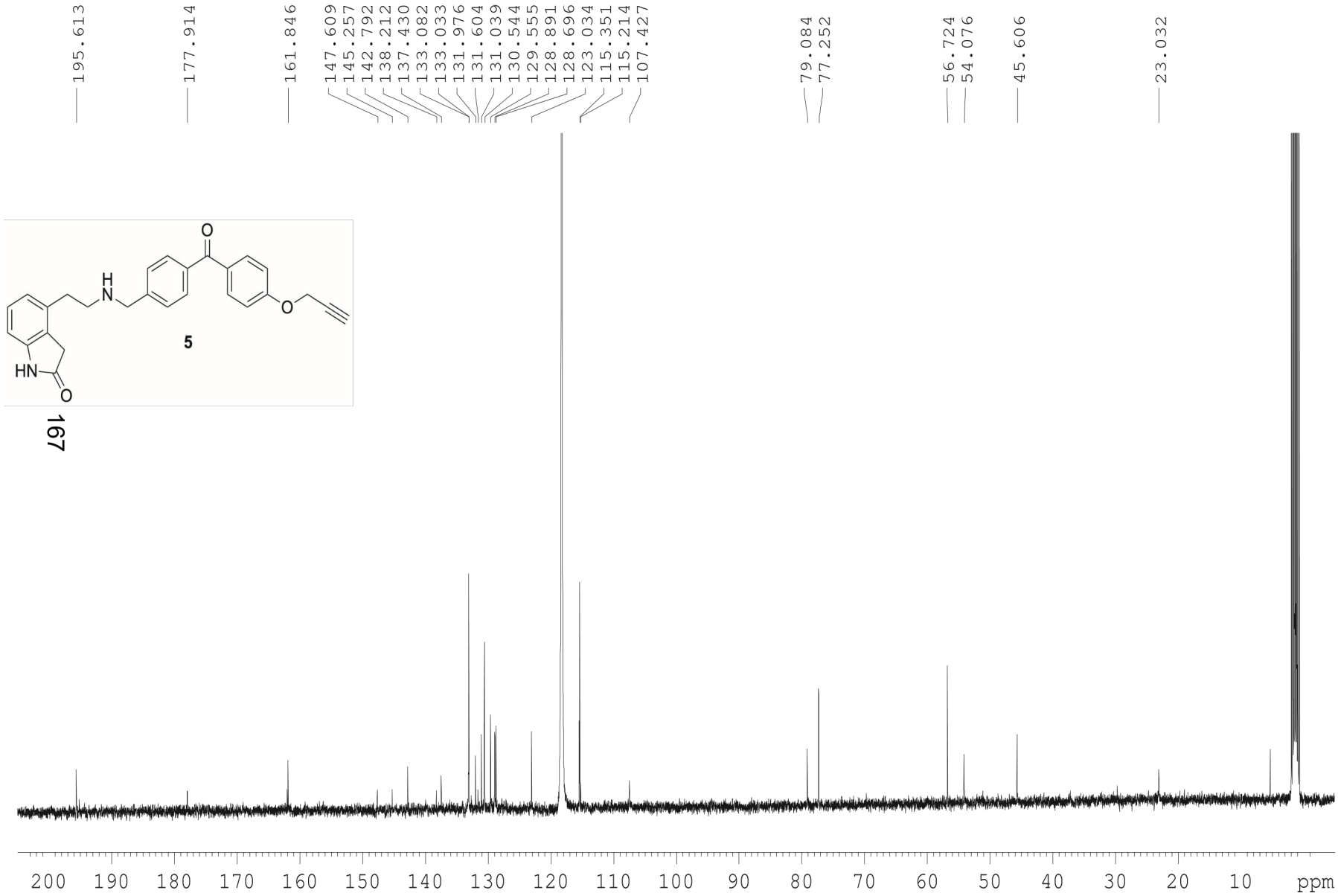
195.613
177.914
161.846
147.609
145.257
142.792
138.212
137.430
133.082
133.033
131.976
131.604
131.039
130.544
129.555
128.891
128.696
123.034
115.351
115.214
107.427
79.084
77.252
56.724
54.076
45.606
23.032
5
200 190 180 170 160 150 140 130 120 110 100 90 80 70 60 50 40 30 20 10 ppm

H
N
N=N
O
6
HN
O

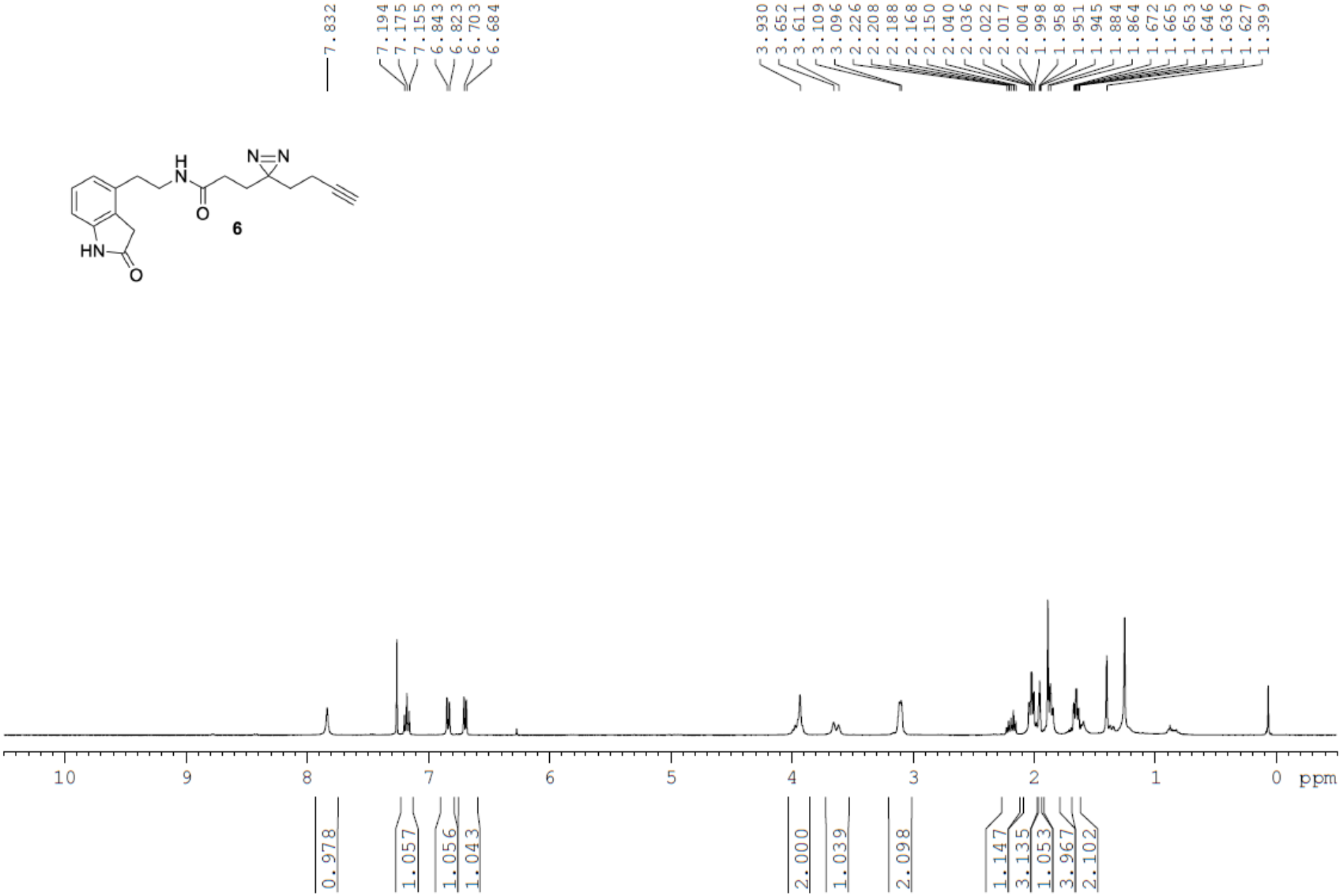
7.832
7.194
7.175
7.155
6.843
6.823
6.703
6.684
3.930
3.652
3.611
3.109
3.096
2.226
2.208
2.188
2.168
2.150
2.040
2.036
2.022
2.017
2.004
1.998
1.958
1.951
1.945
1.884
1.864
1.672
1.665
1.653
1.646
1.636
1.627
1.399
10
9
8
7
6
5
4
3
2
1
0
ppm
0.978
1.057
1.056
1.043
2.000
1.039
2.098
1.147
3.135
1.053
3.967
2.102

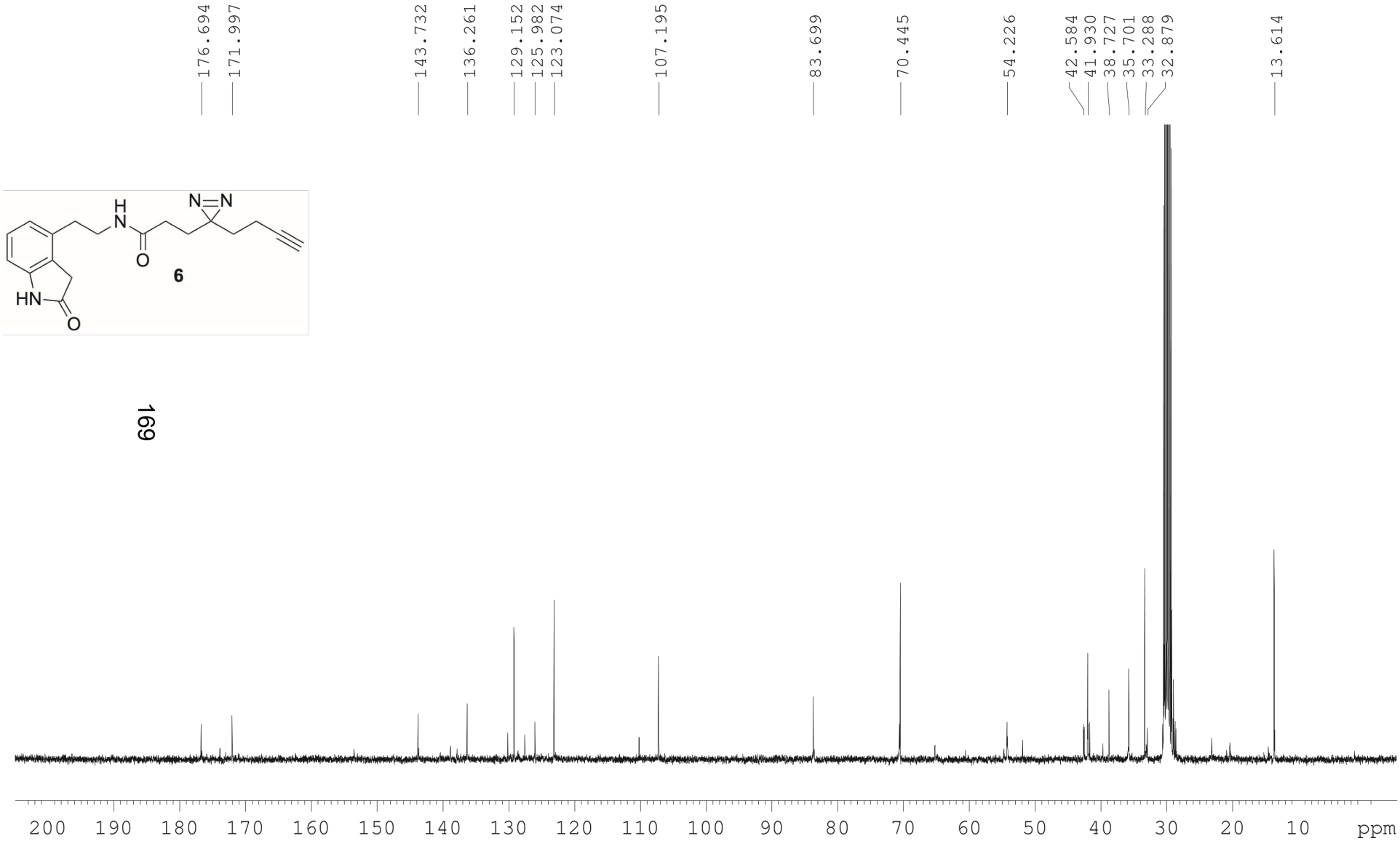
176.694
171.997
143.732
136.261
129.152
125.982
123.074
107.195
83.699
70.445
54.226
42.584
41.930
38.727
35.701
33.288
32.879
13.614
H
N
N=N
O
6
HN
O
200 190 180 170 160 150 140 130 120 110 100 90 80 70 60 50 40 30 20 10 ppm

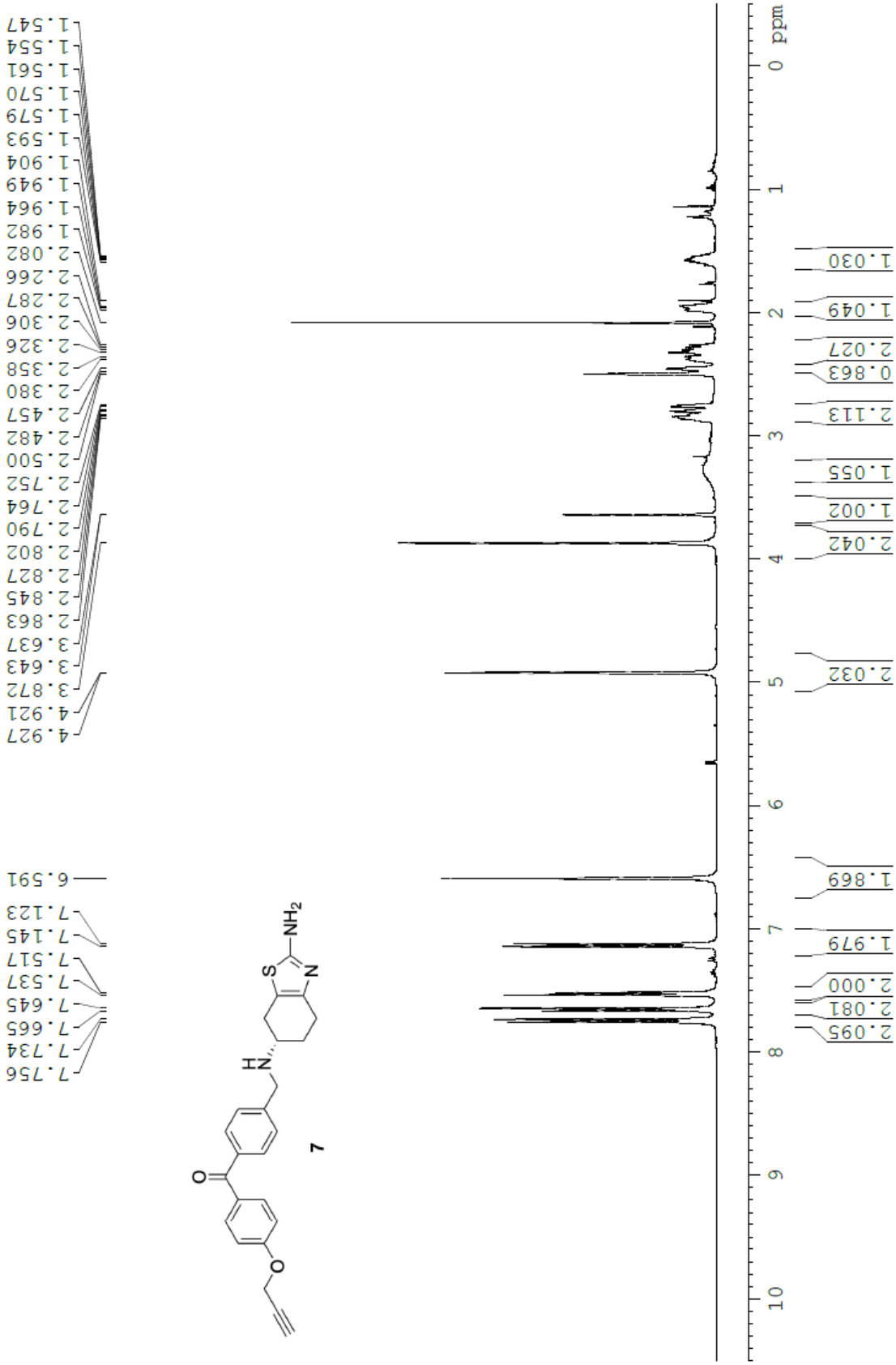
7
ppm
0
1
2
3
4
5
6
7
8
9
10
1.030
1.049
2.027
0.863
2.113
1.055
1.002
2.042
2.032
1.869
1.979
2.000
2.081
2.095
4.927
4.921
3.872
3.643
3.637
2.863
2.845
2.827
2.802
2.790
2.764
2.752
2.500
2.482
2.457
2.380
2.358
2.326
2.306
2.287
2.266
2.082
1.982
1.964
1.949
1.904
1.593
1.579
1.570
1.561
1.554
1.547
6.591
7.123
7.145
7.517
7.537
7.645
7.665
7.734
7.756

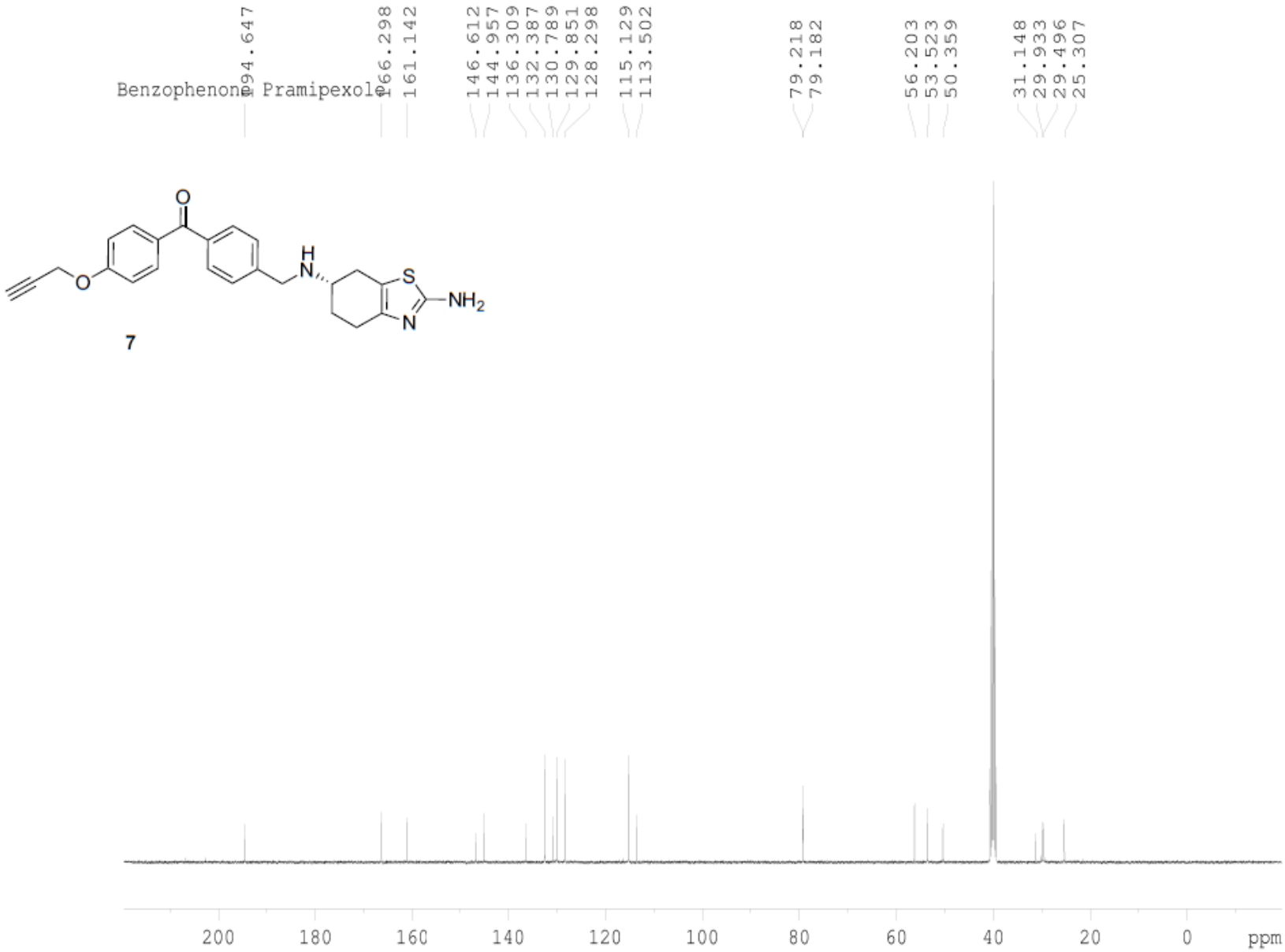
Benzophenone
Pramipexole
194.647
166.298
161.142
146.612
144.957
136.309
132.387
130.789
129.851
128.298
115.129
113.502
79.218
79.182
56.203
53.523
50.359
31.148
29.933
29.496
25.307
O
O
H
N
S
N
NH2
7
200
180
160
140
120
100
80
60
40
20
0
ppm

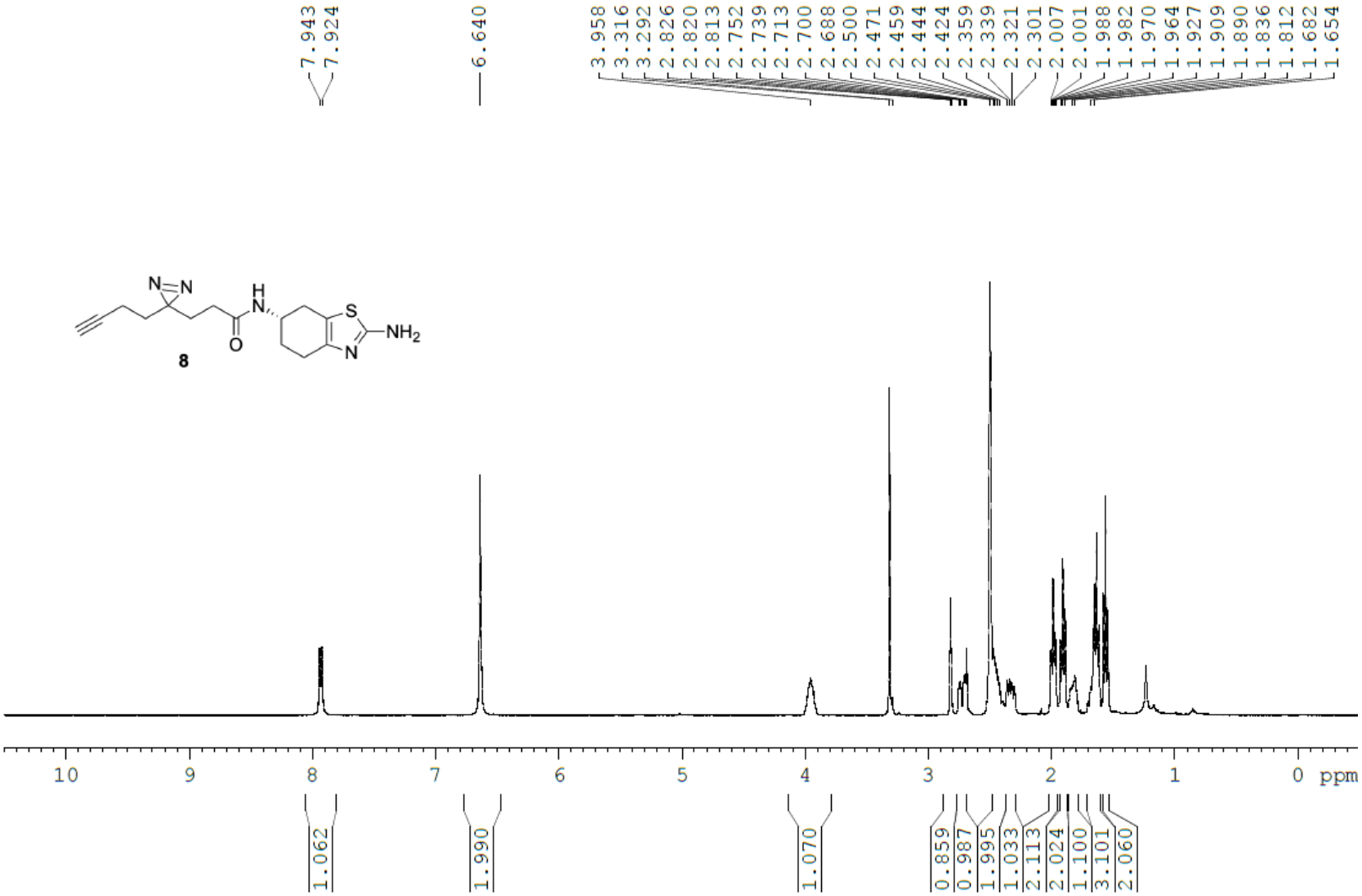
7.943
7.924
6.640
3.958
3.316
3.292
2.826
2.820
2.813
2.752
2.739
2.713
2.700
2.688
2.500
2.471
2.459
2.444
2.424
2.359
2.339
2.321
2.301
2.007
2.001
1.988
1.982
1.970
1.964
1.927
1.909
1.890
1.836
1.812
1.682
1.654
N
N
H
N
S
NH2
N
O
8
10
9
8
7
6
5
4
3
2
1
0 ppm
1.062
1.990
1.070
0.859
0.987
1.995
1.033
2.113
2.024
1.100
3.101
2.060

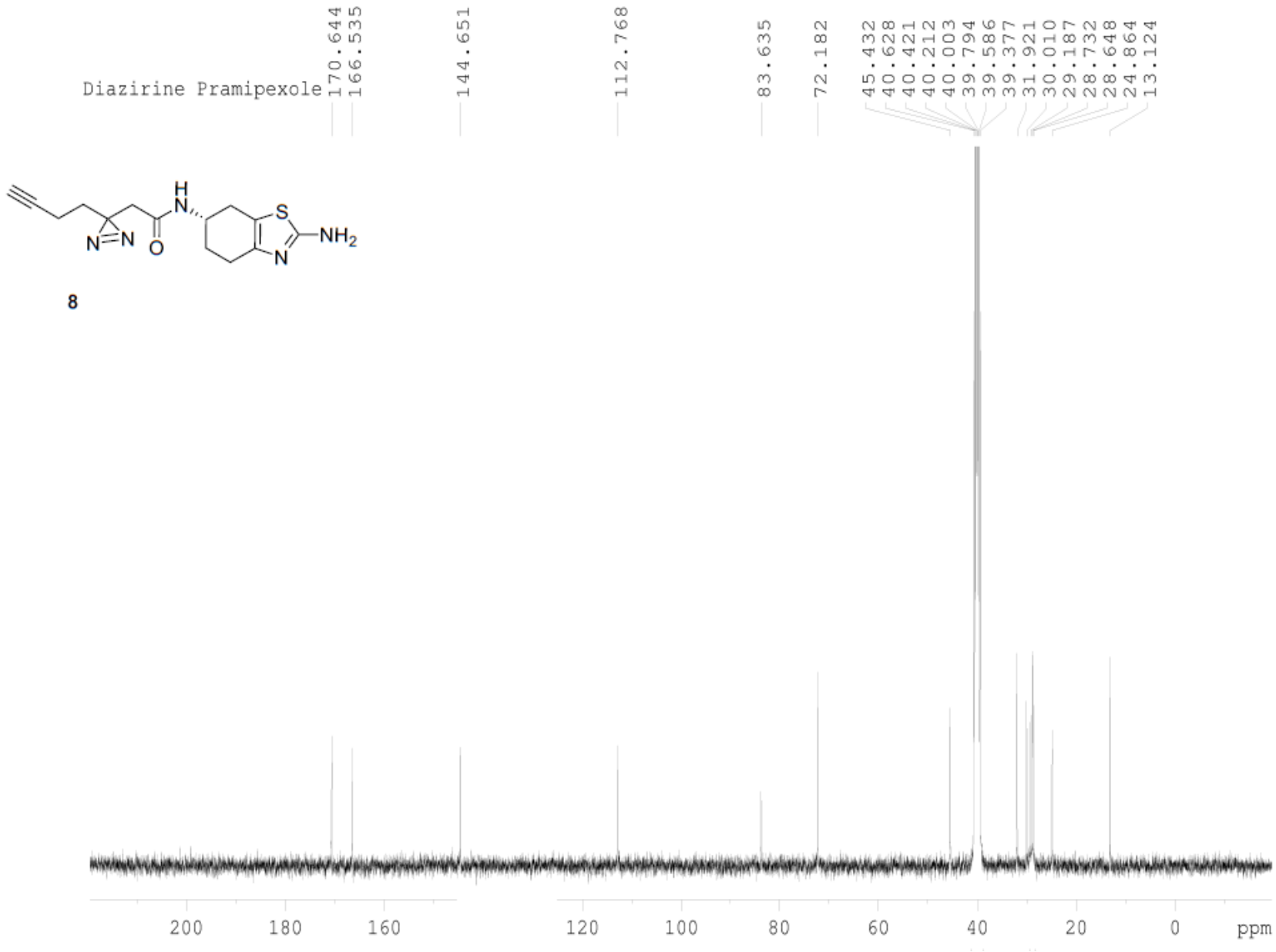
Diazirine Pramipexole
170.644
166.535
144.651
112.768
83.635
72.182
45.432
40.628
40.421
40.212
40.003
39.794
39.586
39.377
31.921
30.010
29.187
28.732
28.648
24.864
13.124
H
N
S
NH2
N
N=N
O
8
200
180
160
120
100
80
60
40
20
0
ppm

OMs
O
HN
10
8.343
7.218
7.199
7.179
6.904
6.884
6.807
6.788
4.446
4.429
4.412
3.507
3.021
3.004
2.988
2.904
0.942
1.005
0.998
1.016
2.038
1.990
2.065
2.987
ppm
11
10
9
8
7
6
5
4
3
2
1

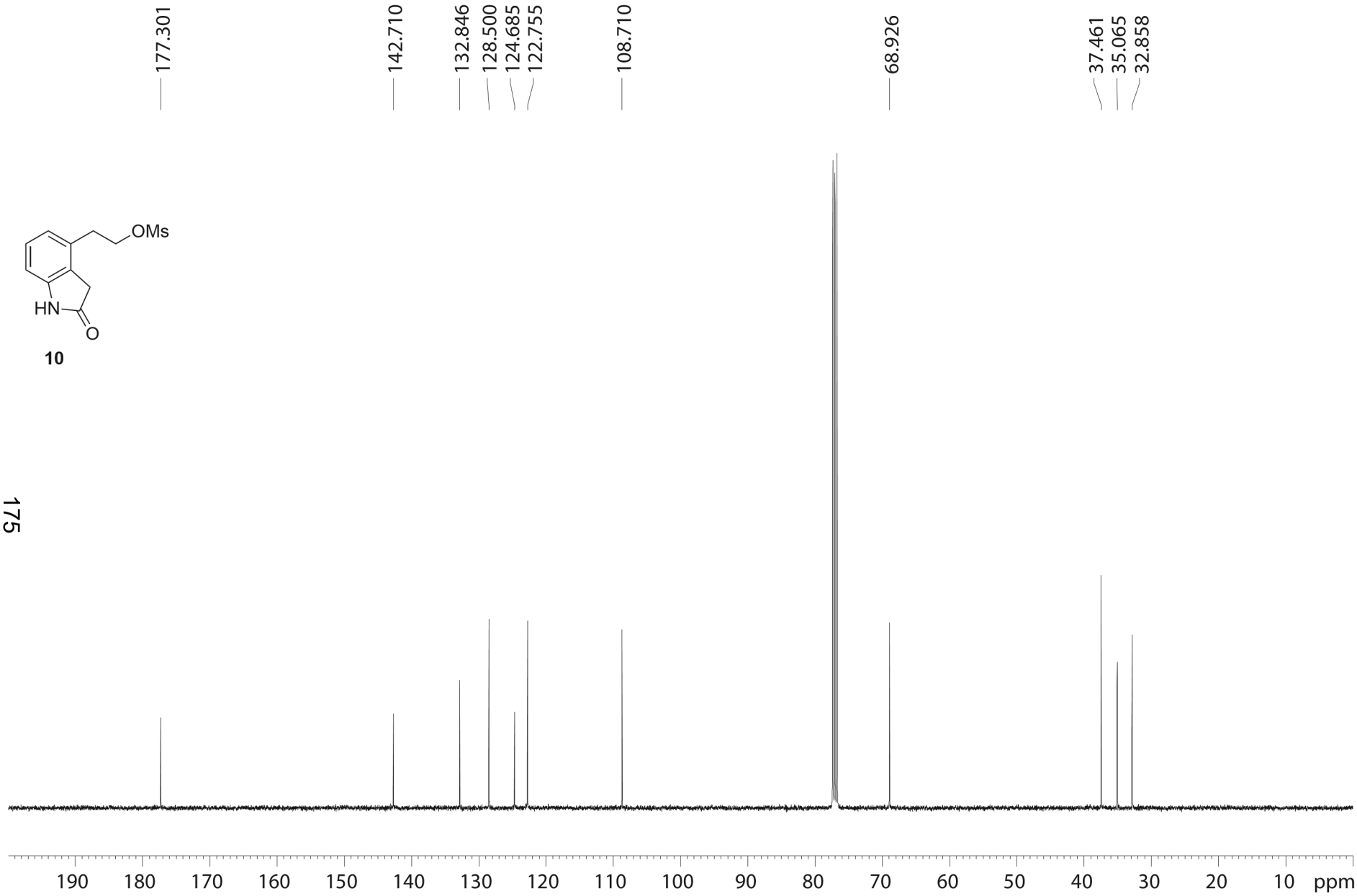
177.301
142.710
132.846
128.500
124.685
122.755
108.710
68.926
37.461
35.065
32.858
OMs
HN
O
10
190
180
170
160
150
140
130
120
110
100
90
80
70
60
50
40
30
20
10
ppm

9.021
7.214
7.194
7.175
6.889
6.870
6.816
6.797
3.562
3.545
3.527
3.515
2.840
2.822
2.805
0.946
1.035
0.973
0.988
2.133
2.101
2.000
ppm
0
1
2
3
4
5
6
7
8
9
10
N3
H
N
O
11

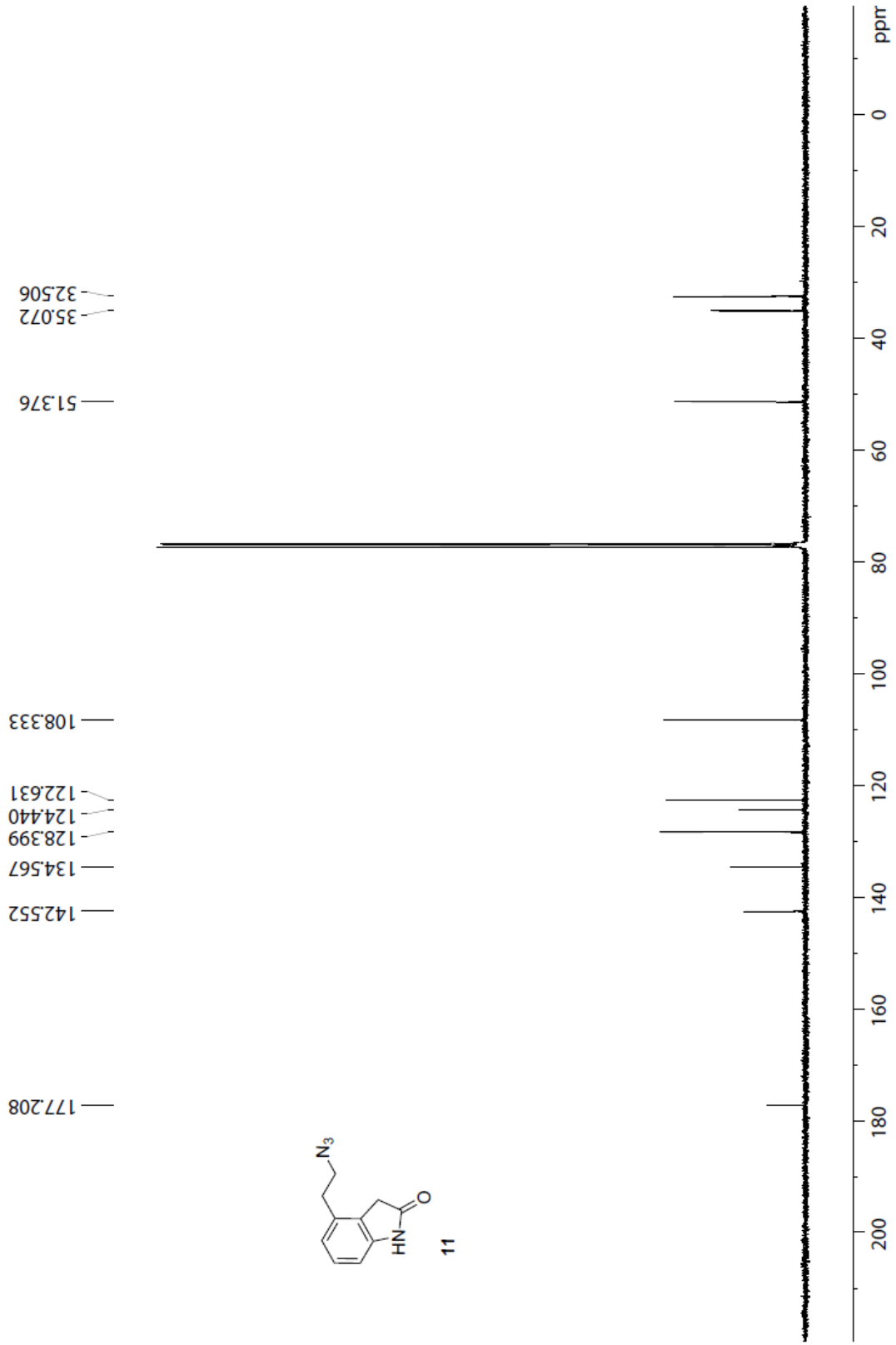
177.208
142.552
134.567
128.399
124.440
122.631
108.333
51.376
35.072
32.506
11
ppm

9.299
7.118
7.098
7.079
6.853
6.833
6.728
6.709
3.479
3.459
3.442
3.422
2.825
2.807
2.792
0.688
0.988
0.976
1.070
4.143
4.441
ppm
1
2
3
4
5
6
7
8
9
10
11
NH
O
NH2
12

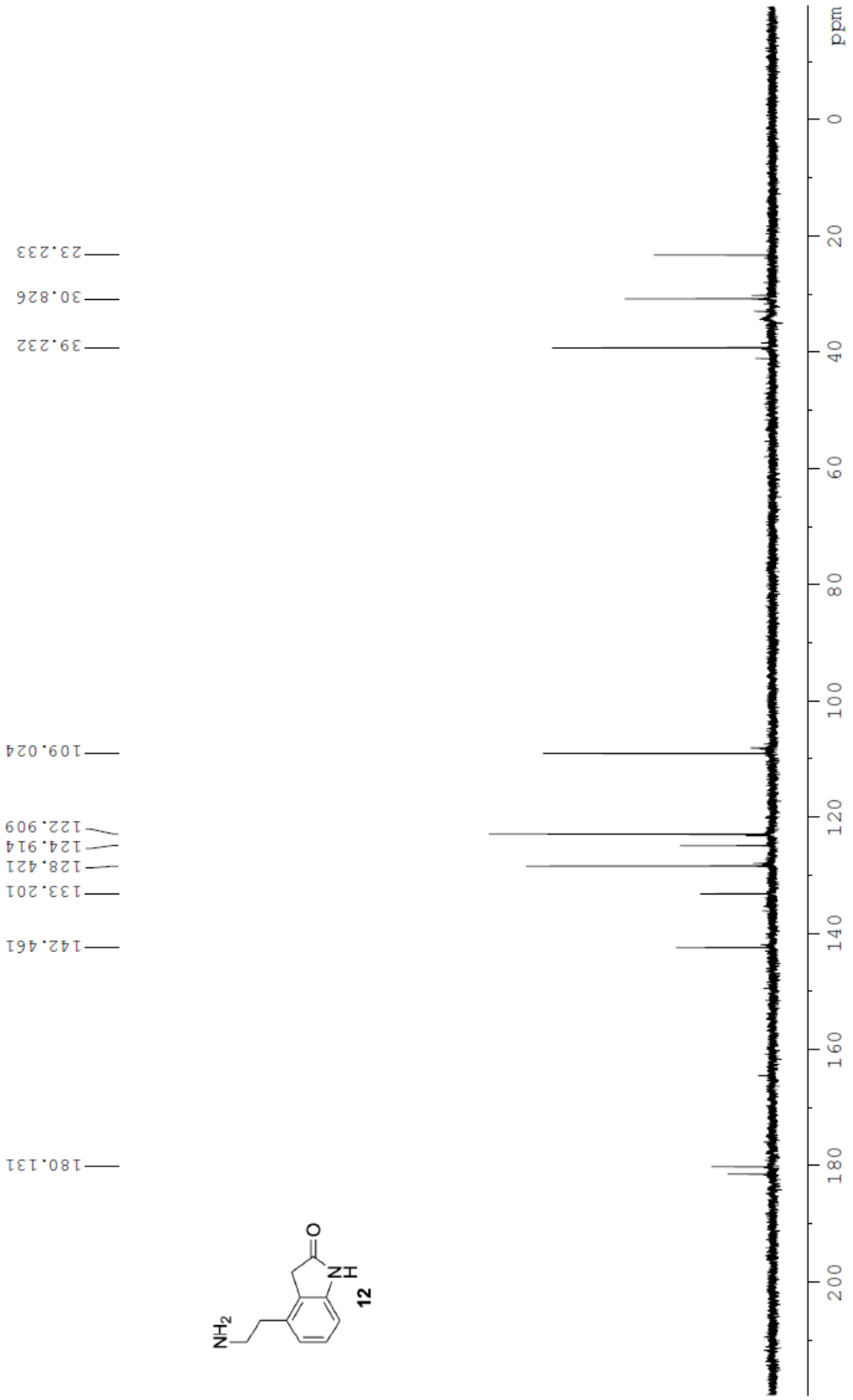
NH2
O
N
H
12
180.131
142.461
133.201
128.421
124.914
122.909
109.024
39.232
30.826
23.233
ppm
0
20
40
60
80
100
120
140
160
180
200

7.2 Chapter 4: Photocaged Probes for $5HT_{2C}$

HPLC traces of WinterGreen-WAY and WinterRed-NDMC are provided below. NMR spectra begin on the following page.

HPLC trace of WinterGreen-WAY

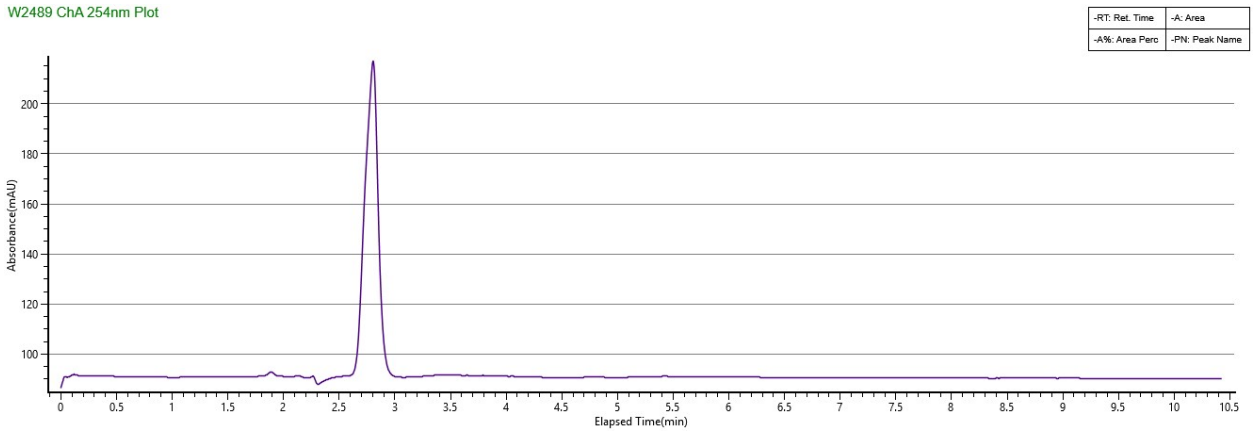

HPLC trace of WinterRed-NDMC

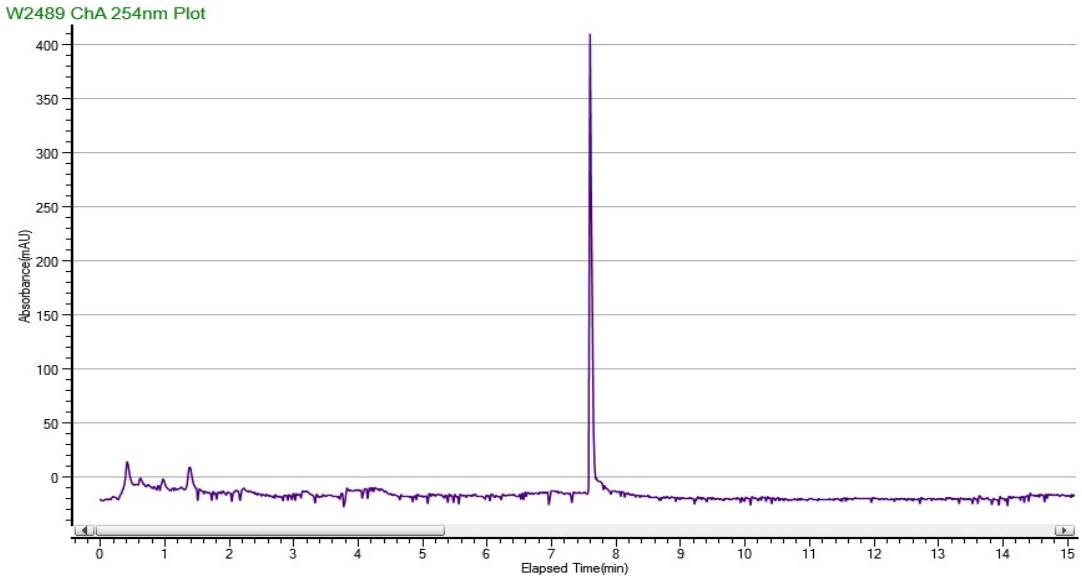

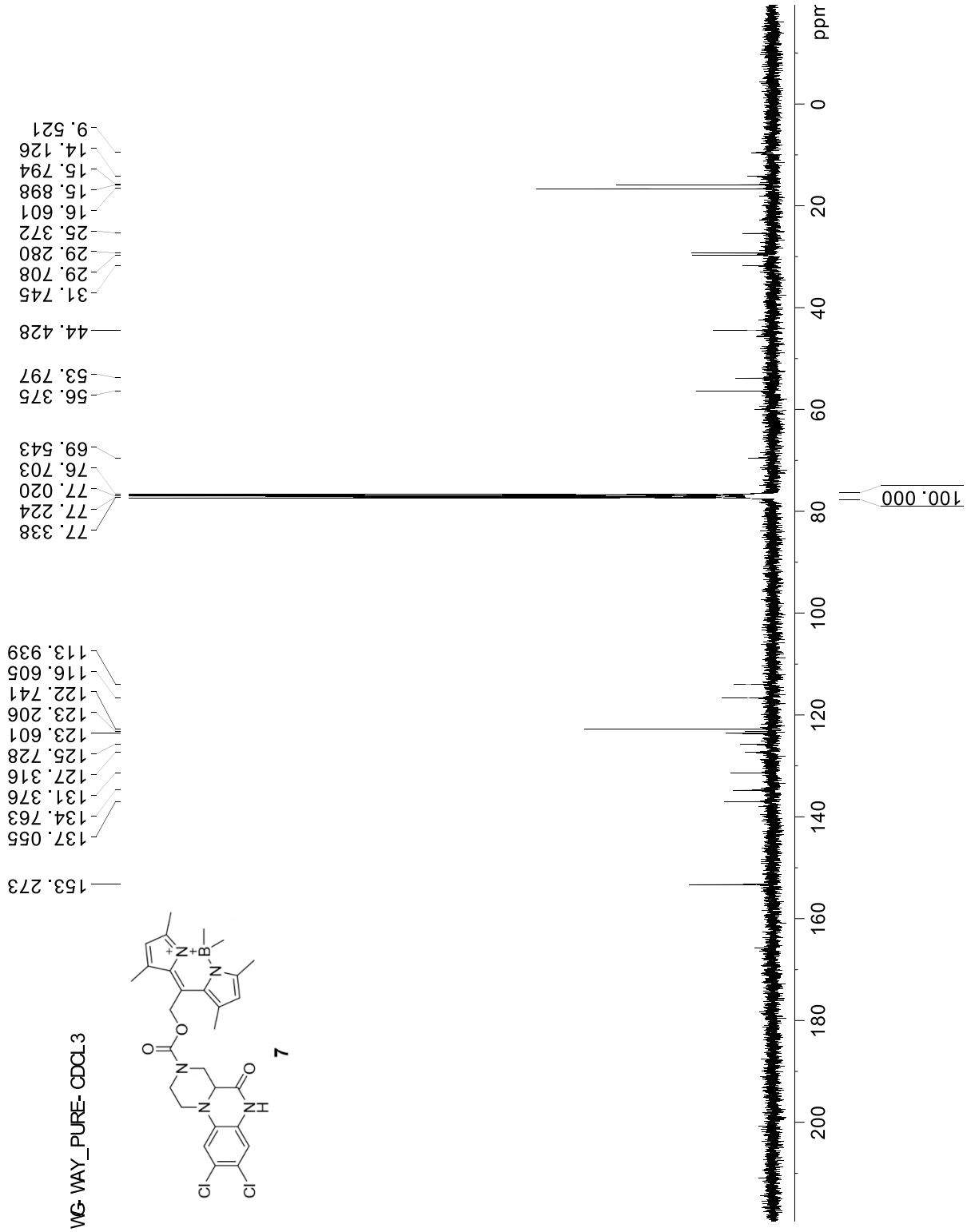
WG-WAY_PURE-CDCL3
7
153.273
137.055
134.763
131.376
127.316
125.728
123.601
123.206
122.741
116.605
113.939
77.338
77.224
77.020
76.703
69.543
56.375
53.797
44.428
31.745
29.708
29.280
25.372
16.601
15.898
15.794
14.126
9.521
100.000
ppm

WG-WAY_PURE-CDCL3

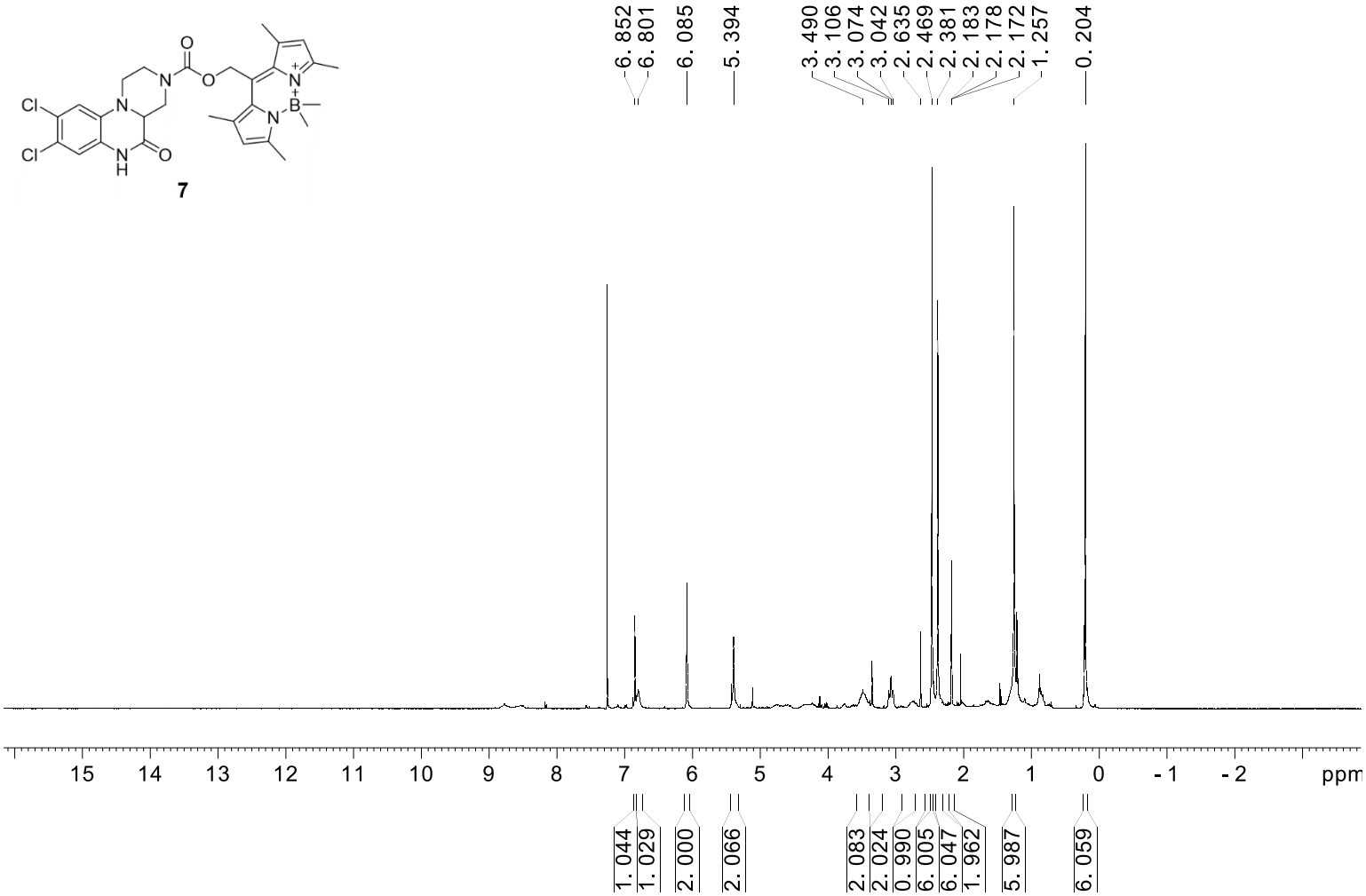

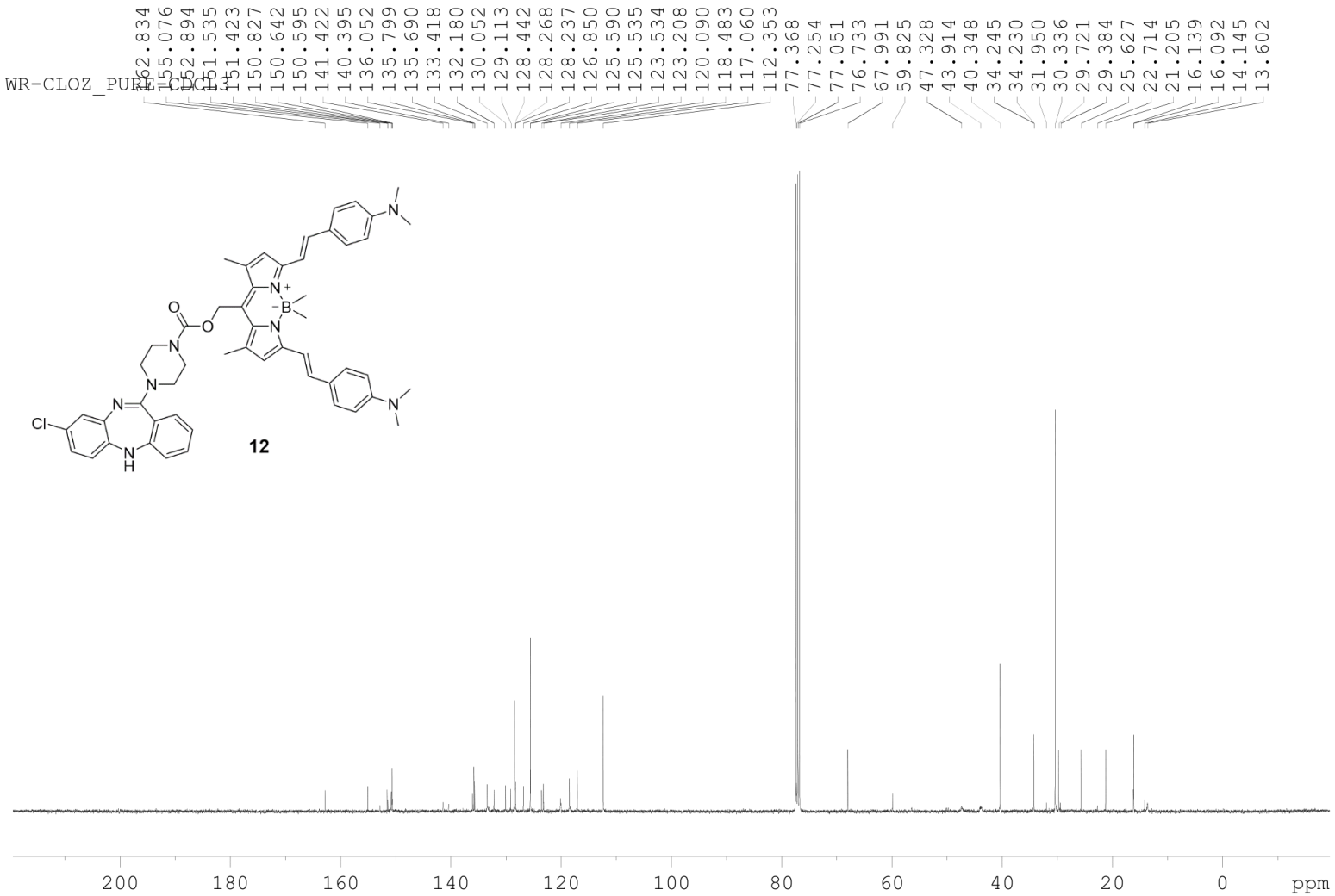
WR-CLOZ_PURE_CDCL3
162.834
155.076
152.894
151.535
151.423
150.827
150.642
150.595
141.422
140.395
136.052
135.799
135.690
133.418
132.180
130.052
129.113
128.442
128.268
128.237
126.850
125.590
125.535
123.534
123.208
120.090
118.483
117.060
112.353
77.368
77.254
77.051
76.733
67.991
59.825
47.328
43.914
40.348
34.245
34.230
31.950
30.336
29.721
29.384
25.627
22.714
21.205
16.139
16.092
14.145
13.602
12
200
180
160
140
120
100
80
60
40
20
0
ppm

WR-CLOZ_PURE-CDCL3

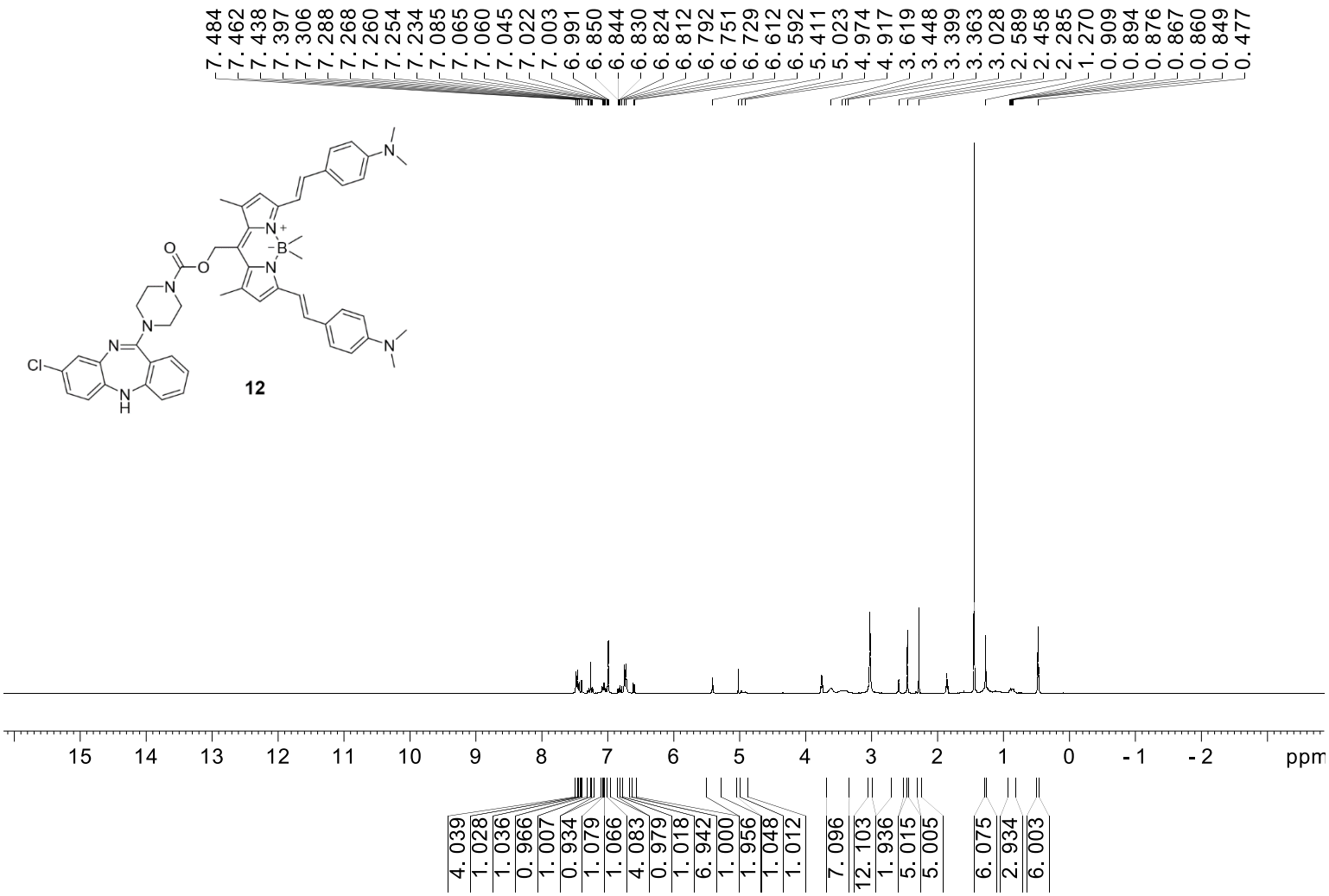

7.3 Chapter 5: Progress Toward the Synthesis of LSA

NMR spectra begin on the following page.

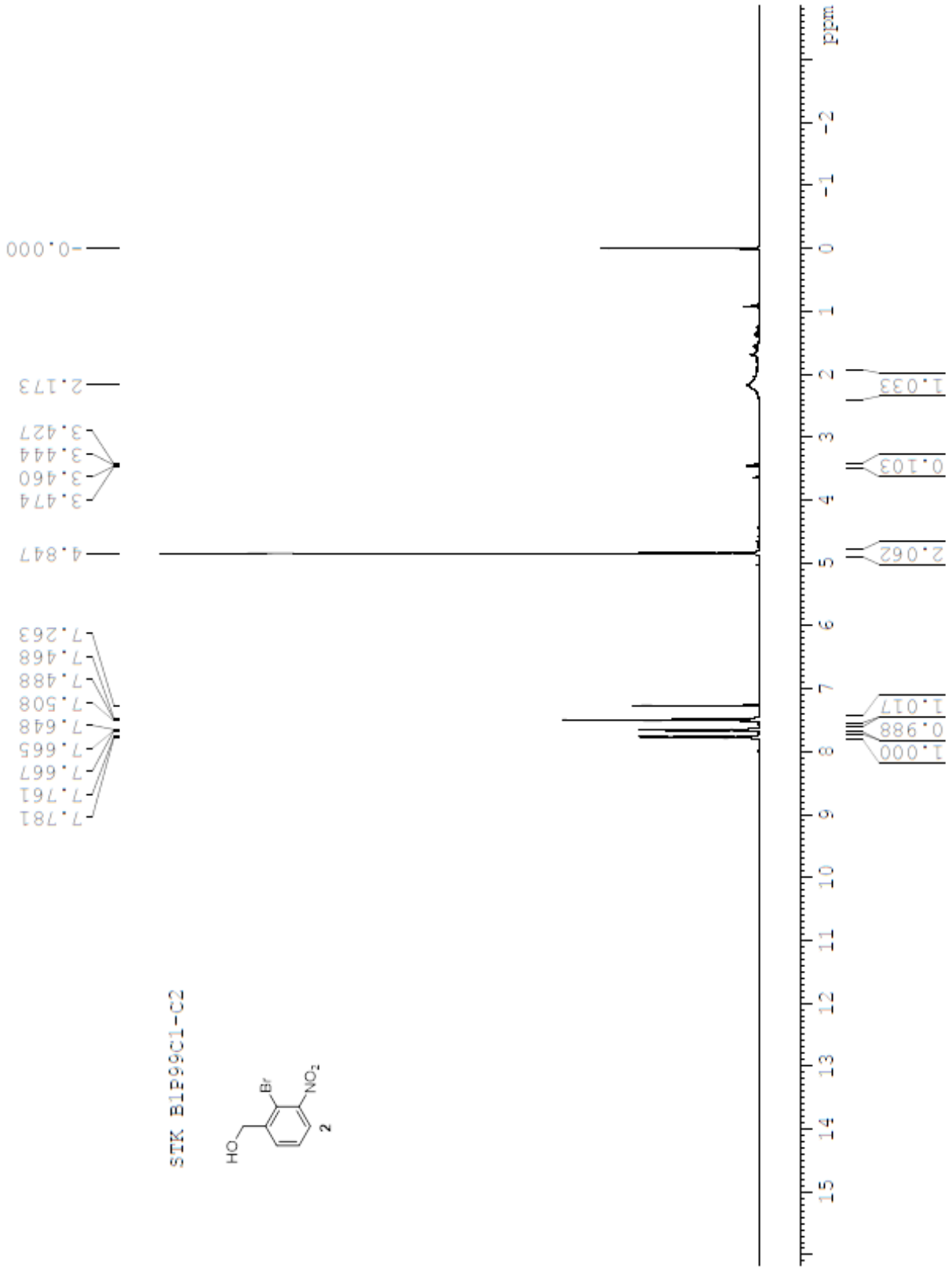
STK B1P99C1-C2
HO
Br
NO2
2
7.781
7.761
7.667
7.665
7.648
7.508
7.488
7.468
7.263
4.847
3.474
3.460
3.444
3.427
2.173
-0.000
1.000
0.988
1.017
2.062
0.103
1.033
ppm

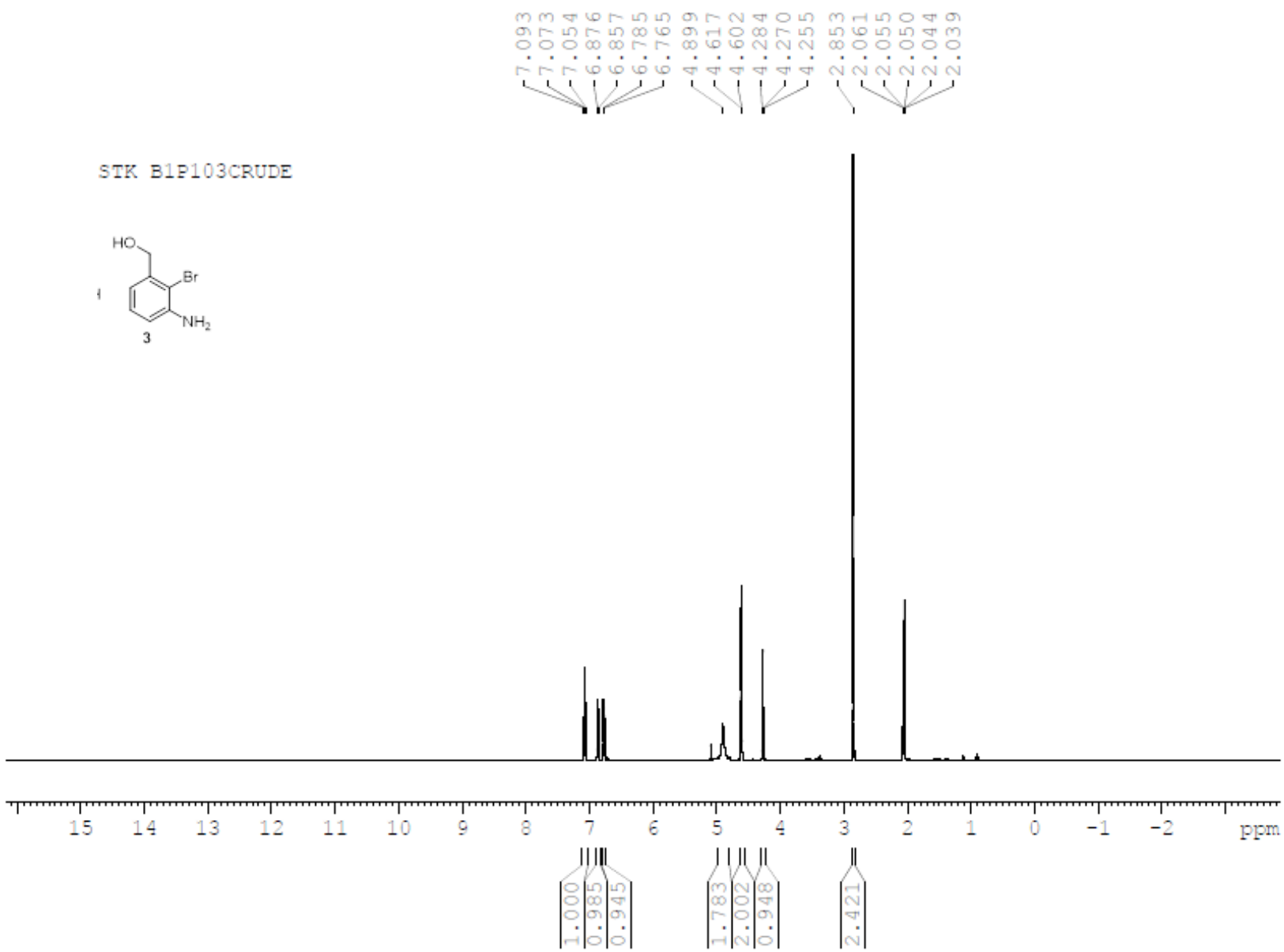
7.093
7.073
7.054
6.876
6.857
6.785
6.765
4.899
4.617
4.602
4.284
4.270
4.255
2.853
2.061
2.055
2.050
2.044
2.039
STK B1P103CRUDE
HO
Br
NH2
3
15 14 13 12 11 10 9 8 7 6 5 4 3 2 1 0 -1 -2 ppm
1.000
0.985
0.945
1.783
2.002
0.948
2.421

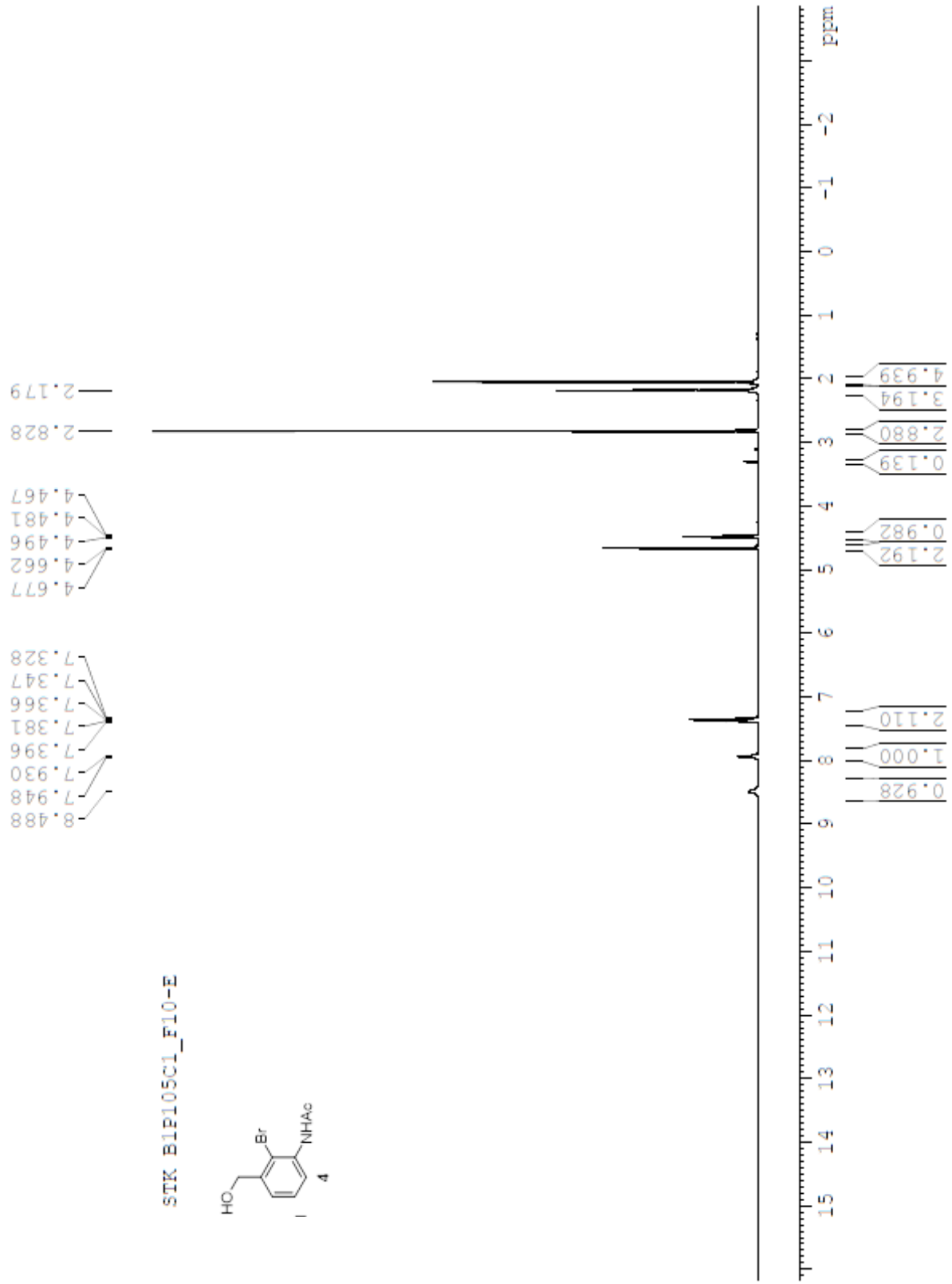
STK B1P105C1_F10-E
HO
Br
NHAc
4
8.488
7.948
7.930
7.396
7.381
7.366
7.347
7.328
4.677
4.662
4.496
4.481
4.467
2.828
2.179
0.928
1.000
2.110
0.982
2.192
0.139
2.880
3.194
4.939
ppm

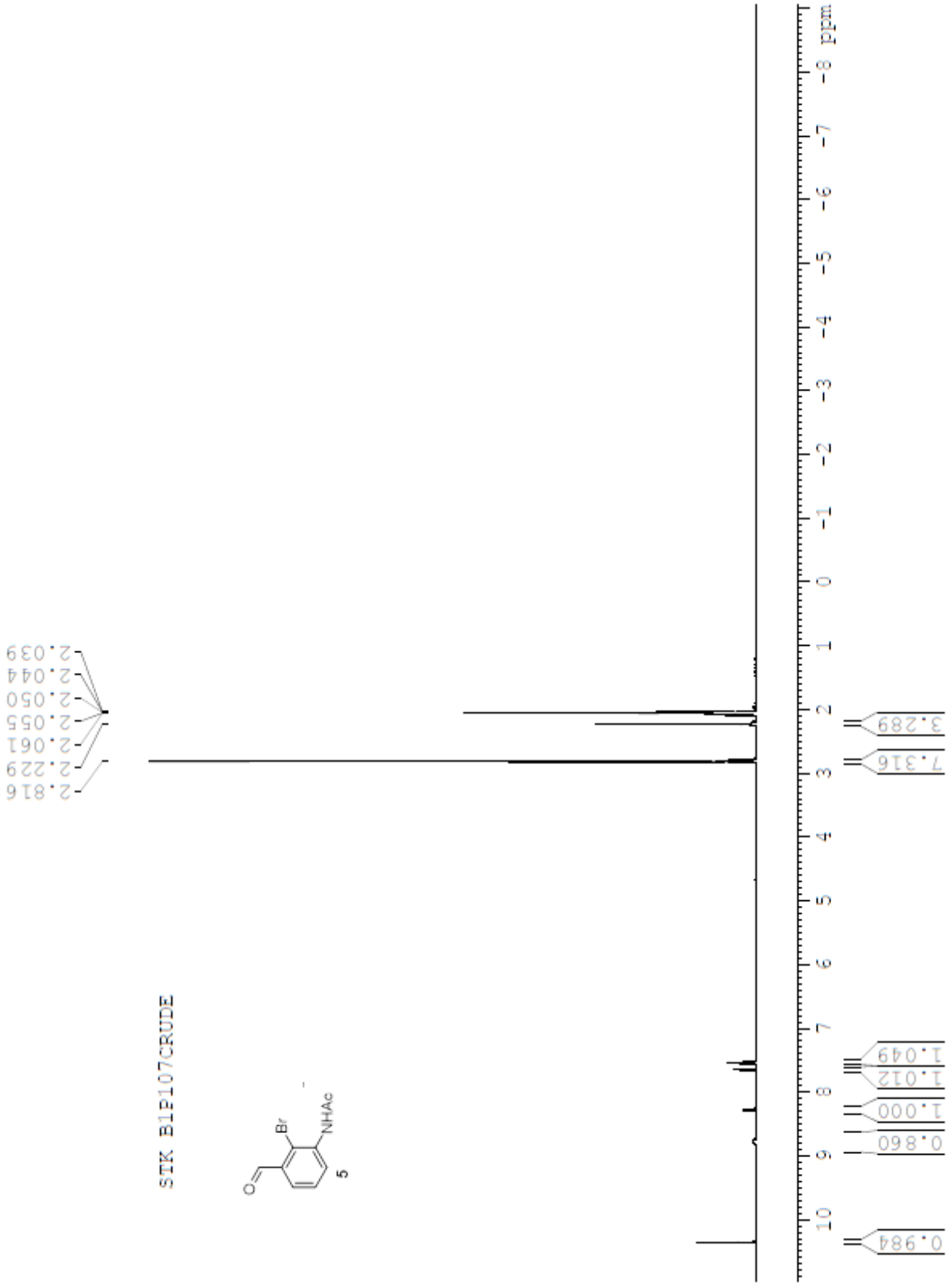
STK B1E107CRUDE
Br
NHAc
O
5
2.816
2.229
2.061
2.055
2.050
2.044
2.039
0.984
0.860
1.000
1.012
1.049
7.316
3.289
ppm

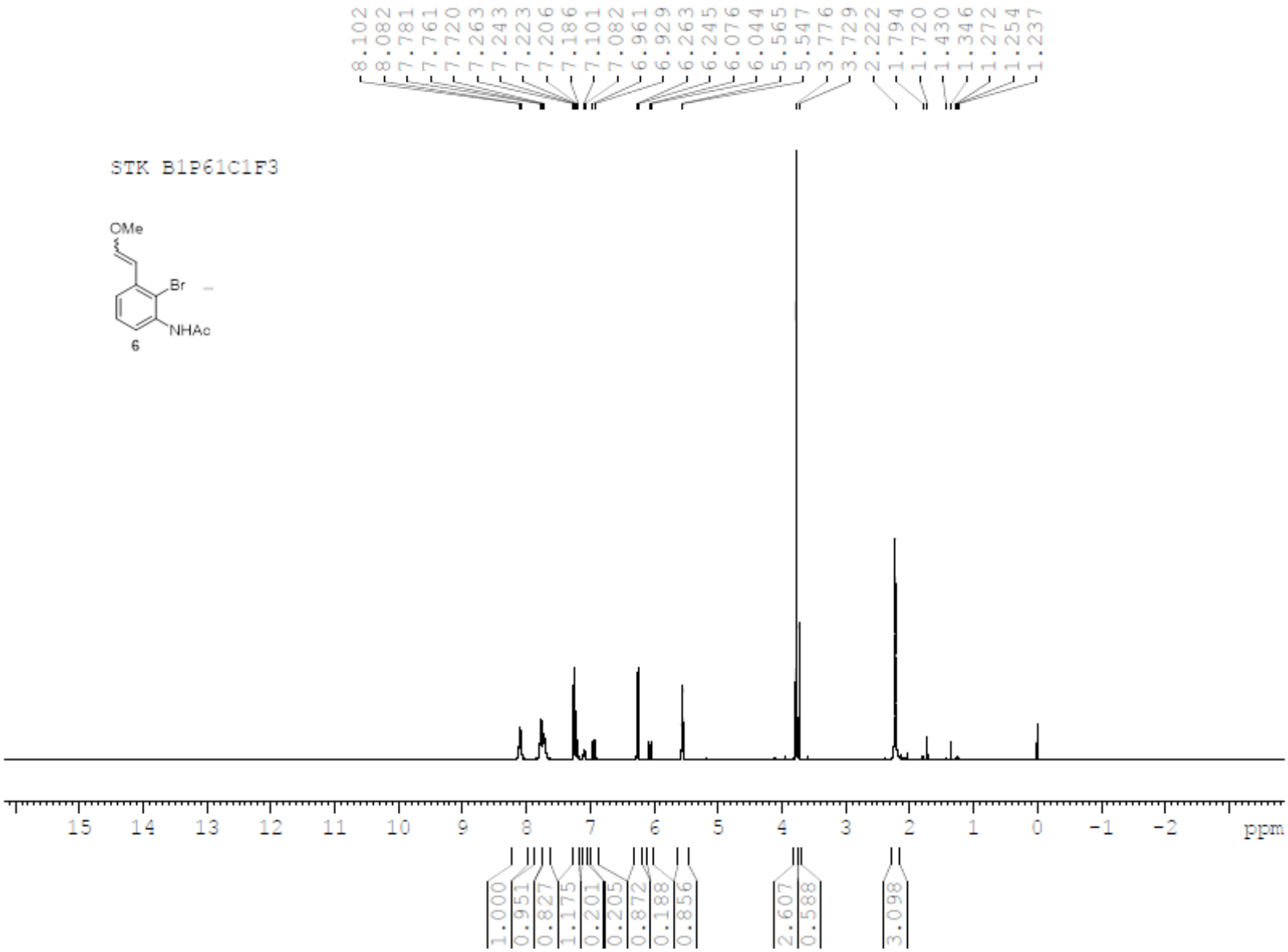
8.102
8.082
7.781
7.761
7.720
7.263
7.243
7.223
7.206
7.186
7.101
7.082
6.961
6.929
6.263
6.245
6.076
6.044
5.565
5.547
3.776
3.729
2.222
1.794
1.720
1.430
1.346
1.272
1.254
1.237
STK B1P61C1F3
OMe
Br
NHAc
6
15
14
13
12
11
10
9
8
7
6
5
4
3
2
1
0
-1
-2
ppm
1.000
0.951
0.827
1.175
0.201
0.205
0.872
0.188
0.856
2.607
0.588
3.098

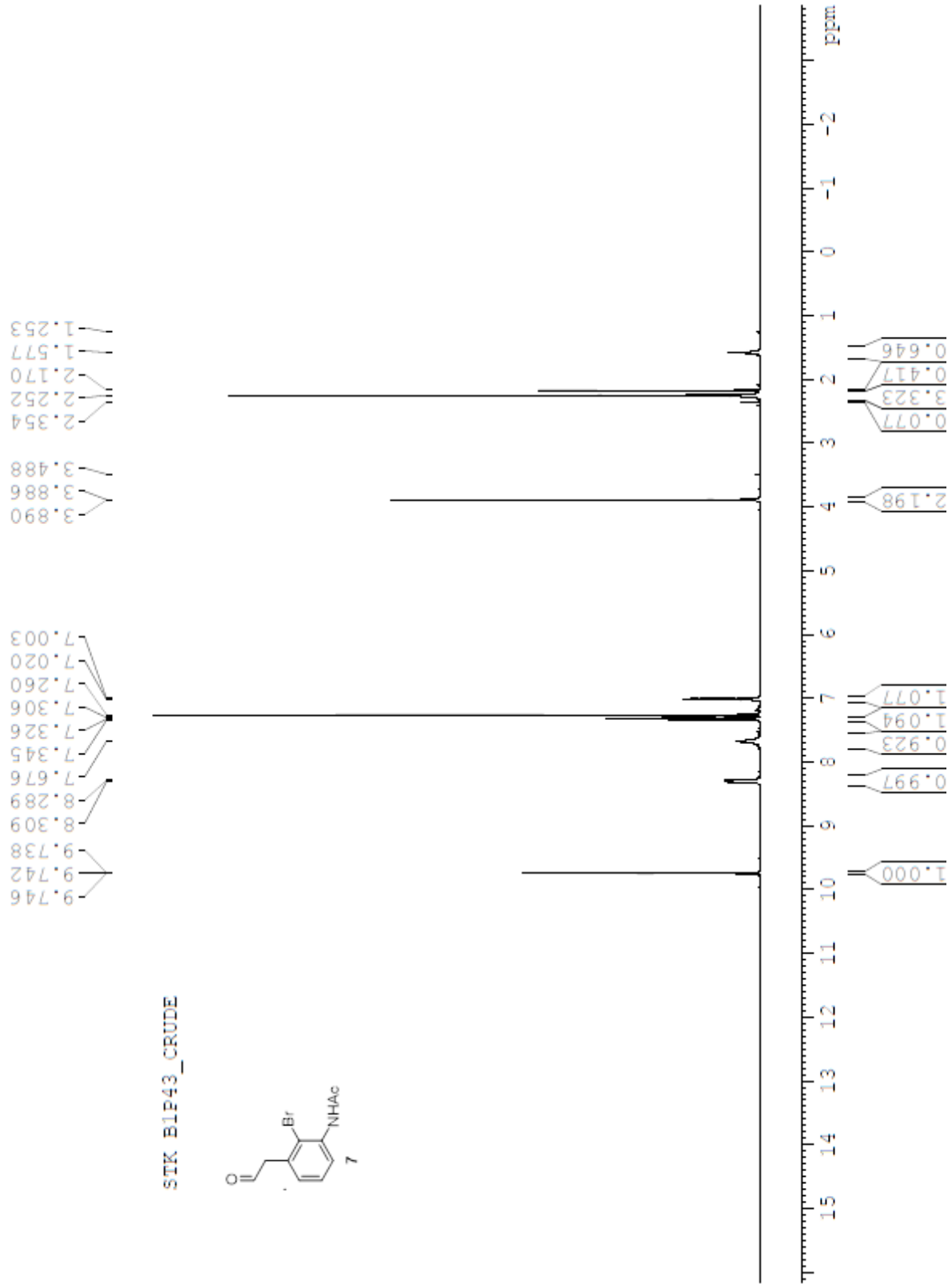
STK B1P43_CRUDE
O
Br
NHAc
7
9.746
9.742
9.738
8.309
8.289
7.676
7.345
7.326
7.306
7.260
7.020
7.003
3.890
3.886
3.488
2.354
2.252
2.170
1.577
1.253
1.000
0.997
0.923
1.094
1.077
2.198
0.646
0.417
3.323
0.077
ppm
15
14
13
12
11
10
9
8
7
6
5
4
3
2
1
0
-1
-2

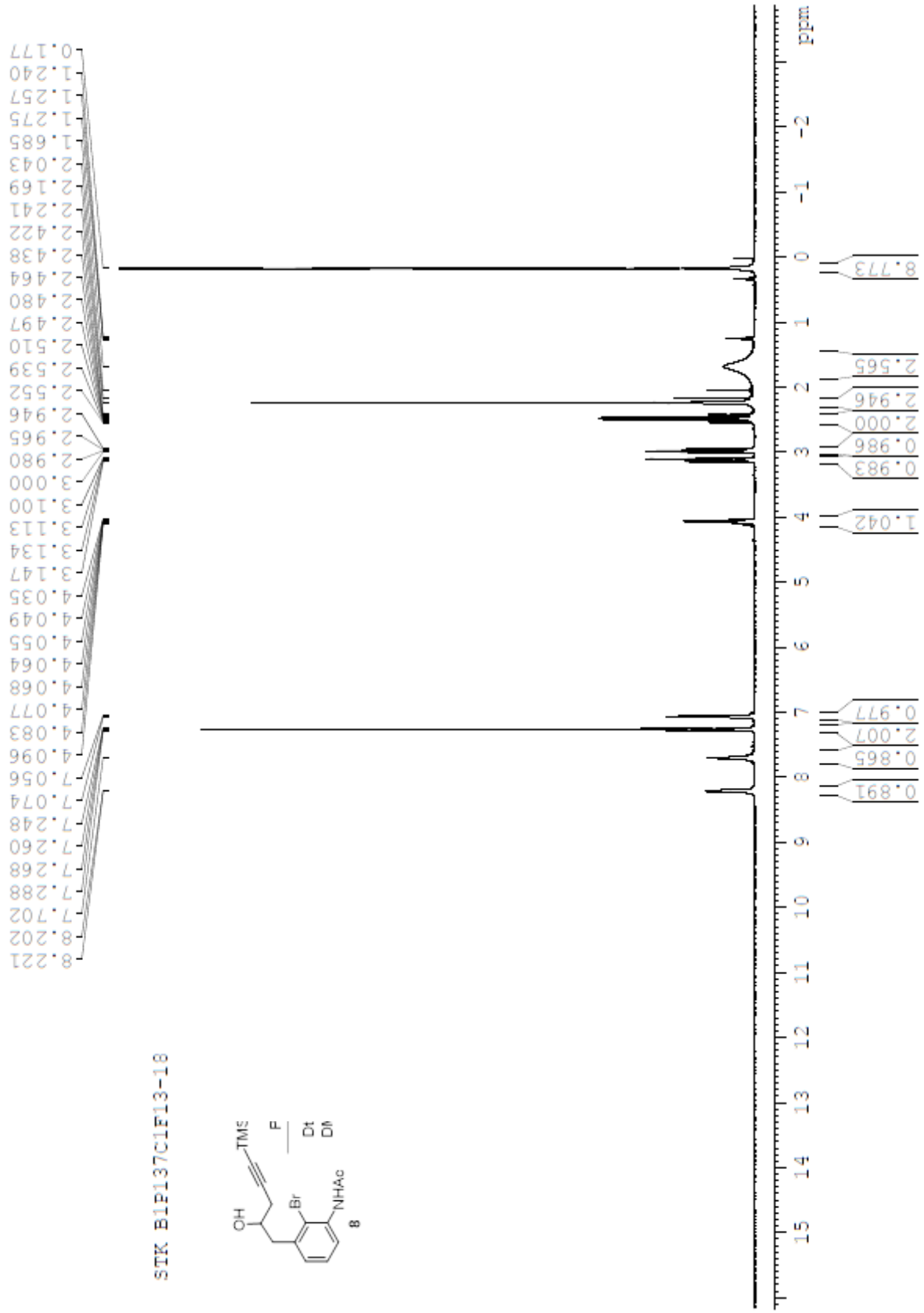
STK B1P137C1F13-18
OH
TMS
F
Br
NHAc
8
Dt
DM
ppm
8.773
2.565
2.946
2.000
0.986
0.983
1.042
0.977
2.007
0.865
0.891
8.221
8.202
7.702
7.288
7.268
7.260
7.248
7.074
7.056
4.096
4.083
4.077
4.068
4.064
4.055
4.049
4.035
3.147
3.134
3.113
3.100
3.000
2.980
2.965
2.946
2.552
2.539
2.510
2.497
2.480
2.464
2.438
2.422
2.241
2.169
2.043
1.685
1.275
1.257
1.240
0.177

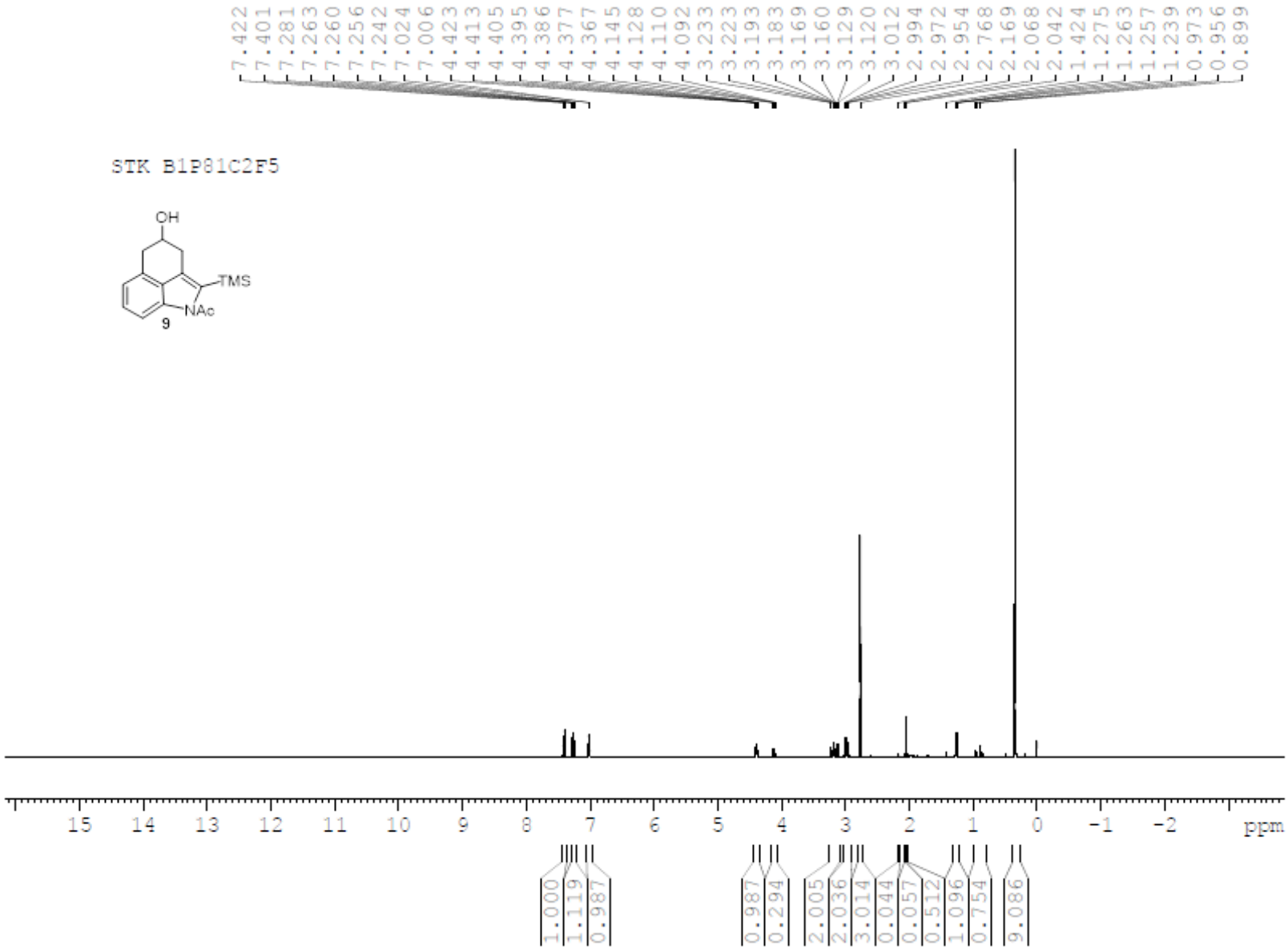
7.422
7.401
7.281
7.263
7.260
7.256
7.242
7.024
7.006
4.423
4.413
4.405
4.395
4.386
4.377
4.367
4.145
4.128
4.110
4.092
3.233
3.223
3.193
3.183
3.169
3.160
3.129
3.120
3.012
2.994
2.972
2.954
2.768
2.169
2.068
2.042
1.424
1.275
1.263
1.257
1.239
0.973
0.956
0.899
STK B1P81C2F5
OH
TMS
NAc
9
15
14
13
12
11
10
9
8
7
6
5
4
3
2
1
0
-1
-2
ppm
1.000
1.119
0.987
0.987
0.294
2.005
2.036
3.014
0.044
0.057
0.512
1.096
0.754
9.086

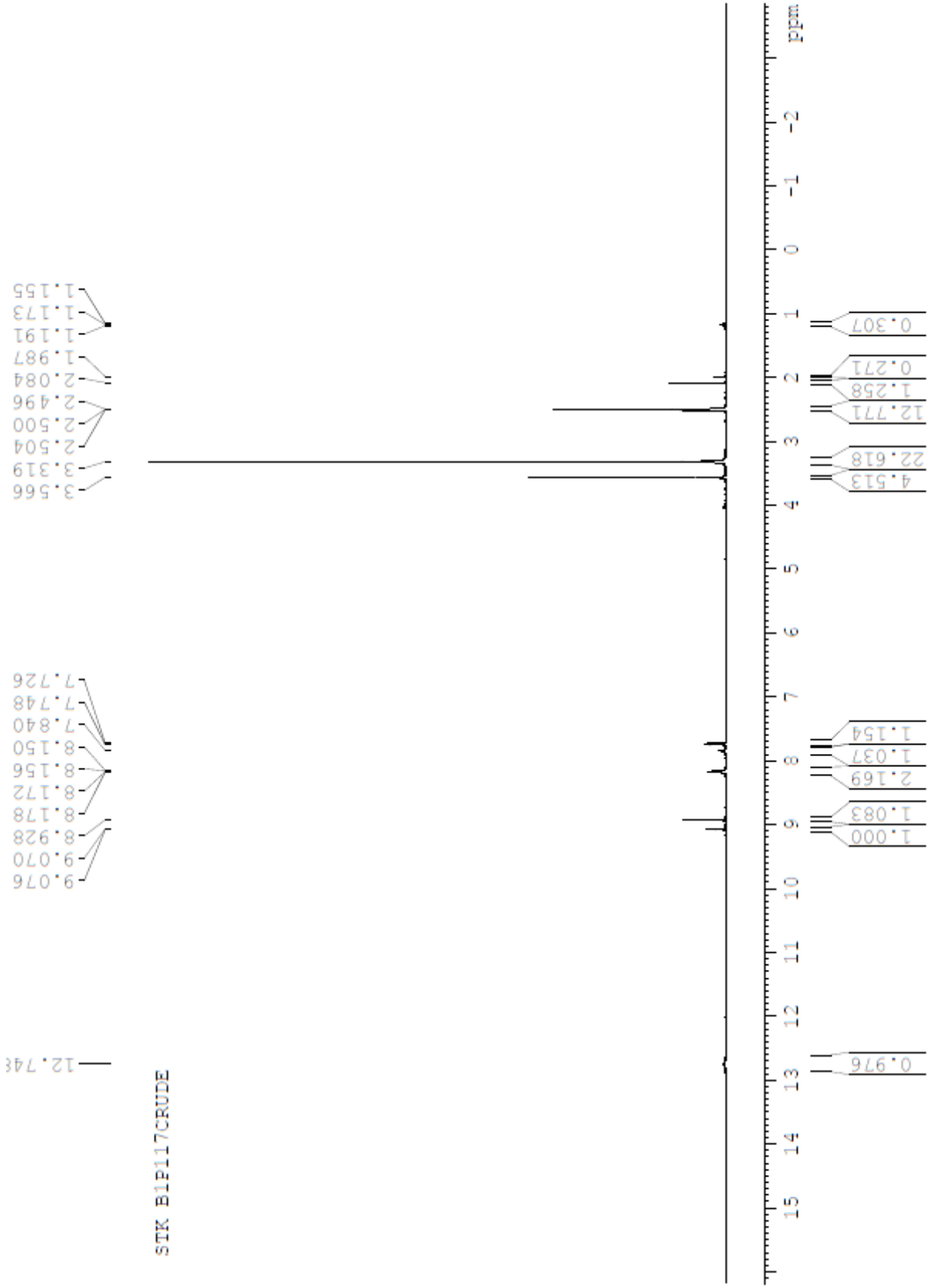
STK B1P117CRUDE
ppm
12.743
9.076
9.070
8.928
8.178
8.172
8.156
8.150
7.840
7.748
7.726
3.566
3.319
2.504
2.500
2.496
2.084
1.987
1.191
1.173
1.155
0.976
1.000
1.083
2.169
1.037
1.154
4.513
22.618
12.771
1.258
0.271
0.307

Appendix B: Curriculum Vitae

CV begins on the following page.

SPENCER KIM

Phone: (443) 822-9209
Email: skim180@syr.edu

EDUCATION

PhD Syracuse University, Chemistry — Anticipated: May 2024
Advisor: Rachel Steinhardt

PhM Syracuse University, Chemistry — May 2020
Advisor: Rachel Steinhardt

BS University of Maryland, College Park, Chemistry — May 2016

INDUSTRY AND RESEARCH EXPERIENCE

Chemistry Doctoral Program, Syracuse University, Syracuse, NY 2018-Ongoing
Advisor: Dr. Rachel Steinhardt
Thesis work was highly interdisciplinary focusing on development of chemical biological tools to visualize dynamic biological processes using small molecule ligands. Advancements to the field included elucidation of signaling pathway disruptions caused by commonly prescribed Parkinson's drugs through the development and application of DRD2 photoaffinity ligands. Other advancements included the development of novel photo-controlled neuronal perturbation techniques that allow for previously inaccessible levels of spatiotemporal control of neuronal signaling using photo-released small molecule drugs. Contributions to the field of protein biology and virology included reduction of *Dabie bandavirus* virulence through characterization and genetic modulation of liquid-liquid phase separating properties of NSs, a key immune suppressing protein. Advancements in the field of smart materials included the development and applications testing of thermally expandable microspheres and liquid-marble soft actuators as stimuli-responsive and biocompatible substrates.

Associate Scientist, **Pixelligent Technologies LLC**, Baltimore, MD 2017-2018
Direct supervisor: Dr. Sirpil Gonen Williams
Projects involved development and characterization of high refractive index zirconia nanoparticle-polysiloxane composite optical adhesives. Major responsibilities included independent formulation of composites, evaluation of thin-film and bulk polymer physical properties, and thermal stability testing.

Associate Scientist, Happy Farm Botanicals, Odenton, MD 2016-2017
Direct Supervisor: Ronald Cruz
Projects involved development, large batch formulation, and stability testing of cosmetics. In addition to development of cosmetic formulations, acquisition and

communication with clients throughout the product development process was a critical role for this position.

PUBLICATIONS

1. **Kim S. T.**, Doukmak E. J., Shanguhyia M., Gray D. J., Steinhardt R. C. "Photoactivatable Agonist-Antagonist Pair as a Tool for Precise Spatiotemporal Control of Serotonin Receptor 2C Signaling". *ACS Chem Neurosci.* 2023 Oct 4;14(19):3665-3673.

2. Gomez, J. C., Vishnosky, N. S., **Kim S. T.**, Grafstein, J. T., Steinhardt, R. C., "Robotic locomotion and Piezo1 activity controlled with novel liquid marble-based soft actuators" Adv. Funct. Mat. 2023, 202214893..

3. **Kim, S. T.,** Gray, D. J., Shanguhyia, M., Steinhardt, R. C., "Photoactivable WAY-161503 and Desmethylclozapine for Tight Regulation of Serotonin Receptor 2C Signaling" ChemRxIV 2022. DOI:10.26434/chemrxiv-2022-mg53z

4. Gomez, J. C., Vishnosky, N. S., **Kim, S. T.**, Dinca, S. M., Steinhardt, R. C., "Near-IR actuator bimorphs: soft robot locomotion and Piezo protein activation" ChemRxiv. 2022 DOI: 10.26434/chemrxiv-2022-gfzjs

5. **Kim, S. T.,** Doukmak, E. J., Flax, R. F., Gray, D. J., Zirimu, V. N., Jong, E. D., Steinhardt, R. C. "Developing Photoaffinity Probes for Dopamine Receptor D2 to Determine Targets of Parkinson's Disease Drugs" ACS Chemical Neuroscience 2022 13 (20), 3008-3022 DOI: 10.1021/acschemneuro.2c00544 ***Featured as an ACS Editors' Choice Article***

6. Gomez, J. C., Vishnosky, N. S., Grafstein, J. T., **Kim, S. T.,** Steinhardt, R. C., "Thermally expandable microspheres with high expansion ratios: Design of core and shell for largest size change" J. Appl. Polym. Sci. 2022, e52517.

7. Vishnosky, N., Gomez, J.C., **Kim, S. T.,** Doukmak, E.J., Grafstein, J., Steinhardt, R.C., "Micron-scale soft actuators fabricated from multi-shell polystyrene particle-gold nanoparticle nanohybrids" Macromol. Mater. Eng. 2021, 306, 21002222021. ***Featured as a merit-based cover article***

8. Wu, M., Moser, B.A., Steeves, T.M., Figueroa, A., Wallace, B.M., **Kim, S. T.,** Esser-Kahn A.P., Steinhardt, R.C., "Photon upconversion for the enhancement of microfluidic photochemical synthesis", RCS Advances, 2019, 9, 26172

TEACHING EXPERIENCE

Discipline-based Education Research, Syracuse University. March 2022-Ongoing
Advisor: Dr. Jonathan French
Novel active learning methods were designed for, and implemented in, a large-format general chemistry course. Surveys were developed to quantitatively measure impact on sense of student belonging and science identity.

Mentored Independent Teaching Experience, Syracuse University, Syracuse, NY
General Chemistry Lecture September 2022
Independently led a one semester large-format General Chemistry lecture, where I incorporated active small group problem solving to encourage student participation and increase student engagement. Teaching experience was in consultation with Dr. Jonathan French, with weekly meetings to discuss strengths and areas for improvement in my teaching.

Teaching Assistant, Syracuse University, Syracuse, NY August 2018-Ongoing
Courses Taught:
General Chemistry
Practiced active learning techniques including small-group problem solving and weekly reflection.

General Chemistry lab
Encouraged active participation in the pre-lab lecture to reinforce key laboratory techniques that were used the current weeks experiment.

Organic Chemistry
Independently developed worksheets tailored to weekly feedback solicited from students. Implemented active learning techniques including small-group discussion that led to full-class discussion.

Guest Lectures
Organic Chemistry March 2022
General Chemistry June 2022

Undergraduate Research Mentorship

Name	Years mentored	Research area	Current position
Raymond Flax	2018-2022	Mammalian protein expression and purification	UNC-Chapel Hill, Pharmaceutical Sciences PhD student.
Morgan Storino	2019-2022	Genetic engineering, bacterial protein expression	Temple University, Medical School, MD program.
Keely Tinsley	2019-2022	Tissue culture and molecular biology	Medical intern.
Dylan Gray	2018-2022	Organic synthesis	EMT Basic, Freedom EMS
Katherine Winebrake	2018-2021	Recombinant protein purification	Boston University, Dental School, DDS program.
Ryan Hunady	2019-2021	Recombinant protein purification	Ohio State University, Chemistry MS student
Nathan Rowell	2019-2021	Recombinant protein purification	Medical intern.
Matthew Washburn	2018-2020	Organic synthesis	Curia, Associate R&D scientist
Michelle Shanguhyia	2020-Ongoing	Organic synthesis, Mammalian protein expression	Undergraduate researcher
Deva Mark	2020-Ongoing	Recombinant protein purification, Tissue culture	Undergraduate researcher
Betul Bektas	2021-Ongoing	Tissue culture and molecular biology	Undergraduate researcher
Didier Dumervil	2021-Ongoing	Tissue culture and molecular biology	Undergraduate researcher

PRESENTATIONS

1. **Kim, S. T**., Steinhardt, R. C., (2022) Photo-controlled serotonin receptor modulation as a model for neuron signaling using non-neuronal cell lines. ***Poster presentation*** at the ACS Division of Biological Chemistry Graduate Student Symposium, Chicago, IL.

2. **Kim, S. T**., Steinhardt, R. C., (2022) Interacting with Interactions: Design and Evaluation of Clickable Photoaffinity Ligands for the Human Dopamine D2 Receptor. ***Oral presentation*** at the 2022 American Chemical Society (ACS) National Meeting, Chicago, IL.

3. **Kim, S. T**., Steinhardt, R. C., (2022) Photo-controlled serotonin receptor modulation as a model for neuron signaling using non-neuronal cell lines. ***Poster presentation*** at the ACS Diversity, Equity, and Inclusion Reception, Chicago, IL.

4. **Kim, S. T**., Steinhardt, R. C., (2022) Photo-controlled serotonin receptor modulation as a model for neuron signaling using non-neuronal cell lines. ***Oral presentation*** at the Buffalo Chemistry Graduate Student Symposium (GSS), Buffalo, NY.

5. **Kim, S. T**., Steinhardt, R. C., (2021) Interacting with Interactions: Design and Evaluation of Clickable Photoaffinity Ligands for the Human Dopamine D2 Receptor. ***Poster presentation*** at the American Chemical Society (ACS) National Meeting, Atlanta, GA.

6. **Kim, S. T**., Steinhardt, R. C., (2021) Interacting with Interactions: Design and Evaluation of Clickable Photoaffinity Ligands for the Human Dopamine D2 Receptor. ***Poster presentation*** at the Neuroscience Research Symposium, Syracuse, NY.

AWARDS AND HONORS

Pfizer/ACS Travel and Research Award	June 2022
Division of Biological Chemistry Travel Award	August 2022
GSO Professional, Academic, and Creative Work Grant (2x)	May 2021/2022

COMMUNITY OUTREACH

Chemistry Graduate Student Association, Chair, Syracuse University.	2021-Ongoing
Professional Development Committee, Chair, CGSA	2021-Ongoing
Graduate Student Organization (GSO), Senator, Syracuse University.	2021-Ongoing
Civic Engagement and Community Outreach Committee, Member, GSO	2021-Ongoing
Engineering Ambassadors, Volunteer, Syracuse University	2022-Ongoing
Chemistry Graduate Student Symposium, Oral Session Moderator	May 2022

PROFESSIONAL TRAINING

Certificate in University Teaching, Syracuse University	2022
Future Professoriate Program, Syracuse University.	2021-Ongoing

PROFESSIONAL AFFILIATIONS

American Chemical Society, Division of Medicinal Chemistry	2021-Ongoing
American Chemical Society, Division of Organic Chemistry	2021-Ongoing
American Chemical Society, Division of Chemical Education	2022-Ongoing

REFERENCES

Dr. Rachel Steinhardt, Assistant Professor
Department of Chemistry
Department of Biomedical and Chemical Engineering
Syracuse University
3-008 Center for Science and Technology
Syracuse, NY 13244
Phone: 315.443.2127
Email: rcsteinh@syr.edu

Dr. Jonathan French, Associate Teaching Professor
Department of Chemistry
Syracuse University
4-014D Center for Science and Technology
Syracuse, NY 13244
Phone: 315.443.3743
Email: jmfrench@syr.edu

Dr. John Chisholm, Professor
Department of Chemistry
Syracuse University
4-006 Center for Science and Technology
Syracuse, NY 13244
Phone: 315.443.6894
Email: jdchisho@syr.edu